

Northumbria Research Link

Citation: Mansour Abadi, Mojtaba (2017) A hybrid free space optics/radio frequency antenna - design and evaluation. Doctoral thesis, Northumbria University.

This version was downloaded from Northumbria Research Link:
<https://nrl.northumbria.ac.uk/id/eprint/36012/>

Northumbria University has developed Northumbria Research Link (NRL) to enable users to access the University's research output. Copyright © and moral rights for items on NRL are retained by the individual author(s) and/or other copyright owners. Single copies of full items can be reproduced, displayed or performed, and given to third parties in any format or medium for personal research or study, educational, or not-for-profit purposes without prior permission or charge, provided the authors, title and full bibliographic details are given, as well as a hyperlink and/or URL to the original metadata page. The content must not be changed in any way. Full items must not be sold commercially in any format or medium without formal permission of the copyright holder. The full policy is available online: <http://nrl.northumbria.ac.uk/policies.html>

Northumbria Research Link

Citation: Mansour Abadi, Mojtaba (2017) A hybrid free space optics/radio frequency antenna - design and evaluation. Doctoral thesis, Northumbria University.

This version was downloaded from Northumbria Research Link:
<http://nrl.northumbria.ac.uk/id/eprint/36012/>

Northumbria University has developed Northumbria Research Link (NRL) to enable users to access the University's research output. Copyright © and moral rights for items on NRL are retained by the individual author(s) and/or other copyright owners. Single copies of full items can be reproduced, displayed or performed, and given to third parties in any format or medium for personal research or study, educational, or not-for-profit purposes without prior permission or charge, provided the authors, title and full bibliographic details are given, as well as a hyperlink and/or URL to the original metadata page. The content must not be changed in any way. Full items must not be sold commercially in any format or medium without formal permission of the copyright holder. The full policy is available online: <http://nrl.northumbria.ac.uk/policies.html>



**Northumbria
University**
NEWCASTLE



UniversityLibrary

A Hybrid Free Space Optics/Radio Frequency Antenna – Design and Evaluation

Mojtaba Mansour Abadi

A thesis submitted in partial fulfilment of
the requirements of the University of
Northumbria at Newcastle for the degree of
Doctor of Philosophy

Research undertaken in the School of Computing,
Engineering and Information Sciences

January 2017

Abstract

Free space optical (FSO) communication provides high speed data communications with high flexibility and cost-effectiveness. However, FSO links are sensitive to atmospheric effects such as fog, smoke and turbulence. To address the problem, this research is investigating a hybrid FSO and RF technology to ensure link availability under all weather conditions as part of the last mile access networks. The research exclusively investigates design, implementation, and assessment of a novel dual purpose hybrid FSO/RF antenna. The technical issues are interference between FSO and RF parts; compactness of the design; quality of service; and robustness. As part of the design a conventional RF antenna scheme, known as Cassegrain antenna is adopted, and a new design scheme for a hybrid antenna is proposed. For the FSO part an optical transceiver aperture, which is composed of optical lenses and optical fibres, is designed and incorporated in the shadowing region of the sub-reflector of Cassegrain antenna. The use of lens and fibre ensures the isolation between the optical and RF parts. Based on the initial design, modifications are made to enhance the hybrid antenna performance. In this work the focus of the research is on the optical part and how it is incorporated as part of the RF antenna. As part of the optical design, spatial diversity and differential signalling techniques are adopted. Majority-logic combining is adopted from RF technology and the performances of a FSO system implementing combining methods are compared for various turbulent regimes. The concept of differential signalling is investigated in terms of the channels correlation and it is shown that the variation of the detection threshold level reduces in correlated channels. A new design method is given based on spatial

diversity and differential signalling techniques. To simulate the RF part, CST STUDIO SUITE® software is used, whereas Monte-Carlo simulation is used for performance estimation of the FSO link. Also provided are the detailed mathematical modelling of the hybrid FSO/RF system. The proposed hybrid antenna is fabricated and evaluated and results are compared with simulation and predicted data. Based on the recorded data of a real hybrid FSO/RF channel the performance of hybrid FSO/RF link employing the hybrid antenna with a switching mechanism is evaluated. Through this thesis, the detailed guidelines on design of the hybrid antenna are outlined and when necessary, the significant issues are discussed and addressed. Since the propose of this PhD is to outline and demonstrate the proof of concept for the proposed hybrid antenna, therefore the focus has been on the design, evaluation and the minimum performance requirements rather than the best possible performance or optimising the communication link quality. The outcome of the thesis will be a prototype antenna with a gain of 29.2 dBi and efficiency of 59 % at the frequency of 10 GHz for use in a hybrid FSO/RF system. It will be shown that the designed antenna is able to provide a hybrid link with 99.8 % availability and 1 Gbits/sec data rate at the recorded fog and rain channel conditions.

Table of Contents

Abstract	ii
List of Figures	xi
List of Tables	xxiii
Glossary of Abbreviations	xxvi
Glossary of Symbols	xxix
Dedications	xxxiv
Acknowledgments	xxxv
Declarations	xxxvii

1 Introduction	1
1.1 Introduction to Free Space Optics	1
1.2 FSO Communications	3
1.2.1 Background	3
1.2.2 FSO Structure	6
1.3 Hybrid Link	10
1.4 Problem Statement	12
1.5 Aim and Objectives	14
1.6 Original Contributions	16
1.7 Publications and Awards	19
1.7.1 Journal Papers:	19
1.7.2 Conference Papers:	20
1.7.3 Awards	21
1.8 Thesis Structure	21

2 Fundamentals of FSO, RF and Hybrid FSO/RF **22**

2.1 Introduction	22
2.2 FSO	22
2.3 RF	28
2.4 Hybrid FSO/RF	33
2.4.1 Switching Methods	36
2.5 Summary	38

3 FSO Spatial Diversity **40**

3.1 Introduction	40
3.2 Turbulence	41
3.3 Spatial Diversity Configuration	45
3.4 Channel Model in SISO and SIMO	46
3.5 Combining Methods	48
3.6 Weak Turbulence	49
3.6.1 Adaptive Optics Technique	49
3.6.2 SISO and EGC	51
3.6.3 SC	52
3.6.4 MLC	52
3.6.5 Numerical Analysis	53
3.7 Strong Turbulence	57
3.7.1 SISO and EGC	58
3.7.2 SC	58
3.7.3 MLC	59
3.7.4 Numerical Analysis	59
3.8 Summary	63

4 A FSO Link With Differential Signalling 64

4.1 Introduction	64
4.2 Differential Signalling Configuration	67
4.3 Differential Signalling and Turbulence	70
4.3.1 Optimal Detection Threshold Level	70
4.3.2 Correlation Between Channels	71
4.3.3 Channel Modelling	72
4.3.4 BER Expression	79
4.3.5 Numerical Analysis	80
4.3.6 Atmospheric Turbulence Experiment	89
4.4 Differential Signalling and Pointing Errors	96
4.4.1 Channel Modelling	96
4.4.2 Pointing Errors Experiment	100
4.5 Differential Signalling and Manchester Code	103
4.5.1 System Configuration	103
4.5.2 Manchester Code Experiment	105
4.6 Summary	108

5 Hybrid FSO/RF Antenna 110

5.1 Introduction	110
5.2 Antenna Specifications	111
5.3 Antenna Base Structure	112
5.4 Reflector Antenna	113
5.5 First Hybrid FSO/RF Antenna Design	122
5.5.1 Design	122
5.5.2 Simulations Results	123
5.5.2.1 Initial Design with no Tube and Collimator	125
5.5.2.2 Parametric Analysis with no Tube and Collimator	127

5.5.2.3 Optimised Design with Tube and no Collimator	127
5.5.2.4 Optimised Design with Strut and no Collimator	131
5.5.2.5 Optimised Design with Tube and Collimator	131
5.5.3 Hybrid Antenna Fabrication	135
5.5.4 Hybrid RF Antenna Characteristics	135
5.5.5 Hybrid FSO/RF Simplex Link	140
5.5.6 Required Modifications	143
5.6 Final Hybrid FSO/RF Antenna Design	144
5.6.1 RF Antenna	144
5.6.1.1 Cassegrain Antenna	146
5.6.1.2 Sub-reflector Shadow Region	148
5.6.1.3 The Sub-Reflector with Optical Fibre	149
5.6.1.4 Polyethylene Tube	150
5.6.1.1 Circular Feed, Rectangular to Circular Transition and Fibre in the Waveguide	152
5.6.1.2 E-Plane Bend and the Fibre Hole	153
5.6.2 FSO Antenna	154
5.6.3 Simulation Results	157
5.6.3.1 Initial Design	157
5.6.3.2 Parametric Analysis	159
5.6.3.3 Sub-reflector Misalignment Analysis	161
5.6.4 Design Steps Summary	163
5.6.5 Hybrid Antenna Fabrication	167
5.6.6 Hybrid Antenna Characteristics	167
5.6.7 Hybrid FSO/RF Simplex Link	174
5.6.7.1 Link Budget Analysis	174
5.6.7.2 Link Measurements	175
5.7 Detection Method	179
5.8 Summary	179

6 Hybrid FSO/RF Link 181

6.1 Introduction _____	181
6.2 FSO System Configuration _____	181
6.3 Switching Technique _____	182
6.4 System Specifications _____	184
6.5 Recorded Data _____	185
6.6 Simulation Procedure _____	188
6.7 Numerical Analysis _____	191
6.7.1.1 Fixed Link Distance _____	192
6.7.1.2 Fixed RF and FSO Data Rate _____	194
6.7.1.3 Maximum Average Hybrid Data Rate and Guaranteed Link Availability	195
6.8 Summary _____	197

7 Conclusions and Future Work 199

7.1 Conclusions _____	199
7.2 Future Work _____	202

Appendix A: Derivation of Mathematical Expressions 204

A.1 Introduction _____	204
A.2 BER Expression in Weak Turbulence _____	204
A.3 BER Expression in Strong Turbulence _____	205
A.4 Tolerance of Parameters in Differential Signalling technique _____	206
A.5 Applicable Formulas _____	207

Appendix B: Simulation **209**

B.1 Introduction	209
B.2 CST STUDIO SUITE®	209
B.3 AWR Design Environment	210
B.4 Monte-Carlo Method	212

Appendix C: Experimental Setups **215**

C.1 Introduction	215
C.2 RF Setups	215
C.2.1 Tx Module	215
C.2.2 Rx Module	217
C.2.3 RF Transceiver	218
C.2.4 Antenna	225
C.3 FSO Setups	230
C.3.1 Optical Transceiver Aperture	230
C.4 Antenna Components Dimensions	236

Appendix D: Experimental Measurements **237**

D.1 Introduction	237
D.2 RF Measurement	237
D.3 FSO Measurement	242

Appendix E: Student's t-test **248**

E.1 Introduction	248
E.2 Student's t-test	248

E.3 Results	249
-------------	-----

References	250
-------------------	------------

List of Figures

Figure 1.1: Variety of demands for high bit rate access to the data.	2
Figure 1.2: Comparison of communication technologies: (a) in terms of data rate and link coverage, figure taken from [17] with permission, and (b) in terms of cost and data rate (the figure is plotted using the data from [18]).	5
Figure 1.3: The fundamental system diagram of an FSO link. LD and PD are laser diode and photodetector, respectively.	7
Figure 1.4: Measured availability of RF, FSO and hybrid system in percentage versus measurement date. Measurement was taken from December 2001 to January 2003 at Graz University of Technology. FSO wavelength was 850 nm with total transmit power of 8 mW. The link distance was 2.7 km. More details are available in [37]. Figure is taken from [37] with permission.	11
Figure 1.5: Schematic diagram of a hybrid FSO/RF communication system. The original contributions are highlighted with dashed borders.	18
Figure 2.1: The block diagram of an IM/DD FSO communication link. LD, PD, TIA are laser diode, photodetector, and transimpedance amplifier, respectively.	23
Figure 2.2: The block diagram of an RF communication link.	29
Figure 2.3: Attenuations of an RF link due to the rain in Glasgow for various perception rate. 0.01, 0.1, and 1% refers to 25.5, 8.0, and 2.1 mm/h rainfall rate. Figure is taken from [72] with permission.	32
Figure 2.4: Attenuations of an RF link due to the free space path loss (FSPL) against frequency.	32
Figure 2.5: Reflector antenna gain nomograph. The graph is for an antenna with 100% efficiency. Figure is taken from [75] which is open to public.	33
Figure 2.6: FSO and RF link attenuations versus link distance for different channel conditions. The RF and FSO detection threshold show the achievable level of the distance, within which the link is available with BER of 10^{-6} .	34

Figure 2.7: Three hybrid FSO/RF configurations: (a) hybrid FSO/RF switch-over link, (b) hybrid redundant RF link, and (c) hybrid channel coding link.	36
Figure 3.1: Turbulent channel frozen at $t=0$. The turbulent channel consists of eddies with various sizes.	41
Figure 3.2: Spatial diversity configurations [17]. SISO, SIMO, MISO, and MIMO denote single-input single-output, single-input multiple-output, multiple-input single-output, multiple-input multiple-output, respectively.	45
Figure 3.3: A simplified illustration of m -th FSO link in a single-input multiple-output scheme. LD and PD are laser diode and photodetector, respectively.	46
Figure 3.4: Comparison of single-input single-output performance (BER versus SNR) over clear, weak, moderate and strong turbulence regimes with and without aperture averaging. ‘Weak’, ‘Mod’ and ‘Str’ refer to weak, moderate and strong regimes, respectively. ‘+AF’ denotes applying aperture averaging.	47
Figure 3.5: A typical single-input single-output FSO Rx. The received signal is shown at optical, electrical and logical domain for bit stream of $\{1, 0, 1, 1, 0\}$. OptAp refers to the optical aperture.	48
Figure 3.6: Block diagram of combining implementation at different signal levels: (a) optical domain, (b-c) electrical domains, and (d) logical domain. OTx and OptAp and ORx refer to optical transmitter, optical aperture, and optical receiver, respectively.	50
Figure 3.7: Comparison of average BER for average SNR of 0 to 30 dB for different numbers of receiver apertures (M): (a) $M=2$, (b) $M=3$, and (c) $M=5$. Two turbulence regime sets of $\sigma_x=0.2$ and 0.5 have been calculated in each plot. SISO, AOT, EGC, SC, and MLC refer to single-input multiple-output, adaptive optical technique, equal gain combining, selective combining and bit-majority combining, respectively.	54
Figure 3.8: Normalized required optical received power versus the number of receiver apertures (M) for a BER of 10^{-6} at the Rx. The values are normalised with respect to single-input single-output (SISO). AOT, EGC, SC, and MLC refer to adaptive optical technique, equal gain combining, selection combining and majority-logic combining, respectively.	55
Figure 3.9: Normalized required optical received power versus the number of receiver apertures (M) for a BER of 10^{-6} at the Rx implementing EGC and MLC. The values are normalised with respect to SISO.	

EGC, and MLC refer to equal gain combining and majority-logic combining, respectively. _____ 56

Figure 3.10: BER versus SNR for EGC, SC, MLC and SISO. The comparison is carried out for different numbers of apertures (M) and turbulence strengths (C_n^2): (a) $C_n^2=3\times10^{-14} \text{ m}^{-2/3}$ ($\sigma_R^2=1.24$), and (b) $C_n^2=5\times10^{-14} \text{ m}^{-2/3}$ ($\sigma_R^2=2.06$). SISO, EGC, SC, and MLC refer to single-input multiple-output, equal gain combining, selection combining and majority-logic combining, respectively. _____ 59

Figure 3.11: BER versus SNR for EGC, SC, MLC and SISO optical link configurations implementing real aperture averaged Rx. The comparison is carried out for three receiver apertures (i.e., $M=3$), $C_n^2=5\times10^{-14} \text{ m}^{-2/3}$ and different aperture sizes d_s provided $d_0\approx 29$ mm: (a) $d_s=0.5d_0$, and (b) $d_s=d_0$. SISO, EGC, SC, and MLC refer to single-input multiple-output, equal gain combining, selection combining and majority-logic combining, respectively. _____ 61

Figure 4.1: The system block diagram to implement differential signalling in correlated-channels conditions. T is the bit duration. OTx, BC, BS, ORx and TIA refer to optical transmitter, beam combiner, beam splitter, optical receiver, and transimpedance amplifier, respectively. _____ 68

Figure 4.2: Simulation results of: (a) mean of detection threshold $\text{Mean}(V_{\text{thresh}})$, (b) standard deviation of detection threshold $\sqrt{\text{Var}(V_{\text{thresh}})}$, and (c, d) Q-factor versus Rytov variance (σ_R^2). The comparison is performed for a range of turbulences and SNRs for: (a) and (b) $\varepsilon_i=10$, (c) $\varepsilon_i=5$, and (d) $\varepsilon_i=10$. SISO and DS refer to single-input single-output and differential signalling, respectively. ε_i and $\rho_{1,2}$ denote extinction ratio and correlation coefficient, respectively. Note that in (c) and (d) the error bars are too small to be seen. _____ 83

Figure 4.3: $\Delta\lambda/\lambda_0$ plotted with respect to d_r/ρ_0 . The graph shows the relation between the tolerable optical sources wavelengths and the distance between the optical receivers, while the channels are kept independent. The graph is obtained from Equ. (4.28). _____ 85

Figure 4.4: Simulation results of: (a) mean of detection threshold $\text{Mean}(V_{\text{thresh}})$, (b) standard deviation of detection threshold $\sqrt{\text{Var}(V_{\text{thresh}})}$, and (c) Q-factor. The comparison is performed between single-input single-output (SISO) link and differential signalling (DS) and for different values of extinction ratios (ε_i) over a range of correlation coefficient ($\rho_{1,2}$). _____ 86

Figure 4.5: BER versus SNR in dB of an FSO system with the differential signalling method. The comparison is carried out for various

turbulence strengths (C_n^2) and correlation coefficients ($\rho_{1,2}$). Solid lines marked with small markers are based on the derived equations whilst large markers are obtained from the simulation. _____ 88

Figure 4.6: BER versus SNR in dB of an FSO system with the differential signalling method for $C_n^2=5\times10^{-15} \text{ m}^{-2/3}$ and a range of correlation conditions ($\rho_{1,2}$). Solid lines with small markers are based on theory whereas large markers are obtained from simulation. The plus marker denotes the clear channel condition. _____ 89

Figure 4.7: Block diagram of the atmospheric turbulence and differential signalling experiment. PATH1 and PATH2 are referring to uncorrelated and correlated paths, respectively. OTx, BS, OF, and ORx are optical transmitter, beam splitter, optical filter, and optical receiver, respectively. _____ 90

Figure 4.8: Experimental setup of atmospheric turbulence and differential signalling: (a) OTxs and ORxs at one end of the chamber, and (b) atmospheric chamber with temperature sensors to measure temperature gradient, and a pipe to isolate either PATH1 or PATH2 from the turbulent condition of the chamber. OF, OTx, ORx, and BS are optical filter, optical transmitter, optical receiver, and beam splitter, respectively. _____ 91

Figure 4.9: Histograms of the detection threshold levels of the differential signal threshold (V_{thresh}) for atmospheric turbulence and differential signalling experiment: (a) uncorrelated channels in dark room, (b) uncorrelated channels in lit room, (c) correlated channels in dark room, and (d) correlated channels in lit room. _____ 92

Figure 4.10: The sampled v_1 signal with the estimated detection threshold during atmospheric turbulence experiment. The signal is in blue colour, where the dashed red line with circle markers refers to the estimated detection threshold. _____ 93

Figure 4.11: Original (v_1 in yellow and top) and inverted (v_2 in green and bottom) signals captured on the oscilloscope during atmospheric turbulence experiment. _____ 94

Figure 4.12: Rx aperture and a laser beam footprint at the Rx transverse plane. _____ 96

Figure 4.13: Effect of building movement on FSO RxS with exaggeration. On the left there is the Tx building hypothetically without movement and on the right the RxS are installed on top of a building, which is influenced by the effect of building movement. _____ 99

Figure 4.14: The pointing errors and differential signalling experimental setup. OTx and ORx are optical transmitter and optical receiver, respectively.	100
Figure 4.15: An image taken from the oscilloscope screen during the pointing errors and differential signalling experiment. Top yellow signal is v_1 whereas bottom green one is v_2 .	101
Figure 4.16: The sampled v_2 signal with the estimated detection threshold during pointing errors and differential signalling experiment. The signal is blue colour where the dashed red line with circle markers refers to the estimated detection threshold.	101
Figure 4.17: Histogram of the detection threshold levels of the differential signal (V_{thresh}) for pointing errors and differential signalling experiment.	102
Figure 4.18: Jitter standard deviation of the equivalent differential signalling (DS) pointing errors versus correlation coefficient (ρ_{PE}), for the single-input single-output (SISO) system with differential signalling and for receiver diameter (d_s) of 20 cm, beam radius (w_{Rx}) of 100 cm, and jitter variances of 10 cm (i.e., $\sigma_{j,1}=\sigma_{j,2}=10$ cm).	103
Figure 4.19: The required signal processing to perform differential signalling using one FSO link. The procedure is shown for a sequence of 01101 bits as an example: (a) the required signal shaping at the Tx, and (b) the required signal recovery at the Rx where two samples (i.e., r_1 and r_2) are taken at the presented intervals.	104
Figure 4.20: The experimental setup: (a) equipment at the Tx side, and (b) artificial atmospheric channel. AWG and OTx denote arbitrary waveform generator and the optical source, respectively.	105
Figure 4.21: (a, b) histograms of the detection threshold levels of the single-input single-output link, (c, d) histograms of the detection threshold levels of the differential signalling (DS) link, (e, f) histograms of the Q-factor of the SISO link, and (g, h) histograms of the Q-factor of the differential signalling link. (a, c, e, f) are for clear conditions whereas (b, d, f, h) are for turbulent channel with $C_n^2=6.06 \times 10^{-11} \text{ m}^{-2/3}$.	107
Figure 5.1: (a) to (g) Different reflector antenna configurations, (h) proposed antenna configuration for the project. Hatched area labelled by 'A' is the empty available area in front of the sub-reflector.	115
Figure 5.2: X-pol discrimination versus the reflector offset angle. Figure is taken from [124] with permission.	117

Figure 5.3: Strut blockage overall efficiency versus fractional area blockage. Fractional area blockage is defined as the ratio of the effective blocked area by struts to the total area of aperture. Figure is taken from [69] with permission. _____	118
Figure 5.4: (a) Blockage efficiency versus the blockage ratio for illumination efficiency of 0.9. Figure is taken from [69] with permission, and (b) side-lobe level versus blockage ratio for various illumination forms. Figure is taken from [129] with permission. _____	119
Figure 5.5: The hybrid antenna with single collimator schematic diagram. _____	124
Figure 5.6: Simulation results for initial antenna design scheme with no optical part and tube: (a) antenna profile (the distance between the feed and sub-reflector is 38.96 mm), (b) E-, H-planes, and X-pol radiation normalised to the antenna gain of 28.8 dBi, and (c) return loss and voltage standing wave ration (VSWR) against frequency. _____	126
Figure 5.7: Parametric analysis on the initial design with no optical part and tube: (a) gain and X-pol discrimination, (b) side-lobe level in E- and H-planes, and (c) half-power beam-width (HPBW) in E- and H-planes. Negative displacement denotes moving the sub-reflector towards the feed. At displacement of 0 mm, the distance between the feed and sub-reflector is 38.96 mm. _____	128
Figure 5.8: Simulation results for the optimised antenna design scheme with no optical part and tube (the distance between the feed and sub-reflector is 40.96 mm): (a) E-, H-planes, and X-pol radiation normalised to the antenna gain of 29.1 dBi, and (b) return loss and voltage standing wave ration (VSWR) against frequency. _____	129
Figure 5.9: Simulation results for initial antenna design scheme with tube and no optical part: (a) antenna profile (the distance between the feed and sub-reflector is 40.96 mm), (b) E-, H-planes, and X-pol radiation normalised to the antenna gain of 30.0 dBi, and (c) return loss and voltage standing wave ration (VSWR) against frequency. _____	130
Figure 5.10: Simulation results for initial antenna design scheme with struts and no optical part: (a) antenna profile (the distance between the feed and sub-reflector is 40.96 mm), (b) E-, H-planes, and X-pol radiation normalised to the antenna gain of 29.1 dBi, and (c) return loss and voltage standing wave ration (VSWR) against frequency. _____	132
Figure 5.11: Simulation results for initial antenna design with single collimator design scheme including tube: (a) antenna profile (the distance between the feed and sub-reflector is 40.96 mm), (b) E-, H-planes, and X-pol radiation normalised to the antenna gain of 29.7 dBi, and (c) return loss and voltage standing wave ration (VSWR) against frequency. _____	133

Figure 5.12: Near field power distribution of the antenna with and without collimator for single aperture in E- and H-planes: (a) without collimator in E-plane, (b) without collimator in H-plane, (c) with collimator in E-plane, and (d) with collimator in H-plane. The distance between the feed and sub-reflector is 40.96 mm. _____	134
Figure 5.13: The hybrid antenna with single collimator under the pattern measurement test. The distance between the feed and sub-reflector is 40.96 mm. _____	135
Figure 5.14: The return loss simulation and measurement results of the antenna with tube and no collimator. _____	136
Figure 5.15: (a) Measured return loss of the antenna with single collimator before and after tuning, and (b) equivalent voltage standing wave ratio (VSWR) from the measurement before and after tuning. _____	137
Figure 5.16: Radiation pattern of hybrid antenna with single collimator measured in a near field chamber as well as the simulated one for: (a) E-plane, and (b) H-plane. _____	138
Figure 5.17: (a) hybrid link with single collimator antenna experimental block diagram, and (b) hybrid antenna far-field link setup. OTx, MPOF, and ORx refer to optical transmitter, multimode plastic optical fibre, and optical receiver, respectively. _____	141
Figure 5.18: Schematic diagram of the proposed hybrid antenna with multiple collimators. _____	145
Figure 5.19: Schematic diagram of a Cassegrain antenna. _____	146
Figure 5.20: Diagram of different shadow region approximations in front of sub-reflector. Two approximations are shown in this figure. The simplest one is outlined with vertical-hatched line, while the more accurate one is shown with horizontal-hatched line. The former is used in this project. _____	148
Figure 5.21: Diagram of the power leakage due to the fibre hole in the sub-reflector. P_1 , P_2 , and P_3 are RF power emerging from the feed, RF power reflected back towards the feed, and RF power leaked to the front of the sub-reflector. _____	150
Figure 5.22: Diagram showing the effect of tube on the radiation of the feed. _____	151
Figure 5.23: Schematic diagram of optical transceiver aperture. _____	154
Figure 5.24: Simulation results for initial antenna with multiple collimators design scheme based on steps given in Section 5.6.1: (a) antenna profile (the distance between the feed and sub-reflector is 37.2 mm and the sub-reflector diameter is 99 mm), and (b) E-, H-	

planes, and X-pol radiation normalised to the antenna gain of 28.2 dBi. _____ 159

Figure 5.25: Parametric analysis on the initial design with multiple collimator part and tube: (a) gain and X-pol discrimination, (b) side-lobe level in E- and H-planes, and (c) half-power beam-width (HPBW) in E- and H-planes. Negative displacement denotes moving the sub-reflector towards the feed. At displacement of 0 mm, the distance between the feed and sub-reflector is 40.96 mm. _____ 160

Figure 5.26: Simulated radiation pattern for optimised antenna with multiple collimators design scheme. The distance between the feed and sub-reflector is 40.96 mm and the sub-reflector diameter is 85 mm. E-, H-planes, and X-pol radiation are normalised to the antenna gain of 29.3 dBi. _____ 161

Figure 5.27: Near field power distribution of the antenna with and without optical aperture for multiple collimators scheme in E- and H-planes: (a) without optical aperture in E-plane, (b) without optical aperture in H-plane, (c) with optical aperture in E-plane, and (d) with optical aperture in H-plane. The distance between the feed and sub-reflector, the sub-reflector diameter, and the distance from the feed aperture to the main reflector apex are 40.96 mm, 85 mm and 57 mm, respectively. _____ 162

Figure 5.28: Misalignment analysis on the optimised design with no optical part and tube: (a, d) gain and X-pol discrimination, (b, e) side-lobe level in E- and H-planes, and (c, f) half-power beam-width (HPBW) in E- and H-planes. In (a-c) the angle is in vertical (E-plane) direction, whereas (d-f) the angle is in horizontal (H-plane) direction. The distance between the feed and sub-reflector is 40.96 mm. _____ 163

Figure 5.29: Fabricated hybrid antenna with multiple collimators under radiation pattern test. The distance between the feed and sub-reflector is 40.96 mm and the sub-reflector diameter is 85 mm. _____ 168

Figure 5.30: (a) Measured return loss of the antenna with multiple collimators before and after tuning, and (b) equivalent voltage standing wave ratio (VSWR) from the measurement before and after tuning. _____ 169

Figure 5.31: Radiation pattern of hybrid antenna with multiple collimators measured in a near field chamber as well as the simulated one for: (a) E-plane, and (b) H-plane. _____ 170

Figure 5.32: BER versus SNR for the FSO link with equal gain combining (EGC) and selection combining (SC) for two turbulence regimes. _____ 175

Figure 5.33: (a) Block diagram of the performed hybrid link test, and (b) image taken from the experimental hybrid link setup. _____	178
Figure 6.1: The block diagram of the proposed FSO link with hybrid antenna. OTx, SMF, MMF, OF, and ORx are optical transmitter, single mode fibre, multimode fibre, optical filter, and optical receiver, respectively. Green dashed line and solid red line corresponds to two separate wavelengths. _____	183
Figure 6.2: (a) Recorded visibility for January 2014; (b) histogram of recorded visibility. The spike is due to the measurement limitation of the gauge and the visibilities more than 20 km are truncated to 20km; (c) calculated q parameter based on the recorded visibility; and (d) FSO attenuation based on the recorded visibility. The average, standard deviation, minimum and maximum of the recorded visibility in this period are 11.76 km, 6.68 km, 0.14 km, and 20 km, respectively. _____	186
Figure 6.3: (a) Recorded precipitation for January 2014; (b) histogram of recorded precipitation, (c) processed precipitation per hour; and (d) RF attenuation due to the rain. The average, standard deviation, minimum and maximum of the recorded precipitation in this period are 38.05 mm, 12.01 mm, 1.4 mm and 102.3 mm, respectively. _____	187
Figure 6.4: The Flowchart of the time hysteresis (TH) switching process in a hybrid communication system. The TH delay is 10 seconds. _____	189
Figure 6.5: (a) Histogram of the FSO link status; (b) histogram of the RF link status; (c) histogram of active link; and (d) trace of active link versus time. _____	190
Figure 6.6: Minimum required received power versus data rate for FSO and RF links where the system parameters are based on the values from Table 6.1. _____	191
Figure 6.7: Required FSO transmit power versus data rate for 1 km long clear channel where the system parameters are based on the values from Table 6.1. _____	192
Figure 6.8: Hybrid link simulation for link distances of 500 m, 750 m, 1 km, and 1.5 km for FSO data rate of 100 Mbits/sec to 10 Gbits/sec: (a) link load, (b) average hybrid data rate, and (c) link availability. The RF link has a fixed data rate of 67 Mbits/sec and the other system parameters are according to Table 6.1. _____	193
Figure 6.9: Received RF power versus time of channel state. The RF link has a fixed data rate of 67 Mbits/sec, the link span is 1.5 km, and the other system parameters are according to Table 6.1. The black dashed line is the threshold level for acceptable RF performance. _____	194

Figure 6.10: Hybrid link simulation for FSO data rate of 100 Mbits/sec, 1 Gbits/sec, 5 Gbits/sec, and 10 Gbits/sec for link distance of 100 m to 4 km: (a) link load, (b) average hybrid data rate, and (c) link availability. The RF link has a fixed data rate of 67 Mbits/sec and the other system parameters are according to Table 6.1.	195
Figure B.1: Antenna physical structure modelled in CST Microwave Studio: (a) RF antenna without FSO aperture, (b) RF antenna with FSO implementing single collimator, and (c) RF antenna with FSO implementing multiple collimators.	210
Figure B.2: Microwave circuit schematic used in Microwave Office: (a) transmitter module and (b) receiver module.	211
Figure B.3: Block diagram of the performed FSO communication link in turbulence channel based on Monte-Carlo simulation.	212
Figure C.1: RF Tx module: (a) block diagram, (b) practical setup, and (c) packed Tx module. IF, LO BPF, and Amp are intermediate frequency, local oscillator, band-pass filter, and amplifier, respectively.	216
Figure C.2: Measured S parameters of the Tx module: (a) band-pass filter and (b) amplifier.	218
Figure C.3: RF Rx module: (a) block diagram, (b) practical setup, and (c) packed Rx module. LO, Amp, BPF, and IF are local oscillator, amplifier, band-pass filter, and intermediate frequency, respectively.	219
Figure C.4: Measured S parameters of the Rx module: (a) band-pass filter and (b) amplifier.	220
Figure C.5: Block diagram of the RF transceiver test in 1 m free space channel. The cable losses are also included in the diagram.	221
Figure C.6 – Part 1: Simulated and measured powers of the experiment setup in Figure C.5. Each measurement is labelled with corresponding alphabets in Figure C.1(a), Figure C.3(b) and Figure C.5.	222
Figure C.6 – Part 2: Simulated and measured powers of the experiment setup in Figure C.5. Each measurement is labelled with corresponding alphabets in Figure C.1(a), Figure C.3(b) and Figure C.5.	223
Figure C.7: RF Main reflector with given specification in Table C.3.	226
Figure C.8: Modelled sub-reflector in different views used for manufacturing procedure.	227

Figure C.9: A prototype of the printed sub-reflector: (a) without conductive cover and (b) with conductive cover. _____	228
Figure C.10: The Polyethylene tube used to hold sub-reflector. _____	228
Figure C.11: Assembled feed, circular to rectangular transition, bend, and waveguide to coaxial transition. _____	229
Figure C.12: Simulated normalised radiation pattern of the open-ended circular waveguide with an inner diameter of 23.8 mm. _____	229
Figure C.13: Rectangular waveguide tuner with two tuning arms in E- and H- planes. _____	230
Figure C.14: A prototype of the optical transceiver with single Tx/Rx collimator. _____	231
Figure C.15: Measured output radiation pattern of the collimator with SMF at 670 nm at different distances. _____	232
Figure C.16: Measured output radiation pattern of the collimator with MMF at 670 nm at 182 cm distance. _____	232
Figure C.17: The red laser to MMF fibre coupling structure. _____	233
Figure C.18: Coupling multimode fibres (MMFs) to optical receivers (ORxs). _____	234
Figure C.19: (a) Laser to PD connection block diagram, and (b) FSO experiment block diagram. SMF and MMF are multimode fibre and single-mode fibre, respectively. _____	235
Figure C.20: Sub-reflector, tube, and feed size and dimension diagram. _____	236
Figure D.1: RF received signal captured using the spectrum analyser: (a) received signal, (b) received signal after averaging, and (c) received signal with markers. _____	238
Figure D.2: The block diagram of the near-field system. AUT denotes antenna under test. _____	240
Figure D.3: (a) Near-field system used for radiation pattern measurement, and (b) produced results by NSI software. _____	241
Figure D.4: Performed return loss measurement for the same tuned antenna set and two different cable connections. _____	242
Figure D.5: The block diagram of the experimental FSO setup. This setup was used for turbulence assessment purposes. ORx, TIA, Si, OTx, LD, and AWG are optical receiver, transimpedance amplifier, i-th temperature sensor, optical transmitter, laser diode, and arbitrary waveform generator, respectively. _____	243

Figure D.6: Typical FSO experimental setup: (a) transmitter side, (b) channel, and (c) receiver side. OTx, AWG, ORx are optical transmitter, arbitrary waveform generator, and optical receiver, respectively. _____ 244

Figure D.7: The screenshot of the virtual instrument script created in NI LabVIEW. _____ 246

List of Tables

Table 3.1: Comparison of power gains of AOT, EGC, SC and MLC relative to SISO method for a BER= 10^{-6} under weak turbulence regimes (i.e., σ_x of 0.2 and 0.5). SISO, AOT, EGC, SC, and MLC refer to single-input multiple-output, adaptive optical technique, equal gain combining, selection combining and majority-logic combining, respectively. The values are obtained from the results in Figure 3.7. The gains are in dB and M is the number of receiver apertures.	55
Table 3.2: Comparison of power gains of AOT, EGC, SC and MLC relative to SISO method for a BER= 10^{-6} under strong turbulence regimes (i.e., σ_R^2 of 1.24 and 2.06). SISO, EGC, SC, and MLC refer to single-input multiple-output, equal gain combining, selection combining and majority-logic combining, respectively. The values are obtained from the results in Figure 3.10. The gains are in dB and M is the number of receiver apertures.	60
Table 4.1: The summary of FSO system properties used in the differential signalling simulation.	81
Table 4.2: The theoretical analysis accompanied by simulation of mean of detection threshold (Mean) and standard deviation of detection threshold ($\sqrt{\text{Var}}$) of single-input single-output (SISO) and differential signalling (DS) links for different extinction ratios (ϵ) of 5 and 10 but fixed $\Phi_1=\Phi_2=5.7$ mV, $\Phi_{\text{SISO}}=8.1$ mV, where channels are highly correlated $\rho_{1,2}=1$, and Rytov variance (σ_R^2) is 0.5.	82
Table 4.3: The setup parameters for atmospheric turbulence and differential signalling experimental.	93
Table 4.4: The summary of the experimental measurement results for turbulence effect on differential signalling. Mean (mv) and $\sqrt{\text{Var}}$ (mv), denote the measured mean of detection threshold, variance of detection threshold of the differential signal. C_n^2 and $\rho_{1,2}$ denote obtained turbulence strength and correlation coefficient.	94
Table 4.5: The summary of the measurements results for pointing errors and differential signalling experiment.	102
Table 4.6: The summary of the measurement for single-input single-output (SISO) differential signalling (DS) link. These results are for DS and Manchester code scheme.	106

Table 5.1: Required RF antenna specifications. _____	113
Table 5.2: Comparison between antenna schemes in Figure 5.1 according to the required specifications. _____	120
Table 5.3: Summary of all required RF antenna specifications. _____	122
Table 5.4: First hybrid antenna with single collimator prototype characteristics. _____	125
Table 5.5: The antenna (design with single collimator) characteristics obtained from simulation and measurement. X-pol disc, SLL, HPBW, and FNBW are X-pol discrimination, side-lobe level, half-power beam-width, and first null beam-width, respectively. _____	139
Table 5.6: The hybrid FSO/RF link characteristics. The antenna with single collimator is implemented in the link. _____	142
Table 5.7: RF antenna with multiple collimators parameters. “Initial Design” is based on the steps given in Section 5.6.1. “Modified Design” refers to design based on the experimental limitations. _____	157
Table 5.8: FSO aperture with multiple collimators parameters. NEP is the receiver noise equivalent power. _____	158
Table 5.9: Hybrid antenna design calculations based on the steps given in Section 5.6.4. _____	167
Table 5.10: The antenna (design with multiple collimators) characteristics obtained from simulation. X-pol disc, SLL, HPBW, and FNBW are X-pol discrimination, side-lobe level, half-power beam-width, and first null beam-width, respectively. _____	171
Table 5.11: The hybrid antenna calculated characteristics based on section 5.6.1. _____	173
Table 5.12: Comparison of gain, directivity and total efficiency (η_{CA}) of the antenna for design steps. _____	174
Table 5.13: FSO Link budget for different turbulence conditions and combining methods. _____	176
Table 5.14: Summary of the measured and predicted link characteristics of the hybrid link of 13.3 m. _____	177
Table 6.1: hybrid FSO/RF system parameters. _____	185
Table 6.2: Comparison between various hybrid system performances in terms of data rate and availability. _____	190
Table 6.3: Maximum average hybrid data rate and guaranteed link availability for various distances. The required FSO and RF data rates are denoted for each case and the other system parameters are	

according to Table 6.1. The FSO data rate range was from 10 Mbits/sec to 10 Gbits/sec, whereas the RF data rate range was from 1 Mbits/sec to 67 Mbits/sec. _____	197
Table B.1: Configuration used in CST Microwave Studio to simulate the antenna structure. _____	211
Table C.1: Tx module measured components characteristics at central frequency. CL, LO, IL, and NF are conversion loss, local oscillator, insertion loss, and noise figure, respectively. _____	217
Table C.2: Rx module measured components characteristics at the central frequency. CL, LO, IF, IL, and NF are conversion loss, local oscillator, intermediate frequency, insertion loss, and noise figure, respectively. _____	220
Table C.3: Main reflector characteristics summary. _____	226
Table C.4: Sub-reflector dielectric material characteristics summary. _____	226
Table C.5: Polyethylene tube material characteristics summary. _____	227
Table C.6: THORLABS F810FC-780 collimator characteristics summary. _____	231
Table E.1: Student's t-test calculated results for performed differential signalling experiments in the thesis. For each case, uncorrelated and correlated data sets are used as input data. _____	249

Glossary of Abbreviations

ANSI	American national standards institute
AOT	Adaptive optics technique
AUT	Antenna under test
AWG	Arbitrary waveform generator
AWGN	Additive white Gaussian noise
BER	Bit error rate
BPF	Band-pass filter
BW	Bandwidth
CDF	Cumulative distribution function
CENELEC	European committee of electrotechnical standardization
CNR	Carrier-to-noise ratio
CL	Confidence level
CSI	Channel state information
EGC	Equal gain combining
EIRP	Equivalent isotropically radiated power
ERP	Effective radiated power
FCC	Federal Communications Commission
FEC	Forward error correction
FFT	Fast Fourier transform
FIT	Finite integration technique
FNBW	First null beam-width
FSO	Free space optics
FSPL	Free space path loss
FTTH	Fibre to the home
GG	Gamma-Gamma
HPBW	Half-power beam-width
i.i.d.	Independent and identically distributed
IEC	The international electrotechnical commission
IM/DD	Intensity-modulation/direct-detection
ISL	Inter-satellite link

LD	Laser diode
LDPC	low-density parity-check
LOS	Line-of-sight
MIMO	Multiple-input multiple-output
MISO	Multiple-input single-output
MLC	Majority-logic combining
MMF	Multimode fibre
MoM	Method of moments
<i>M</i> -PAM	<i>M</i> order pulse amplitude modulation
MRC	Maximal ratio combining
NI	National Instrument
NSI	Nearfield Systems Inc.
OOK	On-off keying
OOK-NRZ	Non-return-to-zero OOK
OR _x	Optical receiver
OT _x	Optical transmitter
PD	Photodetector
PDF	Probability density function
PMMA	Polymethyl metacrilate
POF	Plastic optical fibre
PS	Pilot symbol
PSAM	PS assisted modulation
RF	Radio frequency
rms	Root mean square
R _x	Receiver
SC	Selection combining
SI	Scintillation index
SIMO	Single-input multiple-output
SISO	Single-input single-output
SLL	Side lobe level
SMF	Single-mode fibre
SNR	Signal-to-noise ratio
TIA	Transimpedance amplifier
T _x	Transmitter
UAV	Unmanned aerial vehicle
Vis	Fog/smoke channel visibility

VSWR

Voltage standing wave ratio

Glossary of Symbols

A	Nominal value of $C_n^2(0)$
AF	Aperture averaging factor
A_{atm}	Atmospheric attenuation
A_{fog}	Fog attenuation
A_{geo}	FSO geometrical attenuation
A_{misc}	Miscellaneous attenuations
A_{total}	Total FSO geometrical loss
α	Effective numbers of large-scale turbulence cells
B_{total}	Bit stream
β	Effective numbers of small-scale turbulence cells
β_λ	Total attenuation due to the absorption and scattering of light
C_{ap}	Optical aperture coupling coefficient
C_{bend}	Coupling of waveguide leak
C_n^2	Index-of-refraction structure
c	Speed of light in Vacuum
D_{ap}	ORx lens diameter
D_{mr}	Main reflector diameter
D_{Rx}	Optical receiver aperture diameter
d_0	Transverse correlation length
d_{bend}	Diameter of hole on the bend
d_{fibre}	Fibre core diameter
d_{optm}	Optimum sub-reflector diameter
d_r	Transversal distance between two optical beams
$d_{\text{r-c}}$	Distance between OTx and ORx lenses
d_s	ORx lens diameter
d_{sr}	sub-reflector diameter
d'_{sr}	sub-reflector modified diameter
$d_{\text{sr_hole}}$	Diameter of sub-reflector hole
δ	Skin depth

$\delta(\cdot)$	Delta function
$erfc(\cdot)$	The complementary error function
$E[\cdot]$	Expected value
E_0	Amplitude of electrical field
E_c	Energy per channel bit
\vec{E}_n	Normal electrical field
e	Hyperbolic eccentricity
η	Optical-to-electrical conversion coefficient
η_{CA}	Total efficiency of Cassegrain antenna
η_{hole}	Efficiency of sub-reflector hole
η_{illum}	Antenna illumination efficiency
η_{misc}	Antenna miscellaneous efficiency
η_{tube}	Efficiency of tube
ε	Extinction ratio
ε_0	Vacuum permittivity
FSPL	Free space path loss
$F_{Im}(\cdot)$	CDF
$f_I(\mathbf{I})$	EGC joint PDF
$f_{Im}(\cdot)$	PDF
$f_{I_{total}}(\cdot)$	AOT PDF
$f_{ISC}(I_{SC})$	SC PDF
F_{mr}	Main reflector focal length
f_s	ORx lens focal length
f_{sr}	Hyperbolic focal length
G_{CA}	Gain of Cassegrain antenna
G_{Rx}	The gain of the Rx antenna
G_{Tx}	The gain of the Tx antenna
G_i	TIA gain
Γ_i	Electrical-to-optical conversion coefficient
$\Gamma(\cdot)$	Gamma function
\vec{H}_t	Tangent electrical field
h	Altitude
h_i	Channel fading coefficient
\mathbf{I}	Irradiance vector
I_0	Signal light intensity mean

I_{SC}	SC irradiance
I_m	Irradiance received at m -th aperture
K	Constant
$K_n(\cdot)$	Modified Bessel function of 2 nd kind and order n
k	Boltzmann constant
k_B	Beam-width constant
k_{dB}	Boltzmann constant in dB
k_{FSO}	FSO wavenumber
L	Communication link span
L_{ch}	Total channel loss
λ_{FSO}	Optical wavelength
λ_{RF}	RF wavelength
Mean(\cdot)	Mean value
μ_0	Vacuum permeability
μ_{DS}	Log-normal PDF mean of differential signalling
$\mu_{h,i}$	Log-normal PDF mean
μ_{total}	Log-normal PDF mean
μ_x	Log-normal PDF mean
NA	Fibre numerical aperture
N_0	Noise spectral density
n_0	Number of simultaneous received 0s
n_1	Number of simultaneous received 1s
n_m	AWGN variance
P	Electrical/optical power
\bar{P}_e	Infinitesimal electric field, BER
P_i	Propagating RF power
\bar{P}_m	Infinitesimal magnetic field
P_T	Transmit power
$P(0)$	Probability of transmitting 0
$P(1)$	Probability of transmitting 1
$P(e bit)$	Conditional probabilities
p_{sr}	Distance between the apex and the focal point of the hyperbolic trajectory
Ψ_{RF}	Half of feed HPBW
Q	Q-factor

$Q(\cdot)$	Gaussian Q-function
R	Random variables
R_0	Signal light intensity mean
R_d	Data rate
r	Radial displacement
r_m	Received signal at m-th aperture
r_{total}	AOT received signal
\Re_i	PD responsivity
\mathbb{R}_{FSO}	Ratio of FSO state 1 to 0
\mathbb{R}_{RF}	Ratio of RF state 1 to 0
ρ_0	Spatial coherence radius
$\rho_{1,2}$	Correlation coefficient
ρ_c	Channel coherence radius
ρ_{PE}	Pointing errors correlation
S	Constant
S	Transmit information bit
\bar{S}	Transmit information bit
S_{bend}	Area of waveguide cross section
S_{thresh}	Optimum detection threshold level
$\sigma_{I_m}^2$	SI
$\sigma_{\ln X}^2$	Large-scale irradiance fluctuations variances
$\sigma_{\ln Y}^2$	Small-scale irradiance fluctuations variances
σ_m^2	Variance
$\sigma_{n,i}^2$	Noise variance
σ_R^2	Rytov variance
σ_{DS}^2	Log-normal PDF variance of differential signalling
$\sigma_{h,i}^2$	Log-normal PDF variance
σ_{total}^2	Log-normal PDF variance
σ_x^2	Log-normal PDF variance
T	Bit duration
T_R	Noise temperature
θ_0	OTx divergence angle
V	V-number, Electrical signal level
$\text{Var}(\cdot)$	Variance value
V_{thresh}	Optimum detection threshold level

v	rms wind speed
v_i	Received electrical signal
W	Light beam with a spot size at the Rx of diameter
W_{bend}	Waveguide wall width
w_{Rx}	Optical beam radius at Rx plane
w_{Tx}	OTx lens radius
w_{eq}	Equivalent optical beam-width
X	Random variable
X_{DS}	Signal light intensity mean
x	Transmit information bit
y_i	Received signal
Z_0	Impedance of free space

Dedications

To whom he/she might find this thesis useful.

... but just to let you know that

بسی رنج بردم در این چار سال	بشتن شروع کردم از پار سال
چو اکنون تمام است تحقیق من	در افتاد گران سنگ از دوش و تن
بدانم هیچیز و هر مساله	بخندم به نادان و پیرو هر مسخره
اگر هم کسی گفت کنم اشتباه	بگویم که من دکترا حرف خاش نماه
از این پس بگردم به دنبال کار	توانم دهم پول قسط و لباس و ناهار

☺!!!

Acknowledgments

I am sure this PhD could not end without the help of family, colleagues, and friends. If I compare myself at this moment with the time I started my PhD, having a title and a certificate is the least thing I obtained. For me this PhD was a journey which took me from the immaturity to maturity. I learned how to do the research and how to contribute to the human being knowledge; where if the knowledge and science is a sea, my contribution is a drop. However, I know that the sea is nothing but many of drops put together.

I must thank my principle supervisor Professor Zabih (Fary) Ghassemlooy who showed a lot of patience toward me and never stopped helping and encouraging me. Today I do not consider Professor Fary as my mentor but as a friend who kindly inspired and guided my research. I also need to thank Professor David Smith for his valuable help since none of the practical work and designs was possible without him.

This research gave me the chance to meet wonderful people including Professor Stanislav Zvanovec from the Department of Electromagnetic Field, Faculty of Electrical Engineering, Czech Technical University in Prague, Czech; Dr Mohammad-Ali Khalighi from Ecole Centrale Marseille, Institut Fresnel in Marseille, France; and Dr Manav R. Bhatnagar from the Department of Electrical Engineering Indian Institute of Technology Delhi, in New Delhi, India. The researchers, who kindly helped me through the project and taught me a lot without expecting any favour.

I wish to express my gratitude to Northumbria University, Faculty of Engineering and Environment for awarding me studentship to complete my PhD. I also thank to my colleagues from E411 of Ellison building that always kept the environment to be both

friendly and scientific.

The last but not the least, I must express my gratitude to my family who were always supporting me. In spite of all the problems and all the hard days we went through, they never left my back and never remove the happy encouraging smile from their faces.

Declarations

I hereby certify that this material, which I now submit for assessment on the programme of study leading to the award of Doctor of Philosophy is entirely my own work, that I have exercised reasonable care to ensure that the work is original, and does not to the best of my knowledge breach any law of copyright, and has not been taken from the work of others save and to the extent that such work has been cited and acknowledged within the text of my work.

I declare that the Word Count of this Thesis is 35,542 words

Signed:

ID No: W11033645

Date: 12/01/2017

1 INTRODUCTION

1.1 Introduction to Free Space Optics

One of the current challenges in wireless communications is to be able to provide a cost effective high speed data link in applications, where the radio frequency (RF) based technology cannot be used or is not suitable. For example, in highly populated indoor environments (train station, airports, etc.), and ‘the last mile access’ network, where the end users, using the RF based wireless technologies, do experience lower data rates and low quality services due to the spectrum congestion (i.e., bandwidth bottleneck). The high speed optical wireless connection is defined as a data link with a minimum speed of few Gbps, where a 2-hour long high definition movie can be downloaded within few seconds [1], in emergency situations such as flooding, earthquake, etc., and massive public events including concerts, festivals, as well as optical fibre networks maintenance and repair.

Nowadays, using the internet and, in general, having access to the data network have become a typical daily task for everyone. With the rapid growth of smart devices, the RF spectrum, which is already being stretched too thinly, is experiencing congestion at a global level, which needs addressing. Nowadays, there are a growing number of applications as shown in Figure 1.1, which require access quality to the data services anywhere, anytime and under all conditions. In a perfect scenario, all end users should have access to the optical fibre based backbone network with an ultra-high capacity, to

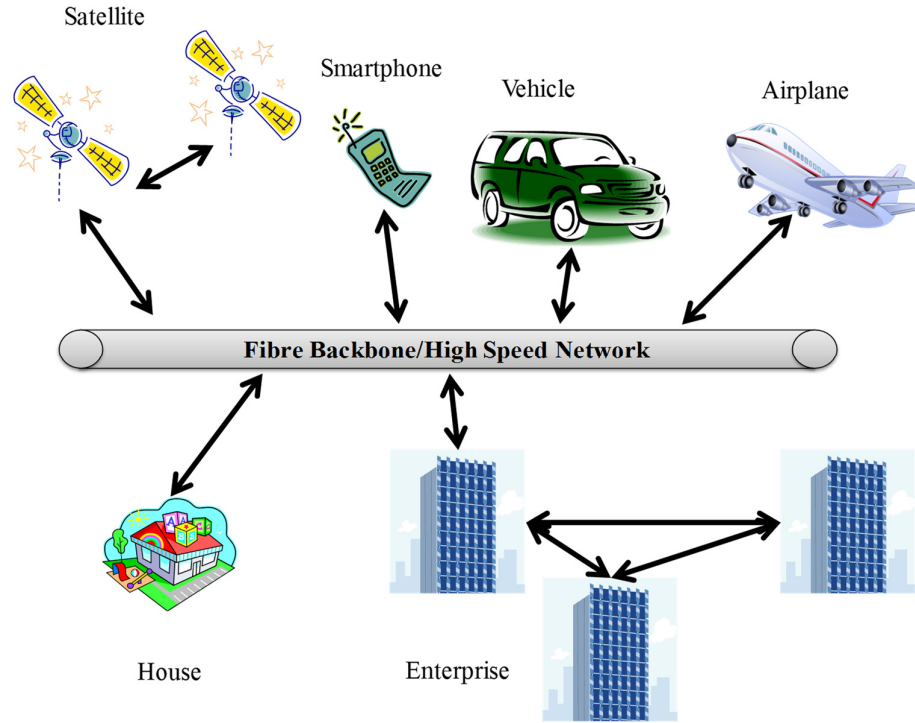


Figure 1.1: Variety of demands for high bit rate access to the data.

benefit from truly high-speed data communications with a very low end-to-end transmission latency.

Of course, for environment where deployment of optical fibre is not economical a combination of satellite communications and optical fibre communications technologies would be the most suitable option. However, this could also be quite costly and therefore may not be feasible in the long run.

Therefore, because of the limited bandwidth, and high cost of the RF technology [2], there is the need to consider alternative technologies. The cost and challenges associated with installation of optical fibre particularly in rural areas as well as maintenance of such a network is rather high, therefore is not considered for the last mile access network. Whereas bandwidth limited RF technologies are also not suitable, thus the need for the most attractive and relatively cost effective solution still exists. Free space optical (FSO) communications also known as optical wireless communications have been used to provide high speed data service for aforementioned applications [3]. The FSO technology

is license free, easily deployable, secure and capable of offering low bit error rate as well as high speed link over a range of link span up to 10 km for civilian applications [4], which has been adopted in a number of applications including:

- Broadband internet to rural areas [5] – FSO based link could replace optical fibre access technologies such as fibre to the home (FTTH) in order to provide connectivity between in-building networks and to broadband and backbone data networks.
- Inter-building connectivity [4] and electronic commerce [6] – FSO provides high-speed, flexibility and high security.
- Audio and video streaming [7] – FSO is an attractive solution for video surveillance and monitoring, as well as live broadcasting of sporting events, in emergency situation (e.g., the tsunami in Japan in 2011 that almost wiped out all the telecommunications infrastructure [11]) etc.
- Unmanned aerial vehicle (UAV) and high attitude platforms [4, 8] – UAVs and high attitude platforms have been used for military surveillance, monitoring traffic and disaster areas, or broadcasting vital data. UAVs generate a large volume of data, which needs downloading as quickly as possible. This can be achieved by employing the on-board FSO technology.

1.2 FSO Communications

1.2.1 Background

Considering any information transmission via light as a form of optical communication; then the ancient Greeks and Romans around 800 B.C. who used fire beacons for signalling

over a medium range distance were the first users of FSO links [9]. Since then, a growing interest in research, development and deployment in FSO is observed. The first modern system was developed by Alexander Graham Bell back in 1880 by inventing the “Photophone” that used sun rays to transfer voice over a distance of 200 m [10].

However, not much happened until the discovery of the laser in 1960s. In 1962 researchers from MIT Lincoln Laboratory demonstrated a television signal transmission over 48 km using a light emitting GaAs diode based FSO link [9]. For years FSO was used in military and deep space applications with very little commercial use. The reasons were that i) existing communication technologies were more than adequate to meet the demand; ii) lack of cost-efficient reliable optical components; and iii) impact of the atmospheric conditions on the performance of FSO links [10].

As mentioned before, the demand for higher data rate was the main motivation for researchers to reconsider FSO as a promising alternative and complementary technology to the RF. The growing number of research and development activities in FSO both within the academy and industry supported by a large number of scientific articles clearly demonstrate the potential of this emerging technology with optical fibre like capabilities. Currently, there are commercial FSO products available in the market offering data rates beyond gigabits per second [11, 12]. Research and development is going on to push the data rate to higher limits (e.g., 10 Gbps commercial FSO transceiver [13]) and improve the link quality (e.g., it is desirable to achieve ideal 100 % link availability in all weather conditions. In practice, using a hybrid link the availability of five nines (99.999 %) is reported [5]) as well as to reduce the cost of the complete system. The cost effectiveness of FSO system compared to the RF system is more obvious, when the RF system is supposed to deliver the same high data rate connection service [14-16]. To illustrate the comparison between existing technologies and FSO and to show the advantage of FSO

one can refer to Figure 1.2.

In summary the key features of FSO systems for long range line-of-sight (LOS) high speed data connections are outlined as follow:

- **High data rate:** At the moment RF provides 1 to 2 Mbps for unregulated 2.4 GHz ISM bands [19], 20 Mbps 875 Mbps at 5.7 GHz 4G mobile and 60 GHz millimetre wave technologies, respectively [20]. Potentially FSO can provide bandwidth as large as 2000 THz, which is far beyond the maximum data rate of RF technologies [21, 22], see Figure 1.2(a).
- **License free spectrum:** FSO spectrum is not regulated therefore there are no

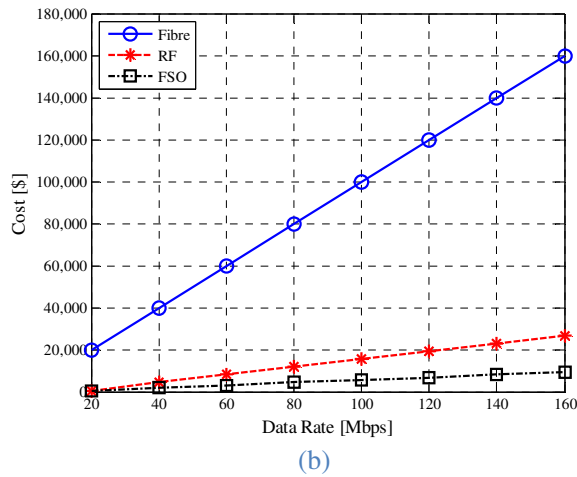
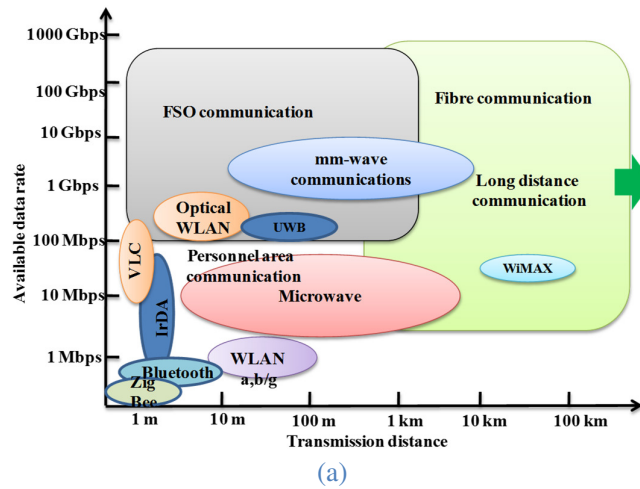


Figure 1.2: Comparison of communication technologies: (a) in terms of data rate and link coverage, figure taken from [17] with permission, and (b) in terms of cost and data rate (the figure is plotted using the data from [18]).

license fees.

- **Power consumption:** The global information and communications technology is responsible for 2 to 10 % of the global energy consumption according to the report smart 2020 [23]. The global warming and the existing concern to reduce the power consumption is a critical motivation to replace RF with FSO in LOS applications since FSO is potentially green in terms of energy consumption compared to RF.
- **Low cost:** Covering installation, maintenance and license fees, see Figure 1.2(b).
- **High security:** FSO links are inherently secure due to highly narrow, well confined and directional beam profile.
- **Back-bone network compatibility:** FSO operating at all three optical transmission windows of 850, 1300 and 1550 nm are compatible with optical fibre based back bone networks.

1.2.2 FSO Structure

Figure 1.3 illustrates the general schematic system block diagram of a typical FSO communication link (Note that in the following chapters, the detailed block diagram will be presented for each case).

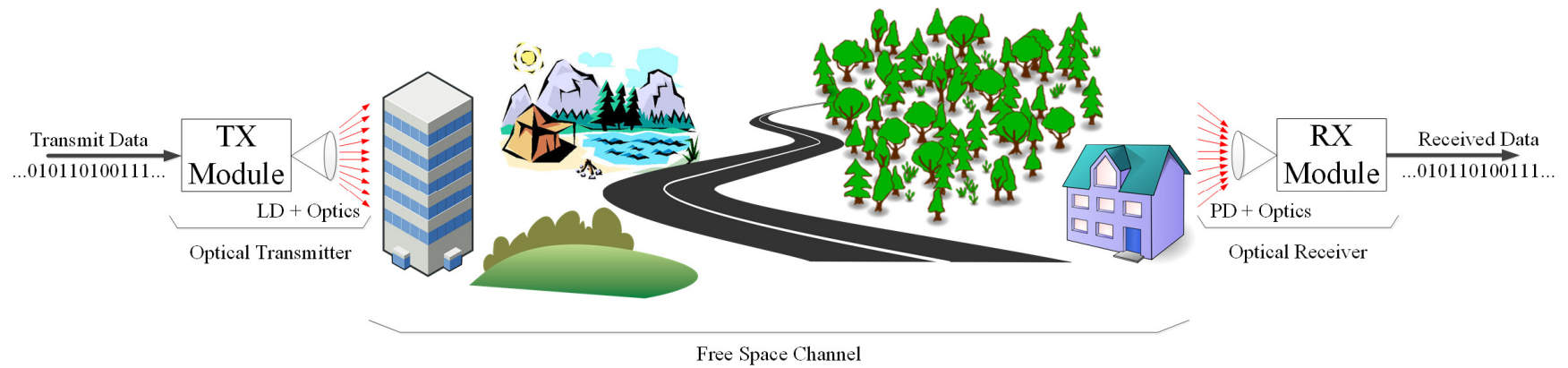


Figure 1.3: The fundamental system diagram of an FSO link. LD and PD are laser diode and photodetector, respectively.

The modulated or unmodulated version of the transmit information, (i.e., a digital bit stream) is used for intensity modulation of the optical source. Note that, for much higher data rates (i.e., in excess of 10 Gbps) external modulation schemes should be used). As shown in Figure 1.3, the modulation procedures are assumed to be performed in the transmitter (Tx) module. The optical source adopted could be a light emitting diode (LED) or a laser diode (LD). The latter is more widely used because of the LOS transmission requirement, longer transmission span and higher data rates in outdoor environments. Note that additional optics such as lens, beam splitters, beam polarizer, optical filter, optical fibre, etc. are also used as part of the Tx.

Particularly, locating the LD at the focal length of a lens is a common practice used in beam forming and collimation of the laser output. The generated optical beam is launched into the free space channel and is captured at the receiver (Rx) using a combination of optics and an optical photodetector (PD). As in the Tx, typically a lens is used at the Rx to focus the received beam into the PD. The generated electrical signal at the output of the PD is then amplified, processed and converted back into the digital bit stream at the Rx, see Figure 1.3.

Depending on the application, the free space channel condition and the data rate, the aforementioned elements (i.e., LD, PD, and interface block) can be different. For instance, in a short range clear channel, a single Tx and Rx as well as a simple on-off-keying non-return-to-zero (NRZ-OOK) modulation scheme would be sufficient to meet the link requirements [17].

For most cost-effective typical systems, intensity-modulation/direct-detection (IM/DD) based FSO links are more adequate [7, 24-27]. In IM/DD technique, based on the information data, only the intensity of the light is modulated. Another technique to modulate and detect the light is the external modulation and the coherent detection, where

in contrary to IM/DD, both intensity and phase/frequency of the light can be modulated [28]. Coherent systems require an external modulator such as Mach-Zehnder modulator to perform the modulation operation. Besides at the Rx, a light source synchronized with the one at the Tx is needed to down-convert the received optical beam [29]. Although coherent systems are shown to have impressive performance in terms of background noise rejection, atmospheric-induced fading mitigation and higher sensitivity of the Rx; the cost and complexity of practical implementation, in particular stability and synchronization of laser sources at the Tx and the Rx, make them less popular than IM/DD based systems [7].

Although the FSO technology has many benefits, it cannot provide 100% link availability under all weather conditions as outlined below [8]:

1. Turbulence induced fading - This is due to the temperature gradient along the optical propagation path and the movement of air perpendicular to the propagating optical beam [30]. In Chapter 3, more detail is given about turbulence phenomena.
2. Atmospheric loss – This is mainly due to the fog, aerosol, haze, smoke particles [7], where the induced loss by fog/smoke is dominant [31]. The attenuation is the contribution of molecular absorption and light scattering [32]. Absorption occurs at the molecular level and is resulted from absorption of photon energy by molecules of gases in the atmosphere [33]. Since the dimension of fog particles varies between 0.5 μm to 2 μm , which is in the range of FSO wavelengths, therefore Mie scattering is the major cause of scattering attenuation [32, 33].
3. Pointing errors induced fading - Is due to the vibration or small movements of both Tx and/or Rx [34]. In Chapter 4, more detail is given about this

phenomena.

4. Link blockage - Mostly due to flying object or birds, which results in a burst error [17].
5. Ambient noise – This can be considered as the main noise source in many scenarios [35]. The ambient noise is mostly due to sunlight or artificial lighting sources [35].

In particular, among these effects, the atmospheric loss can lead to attenuation as high as 50 dB/km for < 500 m visibility under the fog condition [40, 41]. As reported in [3] the fog attenuation in moderate continental fog environment (Graz, Austria) in winter season and in dense maritime fog environment (La Turbie, France) in summer months can lead to 120 dB/km and 480 dB/km, respectively [42]. Indeed, the FSO link undergoes a wide range of attenuation in presence of fog and smoke [3], which results in reduced link availability in a significant way so that it was shown in [2] that for the weather condition recorded in Graz, the link availability could drop to ~67 %.

1.3 Hybrid Link

The FSO system has been shown to be a high speed cost-effective link for a number of application where the RF technology may not be able to offer the required data throughput or be employed. However, the performance of the FSO link in outdoor environment is affected because of the weather conditions in particular fog, turbulence, dust, etc. Note that, the RF link performance is also determined by the weather condition mostly, rain and snow. Therefore, under all weather conditions no single wireless technology is able to provide full link availability at all times resulting in the need for a hybrid link to ensure link availability under all weather conditions [2, 36]. In a hybrid link based on FSO and

RF technologies, FSO is used at all-time, except under the fog condition, where it is changed over to the lower data rate RF link. Once the weather is cleared of fog, the RF link is switched over to FSO [4, 6, 8]. Figure 1.4 depicts an example in which the availability of RF, FSO and hybrid FSO/RF are compared [37]. In situations where individual FSO or RF system fails to provide total link availability, it has been shown that the hybrid system is capable of delivering a link average availability of 99.926 % over almost 2 years of measurements [37].

The high link availability (i.e., 100 % at all weather conditions) of a hybrid FSO/RF link makes it a promising solution for the last mile access networks. It can also be used between two buildings where due to natural obstacles such as river and lake; or regulations and environmental considerations such as railways, highways, metros and power grids, it is not possible to establish cable based communication links. In recent years a growing number of research activities in this area is seen, where most of the published work focused on investigating the channel models [38-40], hybrid system measurements [4, 41, 42], coding schemes [3, 36, 40, 43-45], modulation techniques [46, 47], and diversity schemes [36, 48].

However, very little work has been reported on the devices and components and more

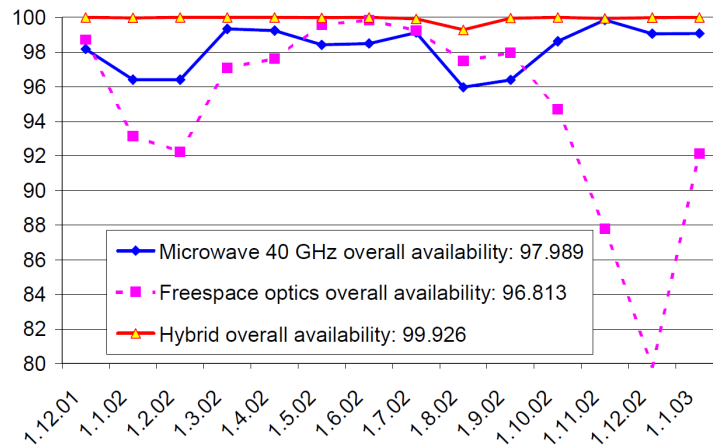


Figure 1.4: Measured availability of RF, FSO and hybrid system in percentage versus measurement date. Measurement was taken from December 2001 to January 2003 at Graz University of Technology. FSO wavelength was 850 nm with total transmit power of 8 mW. The link distance was 2.7 km. More details are available in [37]. Figure is taken from [37] with permission.

specifically on the single antenna in hybrid FSO/RF based system. In this research work the focus is on the frontend component (i.e., antenna and aperture for RF and FSO parts, respectively). The term concept of hybrid FSO/RF antenna refers to a single antenna unit with dual functionalities, which covers both FSO and RF transmissions. The proposed hybrid system is mainly intended for outdoor environments with a LOS link configuration over a few kilometres. However, the proposed system could also be used in large area indoor environment to cover full connectivity in case the FSO link is down due to other reasons than atmospheric conditions. The key features of the hybrid system are summarised as follow:

1. Reduced power consumption and costs – This is achieved by means of incorporating the optical aperture as part of the RF antenna and only utilizing FSO or RF path at any given time.
2. Link alignment – Both FSO and RF could be used to establish the link alignment and maintain it via auto-tracking system within a certain degree.
3. High link availability – A wireless technology based on the hybrid antenna can ensure full link availability under all weather conditions with higher data rates capability.
4. Installation cost and complexity - This is much lower in the hybrid antenna based wireless link than the dual antenna base systems.

1.4 Problem Statement

In recent years, one can see research activities on the hybrid antenna based transmission scheme. Here are some important ones:

1. In [49, 50] packaging of a dual-mode wireless communications module based on RF/optoelectronic devices with shared functional components was investigated. The RF antenna and FSO Tx and Rx were mounted on the same PCB with separate feed lines. However, this scheme with a 3 dB full divergence angle not more than 20 degrees is not applicable for outdoor applications. This radiation pattern is not suitable for peer-to-peer connections, where the link is considered to be directive and LOS. The authors also reported that in the worst scenario the coupling between FSO and RF can be as high as -15 dB. In situations where the FSO beam is attenuated but still detectable at the Rx, the link suffers from interference due to leakages from the high power RF signal, which will affect the FSO link availability.
2. In [51], a dual band RF and optical antenna and a terminal design technology were proposed for the ground to satellite link, which also can be adopted for terrestrial outdoor applications. The proposed design was suitable for long-to extremely long-range (space-to-ground) transmission spans. The RF antenna was a direct feed reflector whereas the optical aperture was based on Cassegrain telescope. This necessitates the existence of a shared large concave mirror for RF and optical aperture as well as adopting adaptive optics, which resulted in increased system and maintenance costs.
3. In [52], a hybrid antenna system based on the adaptive optics and signal processing as well as using a large optical mirror as the aperture was reported. Here the same mirrors for both FSO aperture and the RF antenna in a Cassegrain configuration were used. However, employing a large mirror is a major issue and using a secondary mirror results in blocking of the main reflector, which results in additional attenuation of the received optical power. On the other

hand, the performance of optical Rx (ORx) depends on the wavefront correction mechanism, thus making the entire system more complex and costly.

To the best of our knowledge, no simple hybrid antenna for outdoor wireless applications particularly for the last mile access networks in urban areas have been reported. Thus, the motivation in this research work is to design, fabricate, and characterize a hybrid FSO/RF antenna for wireless communications. The research will address a number of challenges as outlined below:

1. A compact and less complex design, which can be readily connected to FSO and RF transceivers.
2. The RF part of hybrid antenna must provide a directive pencil beam pattern to ensure high directionality and improved security.
3. The FSO part must be incorporated as part of the RF antenna and should be able to reduce the weak turbulence effects (see next chapters for more details) without the need for adaptive optics or wavefront correction techniques.
4. Meeting much wider specifications so that it can be adopted for a wide range of frequencies and wavelengths. Thus making the design more flexible that can be reused for different configurations and applications.
5. Minimum interference between FSO and RF links to ensure high-quality signal at both ends of the link.

1.5 Aim and Objectives

The aim of this research is to propose, design, implement, model and characterise a hybrid FSO/RF antenna for few Gbps data rate outdoor wireless applications over at least

1 km link span. The desired antenna should provide narrow directive beams (for both optical and RF links) with sufficient gains to overcome the attenuation due to the atmospheric channel conditions as well as mitigating the turbulence effect [38] on the FSO link.

Based on the research aim, the objectives are as follow:

1. Proposing a novel design for hybrid antenna supported by detailed analytical modelling.
2. Comprehensive simulation of the proposed antenna for verification of the design.
3. Comprehensive characterizing of the proposed antenna.
4. Investigating the potential channel effects of the communication link employing hybrid FSO/RF antennas.
5. Investigating existing methods for mitigation of the atmospheric channel effects particularly for FSO, since it is the main link.
6. Optimization of the FSO part of the antenna and investigating diversity and detections techniques for the FSO link.
7. Fabrication of the proposed hybrid antenna based on the optimized design.
8. Experimental measurements and comparison with analytical and simulation results.
9. Assessment of the system performance in terms of the bit error rate (BER) and the link availability.

1.6 Original Contributions

The original contributions made to the research field are best outlined with reference to Figure 1.5, see blocks shown in dashed lines, and are also summarised as follow:

1. **Chapter 3** – Categorizing and investigation of the combining scheme for mitigating the effect of turbulence for the FSO link including (i) introduction of a new combining method known as the majority-logic combining (MLC) (adopted from RF) for the turbulence channel; (ii) deriving closed-form mathematical expressions for BER for the proposed combining under weak to strong turbulence regimes; and (iii) investigation of the performance of link employing combining methods including equal gain combining (EGC), selection combining (SC) and MLC under different turbulence regimes.
2. **Chapter 4** – Investigation of a new detection scheme known as the differential signalling to mitigate the effect of turbulence and pointing errors. This includes (i) mathematical analysis to demonstrate the functionality of the proposed method; (ii) developing theoretical analysis for the variance of detection level of the received signal, Q-factor of the received electrical signal, and BER; (iii) extensive Monte-Carlo simulation in support of the proposed theory; (iv) experimental verification of the variance of detection threshold level and the Q-factor of the received signal; and (v) employing Manchester coding scheme as an alternative for differential signalling and performing experimental measurement of the Q-factor.
3. **Chapters 5** – Investigation of the design process of the hybrid antenna including (i) the key design requirements and parameters; (ii) investigation of the existing RF antenna with the aim of proposing the best possible fundamental

structure for hybrid antenna; (iii) derivation of closed form mathematical expressions to characterize the antenna and corresponding components; (iv) simulation of the radiation pattern and gain of the designed antenna using CST STUDIO SUITE®; (v) experimental test and measurement of the radiation pattern, return loss and the gain of the designed antenna; and (vi) comprehensive assessment of the communications link employing two hybrid antennas in terms of the received RF signal-to-noise ratio (SNR) and the received FSO Q-factor and comparison with the predicted results.

4. **Chapter 6** – Investigation of the performance of the final design including (i) the FSO system configuration based on combining and detection methods outlined in Chapters 3 and 4, respectively; (ii) analysis of the recorded data based on measurements carried out in Faculty of Electrical Engineering, Czech Technical University in Prague, Czech Republic; (iii) simulation of the FSO link availability over the recorded channel conditions, (iv) simulation of the hybrid FSO/RF link availability over the recorded channel conditions while employing a time hysteresis (TH) switching technique, (v) investigation of effects of FSO data rate and the transmission span on the hybrid link availability and the hybrid data rate, and (vi) outlining the method to achieve the maximum hybrid data rate and guaranteed availability over a given channel link span.

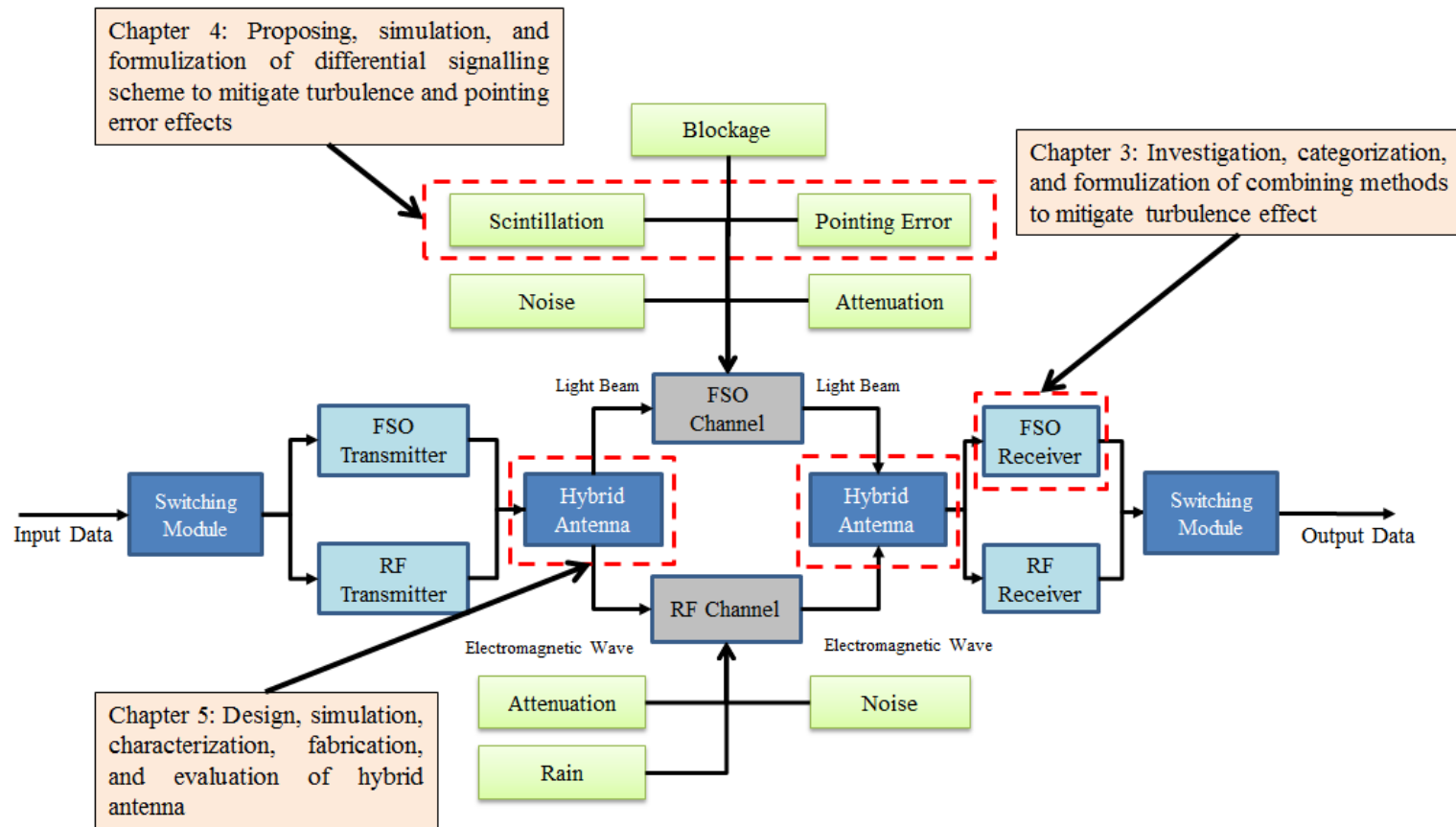


Figure 1.5: Schematic diagram of a hybrid FSO/RF communication system. The original contributions are highlighted with dashed boards.

1.7 Publications and Awards

1.7.1 Journal Papers:

1. **M. Mansour Abadi**, Z. Ghassemlooy, S. Zvanovec, D. Smith, M. R. Bhatnagar, and Y. Wu, “Dual Purpose Antenna for Hybrid Free Space Optics/RF Communication Systems”, *IEEE Journal of Lightwave Technology (JLT)*, Vol. 34, Issue 14, 3432-3439, 2016
2. **M. Mansour Abadi**, Z. Ghassemlooy, M.-A. Khalighi, S. Zvanovec, and M. R. Bhatnagar, “FSO detection using differential signalling in correlated channels Condition”, *IEEE Photonics Technology Letters (PTL)*, Vol. 28, Issue 1, 55-58, 2016
3. **M. Mansour Abadi**, Z. Ghassemlooy, S. Zvanovec, M. R. Bhatnagar, and M.-A. Khalighi, “Impact of Link Parameters and Channel Characteristics on the Performance of FSO Systems with Differential Signalling Technique”, accepted in *IEEE Journal of Optical Communications and Networking (JOCN)*
4. **M. Mansour Abadi**, Z. Ghassemlooy, D. Smith, and W. Pang Ng, “ABCD matrix for reflection and refraction of laser beam at tilted concave and convex elliptic paraboloid interfaces and studying laser beam reflection from a tilted concave parabola of revolution”, *Journal of Electrical and Computer Engineering Innovations (JECEI)*, Vol. 2, No. 3, 2014
5. J. Bohata, S. Zvanovec., T. Korinek, **M. Mansour Abadi**, and Z. Ghassemlooy, “Characterization of dual-polarization LTE radio over free space optical turbulence channel”, *OSA Applied Optics Journal*, Vol. 54, Issue 23, 7082-7087, 2015
6. J. Bohata, S. Zvanovec., P. Pesek, T. Korinek, **M. Mansour Abadi**, and Z. Ghassemlooy, “Experimental verification of LTE radio transmissions over dual-polarization combined fibre and FSO optical infrastructures”, *OSA Applied Optics Journal*, Vol. 55, Issue 8, 2109-2116, 2016
7. M. R. Bhatnagar, Z. Ghassemlooy, S. Zvanovec, M.-A. Khalighi, and **M. Mansour Abadi**, “Quantized Feedback Based Differential Signaling for Free-Space Optical Communication System”, *IEEE Transactions on Communications*, vol. 64, pp. 5176-5188, 2016
8. **M. Mansour Abadi**, Z. Ghassemlooy, M. R. Bhatnagar, S. Zvanovec, and M.-A. Khalighi, “Differential Signalling in Free-Space Optical Communication Systems”, submitted to *IEEE Journal of Optical Communications and Networking (JOCN)* special issue on 15th January 2017

1.7.2 Conference Papers:

1. **M. Mansour Abadi**, Z. Ghassemlooy, D. Smith, and W. Pang Ng, “A report on H-FSO/RF antenna measurement for outdoor applications”, presented in the IWOW 2013: 2nd International Workshop on Optical Wireless Communications, Newcastle, United Kingdom, 2013
2. **M. Mansour Abadi**, Z. Ghassemlooy, D. Smith, W. Pang Ng, M.-A. Khalighi, and S. Zvanovec, “Comparison of different combining methods for space-diversity FSO systems”, presented in the CSNDSP 2014: 9th International Symposium on Communication Systems, Networks and Digital Signal Processing, Manchester, United Kingdom, 2013
3. **M. Mansour Abadi**, Z. Ghassemlooy, M. R. Bhatnagar, S. Zvanovec, M.-A. Khalighi, and A.-R. Maheri, “Using differential signalling to mitigate pointing errors effect in FSO communication link”, presented in IEEE International Conference on Communications 2016 (ICC'16), Kuala Lumpur, Malaysia, 2016
4. E.T. Fabiyi, X. Tang, Z. Ghassemlooy, **M. Mansour Abadi**, and W.O. Popoola, “Performances of free space optical link under a controlled atmospheric turbulence channel”, presented in PGNet2014: the 15th Annual PostGraduate Symposium on the Convergence of Telecommunications, Networking and Broadcasting, Liverpool, United Kingdom, 2014
5. H. K. Al-Musawi, T. Cseh, **M. Mansour Abadi**, W. P. Ng, Z. Ghassemlooy, E. Udvary, and T. Berceli, “Experimental demonstration of transmitting LTE over FSO for in-building POF networks”, presented in ICTON2015: The International Conference on Transparent Optical Networks 2015, Budapest, Hungary, 2015
6. T. Cseh, H. K. Al-Musawi, **M. Mansour Abadi**, Z. Ghassemlooy, W. P. Ng, E. Udvary, T. Berceli, and S. Zvanovec, “Improvements in combined radio over multimode fibre and radio over FSO systems by applying mode filtering”, presented in ICTON2015: The International Conference on Transparent Optical Networks 2015, Budapest, Hungary, 2015
7. N. A. M. Nor, E. Fabiyi, **M. Mansour Abadi**, X. Tang, and Z. Ghassemlooy, “Investigation of Moderate-to-Strong Turbulence Effects on Free Space Optics - A Laboratory Demonstration”, presented in CONTEL2015: The 13th International Conference on Telecommunications, Graz, Austria, 2015
8. J. Bohata, S. Zvanovec, **M. Mansour Abadi**, and Z. Ghassemlooy, “Channel characterization of a last-mile access radio over combined fibre and free-space optics system”, presented to ICACOMIT2015: The 2015 International Conference on Automation, Cognitive Science, Optics, Micro Electro Mechanical System, and Information Technology, 2015
9. **M. Mansour Abadi**, Z. Ghassemlooy, and S. Zvanovec, “Hard Switching in Hybrid FSO/RF Link: Investigating Data Rate and Link Availability”, presented in IEEE International Conference on Communications 2017 (ICC'17), Paris, France, 2017

1.7.3 Awards

1. Receiving full scholarship from Northumbria University (2012-2015)
2. Winning the best design poster of 3rd year PhD research Student at Northumbria Conference March 2014

1.8 Thesis Structure

The thesis is arranged into seven chapters and five appendices. Chapter 1 outlines the introduction, background, aim and objectives of the thesis as well as original contributions. Chapter 2 is devoted to the fundamental theories to prepare the reader for the following chapters. The chapter covers both FSO and RF technologies as well as required material for hybrid FSO/RF link. Chapter 3 investigates spatial diversity and combining techniques for the FSO part. In Chapter 4, a new detection method is proposed and described. Chapter 5 represents the design procedure of the hybrid antenna whereas Chapter 6 studies the performance of the communication link employing a pair of hybrid antenna. The conclusions together with the future works are outlined in Chapter 7 .

In Appendix A, the derivations of the mathematical equations are discussed. Appendix B describes the simulation methods used in the thesis. Appendix C is devoted to the practical setups and summarises them, whereas Appendix D explains the measurement methods used to evaluate the systems and Appendix E is devoted to confirmation of the experimental results by means of Student's t-test.

2 FUNDAMENTALS OF FSO, RF AND HYBRID FSO/RF

2.1 Introduction

In this chapter the necessary materials, which are essential for the following chapters are presented for both FSO and RF technologies. For each technology, a system block diagram with the description of each part is given. The chapter also highlights the existing problems focusing on the most relevant issues. Additionally, the chapter introduces the hybrid FSO/RF based system, in particular focusing on the switching methods, as well as outlining the key design considerations.

2.2 FSO

The general FSO system block diagram is illustrated in Figure 2.1. Note that the FSO link is based on IM/DD technique. The digital input bit stream S or the information data is applied to the modulation block. Depending on the application, the modulation could be a simple OOK scheme or more complex multilevel amplitude, frequency and phase scheme [7].

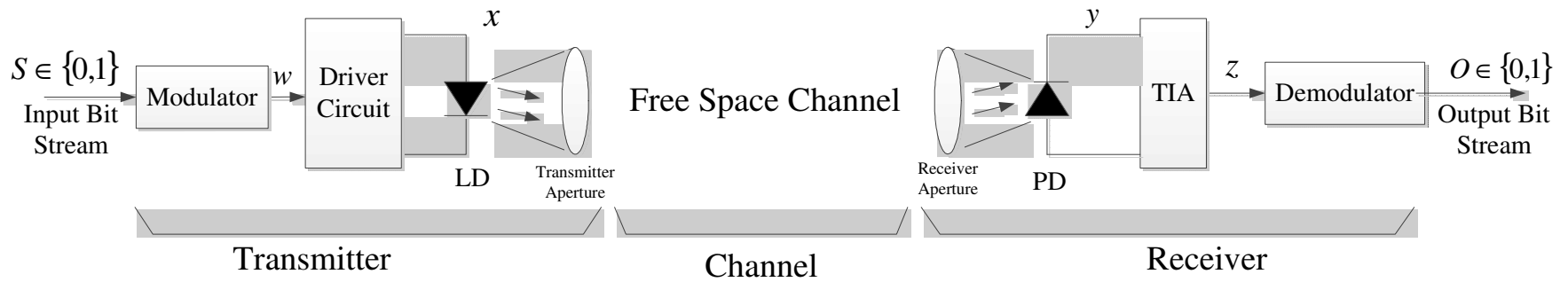


Figure 2.1: The block diagram of an IM/DD FSO communication link. LD, PD, TIA are laser diode, photodetector, and transimpedance amplifier, respectively.

In this research work the NRZ-OOK data format is adopted, which is the most widely used in commercial FSO systems [53]. NRZ-OOK is used because of its simplicity and a balanced power and spectral efficiency compared to other digital modulation schemes [54]. Note that the research main focus is on the design of the hybrid antenna and less on the modulation schemes. However, the system employing a hybrid antenna could readily be adopted for other modulation schemes. Then the output of the modulator w (i.e., a bipolar NRZ-OOK signal in this case) with a bandwidth $BW = 1/T$, where T is the bit duration is DC-level shifted to convert it into a unipolar format prior to intensity-modulate the light source (i.e., LD in this case). The data rate of NRZ-OOK equals to BW [55].

The output of the LD (i.e., x) has four key parameters, wavelength λ_{FSO} , divergence angle θ_0 , beam waist w_0 , and output power P_{opt} . The wavelength used in FSO is in the red to infrared range of the spectrum. In this work only two wavelengths of 670 nm and 830 nm have been adopted in the experimental investigation. The visible LD at 670 nm is also used for the alignment of the FSO link.

The laser beam is collimated using a lens in order to reduce the geometrical loss [56]. This means that the divergence angle θ_0 should be kept small, and w_0 will be the minimum radius of the propagating laser beam, which can be considered prior to the beam divergence [57]. However, the output power of the LD is subject to the eye and safety regulations. There are different standards for laser safety such as the international electrotechnical commission (IEC) [58], American national standards institute (ANSI) [59] and European committee of electrotechnical standardization (CENELEC) [60]. In this work one class 3R pointer laser with wavelength of 670 nm and 2 mW output power is used, which is considered to be safe if handled carefully. Also another class 3B pointer laser with wavelength of 830 nm and 10 mW output power which needs eyes protection is used. Note that class 3B lasers are only used for experimental proof of concept in

laboratory and in an outdoor real scenario, safe lasers must be implemented [61].

In FSO systems with LOS configuration the link performance will be affected by blocking mostly due to flying objects (e.g., birds) and the atmospheric channel conditions (i.e., fog, smoke, turbulence, etc.). The channel affects are defined as the attenuation (loss) and a random fading. The attenuation is due to:

1. **Geometrical loss A_{geo}** - The real laser light is not an ideal collimated beam. With even a small divergence angle of θ_0 , it experiences beam spreading and since the PD has a finite physical size, only a fraction of the laser power is captured and collected at the Rx. Therefore, the geometrical loss is defined by A_{geo} [62], and is described in details in Chapter 5.
2. **Atmospheric attenuation A_{atm}** - This loss is due to Rayleigh scattering and molecule absorption, with a typical value of 0.5 dB [56].
3. **Fog attenuation A_{fog}** - This is the most important loss in FSO links. Generally speaking, fog and smoke, which are composed of small particles floating in the air, are the main cause of attenuation in FSO systems [32]. The optical beam interacting with fog and smoke particles results in both absorption and Mie scattering, which contribute to A_{fog} [63]. The fog attenuation is determined based on the channel's visibility (Vis) in km and is described by two well-known models of Kim and Kruse [62]. The visibility is define as [32]:

$$\text{Vis} = \frac{17}{\beta_\lambda} \left(\frac{\lambda_{\text{FSO}}}{\lambda_0} \right)^{-q}, \quad (2.1)$$

where λ_{FSO} is LD wavelength, and λ_0 denote the maximum sensitive wavelength for human eye, which is normally set to 550 nm (i.e., the green colour). Based on Kim model q is defined as [63]:

$$q = \begin{cases} 1.6, \text{Vis} > 50 \\ 1.3, 6 < \text{Vis} < 50 \\ 1.6 \times \text{Vis} + 0.34, 1 < \text{Vis} < 6 \\ \text{Vis} - 0.5, 0.5 < \text{Vis} < 0.1 \\ 0, \text{Vis} < 0.1 \end{cases}. \quad (2.2)$$

The relation between the total attenuation due to the absorption and scattering of light β_λ and A_{fog} is given by Beer-Lambert law as [63]:

$$\beta_\lambda = -\frac{10 \log A_{\text{fog}}}{4.343L}, \quad (2.3)$$

where L denotes the link distance. Depending on visibility (Vis), fog can be defined as thick ($\text{Vis} < 0.1$), medium ($0.1 < \text{Vis} < 1$) or thin ($\text{Vis} > 1$).

4. **Miscellaneous attenuation A_{misc}** - This includes additional losses due to misalignment, devices or other unknown factors [56].

Rain also introduces a loss in FSO systems, which is not significant compared to fog, and smoke [2]. However, rain is a major source of attenuation in RF systems. The received power in terms of the transmit power P_t and all losses is given by [64]:

$$P_r = P_t - A_{\text{geo}} - A_{\text{atm}} - A_{\text{fog}} - A_{\text{misc}}. \quad (2.4)$$

For a system point of view, knowing that the total noise variance at the Rx and the PD's responsivity are σ_{total}^2 and \mathfrak{R} , respectively, the link electrical signal-to-noise ratio (SNR) is defined as [64]:

$$\text{SNR} = \frac{(\mathfrak{R}P_r)^2}{\sigma_{\text{total}}^2}. \quad (2.5)$$

In a clear channel with no fading the system BER is given by [64]:

$$\text{BER} = Q(\sqrt{\text{SNR}}), \quad (2.6)$$

where $Q(\cdot)$ denotes the Gaussian Q -function defined as $Q(x) = \int_x^{+\infty} \exp(-t^2/2) dt$.

Thus in clear channel (i.e., no channel fading), to achieve $\text{BER} < 10^{-6}$ one needs

SNR > +13.54 dB.

In this research work, a channel with fading is considered as outlined below:

1. **Scintillation/turbulence** - In a clear channel with no turbulence the propagating optical beam only experiences attenuation. Whereas in turbulence channel the propagating beam will experience both attenuation and phase variation due to randomly varying refractive index of the air, thus leading to fading and link failure [7, 65]. Note that, turbulence is caused by the presence of temperature gradient along the laser propagation path and the air movement (wind) perpendicular to the laser beam [17]. Turbulence randomly changes the refractive index along the propagation path, which consequently causes the beam wandering [30]. Depending on the fading intensity, the turbulence can be classified as the weak, moderate, strong and saturated [17].
2. **Pointing errors** - This is due to the movement of building, mast, tower, and in general the structures on which the FSO units are mounted [34]. Pointing errors lead to the amplitude fluctuation (or oscillation) of the received optical signal in the transverse plan, thus contributing to deterioration of the link's performance [66].

More details on these fading effects will be given in the next chapters. Also mitigation methods to overcome them will be introduced.

As shown in Figure 2.1 in the IM/DD system the received optical signal is captured using a lens and focused onto a PD the output of which is amplified using a transimpedance amplifier (TIA) prior to be demodulated in order to recover the transmitted information.

2.3 RF

Figure 2.2 depicts the block diagram of a general RF communication system. The modulator and demodulator blocks are basically the same as the FSO system. The output of the modulator is fed into an up-converter block. The output of the up-converter is the desired RF signal, which is used for transmission via the transmit antenna (frontend antenna at Tx side). In this research a binary phase shift keying (BPSK) modulation scheme, which is simple and does perform well in turbulence channel is adopted [55]. As in the FSO link, the simplicity of the modulation scheme is the major motivation for selecting BPSK. For BPSK the BER is expressed as [67]:

$$\text{BER} = 1/2 \operatorname{erfc}(\sqrt{E_c/N_0}), \quad (2.7)$$

where E_c , N_0 , and $\operatorname{erfc}(x) = 2/\sqrt{\pi} \int_x^\infty e^{-u^2} du$ are the energy per channel bit, noise spectral density and the complementary error function, respectively. In a channel with no fading, for a $\text{BER} = 10^{-6}$, the desired E_c/N_0 is ~ 10.5 dB. The carrier power to noise power spectral density ratio is given by [67]:

$$(C/N_0)_{\text{dB}} = (E_c/N_0)_{\text{dB}} + 10 \log_{10} R_d, \quad (2.8)$$

where C is signal power at the Rx and R_d denotes the data rate.

Considering both the Tx and Rx antenna gains G_{Tx} and G_{Rx} , respectively and the total channel loss L_{ch} , Equ. (2.8) can be also written as [67]:

$$(C/N_0)_{\text{dB}} = (P_T G_{\text{Tx}})_{\text{dB}} - L_{\text{ch}} + \left(\frac{G_{\text{Rx}}}{T_R}\right)_{\text{dB}} - k_{\text{dB}}, \quad (2.9)$$

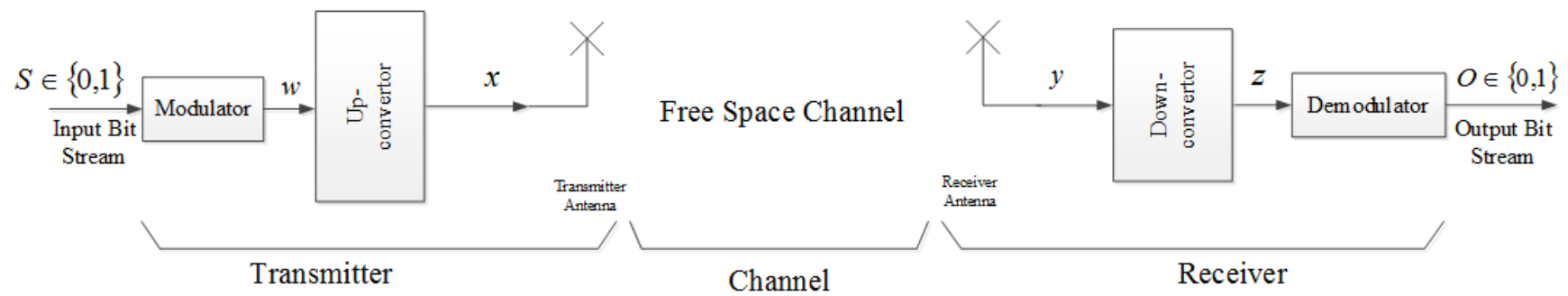


Figure 2.2: The block diagram of an RF communication link.

where P_T , T_R , and k_{dB} are the transmit power, noise temperature and Boltzmann constant in dB, respectively. The bandwidth of BPSK signal is related to data rate (R_d) as given by [68]:

$$BW = 2 \times R_d \times K / \log_2^S. \quad (2.10)$$

For BPSK, K and S are 0.75 and 2, respectively, and for a 10 MHz available bandwidth $R_d = 6.67$ Mbps. Thus, the relation between carrier-to-noise ratio (CNR) and (E_c/N_0) is given by [67]:

$$CNR = \left(\frac{E_c}{N_0} \right)_{dB} + 10 \log_{10} R_d - 10 \log_{10} BW. \quad (2.11)$$

In this research, for a BER $< 10^{-6}$, which is much lower than forward error correction (FEC) limit of 10^{-3} , the required CNR $> \sim 8.8$ dB.

The equivalent isotropic radiated power (EIRP) in dB is given by [67]:

$$EIRP = CNR + L_{ch} - G_{Rx} + T_R + k_{dB} + 10 \log_{10} BW, \quad (2.12)$$

where T_R is the summation of the antenna and the Rx system noise temperatures. In Appendix C, the noise temperature of the system is calculated and for most terrestrial applications, a typical value of 300° K is adopted for the antenna [69]. Note that $EIRP = P_T + G_{Tx}$ is the common parameter used in standards and regulations for wireless communications [70]. Depending on the antenna type, frequency range and applications, EIRP will be different. For more information refer to [71].

As in FSO, the RF link propagation mechanism is also LOS, where the link experience very little or no fading, but it undergoes attenuations as outlined below:

1. **Free space path loss (FSPL)** - Is equivalent to the geometrical loss in FSO, which is given as [67]:

$$\text{FSPL} = 20 \log \frac{4\pi L}{\lambda_{\text{RF}}}, \quad (2.13)$$

where λ_{RF} is the RF signal wavelength. For a frequency of 10 GHz and a link distance of 1 km, $\text{FSPL} \cong 112.5$ dB.

2. **Rain attenuation A_{rain}** - Is the main cause of RF link unavailability, and is caused by the absorption phenomena when the RF energy is absorbed by rain [72]. A_{rain} in dB for lower part of RF spectrum is given by [73]:

$$A_{\text{rain}} = L \times 1.076 \times R^{2/3}, \quad (2.14)$$

where R is the precipitation rate in mm/h. E.g., for precipitation of 64.8 mm/h in Glasgow, the attenuation is ~ 18 dB over a 1 km link.

Thus the total channel loss $L_{\text{ch}} = \text{FSPL} + A_{\text{rain}}$ in (2.12) will be:

$$L_{\text{ch}} = 20 \log \frac{4\pi L}{\lambda_{\text{RF}}} + L \times 1.076 \times R^{2/3}. \quad (2.15)$$

Note that attenuation due to turbulence and fog are negligible for RF links, and therefore are not considered as part of the total channel loss [2].

The central carrier frequency of the RF signal is chosen to be 10.00 GHz, which lies within the microwave range and is categorized as the X-band or the super high frequency (SHF) band. This frequency range is adopted for the RF link due to the followings:

1. At lower microwave frequency ranges the loss due the atmospheric channel is low [74]. This is clearly demonstrated in Figure 2.3 [72].
 2. The path loss attenuation given by (2.13) is also included in Figure 2.4, which also shows lower loss at lower frequencies.
 3. Relatively smaller antenna size as well as the LOS transmission mode [74].
- Figure 2.5 illustrates the reflector antenna nomograph for 100 % efficiency [75].

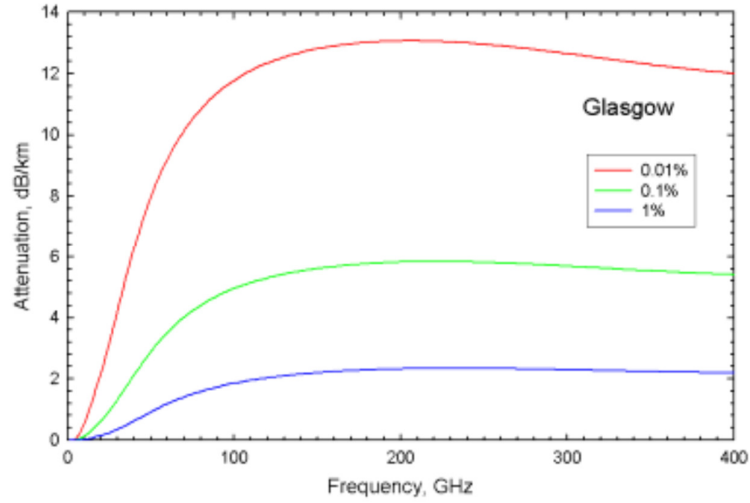


Figure 2.3: Attenuations of an RF link due to the rain in Glasgow for various perception rate. 0.01, 0.1, and 1% refers to 25.5, 8.0, and 2.1 mm/h rainfall rate. Figure is taken from [72] with permission.

The solid red line shows that at a frequency of 9 GHz an antenna with a diameter of ~ 1.8 m is needed to ensure 45 dB of gain. Whereas at the frequency of ~ 4.5 GHz an antenna with a minimum diameter of 3 m is required, as shown with dashed green line.

4. This frequency can be adopted for the satellite-to-ground link and for amateur radio applications since it is very close the amateur band of 10.225 to 10.500 GHz [23], hence providing the chance to adopt the design for non-terrestrial applications.

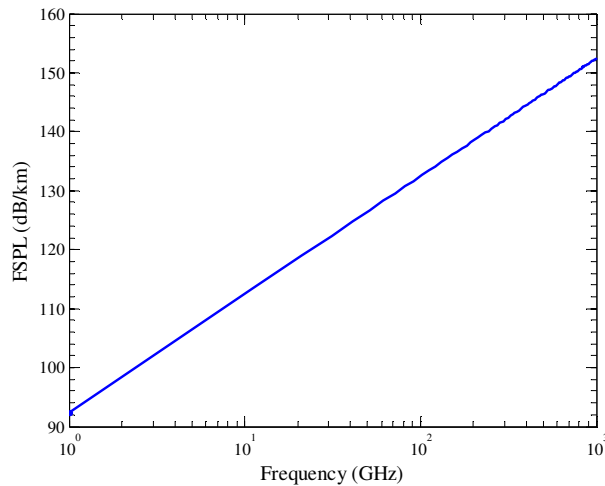


Figure 2.4: Attenuations of an RF link due to the free space path loss (FSPL) against frequency.

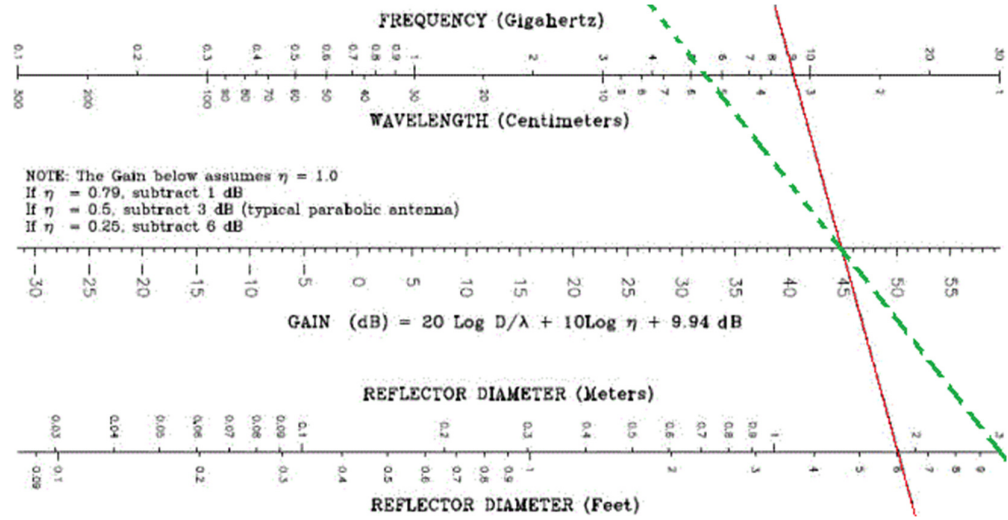


Figure 2.5: Reflector antenna gain nomograph. The graph is for an antenna with 100% efficiency. Figure is taken from [75] which is open to public.

5. As a proof concept and considering the above points and availability of devices, the carrier frequency of 10 GHz was the best option for the RF link. However, higher frequencies could be adopted.

In Chapter 5, additional details on the selected central frequency are given. Referring to [76, 77], for the purpose of this thesis the effective radiated power (EIRP) at 10 GHz Tx can be limited to 2.15 dBW [76]. In this work $EIRP_{max}$ of 0 dBW is adopted, though other values less than 2.15 dBW could also be used.

2.4 Hybrid FSO/RF

A hybrid transmission system is basically a combination of FSO and RF technologies. All the points outlined in the previous sections are applicable to the hybrid system too. In this section, the focus will be on the concept of the hybrid link and switching methods adopted. As was outlined in Chapter 1, FSO provides a high speed and a low cost data link under a clear channel. However, under medium to heavy fog conditions the FSO link availability drops considerably. Thus, the need for a hybrid system to ensure link

connectivity under all channel conditions, but at the cost of reduced data throughput, still exists. Under fog, smoke and turbulence condition the link can be switched to the RF to ensure link availability, which is then switched back to FSO when the channel is almost clear.

To show that the channel condition can influence the performance of FSO and RF links, an analytical comparison between FSO and RF channel attenuations is carried out with the results presented in Figure 2.6.

The link setup for both FSO and RF was based on the block diagram shown in the Appendix C. The gain of RF antennas was set to 27 dBi. The noise floor of the RF Rx module was set to be -91.48 dBm whereas for the ORx (THORLABS PDA10A Detector) the noise floor or sensitivity was at -39.56 dBm. An optical aperture with a 3 mRad divergence angle and a 2 mm diameter was employed at the Tx and an aperture with a

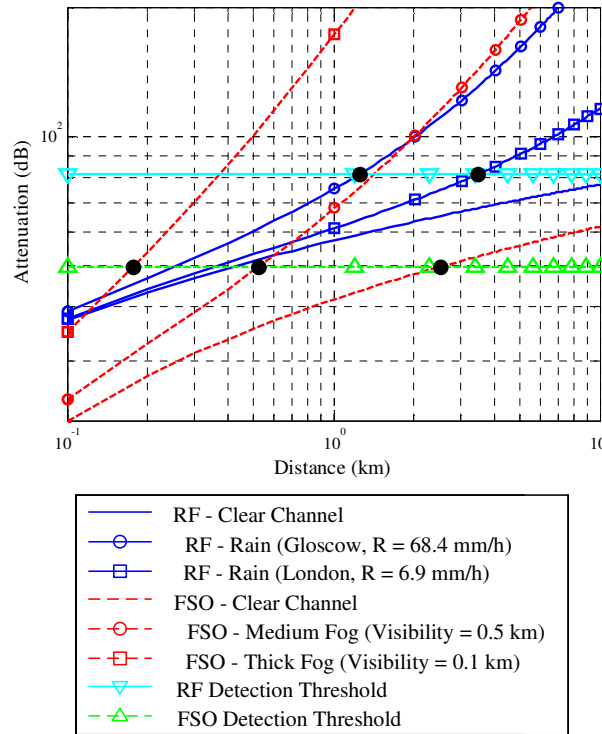


Figure 2.6: FSO and RF link attenuations versus link distance for different channel conditions. The RF and FSO detection threshold show the achievable level of the distance, within which the link is available with BER of 10^{-6} .

diameter of 50.00 mm was used at the Rx. The total attenuation of the optical link under medium and thick fog conditions based on Kim model is also included in Figure 2.6. Assuming rain fall rates of 68.4 mm/h in Glasgow and 6.9 mm/h in London, with 0.001 and 0.1 % time the rain rate exceeded, respectively, the rain attenuation was also included in the analysis. Based on the model as in [78], at a visibility of 100 m the fog attenuation at a temperature and frequency of 1°C and 10 GHz, respectively was almost 0.04 dB/km, which is negligible and can be ignored.

As part of analytical investigations, the output power of FSO and RF links were assumed to be 10 and -10 dBm, respectively. Considering a BER of 10^{-6} , one can find the required signal power for both FSO and RF links at the Rx using Eqs. (2.6) and (2.7). Considering the expected attenuations along the channels, it is possible to find the maximum attenuation at which the BER is still $< 10^{-6}$. This point is called the detection threshold, hence the detection threshold of 49.55 dB and 91.47 dB for FSO and RF Rxs, respectively. From Figure 2.6, the RF link with given parameters can be used for a transmission span up to 1.23 km and 3.43 km under heavy rain in Glasgow and London, respectively. On the other hand, in a clear channel the FSO link can cover up to a transmission distance of 2.53 km, which is well within the project target distance under a clear channel condition. However, in medium and thick fog conditions the maximum obtainable transmission spans for the FSO link are reduced to 0.52 km and 0.18 km, respectively. This drop in transmission range leads to the link unavailability, which can be addressed by switching over to the RF link until the channel condition is relatively clear for the link to be switched over back to the FSO.

In addition to the fog and link blockage induced attenuation, the FSO system is also affected by the scintillation induced fading and pointing errors. Provided fading is not strong, the FSO link can be used for transmission as long as an appropriate mitigation

method is adopted at the Rx. In this research work, to combat fading both spatial diversity and differential signalling schemes as outlined in Chapter 3 and Chapter 4, respectively are investigated. However, under a severe fading channel the transmission should be switched over to the RF link in order to maintain the link and ensure transmission quality at all times, see Chapter 6 for more information.

2.4.1 Switching Methods

In a hybrid transmission system to ensure continuous link availability under all channel conditions, a range of switching schemes between FSO and RF have been proposed. Figure 2.7 shows three possible switching configurations that could be adopted in a typical hybrid FSO/RF system [79]. The first configuration is the simplest, where both

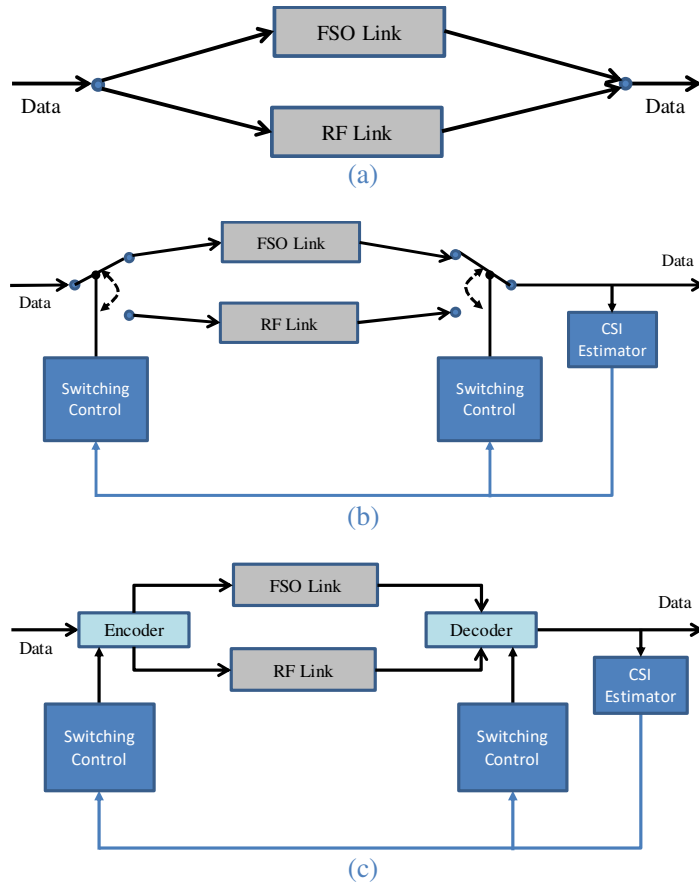


Figure 2.7: Three hybrid FSO/RF configurations: (a) hybrid FSO/RF switch-over link, (b) hybrid redundant RF link, and (c) hybrid channel coding link.

channels are simultaneously transmitting at the same data rate, see Figure 2.7(a), thus ensuring 100 % link availability under all weather conditions [80]. In this configuration there are two scenarios: (i) both links are operating at the data rate of the RF link, which could result in lower data throughput; and (ii) the RF link is transmitting at a lower data rate than the FSO link, thus resulting in the need for buffering at the Tx side. The second scenario is widely adopted in most commercial systems currently available. Note that the parallel transmission scheme is power inefficient, since both links are active at all times.

The second configuration is based on only one link being active at any given time, with a hard switching mechanism to select the FSO or RF depending on the channel condition, see Figure 2.7(b) [2]. In this technique to select the correct link a feedback signal containing the channel state information (CSI) is transmitted from the Rx to the Tx [2]. Although this method is more complex than the parallel transmission it can provide a communication service with higher data rates and 99.9 % link availability [2]. However the inclusion of a feedback signal and the drop in data rate when using the RF link are the main disadvantages of this scheme [81]. Note that in this configuration, the FSO link is selected as the default link and in case of link outage, the link is switched over to the RF.

In the case of a link with hard switching and under high scintillation and attenuation the FSO link is rarely selected therefore, the full FSO capacity is not utilised at all. To overcome this problem one option would be to adopt soft switching (i.e., using channel coding), see Figure 2.7(c). Here the coded data (for example using low-density parity-check (LDPC) code) is divided into two parts for both FSO and RF links and the code rate is selected based on the channel conditions. In this scheme both Tx and Rx should have information on CSI. Alternatively, raptor codes, which requires no CSI, could be used that can adapt its code rate based on a single feedback bit per message. In [82], a practical soft-switching H-FSO/RF system was implemented using short-length raptor

codes with an adaptive code rate based on the channel conditions. In addition to coding, it is also possible to use adaptive modulation schemes, where the constellation of symbols is split into two parts for each arm of the link (i.e., FSO and RF). Depending on the channel condition more points could be included on the constellation for each part [43]. However, this is achieved at the cost of increased system complexity as in the soft-switching scheme.

Although using pure hard switching can lead to improved link availability and increased average data rate, it cannot increase the reliability of the overall system. To mitigate the problem of random variation of received signal, which results in unnecessary switching between FOS and RF and vice versa [83], power hysteresis (PH), time hysteresis (TH), filtering, or combined methods have been used [84]. In PH, two threshold levels are used in a hysteresis loop manner, whereas in TH a time delay is introduced prior to switching to avoid transient changes in the received power. Filtering of the variation of the received power is also capable of removing temporary sudden changes in the received power level. In this work TC with TH is adopted.

2.5 Summary

This chapter was devoted to introducing of FSO, RF and H-FSO/RF systems. The chapter discussed the source of errors in FSO and RF channels. For the FSO system, fog, smoke and blockage were considered to be the cause of link discontinuity whereas turbulence was described as the cause of high BER at the Rx. On the other hand, for the RF link rain was considered to be the main issue. As part of the proposed hybrid system, two simple modulation schemes of NRZ-OOK and BPSK were selected for FSO and RF links, respectively and the fundamental theories outlining the BER performance were discussed. To ensure link reliability, availability and high performance, a hybrid FSO/RF

system was introduced and the key issues in such a system were outlined, in particular the switching mechanism between the FSO and RF link under changing weather condition. Finally, the existing switching methods adopted in hybrid FSO/RF systems were introduced and the TH method was adopted as the switching method in this research work.

3 FSO SPATIAL DIVERSITY

3.1 Introduction

In Chapter 2, it was mentioned that turbulence is a source of error in FSO communication. In this chapter a common technique to mitigate the effect of turbulence is studied. Spatial diversity is known to be an effective mitigation scheme in FSO fading channels [7, 85-87], which is implemented by means of using multiple Tx's or Rx's. Basically transmitting data information over several path increases the chance of receiving a signal less affected by fading. Therefore, logically multiple Tx's or Rx's will enhance the performance of the link (in this case the FSO link). Thus, the motivation is to investigate different aspects of spatial diversity under various channel conditions as well as system configurations in this research work.

This chapter will give an overview of the spatial diversity technique currently being adopted. First different types of spatial diversity are introduced. Then existing combining methods are presented and a new categorization is outlined. The Chapter also outlines the closed form expressions for the BER and discusses the performance of each combining method for a range of turbulence regimes (weak and strong). A well-known majority logic combining method, which is already used in RF, is adopted for the FSO link. The performances of a FSO system under various turbulence regimes with different combining methods are compared and the results are discussed.

3.2 Turbulence

If hypothetically the turbulent channel is frozen at $t = 0$, the channel can be considered as in Figure 3.1. The input wavefront in this case is planar, which encounters random changes in the refractive index. The refractive index variation is a function of the atmospheric temperature, pressure, altitude and wind speed. The variation is modelled as small cells with different refractive index from the adjacent cells. These cells are called turbulence eddies. The size of eddies might change from a few millimetre to several metres [30, 88]. Turbulence is a slow varying fading channel and has the temporal coherence in the order of 1 to 10 ms [89].

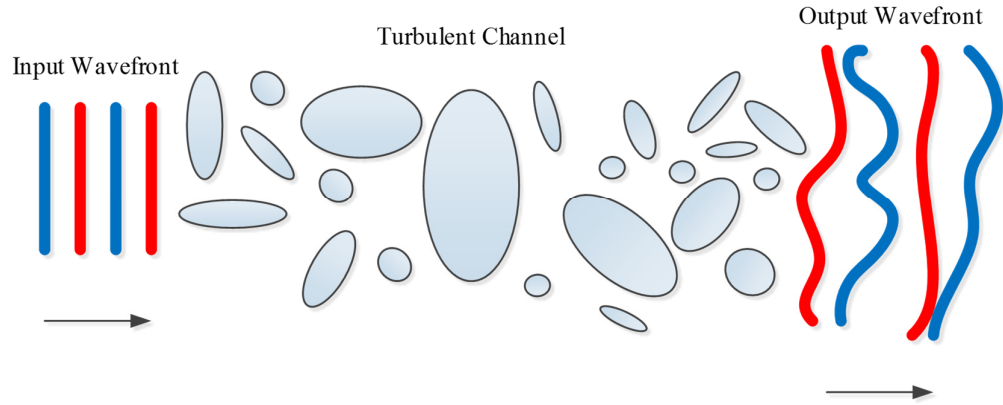


Figure 3.1: Turbulent channel frozen at $t=0$. The turbulent channel consists of eddies with various sizes.

A useful parameter is the channel correlation radius ρ_c , which is defined as [90]:

$$\rho_c \approx d_0^2 / \pi \rho_0, \quad (3.1)$$

where correlation length d_0 is given by [91]:

$$d_0 \approx \sqrt{\lambda_{\text{FSO}} L}. \quad (3.2)$$

Also ρ_0 is spatial coherence radius and is defined as [90]:

$$\rho_0 = (1.46 k_{\text{FSO}}^2 C_n^2 L)^{-3/5}, \quad (3.3)$$

where $k_{\text{FSO}} = 2\pi/\lambda_{\text{FSO}}$ is the wavenumber and C_n^2 is the index-of-refraction structure

parameter. ρ_c is an important parameter to choose the spacing between various independent Rxs in a system with multiple Rxs. The term ‘independent Rxs’ means that the correlation between the fading effects of two received signals from two independent Rxs is negligible. ρ_c is a general use parameter and can be employed in different turbulence regimes, whereas correlation length (d_0) is an approximation of ρ_c for the weak turbulence regime [90].

For the index-of-refraction structure (C_n^2) there are a number of models available but the most widely used is the altitude dependent model developed by Hufnagle-Valley, which is given by [85]:

$$C_n^2 = 0.00594(v/27)^2(10^{-5}h)^{10}\exp(h/1000) + 2.7 \times 10^{-6}\exp(-h/1500) + A \exp(-h/1000), \quad (3.4)$$

where h , v , and A represent the altitude (m), the root mean square (rms) wind speed (m/s), and the nominal value of C_n^2 at $h = 0$, respectively. Depending on the strength of turbulence C_n^2 might be $1.7 \times 10^{-14} \text{m}^{-2/3}$ during daytime for a 1 km link or $8.4 \times 10^{-15} \text{m}^{-2/3}$ during night for the same link [85].

Provided that the received optical signal intensity is denoted by I , a useful parameter to qualify the effect of turbulence is the scintillation index (SI) σ_I^2 , which is defined as the normalized irradiance variance of the optical beam as given by [91]:

$$\sigma_I^2 = \frac{E[I^2] - E[I]^2}{E[I]^2}, \quad (3.5)$$

where $E[\cdot]$ denotes the expected value. The variance of log-intensity signal fluctuation defined by Rytov variance σ_R^2 is given by [91]:

$$\sigma_R^2 = 1.23 k_{\text{FSO}}^6 C_n^2 L^{\frac{11}{6}}, \quad (3.6)$$

For the light beam with a spot size of diameter W at the Rx, Rytov variance criteria for

the weak turbulence condition are given by [30]:

$$\sigma_R^2 < 1 \text{ and } \sigma_R^2 \Lambda^{\frac{5}{6}} < 1, \quad (3.7)$$

where $\Lambda = 2L/k_{\text{FSO}}W$. Since in this research work $\Lambda \ll 1$, then only the condition $\sigma_R^2 < 1$ is applicable for weak turbulence.

The distribution of fading coefficient for the weak turbulence regime can be modelled using Log-normal distribution, which is practically valid as long as $\sigma_R^2 < 0.3$. Log-normal probability distribution function (PDF) of the normalized irradiance with mean μ_x and variance σ_x^2 is given as [15]:

$$f_I(I) = \frac{1}{2I} \frac{1}{\sqrt{2\pi\sigma_x^2}} \exp\left(-\frac{(\ln(I/I_0) - 2\mu_x)^2}{8\sigma_x^2}\right), \quad (3.8)$$

where $I_0 = E[I]$ is the signal light intensity without turbulence.

To normalize $f_I(I)$ it is assumed that $\mu_x = -\sigma_x^2$ [85]. Under the assumption of weak turbulence σ_I^2 and σ_x^2 are related as follow [30]:

$$\sigma_I^2 = \exp(4\sigma_x^2) - 1 \cong 4\sigma_x^2, \quad (3.9)$$

In the literature depending on the light propagation model different expressions are introduced for the variance of Log-normal distribution. For the plane wave propagation, one has $\sigma_I^2 = \sigma_R^2$ [30].

Aperture averaging is a technique that reduces the variation of optical intensity according to the aperture diameter d_s [92, 93]. To benefit from aperture averaging, the size of d_s needs to be larger than d_0 in Equ. (3.2) [85, 90], which is valid for the weak turbulence regime. In fact, d_0 can be much larger in the moderate-to-strong turbulence regime [90, 93]. With $\sigma_I^2(0)$ and $\sigma_I^2(d_s)$ defined as the scintillation index of the Rx with no aperture and with aperture of d_s , respectively, the aperture averaging factor (AF) is given by [7, 93]:

$$AF = \frac{\sigma_I^2(d_s)}{\sigma_I^2(0)} \approx \left[1 + 1.6682 \left(\frac{d_s}{d_0} \right)^2 \right]^{-7/6}. \quad (3.10)$$

In the moderate-to-strong turbulence regime one has [30]:

$$\sigma_R^2 \approx 1, \text{ for moderate regime,} \quad (3.11.a)$$

$$\sigma_R^2 > 1, \text{ for strong regime,} \quad (3.11.b)$$

and the received signal optical intensity I is based the PDF of Gamma-Gamma (GG) distribution given by [94]:

$$f_I(I) = \frac{2(\alpha\beta)^{\frac{\alpha+\beta}{2}} I^{\frac{\alpha+\beta}{2}-1}}{\Gamma(\alpha)\Gamma(\beta)I_0^{\frac{\alpha+\beta}{2}}} K_{\alpha-\beta} \left(2\sqrt{\alpha\beta \frac{I}{I_0}} \right), \quad (3.12)$$

where $\alpha \geq 0$ and $\beta \geq 0$ are known as the effective numbers of large- and small-scale turbulence cells, respectively [86, 95]. $K_n(\cdot)$, and $\Gamma(\cdot)$ denote the modified Bessel function of 2nd kind and order n , and the Gamma function, respectively.

The two parameters of α and β that characterize the irradiance fluctuation PDF are related to the atmospheric conditions and σ_I^2 , which are given by [30]:

$$\alpha = \frac{1}{\exp(\sigma_{\ln X}^2) - 1}, \quad (3.13.a)$$

$$\beta = \frac{1}{\exp(\sigma_{\ln Y}^2) - 1}, \quad (3.13.b)$$

$$\sigma_I^2 = \frac{1}{\alpha} + \frac{1}{\beta} + \frac{1}{\alpha\beta} = \exp(\sigma_{\ln X}^2 + \sigma_{\ln Y}^2) - 1, \quad (3.13.c)$$

where $\sigma_{\ln X}^2$ and $\sigma_{\ln Y}^2$ represent the variances of large-scale and small-scale irradiance fluctuations, respectively.

As mentioned above the presence of aperture at the Rx will reduce the effect of turbulence. For the plane wave propagation model and considering the aperture size the closed form expressions for $\sigma_{\ln X}^2$ and $\sigma_{\ln Y}^2$ parameters are given by [30]:

$$\sigma_{\ln X}^2 = \frac{0.49\sigma_R^2}{\left(1+0.65d^2+1.11\sigma_R^{12/5}\right)^{7/6}}, \quad (3.14.a)$$

$$\sigma_{\ln Y}^2 = \frac{0.51\sigma_R^2\left(1+0.69\sigma_R^{12/5}\right)^{-5/6}}{1+0.90d^2+0.62d^2\sigma_R^{12/5}}, \quad (3.14.b)$$

where $d = \left(k_{\text{FSO}}d_s^2/4L\right)^{0.5}$ [30].

3.3 Spatial Diversity Configuration

Depending on the number of Tx's and Rx's apertures, there are a number of spatial diversity schemes. Figure 3.2 illustrates a simple block diagram of the existing spatial diversity schemes of single-input single-output (SISO), single-input multiple-output (SIMO), multiple-input single-output (MISO), and multiple-input multiple-output (MIMO). SISO is the simplest option with no spatial diversity, whereas MIMO is the most complex scheme. SIMO is the other scheme, which is used in this thesis and will be discussed later. In this work SISO and SIMO systems are adopted, with SISO being used as a reference scheme. The performance of the SISO/SIMO FSO link will be evaluated under various turbulence conditions.

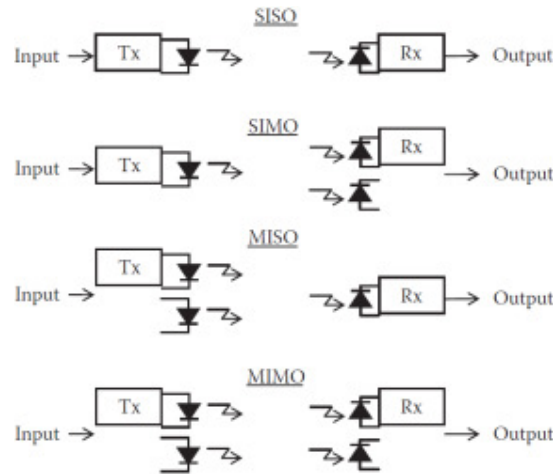


Figure 3.2: Spatial diversity configurations [17]. SISO, SIMO, MISO, and MIMO denote single-input single-output, single-input multiple-output, multiple-input single-output, multiple-input multiple-output, respectively.

3.4 Channel Model in SISO and SIMO

For a SIMO FSO link with OOK employing M -receive apertures, the received signal at the m -th aperture r_m can be written as (see Figure 3.3) [85]:

$$r_m = S\eta I_m + n_m, \quad m = 1, \dots, M, \quad (3.15)$$

where $S \in \{0,1\}$ represents the information bit, η is the optical-to-electrical conversion coefficient, I_m denotes the irradiance received at the m -th aperture, and n_m is additive white Gaussian noise (AWGN) with zero mean and variance of σ_m^2 . The AWGN can be considered as a combination of the thermal, shot, and dark noise sources of the Rx and the background ambient light [96]. It is assumed that the channel for Tx to each Rx is independent, which interprets to the fact that the transversal distance between the adjacent apertures is larger than ρ_c in Equ. (3.1) [90].

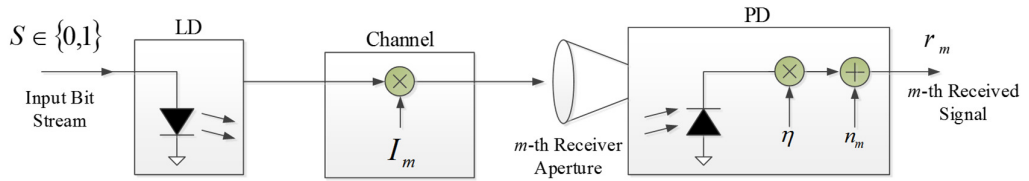


Figure 3.3: A simplified illustration of m -th FSO link in a single-input multiple-output scheme. LD and PD are laser diode and photodetector, respectively.

In SIMO, each m -th FSO link (see Figure 3.3) is equivalent to a SISO FSO link. For an IM/DD based link with AWGN and assuming an equiprobable data transmission ($P(0) = P(1) = 0.5$), the probability of error conditioned on the received irradiance is $\text{BER} = 0.5(P(e|0) + P(e|1))$. Note that $P(e|0)$ and $P(e|1)$ are the conditional probabilities defined by averaging over the PDF of fading coefficient $f_{I_m}(\cdot)$ as [97]:

$$P(e|0) = P(e|1) = \int_0^{\infty} f_{I_m}(I_m) Q\left(\frac{\eta I_m}{\sqrt{2N_0}}\right) dI_m, \quad (3.16)$$

where $N_0 = 2\sigma_m^2$ is the noise spectral density. Note that $f_{I_m}(\cdot)$ will depend on the channel condition. Also note that Equ. (3.16) is valid for SISO and for SIMO the appropriate

expression will be introduced.

The simplified BER expression in a weak and moderate-to-strong turbulence regime will be given later in Eqs. (3.21) and (3.28). Here, however to show the effect of turbulence and the need for mitigation methods, the performance of a SISO link in clear, weak, moderate and strong turbulence regimes with and without the aperture averaging effect are compared, see Figure 3.4. Note that the aperture size $d_s = d_0 \approx 30$ mm, and Rytov variance (σ_R^2) for the weak, moderate and strong regimes are 0.2, 1 and 4, respectively. The graph shows the severe effect of turbulence on the performance of the system. Aperture averaging also helps to reduce the effect of turbulence. But for the given aperture size, the turbulence effect is still significant. Even for the weak turbulence regime with the aperture averaging, there is a ~ 8 dB power penalty in order to maintain the target BER of 10^{-6} as in a clear channel.

Therefore, aperture averaging is not the single sufficient solution to mitigate the turbulence and other techniques should also be considered. Thus as mentioned earlier, spatial diversity along with aperture averaging will be used as the other technique.

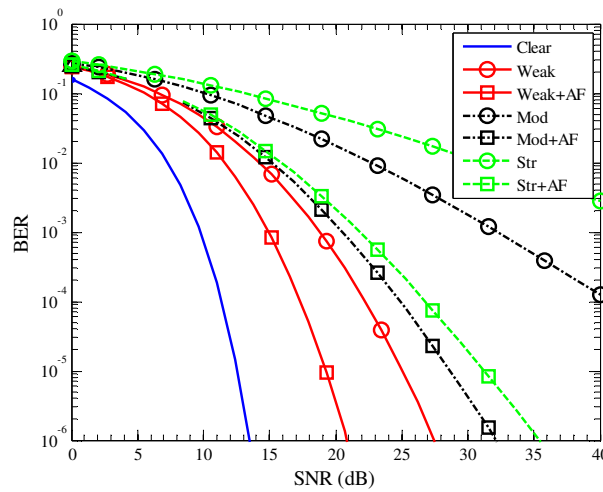


Figure 3.4: Comparison of single-input single-output performance (BER versus SNR) over clear, weak, moderate and strong turbulence regimes with and without aperture averaging. ‘Weak’, ‘Mod’ and ‘Str’ refer to weak, moderate and strong regimes, respectively. ‘+AF’ denotes applying aperture averaging.

3.5 Combining Methods

In [98, 99] Kennedy et. al. proposed using diversity technique in FSO systems and they showed the benefits of diversity techniques in turbulent channels. Since then the researchers have been investigating different diversity configurations in distinct turbulence regimes.

In a SIMO FSO link multiple optical aperture are being used to receive the same signal transmitted from the Tx. Depending on the combining technique, the output bit stream will be extracted from the received multiple optical signals. A typical SISO FSO Rx is shown in Figure 3.5 where optical, electrical and logical signals are depicted for the bit stream of $\{1, 0, 1, 1, 0\}$. Note that at the final stage, using a quantizer, the electrical signal is converted back into a bit stream of 0s and 1s.

Considering these three forms of the received signal, combining can be performed at various levels. Here the performance of an optical SIMO link employing three spatial diversity Rx configurations using different combining techniques is investigated (see Figure 3.6).

In Figure 3.6(a) the output of ORx is fed into a quantizer, which converts the electrical

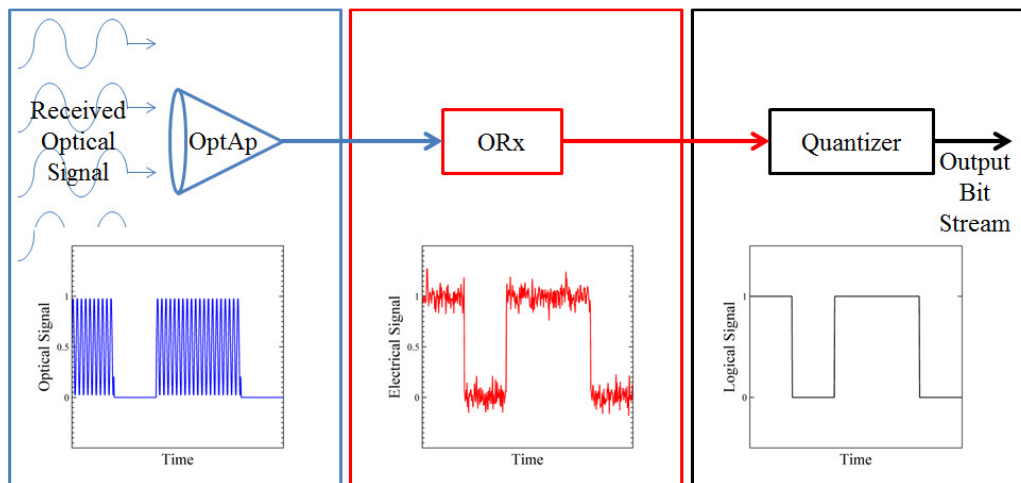


Figure 3.5: A typical single-input single-output FSO Rx. The received signal is shown at optical, electrical and logical domain for bit stream of $\{1, 0, 1, 1, 0\}$. OptAp refers to the optical aperture.

signal into logical levels of 0 and 1, whereas in Figure 3.6(b-c), following the linear combiner, the combined outputs from ORxs is applied to the quantizer. In another configuration the outputs of ORxs are passed through quantizer modules, the outputs of which are applied to the logical combiner, see Figure 3.6(d).

3.6 Weak Turbulence

In this section different combining methods under the weak turbulence regime are studied. Starting from the optical domain, first the existing combining method corresponding to the optical domain are introduced. Next, the combining methods in the electrical domain are explained and finally the logical domain is looked at. Since the weak turbulence regime is considered, thus a point-wise ORx will be used.

3.6.1 Adaptive Optics Technique

In [100] authors have investigated the effect of turbulence in a non-Gaussian receiver optical system, where all channels experienced the turbulence effect. As a result, the phase of the received signals underwent random fluctuation, and using the adaptive optics compensation scheme, it was possible to sum up the channels coherently. In this approach the spatial diversity is applied at the Rx side, where the outputs of optical apertures are combined prior to photodetection, see Figure 3.6(a). The combining method is referred as adaptive optics technique (AOT). AOT is modelled by an equivalent SISO system, whereas Equ. (3.15) is written as $r_{total} = S\eta I_{total} + n_0$, where $I_{total} = \frac{1}{M} \sum_{m=1}^M I_m$ [100]. Therefore, Equ. (3.16) takes the following form:

$$P(e|0) = P(e|1) = \int_0^{+\infty} f_{I_{total}}(I) Q\left(\frac{\eta}{\sqrt{2N_0}} I\right) dI. \quad (3.17)$$

For weak turbulence, $f_{I_{total}}(\cdot)$ will have Log-normal distribution given by Equ. (3.8)

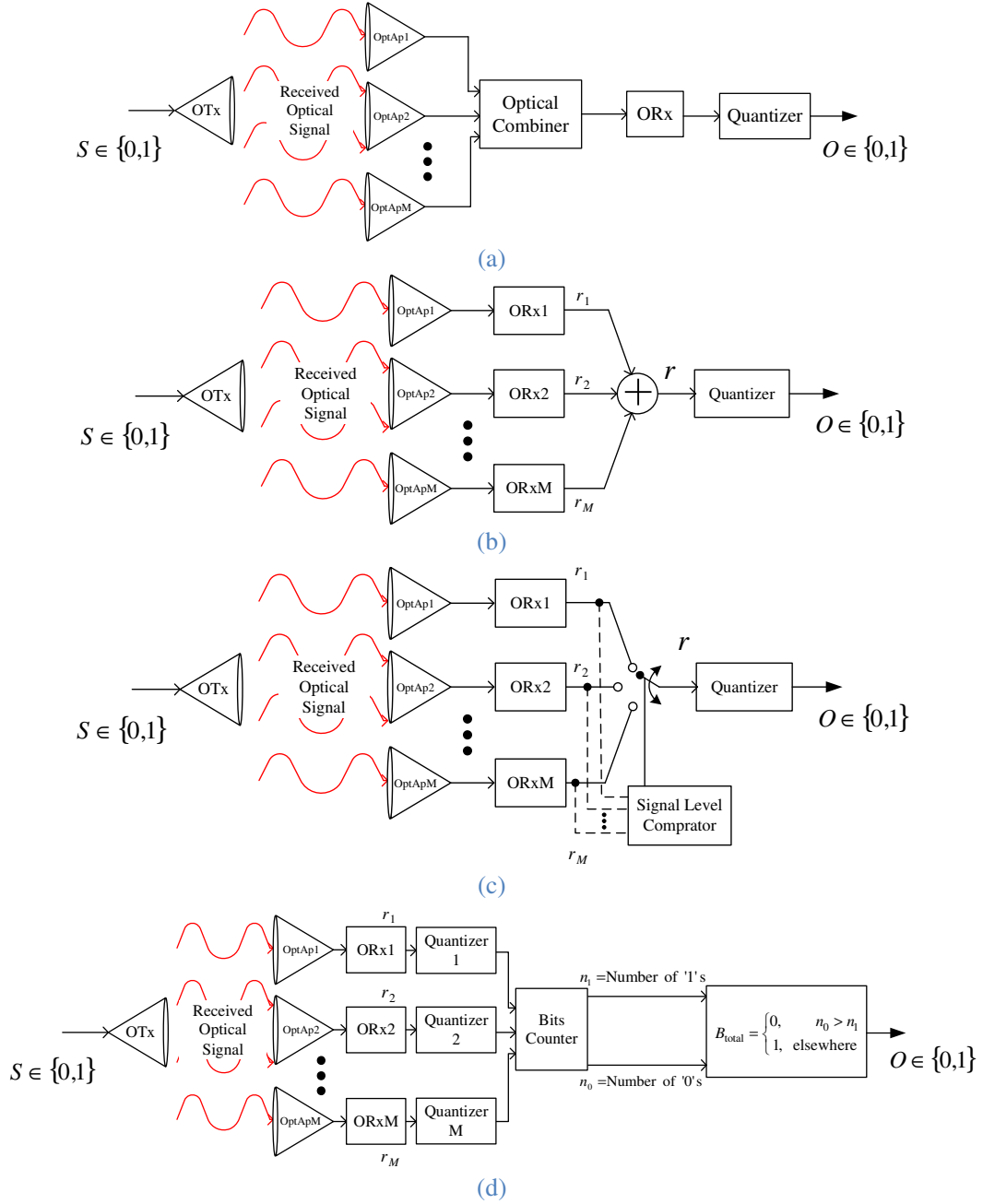


Figure 3.6: Block diagram of combining implementation at different signal levels: (a) optical domain, (b-c) electrical domains, and (d) logical domain. OTx and OptAp and ORx refer to optical transmitter, optical aperture, and optical receiver, respectively.

with the total variance σ_{total}^2 and mean m_{total} given by [100]:

$$\sigma_{total}^2 = \ln[1 + (e^{\sigma_x^2} - 1)/M], \quad (3.18.a)$$

$$\mu_{total} = -0.5(\sigma_x^2 + \sigma_{total}^2). \quad (3.18.b)$$

Equation (3.18) is derived using Wilkinson's method for uncorrelated random variables

[101]. The simplified form of BER for the weak turbulence regime is given by:

$$\text{BER} = \frac{1}{\sqrt{\pi}} \sum_{i=1}^p \omega_i Q \left(\eta I_0 \frac{\exp \left[2\mu_{total} + z_i \sqrt{8\sigma_{total}^2} \right]}{\sqrt{2N_0}} \right). \quad (3.19)$$

Note that to obtain a closed form equation in weak turbulence, Gauss-Hermite quadrature formula is used. p is the order of approximation, ω_i is the weight factor for the p th-order approximation, and z_i is the zero of the p th-order Hermite polynomial. For values of ω_i and z_i refer to mathematical handbooks such as [102]. For further information on mathematical simplification, refer to Appendix A.

3.6.2 SISO and EGC

In this approach the spatial diversity is adopted at the Rx side, where the outputs of ORxs are combined prior to being applied to the quantizer module as shown in Figure 3.6(b). For EGC as seen from Figure 3.6(b), the outputs of ORxs are summed up coherently before quantization. For this combining method, Equ. (3.16) is replaced by [103]:

$$P(e|0) = P(e|1) = \int_{\mathbf{I}} f_{\mathbf{I}}(\mathbf{I}) Q \left(\frac{\eta}{M\sqrt{2N_0}} \sum_{m=1}^M I_m \right) d\mathbf{I}, \quad (3.20)$$

where $f_{\mathbf{I}}(\mathbf{I})$ is the joint PDF of vector $\mathbf{I} = (I_1, I_2, \dots, I_M)$. Following the method reported in [85] it is possible to derive a closed-form expression for Equ. (3.20), so that for the SISO link it results in:

$$\text{BER} = \frac{1}{\sqrt{\pi}} \sum_{i=1}^p \omega_i Q \left(\eta I_0 \frac{\exp \left[-2\sigma_x^2 + z_i \sqrt{8\sigma_x^2} \right]}{\sqrt{2N_0}} \right). \quad (3.21)$$

and for the EGC scheme, the BER is given by:

$$\text{BER} = \frac{1}{\sqrt{\pi}} \sum_{i=1}^p \omega_i Q \left(\eta I_0 \frac{\exp \left[-2\hat{\sigma}_x^2 + z_i \sqrt{8\hat{\sigma}_x^2} \right]}{\sqrt{2N_0}} \right), \quad (3.22)$$

where $\hat{\sigma}_x^2 = \sigma_x^2/M$ [85]. For further information on mathematical simplification, refer to Appendix A.

3.6.3 SC

In SC, by means of a comparator at the Rx, the signal with highest intensity level is selected for further processing, see Figure 3.6(c). Considering an independent and identically distributed (i.i.d.) intensity fading channel and by introducing $I_{SC} = \max(I_1, I_2, \dots, I_M)$ the PDF takes the following form [86]:

$$f_{I_{SC}}(I_{SC}) = \frac{d}{dI_{SC}} \prod_{m=1}^M F_{I_m}(I_{SC}) = M f_I(I_{SC}) [F_I(I_{SC})]^{M-1}, \quad (3.23)$$

where $F_{I_m}(\cdot)$ is cumulative distribution function (CDF). Thus the BER expression for SC is given by [103]:

$$P(e|0) = P(e|1) = M \int_0^{+\infty} f_I(I) [F_I(I)]^{M-1} Q \left(\frac{\eta}{\sqrt{2MN_0}} I \right) dI. \quad (3.24)$$

After some mathematical simplification, it can be shown that:

$$\text{BER} = \frac{M}{\sqrt{\pi}} \sum_{i=1}^p \omega_i Q \left(-\sqrt{2} z_i \right)^{M-1} Q \left(\eta I_0 \frac{\exp \left[-2 - \sigma_x^2 + z_i \sqrt{8\sigma_x^2} \right]}{\sqrt{2MN_0}} \right). \quad (3.25)$$

For further information on mathematical simplification, refer to the Appendix A.

3.6.4 MLC

In this scheme for more than two receivers ($M > 2$) a comparison-based combining method is adopted in the logical domain and is referred to as the MLC scheme, see Figure

3.6(d). The basic concept of MLC is to monitor the output bits at each branch and generate the final output bit B_{total} stream based on the numbers of simultaneous received 1s (n_1) and 0s (n_0) (see Figure 3.6(d)). For this scheme the probability of error is given by [104]:

$$\text{BER} = \begin{cases} \sum_{i=N+1}^M \binom{M}{i} P_b^i P_c^{M-i} + \frac{1}{2} \binom{M}{N} P_b^N P_c^N, & M = 2N \\ \sum_{i=N}^M \binom{M}{i} P_b^i P_c^{M-i}, & M = 2N - 1 \end{cases} \quad (3.26)$$

where P_b denotes the probability of error for each diversity branch that can be obtained by setting I_0 to I_0/M in Equ. (3.22), $P_c = 1 - P_b$, and $N > 2$, which is an integer number. However for $P_b \ll 1$ it can be assumed that $P_c \cong 1$ and since higher SNRs where $P_b \ll 1$, and assuming i.i.d for all channels then Equ. (3.26) can be simplifies to the following:

$$\text{BER} = \begin{cases} \sum_{i=N+1}^M \binom{M}{i} P_b^i + \frac{1}{2} \binom{M}{N} P_b^N, & M = 2N \\ \sum_{i=N}^M \binom{M}{i} P_b^i, & M = 2N - 1 \end{cases} \quad (3.27)$$

3.6.5 Numerical Analysis

In this section the system performance of the mentioned diversity methods in comparison to the SISO based FSO link under the weak turbulence regime is outlined. Figure 3.7 shows the BER performance against the average SNR for aforementioned combining schemes for two values of weak turbulence strength (σ_x) and a range of number of receivers (M) using the expressions given in Eqs. (3.19), (3.21), (3.22), (3.25), and (3.27).

In Figure 3.7(a) a plot for MLC is not shown since $M = 2$. In Figure 3.7(a) EGC and AOT offer the best performance for both turbulence levels. However, in Figure 3.7(b) and Figure 3.7(c) MLC displays the best performance by offering lower SNR values of 2.10, 1.83, 5.29 and 7.18 dB compared to the AOT, EGC, SC and SISO, respectively to achieve the same BER of 10^{-6} for $\sigma_x = 0.2$, and $M = 3$. For the same σ_x and $M = 5$, the SNR gains are 4.27, 3.95, 8.90 and 10.66 dB compared to the AOT, EGC, SC and SISO,

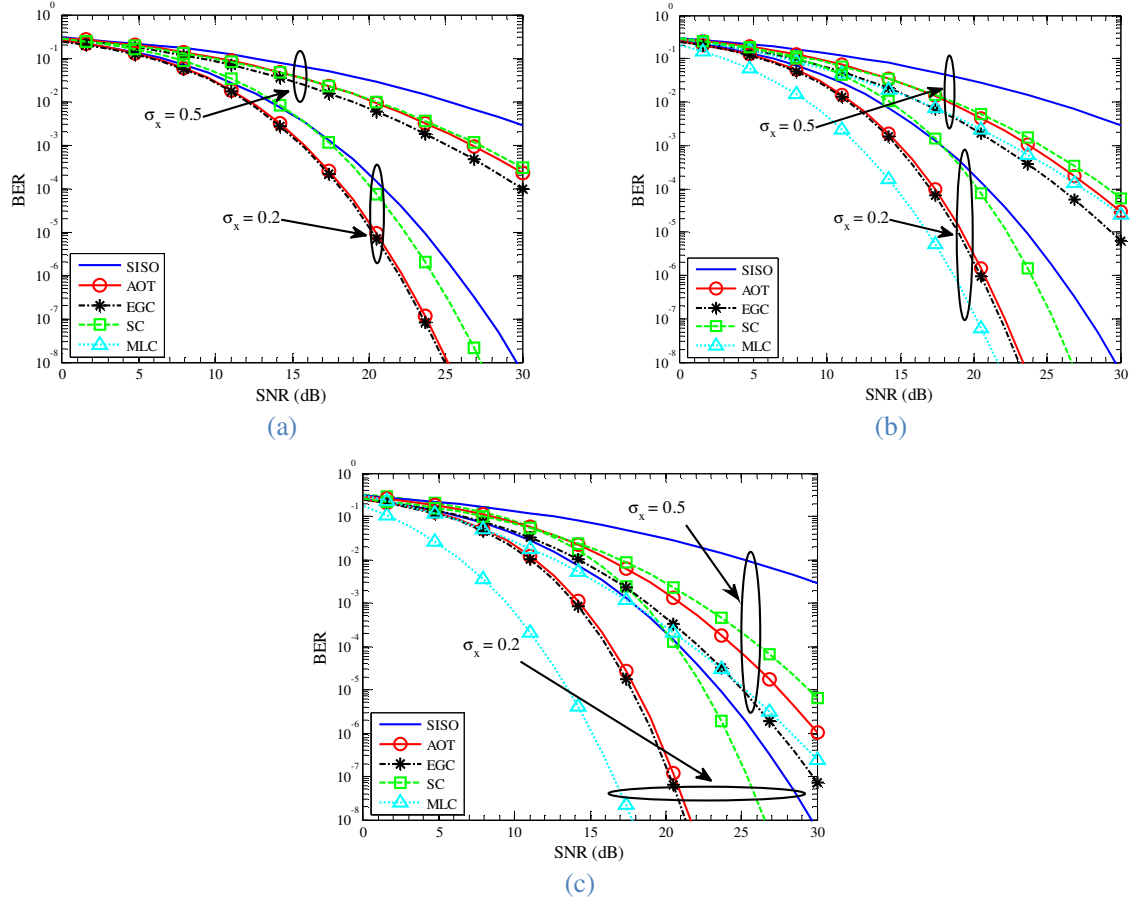


Figure 3.7: Comparison of average BER for average SNR of 0 to 30 dB for different numbers of receiver apertures (M): (a) $M=2$, (b) $M=3$, and (c) $M=5$. Two turbulence regime sets of $\sigma_x=0.2$ and 0.5 have been calculated in each plot. SISO, AOT, EGC, SC, and MLC refer to single-input multiple-output, adaptive optical technique, equal gain combining, selective combining and bit-majority combining, respectively.

respectively. For $\sigma_x = 0.5$ however, the best combining method is EGC while SC still has the worst performance for all cases. Besides all the combining schemes show the same slope in Figure 3.7, which means that diversity order of all combining methods are the same. The summary of power gains relative to the SISO method for a BER of 10^{-6} is presented in Table 3.1.

Next simulation of a 2 km long FSO link with the following parameters is carried out: laser wavelength of 830 nm, ORx with noise floor of -31.06 dBm for 500 MHz bandwidth and C_n^2 of $10^{-15} m^{-2/3}$. The corresponding BER expressions are solved for a BER of 10^{-6} and required received optical power at each PD is calculated using [96, Eq. (23)]. Figure 3.8 illustrates the normalized required optical received power (normalized with

Table 3.1: Comparison of power gains of AOT, EGC, SC and MLC relative to SISO method for a $\text{BER}=10^{-6}$ under weak turbulence regimes (i.e., σ_x of 0.2 and 0.5). SISO, AOT, EGC, SC, and MLC refer to single-input multiple-output, adaptive optical technique, equal gain combining, selection combining and majority-logic combining, respectively. The values are obtained from the results in Figure 3.7. The gains are in dB and M is the number of receiver apertures.

	$\sigma_x = 0.2$			$\sigma_x = 0.5$		
	$M = 2$	$M = 3$	$M = 5$	$M = 2$	$M = 3$	$M = 5$
AOT	3.6	5	6.4	10.72	15.52	20.22
EGC	3.8	5.3	6.7	12.62	17.82	22.72
SC	1.6	1.8	2	10.02	14.12	17.97
MLC	-	7.2	10.6	-	15.12	21.97

respect to SISO) against M for AOT, EGC, SC and MLC. As it was concluded before SC has the worst performance among all combining methods. AOT offers improved performance compared to SC, e.g., for $M = 2$, the power penalty between them is 0.7 dB increasing to 2.4 dB for $M = 10$. However comparing AOT and EGC the power penalties are between 0.43 and 0.60 dB for the values of M in the range of $2 \leq M \leq 9$. Compared to AOT, EGC and SC the proposed MLC method outperforms all for $M > 3$ (e.g., for $M = 10$ the power penalty is 3.29 dB compared to the EGC). The MLC offers superior performance capabilities compared to all other combining schemes at the cost of increased system complexity.

One important issue in this numerical analysis is the superiority of MLC to the EGC method. EGC is almost similar to maximal ratio combining (MRC) and considering the

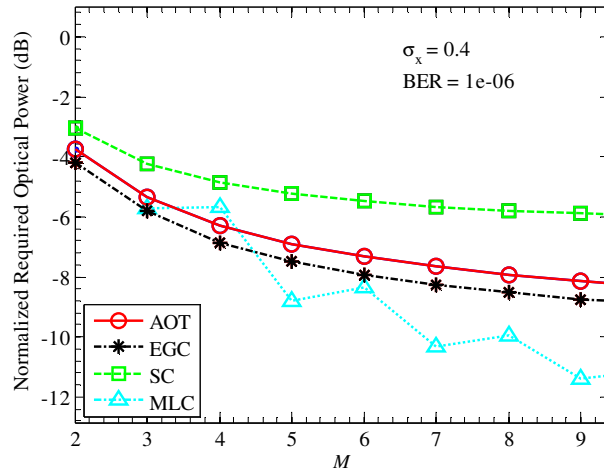


Figure 3.8: Normalized required optical received power versus the number of receiver apertures (M) for a BER of 10^{-6} at the Rx. The values are normalised with respect to single-input single-output (SISO). AOT, EGC, SC, and MLC refer to adaptive optical technique, equal gain combining, selection combining and majority-logic combining, respectively.

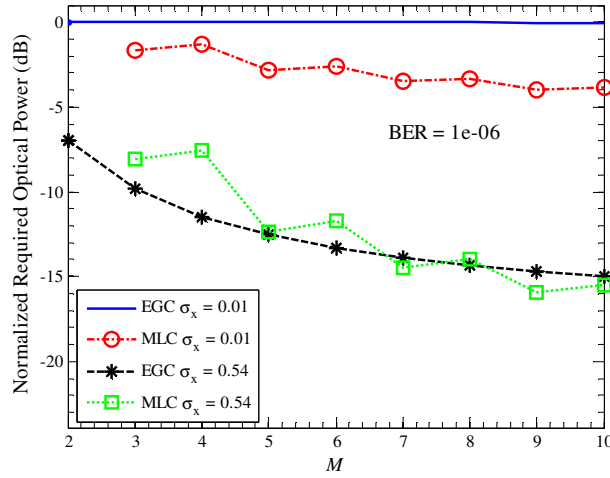


Figure 3.9: Normalized required optical received power versus the number of receiver apertures (M) for a BER of 10^{-6} at the Rxs implementing EGC and MLC. The values are normalised with respect to SISO. EGC, and MLC refer to equal gain combining and majority-logic combining, respectively.

fact that MRC gives the best performance among combining methods, additional comparison, similar to Figure 3.8, only between EGC and MLC for different turbulence strengths and a range of M is performed, see Figure 3.9. For $\sigma_x = 0.01$ the channel is assumed to be clear and Figure 3.9 obviously shows that regardless of the values of M the performance of system with EGC is almost the same as SISO. However, the MLC system shows a different behaviour and increasing the number of Rxs improves the system performance.

In MLC each Rx is an independent SISO link and the final output bit is decided based on the majority rule so that larger number of Rxs results in less chance of receiving a wrong bit. Therefore, the quality of MLC is totally dependent on each individual SISO link and that is why increasing the turbulence strength will degrade the MLC system performance. Figure 3.9 illustrates the calculated results for $\sigma_x = 0.54$ in which the performance of MLC is not as significant of the case where σ_x was 0.01. The value of $\sigma_x = 0.54$ is the limit which beyond it the Log-normal PDF is not valid.

As seen from case of $\sigma_x = 0.01$, increasing M leads to more enhanced system performance and one can see that for small values of M the system with EGC outperforms

the one with MLC. This observation about the MLC method concludes that increasing the number of Rxs of a MLC system improves the system performance under any conditions (i.e., in contrary to EGC even in a clear channel the performance will improve) and for a specific number of Rxs the performance of MLC outperforms EGC. For low values of σ_x MLC outperforms EGC however, the increase in the turbulence strength degrades this superiority.

The MLC curves depicted in Figure 3.8 and Figure 3.9 show two interesting odd behaviours: the ripple in the MLC curve as well as performance degradation for higher number of apertures (e.g. a system with 3 apertures performs better than one with 4 apertures). To describe these behaviour, one should remember that an assumption was made to simplify Equ. (3.26) into Equ. (3.27). Besides, to obtain the required power Equ. (3.27) was numerically solved, which introduced additional approximation. Also it is worth mentioning that the performance of MLC system for $M = 2N$ and $M = 2N - 1$ are the same, which is proved in [104]. Therefore, ideally for instance in Figure 3.9 for $M = 3$ and 4 the same value for normalized required optical received power should be observed. It is worth mentioning that the ideal plot must look like a staircase graph showing that same normalised required optical power for receivers with $2N$ and $2N - 1$ numbers of apertures. However, the existence of errors does not alter the fact that MLC offers improved performance for larger number of apertures and higher values of SNR.

3.7 Strong Turbulence

In this section, the performance of typical combining methods under the strong turbulence regime is investigated. In contrary to the weak turbulence regime, apertures with a given diameter, which results in aperture averaging effect are considered.

3.7.1 SISO and EGC

The procedure of deriving the BER expression is the same as in Section 3.6.2 where as $f_l(\mathbf{I})$ takes a different form. In [95] a closed-form expression is proposed to estimate $f_l(\mathbf{I})$ for the case of a MIMO FSO system. Using the same approach and considering the special case of SIMO with M -aperture, the error probability is obtained as [95]:

$$\text{BER} \approx \frac{2^{k_T+m_T-3}}{\sqrt{\pi^3}\Gamma(k_T)\Gamma(m_T)} G_{5,2}^{2,4} \left[\left(\frac{2}{k_T m_T} \right)^2 \gamma \left| \begin{matrix} \frac{1-k_T}{2}, \frac{2-k_T}{2}, \frac{1-m_T}{2}, \frac{2-m_T}{2}, 1 \\ 0, \frac{1}{2} \end{matrix} \right. \right], \quad (3.28)$$

where $G[\cdot]$ is the Meijer-G function [105], $k_T = M\alpha + \varepsilon(M, \alpha, \beta)$, $m_T = M\beta$, and the parameter $\varepsilon(l, k, m)$ is defined as [95]:

$$\varepsilon(l, k, m) = (l-1) \frac{(-0.127 - 0.95k - 0.0058m)}{(1 + 0.00124k + 0.98m)}. \quad (3.29)$$

Also, γ in Equ. (3.28) is the average electrical SNR defined as $\eta^2 I_0^2 / N_0$.

3.7.2 SC

Knowing that $F_{I_m}(\cdot)$ for the GG distribution is defined as [95]:

$$F_{I_m}(I_m) = \frac{1}{\Gamma(\alpha)\Gamma(\beta)} G_{1,3}^{2,1} \left[\frac{\alpha\beta}{I_0} \left| \alpha, \beta, 0 \right. \right]. \quad (3.30)$$

Thus the following Section 3.6.3 and using Gauss-Laguerre quadrature formula [102], the BER expression for SC is given by [103]:

$$\text{BER} \approx 2M \frac{(\alpha\beta)^{\frac{\alpha+\beta}{2}}}{(\Gamma(\alpha)\Gamma(\beta))^M} \sum_{i=1}^q \chi_i \left\{ \left(G_{1,3}^{2,1} \left[\alpha\beta y_i \left| \alpha, \beta, 0 \right. \right] \right)^{M-1} \times Q \left(\frac{\eta I_0 y_i}{\sqrt{2MN_0}} \right) y_i^{\frac{\alpha+\beta}{2}-1} e^{y_i} \right\}, \quad (3.31)$$

where q , χ_i , and y_i are the order of approximation, the weight factor for the q^{th} -order approximation, and the zero of the q^{th} -order Laguerre polynomial, respectively. For further information on mathematical simplification, refer to the Appendix A.

3.7.3 MLC

The BER expression is obtained by following the same procedure explained in Section 3.6.4. Note that, here P_b denotes the probability of error for each diversity branch that can be obtained by setting the number of apertures (M) to 1 in Equ. (3.28).

3.7.4 Numerical Analysis

In this section, the performance of EGC, SC and MLC with a SISO system under turbulence conditions are compared. An FSO link of 1 km length employing a 830 nm laser source is considered. The plane wave model propagation, and two turbulence regimes with $C_n^2 = 3 \times 10^{-14}$ and $5 \times 10^{-14} \text{ m}^{-2/3}$, which are equivalent to Rytov variance (σ_R^2) of 1.24 and 2.06, respectively, are the other conditions. Using Eqs. (3.28), (3.31) and (3.27), the BER performance of EGC, SC and MLC over the SNR range of 0 to 50 dB and M of 3 and 5 for the case of a point Rx is depicted in Figure 3.10. Also shown for comparison, is the BER plot for SISO.

These results clearly illustrate the benefit of employing diversity techniques compared to SISO. It is observed that for each scenario EGC performance is better than SC. For

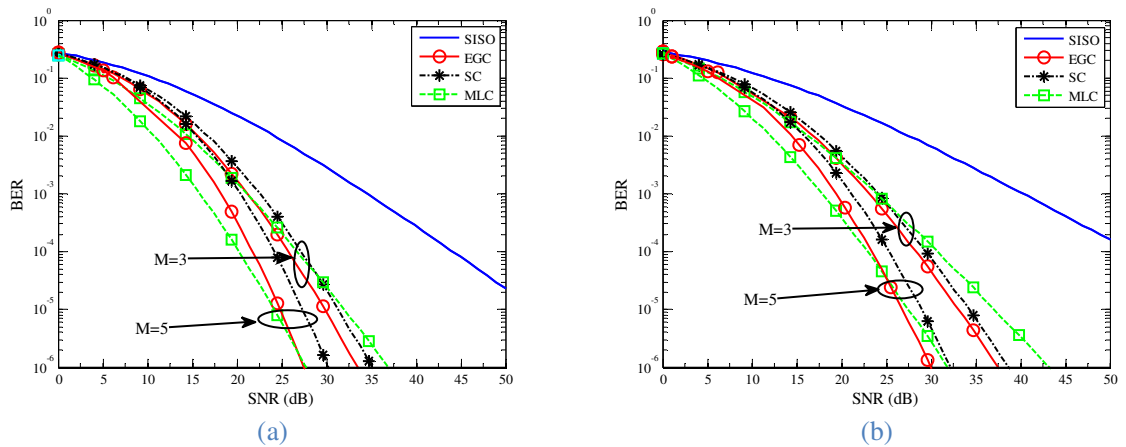


Figure 3.10: BER versus SNR for EGC, SC, MLC and SISO. The comparison is carried out for different numbers of apertures (M) and turbulence strengths (C_n^2): (a) $C_n^2 = 3 \times 10^{-14} \text{ m}^{-2/3}$ ($\sigma_R^2 = 1.24$), and (b) $C_n^2 = 5 \times 10^{-14} \text{ m}^{-2/3}$ ($\sigma_R^2 = 2.06$). SISO, EGC, SC, and MLC refer to single-input multiple-output, equal gain combining, selection combining and majority-logic combining, respectively.

Table 3.2: Comparison of power gains of AOT, EGC, SC and MLC relative to SISO method for a BER= 10^{-6} under strong turbulence regimes (i.e., σ_R^2 of 1.24 and 2.06). SISO, EGC, SC, and MLC refer to single-input multiple-output, equal gain combining, selection combining and majority-logic combining, respectively. The values are obtained from the results in Figure 3.10. The gains are in dB and M is the number of receiver apertures.

	$\sigma_R^2 = 1.24$		$\sigma_R^2 = 2.06$	
	$M = 3$	$M = 5$	$M = 3$	$M = 5$
EGC	35	28.9	46	38.5
SC	32.2	25.5	43.8	37.3
MLC	34.6	27.2	44.1	32.75

example for a BER of 10^{-6} , $C_n^2 = 3 \times 10^{-14} \text{ m}^{-2/3}$ and $M = 5$, EGC provides an SNR gain of 2.6 dB compared to SC. For $C_n^2 = 5 \times 10^{-14} \text{ m}^{-2/3}$ and $M = 5$ EGC still provides the best performance followed by MLC and SC for SNR > 24.5 dB. However, for SNR < 24.5 dB MLC offers marginally improved BER performance compared to others.

Therefore, it can be concluded that in the case of either increasing the number of Rx's or reducing the turbulence strength the performance of MLC drastically improves compared to EGC and SC. The summary of power gains relative to the SISO method for a BER of 10^{-6} is presented in Table 3.2.

To assess and compare the performance of MLC in a turbulence channel with other methods the performance of all three combining schemes as well as SISO for a range of real Rx aperture sizes d_s are investigated. For the SIMO case the aperture size of each Rx is set to $0.5d_0$ and d_0 , where d_0 is obtained from Equ. (3.2). In order to make a fair comparison between SISO and SIMO systems the aperture area of SISO is kept the same as the total apertures area of SIMO. Figure 3.11 shows the BER performance as a function of the SNR for EGC, SC, MLC and SISO configurations for $M = 3$ and $C_n^2 = 5 \times 10^{-14} \text{ m}^{-2/3}$.

In Figure 3.11(a) the aperture diameters for SIMO and SISO are approximately 14.5 mm and 25 mm, respectively. It is worth to compare results with the predicted data but for non-real cases with a point Rx in Figure 3.10(b). At a BER of 10^{-6} the SNR requirements has dropped by 38.3, 8.4, 7.75, and 13 dB for SISO, EGC, SC and MLC,

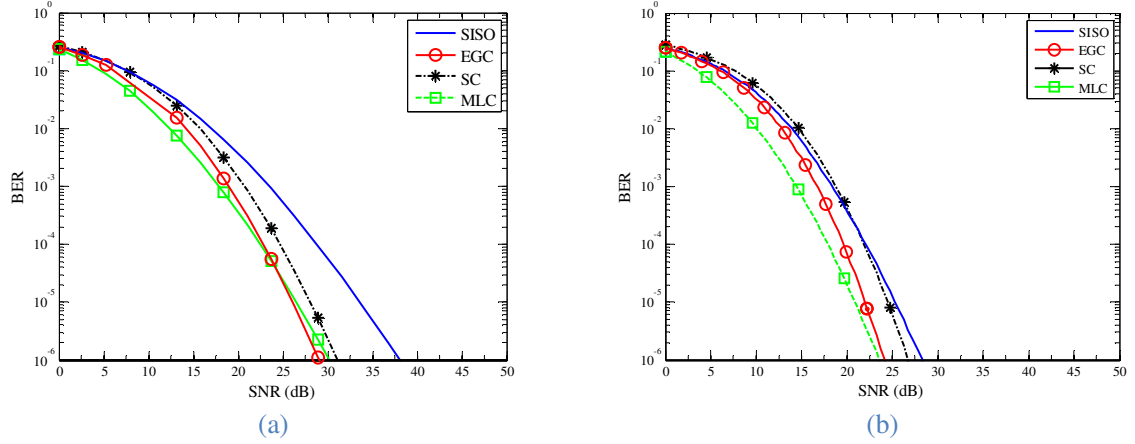


Figure 3.11: BER versus SNR for EGC, SC, MLC and SISO optical link configurations implementing real aperture averaged Rx. The comparison is carried out for three receiver apertures (i.e., $M=3$), $C_n^2=5 \times 10^{-14} \text{ m}^{-2/3}$ and different aperture sizes d_s provided $d_0 \approx 29 \text{ mm}$: (a) $d_s = 0.5d_0$, and (b) $d_s = d_0$. SISO, EGC, SC, and MLC refer to single-input multiple-output, equal gain combining, selection combining and majority-logic combining, respectively.

respectively. This improvement in SNR is clearly due to the aperture averaging, which has reduced σ_I^2 from 1 to 0.35 and 0.57 in SISO and SIMO cases, respectively. For the same aperture sizes of $0.5d_0$ and d_0 MLC displays similar performance like two other combining methods. This was expected as reducing the turbulence strength improves the performance of MLC to the level that it outperforms other combining methods. For this case considering the minimum distance of ρ_0 obtained from Equ. (3.3) between apertures in SIMO system, the SIMO Rx must have at least a diameter of 30.69 mm¹.

It is worth mentioning that the SISO Rx with a diameter of 24.95 mm and an SNR of 38.10 dB can provide the same BER of 10^{-6} as EGC with the SNR of 29.10 dB. This is interesting since at higher values of SNR it is possible to implement a smaller and less complex SISO system instead of a SIMO link. Figure 3.11(b) depicts the BER versus the SNR for SIMO and SISO with aperture sizes of 29 mm and 50 mm, respectively.

It is noticeable that SISO displays a similar performance to SC with an additional SNR requirement of 1.5 dB at a BER of 10^{-6} while the diameters of SISO and SC Rxs are kept

¹It can be shown that minimum Rx diameter for SIMO when $M = 3$ is $d_s + 2\rho_0/\sqrt{3}$. See Appendix A for details.

at ~ 50 mm and ~ 45 mm, respectively. Therefore, using a ~ 50 mm diameter Rx with a 1.5 dB additional SNR a simpler SISO could be used instead of SIMO employing SC with a ~ 45 mm diameter Rx. For the same aperture size MLC and EGC offer the same performance and based on the first analysis it can be predicted that for higher aperture sizes MLC offers improved performance compared to EGC. This is proved by letting the SIMO aperture size to be $1.5d_0 \approx 43.2$ mm. For this aperture size and at a BER of 10^{-6} MLC achieves 2.8 dB gain in SNR when compared to EGC. Note that for $\text{SNR} < 21$ dB the marginal improvement in SISO compared to SC, see Figure 3.11(b), is due to the larger aperture size of SISO.

The analysis carried out in this chapter leads to two important conclusions:

1. Based on the system requirements it is possible to determine the Rx configuration using the closed-form BER expressions. For example for SIMO with the aperture diameter of $0.8d_0 \approx 23$ mm both SISO and SIMO have the same Rx diameter of ~ 40 mm. In this case the less complex SISO link require 3.4 dB higher values of SNR than more complex SC link to achieve a BER of 10^{-6} ;
2. MLC method offers improved performance compared to EGC either by increasing the number of Rxs or by reducing the effect of turbulence via aperture averaging.

Although EGC can provide an optimum performance over a wide range of turbulence regimes, it is essential to ensure coherently synchronized signal summation in the physical layer of the network. Whereas since MLC deals with logical 0 and 1 data streams, it can be implemented in the higher layers of the network rather than the physical layer.

Although it was shown that the MLC offers an improved performance at higher values

of SNR and a large number of apertures, for the rest of this thesis the EGC method is used where the best performance is needed; and if the easiest combining method is required, SC will be implemented.

3.8 Summary

In this chapter, first the existing combining techniques used in spatial diversity were categorized into three optical, electrical and logical domains. Then existing combining methods were studied and categorized based on three aforementioned domains. Also the performance of each combining method in two different turbulence regimes (i.e., weak and strong) were discussed. It was shown that for high SNR and larger number of apertures, MLC method has a better performance compared to well-known methods such as EGC or SC. The numerical analysis showed that to achieve the same BER of 10^{-6} the SNR improvement were 2.10, 1.83, 5.29, and 7.18 dB compared to AOT, EGC, SC, SISO, respectively for $\sigma_x = 0.2$, and $M = 3$. The performance of SISO, EGC, SC, and MLC were also compared under moderate and strong regimes, where the same behaviour as in weak regime was observed. Once again MLC offered improved performance for a larger number of apertures and higher values of SNR.

However, here considering a wide range of system parameters, EGC could be used for its best performance whereas SC is preferred for its simplicity.

4 A FSO LINK WITH DIFFERENTIAL SIGNALLING

4.1 Introduction

The received signal in a FSO communication system is highly sensitive to the atmospheric effects such as fog, smoke, low clouds, snow, rain and the atmospheric turbulence [7, 17, 106, 107] that may result in severe power loss and channel fading. In NRZ-OOK IM/DD based systems, an optimal detection threshold level at the Rx can be used to distinguish the received ‘0’ and ‘1’ bits. However, under atmospheric turbulence the received optical signal will experience random intensity fluctuation as well as fading [108], which can result in the received signal power dropping below the Rx's threshold for a duration of milliseconds. For deep fading simply increasing the transmit power level and using a fixed optimal threshold level at the Rx are not the best options [107].

Most already-proposed detection methods rely on the knowledge of instantaneous or statistical CSI. For instance, to resolve the fluctuation of threshold level, in [88] the maximum-likelihood sequence detection (MLSD) scheme was adopted, and it was shown that provided the temporal correlation of atmospheric turbulence τ_0 is known MLSD outperforms the maximum-likelihood (ML) symbol-by-symbol detection technique. In

practical applications $\tau_0 \cong 1 - 10$ ms; then to maximize the link performance τ_0 needs to be adjusted dynamically. In addition, MLSD suffers from high computational complexity. In [109] two sub-optimal MLSD schemes, based on the single-step Markov chain model, were proposed to reduce the Rx computational complexity; however they still require the CSI knowledge. Employing the pilot symbol (PS) assisted modulation (PSAM) scheme, and assuming that τ_0 is known, CSI is acquired by inserting PS within the data stream [110]. However, obtaining an accurate-enough instantaneous CSI necessitates a non-negligible pilot overhead. In commercial FSO products, it is desirable to employ low complexity signal detection schemes with simple data framing and packetization structures in order to ensure infrastructure transparency [111].

In outdoor FSO links, a differential signalling scheme, also known as differential detection, was investigated in [35] to remove the effect of background noise. Also the same idea was adopted in [107] that used a pre-fixed optimal threshold level for various atmospheric channel conditions (rain, atmospheric turbulence, etc.). The detection technique did not rely on the CSI (with increased computational load at the Rx) and PS or a training sequence [107]. However, the simulation based investigation only considered narrow collimated beams without overlapping and with no experimental verification. To mitigate the fluctuation of pre-fixed optimal threshold level, the differential signalling scheme is preferred to AC-coupling (i.e., high pass filtering method) for a number of reasons including (i) no need to increase the transmit power to compensate for the filter attenuation; (ii) no baseline wander effect (i.e., disturbing the DC level of a signal); and (iii) removing the effects of the background noise.

The basic concept of differential signalling is to send the signal and its inverted version simultaneously by using two pairs of Tx's and Rx's over the same communication channel. Following reception of each signal by the corresponding Rx's and performing a

subtraction operation at the final stage, the output signal is regenerated for further processing. With this scheme the challenges are to identify the received signals at the receiver and effectively exploit the potential of differential signalling method under various channel conditions.

There are two main motivations for using the differential signalling method. First, it has been shown theoretically that provided Rx's are not saturated by the combined power of the received signal and the background noise level, the effect of ambient illumination can be cancelled out [35]. Second, in [107] a differential signalling scheme was adopted in an IM/DD OOK FSO links to overcome the variation of the threshold level caused by the channel fading. The benefit of differential signalling method in channels with large ambient illumination has been fully investigated in [35]. Therefore, in this research, only the performance of differential signalling in a fading channel is investigated.

In addition to turbulence, pointing errors also results in threshold level fluctuations at the Rx, which can affect the link performance as well as making signal detection a challenging task [106, 112]. To mitigate signal degradation researchers have proposed a number of techniques including adaptive detection [106], more complex tracking systems [34], and spatial diversity [113]; also see [7] and the references therein. Adaptive detection techniques (ADT) either imposes computational load at the Rx or reduces the link throughput [109, 110]. When using ADT, the CSI or the temporal correlation of fading is required for data detection at the Rx [106]. FSO links with tracking systems requiring optics, monitoring and controlling circuits [114] are complex and costly to be used in commercial IM/DD NRZ-OOK FSO systems. Using spatial diversity with a number of Tx's and Rx's will result in improved system performance for various channel conditions. However, there is still the need for a detection technique to extract the information bits from the combined signal [88]. The differential signalling technique can

also be used to mitigate the fluctuation of threshold level due to the pointing errors.

In this chapter, first the basic idea of differential signalling method is introduced. Then the challenges associated with the existing differential signalling methods are discussed and a solution is outlined. To the best of our knowledge no research work has been reported on the correlation between two channels in FSO systems with differential signalling. In this work theoretical, simulation and experimental investigation of the correlation are carried out. Correlation is shown to be an important key factor that needs considering. Also the theory of differential signalling method will be extended into channels with the pointing errors effect.

4.2 Differential Signalling Configuration

The differential signalling system block diagram is depicted in Figure 4.1. The NRZ-OOK signal S and its inverted version \bar{S} are used to intensity-modulate two optical sources at wavelengths of λ_1 and λ_2 , respectively. By comparing S with the optimal threshold level $S_{\text{thresh}} = E[S]$, where $E[\cdot]$ denotes expected value, the original data bit stream can be recovered (i.e., bit is 0 for $S < S_{\text{thresh}}$ and 1 elsewhere).

Note that the optimal threshold level for \bar{S} is also S_{thresh} . The output intensities I_i ($i = 1, 2$) of optical sources are given by:

$$\begin{bmatrix} I_1 \\ I_2 \end{bmatrix} = \begin{bmatrix} \Gamma_1 & 0 \\ 0 & \Gamma_2 \end{bmatrix} \begin{bmatrix} S \\ \bar{S} \end{bmatrix}, \quad (4.1)$$

where Γ_i denotes the electrical-to-optical conversion coefficient of optical sources.

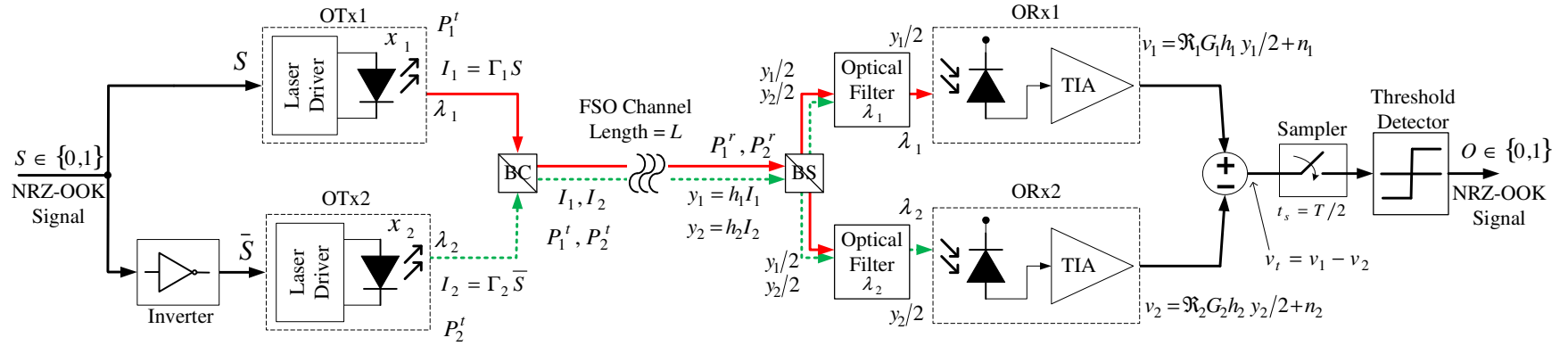


Figure 4.1: The system block diagram to implement differential signalling in correlated-channels conditions. T is the bit duration. OTx, BC, BS, ORx and TIA refer to optical transmitter, beam combiner, beam splitter, optical receiver, and transimpedance amplifier, respectively.

The outputs of optical sources are then passed through a beam combiner to ensure that both beams will be transmitted over the FSO channel of length L . Note that the beam combiner is only used for alignment purposes and not for combining signals in the optical domain.

The optical signals \mathbf{y} at the Rx end are given by:

$$\begin{bmatrix} y_1 \\ y_2 \end{bmatrix} = \begin{bmatrix} h_1 & 0 \\ 0 & h_2 \end{bmatrix} \begin{bmatrix} \Gamma_1 & 0 \\ 0 & \Gamma_2 \end{bmatrix} \begin{bmatrix} S \\ \bar{S} \end{bmatrix}, \quad (4.2)$$

where h_i denotes the channel response including the effect of geometrical and atmospheric losses, pointing errors, and the turbulence. Here only the effect of turbulence is considered.

At the Rx, the optical signal is passed through a 50/50 beam splitter and optical filters with the centre wavelengths of λ_1 and λ_2 , prior to being collected by an ORx. The generated photocurrents are amplified by TIA with outputs given by:

$$\begin{bmatrix} v_1 \\ v_2 \end{bmatrix} = \frac{1}{2} \begin{bmatrix} \mathfrak{R}_1 G_1 h_1 \Gamma_1 & 0 \\ 0 & \mathfrak{R}_2 G_2 h_2 \Gamma_2 \end{bmatrix} \begin{bmatrix} S \\ \bar{S} \end{bmatrix} + \begin{bmatrix} n_1 \\ n_2 \end{bmatrix}, \quad (4.3)$$

where \mathfrak{R}_i is the PD responsivity, G_i is gain of TIA, n_i is the AWGN with the zero mean and variance $\sigma_{n,i}^2$. The combined output $v_t = v_1 - v_2$ is given by:

$$v_t = \frac{1}{2} \Gamma_1 h_1 \mathfrak{R}_1 G_1 S - \frac{1}{2} \Gamma_2 h_2 \mathfrak{R}_2 G_2 \bar{S} + n_1 - n_2. \quad (4.4)$$

Note that in [35] it shown that for outdoor applications where the ambient noise effect is also embedded in n_i , the impact of background noise is significantly reduced.

4.3 Differential Signalling and Turbulence

4.3.1 Optimal Detection Threshold Level

A sampler with sampling at the centre of bit duration and a threshold detector are used to regenerate the transmit data. From Equ. (4.4), the optimal threshold level for v_t is given by:

$$V_{\text{thresh}} = \frac{1}{2} S_{\text{thresh}} (\Gamma_1 h_1 \mathcal{R}_1 G_1 - \Gamma_2 h_2 \mathcal{R}_2 G_2) + n_1 - n_2. \quad (4.5)$$

Using [115] one obtains:

$$\text{Mean}(V_{\text{thresh}}) = \text{Mean}(h_1) - \text{Mean}(h_2), \quad (4.6.a)$$

$$\begin{aligned} \text{Var}(V_{\text{thresh}}) &= \text{Var}(h_1) + \text{Var}(h_2) \\ &\quad - 2\rho_{1,2} \sqrt{\text{Var}(h_1)\text{Var}(h_2)} + 2\sigma_n^2, \end{aligned} \quad (4.6.b)$$

where $\text{Mean}(\cdot)$ denotes the average and $\text{Var}(\cdot)$ introduces the variance. Here, $\rho_{1,2}$ is correlation coefficient between the channels (i.e., h_1 and h_2). For simplicity, in Equ. (4.6) $\Gamma_i \mathcal{R}_i G_i = 2/S_{\text{thresh}}$ and $\sigma_{n,1}^2 = \sigma_{n,2}^2 = \sigma_n^2$ are set. For the weak turbulence regime h_i follows Log-normal distribution with mean and variance $\mu_{h,i}$ and $\sigma_{h,i}^2$, respectively [115]. For Log-normal distribution one has [85]:

$$\text{Mean}(h_i) = \exp(2\mu_{h,i} + 2\sigma_{h,i}^2), \quad (4.7.a)$$

$$\text{Var}(h_i) = (\exp(4\sigma_{h,i}^2) - 1) \times \exp(4\mu_{h,i} + 4\sigma_{h,i}^2), \quad (4.7.b)$$

where $\mu_{h,i} = -\sigma_{h,i}^2$. Therefore, one has:

$$\text{Mean}(V_{\text{thresh}}) = 0, \quad (4.8.a)$$

$$\text{Var}(V_{\text{thresh}}) = \exp(4\sigma_{h,1}^2) + \exp(4\sigma_{h,2}^2) - 2 \quad (4.8.b)$$

$$-2\rho_{1,2}\sqrt{\exp(4\sigma_{h,1}^2) - 1}\sqrt{\exp(4\sigma_{h,2}^2) - 1} + 2\sigma_n^2.$$

Since optical beams are in parallel and propagating very close to each other over the channel, then both beams will experience the same turbulence effects (i.e., $\sigma_{h,1}^2 \approx \sigma_{h,2}^2$).

Considering this approximation, one obtains:

$$\text{Mean}(V_{\text{thresh}}) = 0, \quad (4.9.a)$$

$$\text{Var}(V_{\text{thresh}}) = 2(1 - \rho_{1,2})[\exp(4\sigma_{h,1}^2) - 1] + 2\sigma_n^2. \quad (4.9.b)$$

From Equ. (4.9.a), it is seen that to recover the transmit bit stream, the optimal threshold level should be set to 0. This is similar to the work in [107] except for not considering the variance of the detection threshold in Equ. (4.9.b) due to turbulence. The method proposed in [107] is effective only under constant fading conditions. However, for randomly varying fading scenario a Rx employing a fixed optimal threshold level is not the optimum and therefore alternative scheme should be considered to ensure improve FSO link performance.

4.3.2 Correlation Between Channels

From Equ. (4.9.b), for $\rho_{1,2} = 1$ (i.e., the highly correlated channels), one has $\text{Var}(V_{\text{thresh}}) = 2\sigma_n^2$. In other words, turbulence does not affect signal detection provided the channels are highly correlated. According to [89], under the weak turbulence regime $\rho_{1,2}$ can be expressed in terms of the transversal distance between the Rx apertures d_r and the spatial coherence radius ρ_0 . Here, with parallel optical beams propagating over a LOS link, d_r is in fact the distance between the propagation axes of beams. Thus the correlation coefficient between channels takes the form of [89]:

$$\rho_{1,2} = \exp \left[- \left(\frac{d_r}{\rho_0} \right)^{5/3} \right], \quad (4.10)$$

where for a plane wave propagation model, the spatial coherence radius ρ_0 is given by Equ. (3.3). From Equ. (4.10), for $(d_r/\rho_0)^{5/3} > 5$ channels are considered uncorrelated $\rho_{1,2} < 0.007$ whilst for $d_r \rightarrow 0$ one can obtain $\rho_{1,2} \rightarrow 1$. So, by adopting a small d_r , one can obtain highly correlated channels and, as a result, use an optimal threshold level independent of turbulence.

This can be the challenging part of the differential signalling scheme; since the goal is to achieve the following features simultaneously:

1. Both channels have to be highly correlated
2. Signals are different, which necessitates minimum interference.

In the next sections, it will be shown how these two challenges can be addressed by using the scheme illustrated in Figure 4.1.

4.3.3 Channel Modelling

In this section the differential signalling method in more details will be investigated and the effect of signal level, modulation extinction ratio, laser wavelengths, and correlation coefficient on the differential signalling performance will be described. Knowing that superscripts *high* and *low* denote corresponding high and low levels of the electrical signal V , respectively, the electrical signals of LD x_i in Figure 4.1 are given by:

$$x_1 = \begin{cases} V_1^{high} & \text{bit 1} \\ (V_1^{high} + V_1^{low})/2 & \text{Threshold,} \\ V_1^{low} & \text{bit 0} \end{cases} \quad (4.11.a)$$

$$x_2 = \begin{cases} V_2^{low} & \text{bit 1} \\ (V_2^{high} + V_2^{low})/2 & \text{Threshold.} \\ V_2^{high} & \text{bit 0} \end{cases} \quad (4.11.b)$$

Each bit in Equ. (4.11) is distinguished by the corresponding electrical signal level. Besides a constant threshold level, which is equivalent to the average signal level, is also included and one can regenerate the information bits by comparing signal to corresponding threshold level. In Section 4.3.1, this threshold level was defined as the optimal threshold level. x_1 and x_2 are used to internal-modulate two optical sources at wavelengths of λ_1 and λ_2 , respectively. The output of optical transmitter (OTx₁) P_1^t is given as:

$$P_1^t = \begin{cases} P_1^{high} & \text{bit 1} \\ P_1^{avg} & \text{Threshold.} \\ P_1^{low} & \text{bit 0} \end{cases} \quad (4.12)$$

Due to equiprobable data transmission link the average power level $P_i^{avg} = (P_i^{high} + P_i^{low})/2$ ($i = 1, 2$). By defining the extinction ratio $\varepsilon_i = P_i^{high}/P_i^{low}$, low and high power levels can be expressed as $P_i^{low} = 2P_i^{avg}/(1 + \varepsilon_i)$ and $P_i^{high} = 2\varepsilon_i P_i^{avg}/(1 + \varepsilon_i)$, respectively. Therefore, outputs of OTxs (P_i^t) are expressed as:

$$P_1^t = P_1^{avg} \times \begin{cases} \frac{2}{1+\varepsilon_i} & \text{bit 1} \\ 1 & \text{Threshold,} \\ \frac{2\varepsilon_i}{1+\varepsilon_i} & \text{bit 0} \end{cases} \quad (4.13.a)$$

$$P_2^t = P_2^{avg} \times \begin{cases} \frac{2\varepsilon_i}{1+\varepsilon_i} & \text{bit 1} \\ 1 & \text{Threshold.} \\ \frac{2}{1+\varepsilon_i} & \text{bit 0} \end{cases} \quad (4.13.b)$$

The received optical power at the Rx $P_i^r = h_i P_i^t$, where h_i represents the atmospheric turbulence. The outputs of ORxs are given by:

$$v_1 = n_1 + 2 \begin{cases} h_1 G_1 \Re_1 \frac{\varepsilon_1 P_1^{avg}}{1+\varepsilon_1} & \text{bit 1} \\ \frac{1}{2} h_1 G_1 \Re_1 P_1^{avg} & \text{Threshold,} \\ h_1 G_1 \Re_1 \frac{P_1^{avg}}{1+\varepsilon_1} & \text{bit 0} \end{cases} \quad (4.14.a)$$

$$v_2 = n_2 + 2 \begin{cases} h_2 G_2 \Re_2 \frac{P_2^{avg}}{1+\varepsilon_2} & \text{bit 1} \\ \frac{1}{2} h_2 G_2 \Re_2 P_2^{avg} & \text{Threshold.} \\ h_2 G_2 \Re_2 \frac{\varepsilon_2 P_2^{avg}}{1+\varepsilon_2} & \text{bit 0} \end{cases} \quad (4.14.b)$$

As seen from Equ. (4.14) the threshold levels are affected by turbulence. If only a link with the wavelength λ_1 is considered then the FSO link in Figure 4.1 is simplified to a SISO link for which the average value and the variance of the received electrical signal v_1 are defined as [115]:

$$\text{Mean}(v_1) = \text{Mean}(h_1) \times \begin{cases} \frac{2\varepsilon_1 \Phi_1}{(1+\varepsilon_1)} & \text{bit 1} \\ \Phi_1 & \text{Threshold,} \\ \frac{2\Phi_1}{(1+\varepsilon_1)} & \text{bit 0} \end{cases} \quad (4.15.a)$$

$$\text{Var}(v_1) = \sigma_{n,1}^2 + \text{Var}(h_1) \times \begin{cases} \left(\frac{2\varepsilon_1 \Phi_1}{(1+\varepsilon_1)} \right)^2 & \text{bit 1} \\ (\Phi_1)^2 & \text{Threshold,} \\ \left(\frac{2\Phi_1}{(1+\varepsilon_1)} \right)^2 & \text{bit 0} \end{cases} \quad (4.15.b)$$

where $\Phi_i = G_i \Re_i P_i^{avg}$. Thus using Equ. (4.7) one has:

$$\text{Mean}(v_1) = \begin{cases} \frac{\varepsilon_1 \Phi_1}{(1+\varepsilon_1)} & \text{bit 1} \\ \Phi_1 & \text{Threshold,} \\ \frac{\Phi_1}{(1+\varepsilon_1)} & \text{bit 0} \end{cases} \quad (4.16.a)$$

$$\text{Var}(v_1) = \sigma_{n,1}^2 + [\exp(4\sigma_{h,1}^2) - 1] \times \begin{cases} \left(\frac{2\varepsilon_1 \Phi_1}{(1+\varepsilon_1)} \right)^2 & \text{bit 1} \\ (\Phi_1)^2 & \text{Threshold.} \\ \left(\frac{2\Phi_1}{(1+\varepsilon_1)} \right)^2 & \text{bit 0} \end{cases} \quad (4.16.b)$$

The expression in Equ. (4.16.a) shows that the average of threshold level depends on

Log-normal variances ($\sigma_{h,1}^2$). Besides based on Equ. (4.16.b), the threshold level fluctuates with the given order as predicted before. The combined output v_t is given as:

$$v_t = n_1 - n_2 + \begin{cases} \frac{2\varepsilon_1\Phi_1}{(1+\varepsilon_1)}h_1 - \frac{2\Phi_2}{(1+\varepsilon_2)}h_2 & \text{bit 1} \\ \Phi_1h_1 - \Phi_2h_2 & \text{Threshold.} \\ \frac{2\Phi_1}{(1+\varepsilon_1)}h_1 - \frac{2\varepsilon_2\Phi_2}{(1+\varepsilon_2)}h_2 & \text{bit 0} \end{cases} \quad (4.17)$$

Mean(\cdot) and Var(\cdot) will be as given in Equ. (4.18). If laser beams are propagating very close to each other, then they experience the same turbulence strength and $\sigma_{h,1}^2 \approx \sigma_{h,2}^2$, therefore Equ. (4.18) leads to Equ. (4.19).

$$\text{Mean}(v_t) = \begin{cases} \frac{2\varepsilon_1\Phi_1}{(1+\varepsilon_1)}\text{Mean}(h_1) - \frac{2\Phi_2}{(1+\varepsilon_2)}\text{Mean}(h_2) & \text{bit 1} \\ \Phi_1\text{Mean}(h_1) - \Phi_2\text{Mean}(h_2) & \text{Threshold} \\ \frac{2\Phi_1}{(1+\varepsilon_1)}\text{Mean}(h_1) - \frac{2\varepsilon_2\Phi_2}{(1+\varepsilon_2)}\text{Mean}(h_2) & \text{bit 0} \end{cases} \quad (4.18.a)$$

$$\text{Var}(v_t) = \sigma_{n,1}^2 + \sigma_{n,2}^2$$

$$+ \begin{cases} \left(\frac{2\varepsilon_1\Phi_1}{(1+\varepsilon_1)}\right)^2 \text{Var}(h_1) + \left(\frac{2\Phi_2}{(1+\varepsilon_2)}\right)^2 \text{Var}(h_2) - 2\rho_{1,2} \frac{4\varepsilon_1\Phi_1\Phi_2}{(1+\varepsilon_1)(1+\varepsilon_2)} \sqrt{\text{Var}(h_1)}\sqrt{\text{Var}(h_2)} & \text{bit 1} \\ (\Phi_1)^2\text{Var}(h_1) + (\Phi_2)^2\text{Var}(h_2) - 2\rho_{1,2}\Phi_1\Phi_2\sqrt{\text{Var}(h_1)}\sqrt{\text{Var}(h_2)} & \text{Threshold} \\ \left(\frac{2\Phi_1}{(1+\varepsilon_1)}\right)^2 \text{Var}(h_1) + \left(\frac{2\varepsilon_2\Phi_2}{(1+\varepsilon_2)}\right)^2 \text{Var}(h_2) - 2\rho_{1,2} \frac{4\varepsilon_2\Phi_1\Phi_2}{(1+\varepsilon_1)(1+\varepsilon_2)} \sqrt{\text{Var}(h_1)}\sqrt{\text{Var}(h_2)} & \text{bit 0} \end{cases} \quad (4.18.b)$$

$$\text{Mean}(v_t) = \begin{cases} \frac{2\varepsilon_1\Phi_1}{(1+\varepsilon_1)} - \frac{2\Phi_2}{(1+\varepsilon_2)} & \text{bit 1} \\ \Phi_1 - \Phi_2 & \text{Threshold} \\ \frac{2\Phi_1}{(1+\varepsilon_1)} - \frac{2\varepsilon_2\Phi_2}{(1+\varepsilon_2)} & \text{bit 0} \end{cases} \quad (4.19.a)$$

$$\text{Var}(v_t) = \sigma_{n,1}^2 + \sigma_{n,2}^2 + [\exp(4\sigma_{h,1}^2) - 1] \times \begin{cases} \left(\frac{2\varepsilon_1\Phi_1}{(1+\varepsilon_1)}\right)^2 + \left(\frac{2\Phi_2}{(1+\varepsilon_2)}\right)^2 - 2\rho_{1,2} \frac{4\varepsilon_1\Phi_1\Phi_2}{(1+\varepsilon_1)(1+\varepsilon_2)} & \text{bit 1} \\ (\Phi_1)^2 + (\Phi_2)^2 - 2\rho_{1,2}\Phi_1\Phi_2 & \text{Threshold} \\ \left(\frac{2\Phi_1}{(1+\varepsilon_1)}\right)^2 + \left(\frac{2\varepsilon_2\Phi_2}{(1+\varepsilon_2)}\right)^2 - 2\rho_{1,2} \frac{4\varepsilon_2\Phi_1\Phi_2}{(1+\varepsilon_1)(1+\varepsilon_2)} & \text{bit 0} \end{cases} \quad (4.19.b)$$

In Section 4.3.1, it is assumed that the links are the same. Here it is good to start with the same concept just to generalize the expressions derived before. Later on the general case where links are not the same be will discussed. By setting $\Phi_1 = \Phi_2$ or equivalently $G_1 \mathfrak{R}_1 P_1^{avg} = G_2 \mathfrak{R}_2 P_2^{avg}$ the average of the threshold level is fixed to ~ 0 no matter how strong the turbulence is. On the other hand, the variance of the detection threshold under the same condition is defined as:

$$\text{Var}(V_{\text{thresh}}) = 2[\exp(4\sigma_{h,1}^2) - 1](\Phi_1)^2(1 - \rho_{1,2}) + \sigma_{n,1}^2 + \sigma_{n,2}^2, \quad (4.20)$$

where V_{thresh} denotes the detection threshold level. The derived expression in Equ. (4.20) is compatible with what was achieved in Equ. (4.9.b).

From Equ. (19), one can formulate the average and the variance of low level $V_{\text{bit } 0}$ and high level $V_{\text{bit } 1}$ of the combined as:

$$\text{Mean}(V_{\text{bit } 0}) = 2\Phi_1 \left[\frac{1}{(1+\varepsilon_1)} - \frac{\varepsilon_2}{(1+\varepsilon_2)} \right], \quad (4.21.a)$$

$$\text{Mean}(V_{\text{bit } 1}) = 2\Phi_1 \left[\frac{\varepsilon_1}{(1+\varepsilon_1)} - \frac{1}{(1+\varepsilon_2)} \right], \quad (4.21.b)$$

$$\begin{aligned} \text{Var}(V_{\text{bit } 0}) = & 4[\exp(4\sigma_{h,1}^2) - 1](\Phi_1)^2 \left[\left(\frac{1}{(1+\varepsilon_1)} \right)^2 + \left(\frac{\varepsilon_2}{(1+\varepsilon_2)} \right)^2 - \right. \\ & \left. 2\rho_{1,2} \frac{\varepsilon_2}{(1+\varepsilon_1)(1+\varepsilon_2)} \right] + \sigma_{n,1}^2 + \sigma_{n,2}^2, \end{aligned} \quad (4.21.c)$$

$$\begin{aligned} \text{Var}(V_{\text{bit } 1}) = & 4[\exp(4\sigma_{h,1}^2) - 1](\Phi_1)^2 \left[\left(\frac{\varepsilon_1}{(1+\varepsilon_1)} \right)^2 + \left(\frac{1}{(1+\varepsilon_2)} \right)^2 - \right. \\ & \left. - 2\rho_{1,2} \frac{\varepsilon_1}{(1+\varepsilon_1)(1+\varepsilon_2)} \right] \\ & + \sigma_{n,1}^2 + \sigma_{n,2}^2. \end{aligned} \quad (4.21.d)$$

Using Equ. (4.21) one can assess the quality of the signal using the Q-factor parameter as given by [116]:

$$Q = \frac{|\text{Mean}(V_{\text{bit } 1}) - \text{Mean}(V_{\text{bit } 0})|}{\sqrt{\text{Var}(V_{\text{bit } 1}) + \text{Var}(V_{\text{bit } 0})}}. \quad (4.22)$$

Equ. (4.22) will be used to study the effect of channel characteristics on the received signal in a differential signalling based FSO system in the following sections.

4.3.4 BER Expression

For simplicity, the subtracted signal R is assumed to be as:

$$R = S\eta I_1 - \bar{S}\eta I_2 + n, \quad (4.23)$$

where $n = n_1 - n_2$ is the total AWGN of the Rx. The fading of received intensities I_i is given as $I = I_0 \exp(2X)$ where I_0 denotes the average signal intensity without turbulence and X is a distributed normal random variable with mean μ and variance σ^2 with Log-normal PDF [85]. Also for normalised PDF $E[I] = I_0$ [85]. To ease the derivation two identical links meanings are considered as $E[I_1] = E[I_2] = I_0$. Furthermore it is assumed that $R = R_0 \exp(2X_{DS})$, where X_{DS} is also a distributed normal random variable with mean μ_{DS} and variance $\sigma_{h,DS}^2$. To normalize R the condition $\mu_{DS} = -\sigma_{h,DS}^2$ is considered. To obtain $\sigma_{h,DS}^2$, the following expression is used [115]:

$$\sigma_{h,DS}^2 = \ln \left(1 + \frac{\text{Var}[R]}{(E[R])^2} \right), \quad (4.24)$$

where $E[R]$ is set to 1 for normalization and $\text{Var}[R]$ can be obtained the same as Equ. (4.8.b). On the other hand, it can be shown that $\text{Var}[I_1]$ and $\text{Var}[I_2]$ are defined as [115]:

$$\text{Var}[I_i] = (e^{4\sigma_{h,i}^2} - 1) (E[I_i])^2. \quad (4.25)$$

Then $\sigma_{h,DS}^2$ will be achieved by the following expression:

$$\sigma_{h,DS}^2 = \ln \left[1 + \left(e^{4\sigma_{h,1}^2} - 1 \right) + \left(e^{4\sigma_{h,2}^2} - 1 \right) - 2\rho_{1,2} \sqrt{\left(e^{4\sigma_{h,1}^2} - 1 \right) \left(e^{4\sigma_{h,2}^2} - 1 \right)} \right]. \quad (4.26)$$

Once equivalent Log-normal variance ($\sigma_{h,DS}^2$) is achieved it is possible to specify the PDF of a differential signalling FSO system by means of Equ. (3.8). Having PDF, one can calculate the average BER of the link using Equ. (3.16).

4.3.5 Numerical Analysis

In this section, the effect of link parameters on the performance of differential signalling system will be analysed. The derived expressions will be used and wherever applicable will be supported with Monte-Carlo simulation. In previous section it was shown that by setting $G_1 \mathfrak{R}_1 P_1^{avg} = G_2 \mathfrak{R}_2 P_2^{avg}$ a constant threshold level of 0 can be used for different turbulent conditions. Also it was shown that for correlation coefficient ($\rho_{1,2}$) of 1 the fluctuation of the threshold level reaches its minimum value.

In the analysis the adopted wavelengths were 830 and 850 nm and link was 1 km long. To calculate $\text{Mean}(V_{\text{thresh}})$ and $\sqrt{\text{Var}(V_{\text{thresh}})}$ of SISO and differential signalling links, Eqs. (4.16) and (4.19) were used, respectively whereas Equ. (4.22) was used for calculation of the Q-factor. The given values of SNR denote the electrical SNR of the signal before the sampler block box as in Figure 4.1. From Eqs. (4.16) and (4.19), it is deduced that the threshold level is dependent from extinction ratio (ε_i). To confirm this, Monte-Carlo simulation was used for both SISO and differential signalling systems for $\varepsilon_i = 5$ and $\varepsilon_i = 10$ with $\Phi_1 = \Phi_2 = 5.7$ mV, $\Phi_{\text{SISO}} = 8.1$ mV, $\rho_{1,2} = 1$, and $\sigma_R^2 = 0.5$. To obtain each corresponding value, a 1 Mbits of data was transmitted with 10 independent iterations. The other parameters of the simulations were set according to

Table 4.1. The obtained results are summarized in Table 4.2. Note that the fading varying frequency of the channel is in the order of 400 Hz [117], thus in both simulations and experiments, a low data rate was selected to avoid the need for storage of large number of samples.

Table 4.1: The summary of FSO system properties used in the differential signalling simulation.

Parameter	Value
Data rate	1 Mbps
Link length	1 km
Turbulence strength C_n^2	1, 2.5, and $5 \times 10^{-15} \text{ m}^{-2/3}$
Correlation coefficient $\rho_{1,2}$	0, 0.5, 0.8, and 1
Received average optical power	-20 dBm
PD responsivity \mathfrak{R}	0.4
Noise spectral density N_0	-102 dB/Hz
Number of transmit bits	1 Mbits
Number of iterations	10

Considering the theoretical and simulation results; it is seen that the proposed theory can predict the system behaviour accurately. Besides in agreement with Eqs. (4.16) and (4.19), for the same link condition but different extinction ratio (ε_i), mean value of threshold detection ($\text{Mean}(V_{\text{thresh}})$) and standard deviation value of threshold detection ($\sqrt{\text{Var}(V_{\text{thresh}})}$) are the same.

As discussed earlier for $\Phi_1 = \Phi_2$ and $\rho_{1,2} = 1$, regardless of turbulence conditions, $\text{Mean}(V_{\text{thresh}}) \approx 0$ and $\text{Var}(V_{\text{thresh}}) = \sigma_{n,1}^2 + \sigma_{n,2}^2$. To prove this, another set of analysis was performed for a range of turbulence strength from almost a clear channel $\sigma_R^2 \approx 0$ to $\sigma_R^2 = 1$. As shown before, the value of ε_i did not affect $\text{Mean}(V_{\text{thresh}})$ and $\sqrt{\text{Var}(V_{\text{thresh}})}$; then for the simulation, the extinction ratio (ε_i) was set to 10 and SNR was changed by setting Φ_i .

The results of the analysis are represented in Figure 4.2. From Figure 4.2 it is observed that the theory can predict the $\text{Mean}(V_{\text{thresh}})$ for both SISO and differential signalling.

Table 4.2: The theoretical analysis accompanied by simulation of mean of detection threshold (Mean) and standard deviation of detection threshold ($\sqrt{\text{Var}}$) of single-input single-output (SISO) and differential signalling (DS) links for different extinction ratios (ϵ) of 5 and 10 but fixed $\Phi_1=\Phi_2=5.7$ mV, $\Phi_{\text{SISO}}=8.1$ mV, where channels are highly correlated $\rho_{1,2}=1$, and Rytov variance (σ_R^2) is 0.5.

ϵ	SNR (dB)	Link	Mean (mV) ^a	$\sqrt{\text{Var}}$ (mV) ^b
5	12.2	SISO	7.6; [8.1, 0.5]	3.0; [3.3, 0.9]
		DS	0.0; [0.0, 0.1]	1.9; [1.8, 0.1]
10	14	SISO	7.6; [8.1, 0.6]	3.0; [3.4, 0.8]
		DS	0.0; [0.0, 0.1]	1.9; [2.0, 0.1]

^{a, b} For each case there is a pair of numbers separated by comma. The first number denotes theoretical analysis result while the pair shows the simulation outcome in form of expected value and standard deviation pair, respectively.

For $\sqrt{\text{Var}(V_{\text{thresh}})}$, there is a slight deviation between the theory and simulation, however both theory and simulation show the same trend. As predicted from Equ. (4.16) $\text{Mean}(V_{\text{thresh}})$ and $\sqrt{\text{Var}(V_{\text{thresh}})}$ of SISO link are changing with the turbulence strength. $\sqrt{\text{Var}(V_{\text{thresh}})}$ of SISO link almost equals to the standard deviation of noise $\sigma_{n,\text{SISO}} = 1.32$ mV for a clear channel condition (i.e., Rytov variance (σ_R^2) of ~ 0) and it increases for higher values of σ_R^2 values, which agrees well with Equ. (4.15.b). Besides, different SNRs results in various $\text{Mean}(V_{\text{thresh}})$ and $\sqrt{\text{Var}(V_{\text{thresh}})}$ of the SISO link.

Since in this analysis ϵ_i was fixed then SNR was changed by setting appropriately $\Phi_i = G_i \Re_i P_i^{\text{avg}}$. Thus, the gain of the TIA (G), PD responsivity (\Re), and LD output power (P^{avg}) can change the required threshold level whereas ϵ_i has no effect on it. On the other hand for the differential signalling link, $\text{Mean}(V_{\text{thresh}})$ is constant for various turbulence conditions and different values of SNRs. This was expected because from Equ. (4.19.a) when links have the same parameters (i.e., $\Phi_1 = \Phi_2$) and the optical beams undergo the same turbulence effect; the required threshold level at the Rx is zero for various turbulence conditions and different SNRs. $\sqrt{\text{Var}(V_{\text{thresh}})}$ of the differential signalling link is also fixed for different turbulence conditions and various SNRs. From Equ. (4.19.b) it is known that $\sqrt{\text{Var}(V_{\text{thresh}})} \approx (\sigma_{n,1}^2 + \sigma_{n,2}^2)^{1/2} = 1.9$ mV, which agrees well

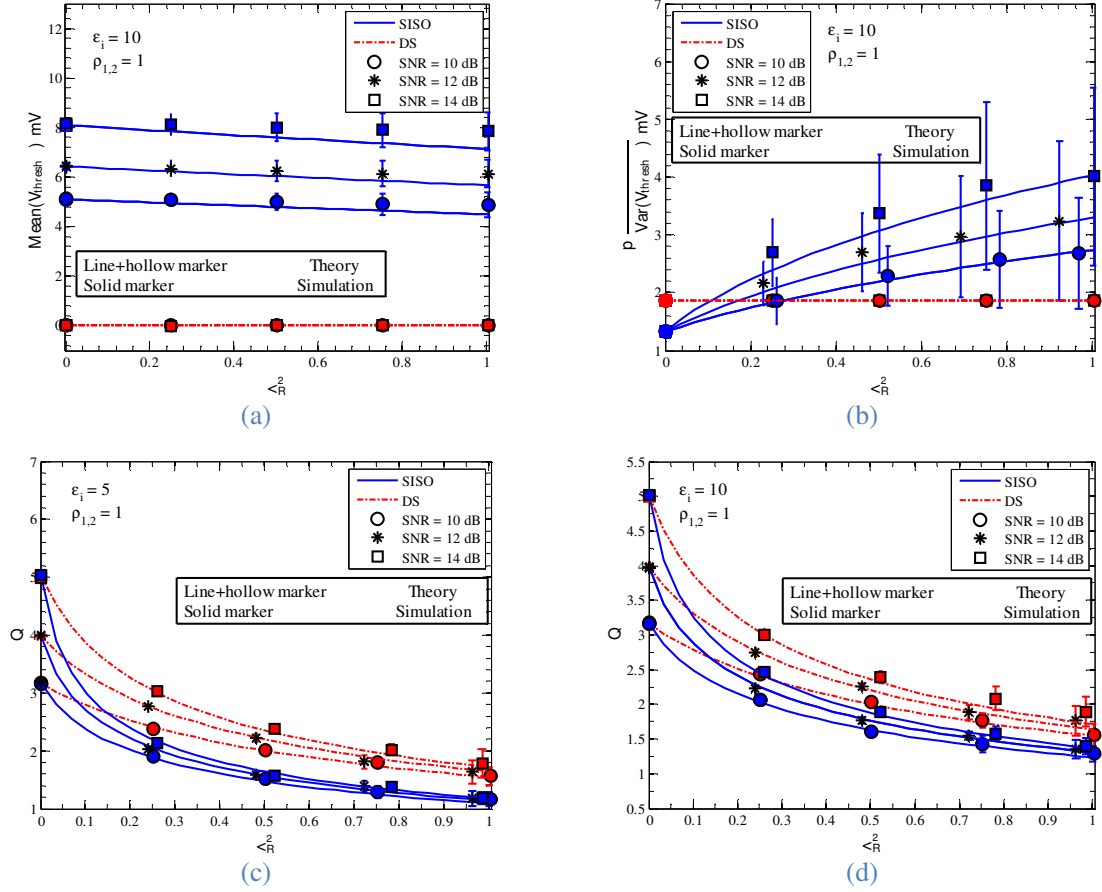


Figure 4.2: Simulation results of: (a) mean of detection threshold $\text{Mean}(V_{\text{thresh}})$, (b) standard deviation of detection threshold $\sqrt{\text{Var}(V_{\text{thresh}})}$, and (c, d) Q-factor versus Rytov variance (σ_R^2). The comparison is performed for a range of turbulences and SNRs for: (a) and (b) $\epsilon_i=10$, (c) $\epsilon_i=5$, and (d) $\epsilon_i=10$. SISO and DS refer to single-input single-output and differential signalling, respectively. ϵ_i and $\rho_{1,2}$ denote extinction ratio and correlation coefficient, respectively. Note that in (c) and (d) the error bars are too small to be seen.

with the simulation results as in Figure 4.2(b). In another set of analysis, the Q-factor for both SISO and differential signalling links are compared under different conditions.

From Eqs. (4.16), (4.19), and (4.22) it is seen that in contrary to the $\text{Mean}(Y_{\text{thresh}})$ and $\sqrt{\text{Var}(V_{\text{thresh}})}$, the Q-factor also depends on ϵ_i . Therefore, ϵ_i is set to 5 and 10 for SNRs of 10, 12, 14 dB and the same turbulence strength is used. The theoretical and simulation results are illustrated in Figure 4.2(c) and Figure 4.2(d). Figure 4.2(c) and Figure 4.2(d) confirm that the proposed theory predicts the Q-factor for both SISO and differential signalling links. In Figure 4.2(c) $\epsilon_i = 5$, where ϵ_i is 10 for Figure 4.2(d). For a clear channel condition, $Q^2 \approx 10^{\text{SNR}/10}$ and as σ_R^2 increases, the Q-factor tends to

reduce. Changing ε_i from 5 to 10 has no effect on the Q-factor of the differential signalling link while the SISO link shows a lower Q-factor for $\varepsilon_{\text{SISO}} = 5$ in a turbulent channel.

So far it has been shown out that for $\rho_{1,2} = 1$ and $\Phi_1 = \Phi_2$, both the $\text{Mean}(V_{\text{thresh}})$ and $\sqrt{\text{Var}(V_{\text{thresh}})}$ of SISO and differential signalling links and the Q-factor of the differential signalling link are independent of ε_i and change with Φ_i . The results also showed that changing Φ_i has no effect on the $\text{Mean}(V_{\text{thresh}})$ and $\sqrt{\text{Var}(V_{\text{thresh}})}$ of the differential signalling link for $\rho_{1,2} = 1$.

It is important to note that Equ. (3.6) gives different results for λ_1 and λ_2 , which results in different Log-normal variances (i.e., $\sigma_{h,1}^2 \neq \sigma_{h,2}^2$). Therefore, the simplified expressions given in Equ. (4.10) are no longer valid. Also note that spatial coherence radius (ρ_0) in Equ. (3.3) is a function of wavelength, which leads to different values of correlation coefficient ($\rho_{1,2}$) for the same FSO system. This issue necessitates us to define a constraint on how distinct the wavelengths can be and also to study the effect of correlation coefficient on the system performance.

To define a constraint for the difference of two wavelengths, which still validates the use of Eqs. (3.3), (3.6), and (4.10), the derivatives of $\sigma_{h,i}^2$, $\rho_{1,2}$ and ρ_0 are taken with respect to λ_i . After a series of mathematical simplification, one has:

$$\Delta\sigma_{h,i}^2 = \frac{7}{6}\sigma_{h,i}^2 \frac{\Delta\lambda}{\lambda_0}, \quad (4.27.a)$$

$$\Delta\rho_0 = \frac{6}{5}\rho_0 \frac{\Delta\lambda}{\lambda_0}, \quad (4.27.b)$$

$$\Delta\rho_{1,2} = -2\rho_{1,2} \ln \rho_{1,2} \frac{\Delta\lambda}{\lambda_0}, \quad (4.27.c)$$

where $\lambda_0 = (\lambda_1 + \lambda_2)/2$ and $\Delta\lambda = |\lambda_1 - \lambda_2|$. See Appendix A for detailed derivation of Equ. (4.27).

Considering the rule of thumb that a 10% tolerance relative to the absolute value is acceptable, from Eqs. (4.27.a) and (4.27.b) the criteria of $\Delta\lambda/\lambda_0 < \frac{5}{60}$ is extracted. This criteria, which is independent from the FSO channel (i.e., C_n^2 and d_r), means that for $\Delta\lambda/\lambda_0 < \frac{5}{60}$, Eqs. (3.3) and (3.6) give approximately the results for both wavelengths with 10% relative deviation. However, in Equ. (4.27.c) a fixed constraint cannot be derived. It can be easily shown that assuming the same rule of thumb of $\Delta\rho_{1,2}/\rho_{1,2} < 0.1$ the criteria based on Equ. (4.27.c) is given by:

$$\frac{\Delta\lambda}{\lambda_0} = \frac{1}{20} \left(\frac{d_r}{\rho_0} \right)^{-5/3}. \quad (4.28)$$

Figure 4.3 shows $\Delta\lambda/\lambda_0$ with respect to d_r/ρ_0 , a characteristic, which is independent from wavelength, and the link distance or the turbulence strength. It is deduced from Equ. (4.28) that for $d_r/\rho_0 \rightarrow 0$ the range of selecting λ_1 and λ_2 broadens (i.e., $\Delta\lambda/\lambda_0 \rightarrow \infty$), whereas for $0 < d_r/\rho_0 < 0.26$ the range of applicable wavelengths is reduced (i.e., $\Delta\lambda/\lambda_0 > 0.47$). Therefore, there is a trade-off between how close the beams have to be and how different the wavelengths can be.

The two differential signalling link conditions (i.e., $\Phi_1 = \Phi_2$ and $\rho_{1,2} \rightarrow 1$) are ideal

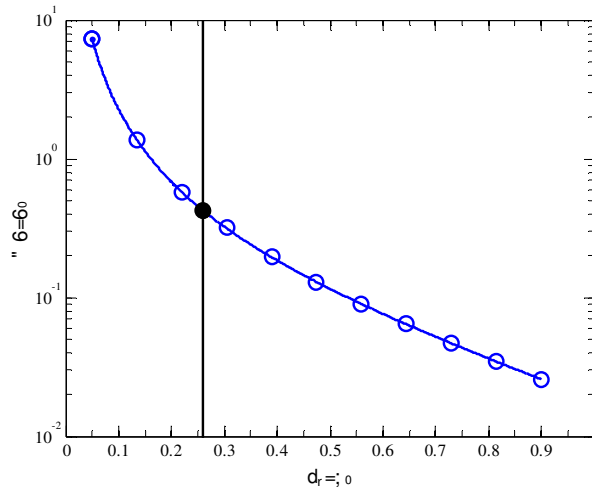


Figure 4.3: $\Delta\lambda/\lambda_0$ plotted with respect to d_r/ρ_0 . The graph shows the relation between the tolerable optical sources wavelengths and the distance between the optical receivers, while the channels are kept independent. The graph is obtained from Equ. (4.28).

and in reality there are deviations from the ideal scenario. Thus, the mean value of threshold detection ($\text{Mean}(V_{\text{thresh}})$), the variance value of threshold detection ($\sqrt{\text{Var}(V_{\text{thresh}})}$) and the Q-factor are compared for SISO and differential signalling links for the same SNR but different values of Φ_i over a range of correlation coefficient ($\rho_{1,2}$). The SNR was set to 12 dB and extinction ratio (ϵ_i) was changed to 5, 10, and 20. The turbulence strength of $\sigma_R^2 \approx 0.5$ was considered and the results are depicted in Figure 4.4. The value of $\rho_{1,2}$ spans from uncorrelated channels conditions (i.e., $\rho_{1,2} = 0$) to fully correlated channels condition (i.e., $\rho_{1,2} = 1$). The accuracy of the proposed theory for $\rho_{1,2}$ range is obvious from the good agreement between simulation and predicted results as depicted in Figure 4.4.

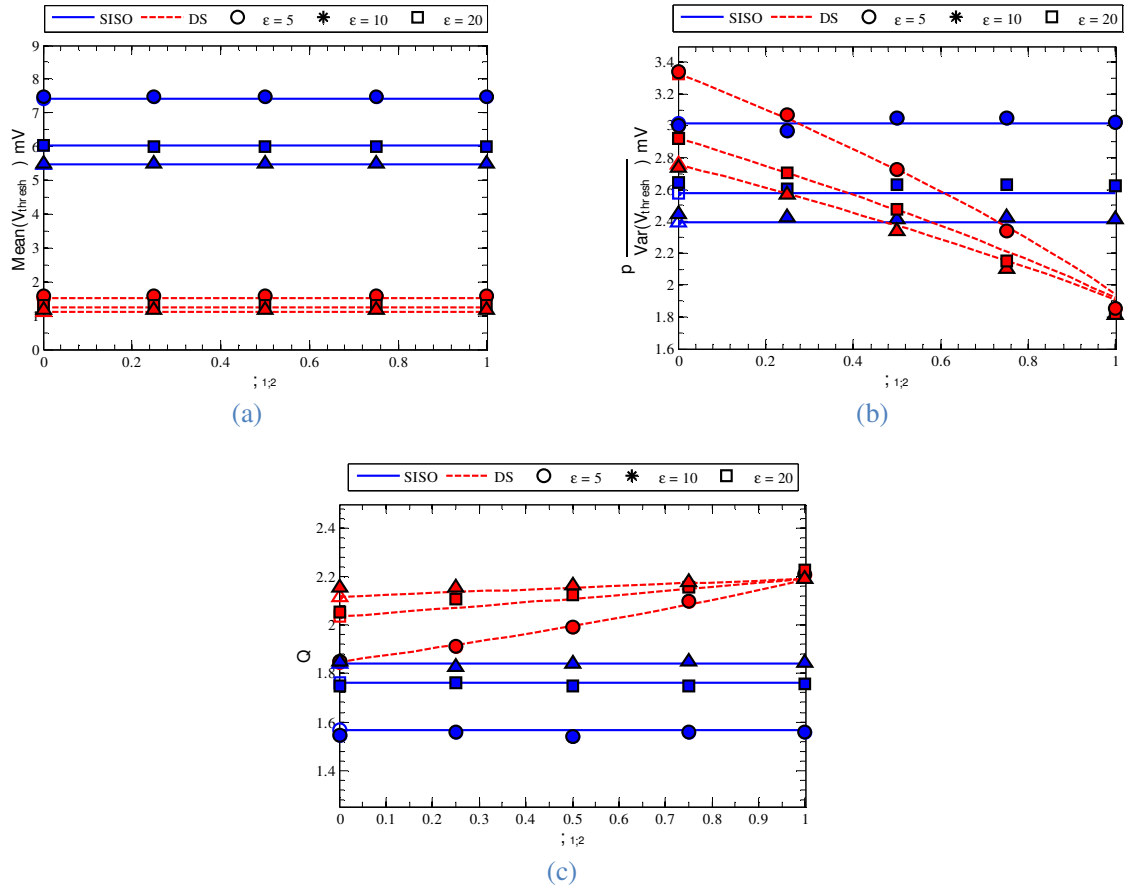


Figure 4.4: Simulation results of: (a) mean of detection threshold $\text{Mean}(V_{\text{thresh}})$, (b) standard deviation of detection threshold $\sqrt{\text{Var}(V_{\text{thresh}})}$, and (c) Q-factor. The comparison is performed between single-input single-output (SISO) link and differential signalling (DS) and for different values of extinction ratios (ϵ_i) over a range of correlation coefficient ($\rho_{1,2}$).

As expected from Equ. (4.15.a) the mean value of the detection threshold ($\text{Mean}(V_{\text{thresh}})$) of the SISO link in Figure 4.4(a) depends on the link parameters. $\text{Mean}(V_{\text{thresh}})$ of the SISO link decreases when extinction ratio of SISO link ($\varepsilon_{\text{SISO}}$) is higher. To keep SNR at 12 dB, the value of Φ_{SISO} was changed to 7.9 , 6.4, and 5.8 mV. On the other hand, from Equ. (4.15.a) it is observed that for higher Φ_{SISO} the resultant $\text{Mean}(V_{\text{thresh}})$ is also higher. The variance value of the detection threshold ($\text{Var}(V_{\text{thresh}})$) of the SISO link in Figure 4.4(b) also is dependent on the link parameters and since for a fixed SNR higher $\varepsilon_{\text{SISO}}$ requires lower Φ_{SISO} , then $\text{Var}(V_{\text{thresh}})$ of the SISO link for higher $\varepsilon_{\text{SISO}}$ is reduced. This deduction is in agreement with Equ. (4.15.b).

Figure 4.4(c) illustrates the Q-factor for the SISO link, which are obtained from Equ. (4.22). The numerator $|\text{Mean}(V_{\text{bit } 1}) - \text{Mean}(V_{\text{bit } 0})|$ in Equ. (4.22) is dependent on both $\varepsilon_{\text{SISO}}$ and Φ_{SISO} , however the effects of Φ_{SISO} and $\varepsilon_{\text{SISO}}$ are opposite, therefore for the same SNR, higher $\varepsilon_{\text{SISO}}$ results in the same $|\text{Mean}(V_{\text{bit } 1}) - \text{Mean}(V_{\text{bit } 0})|$ value. On the other hand, $\sqrt{\text{Var}(V_{\text{bit } 1})} + \sqrt{\text{Var}(V_{\text{bit } 0})}$ is increased for the same SNR and higher Φ_{SISO} . Therefore, the Q-factor of the SISO link is lower for lower values of $\varepsilon_{\text{SISO}}$. $\text{Mean}(V_{\text{thresh}})$ of the differential signalling link in Figure 4.4(a) is also dependent on the link parameters and since $\Phi_1 \neq \Phi_2$ the value of $\text{Mean}(V_{\text{thresh}})$ is non zero. But as discussed for the SISO link, for the same SNR and higher ε_i the value of $\text{Mean}(V_{\text{thresh}})$ is reduced.

$\sqrt{\text{Var}(V_{\text{thresh}})}$ and the Q-factor of the differential signalling link depend on not only the link parameters but also on correlation coefficient ($\rho_{1,2}$). As seen in Figure 4.4(b) $\sqrt{\text{Var}(V_{\text{thresh}})}$ of the differential signalling link reaches the minimum value of total standard deviation of noise $((\sigma_{n,1}^2 + \sigma_{n,2}^2)^{1/2} = 1.9 \text{ mV})$ for $\rho_{1,2} = 1$. Also it can be seen that lower $\varepsilon_{\text{SISO}}$ results in smaller $\sqrt{\text{Var}(V_{\text{thresh}})}$. Figure 4.4(c) shows the Q-factor of the differential signalling link that achieves the maximum value of $Q^2 \approx 10^{\text{SNR}/10}$ at $\rho_{1,2} =$

1. As discussed for the SISO link, the same SNR and higher ε_i leads to higher values of the Q-factor.

Based on the analysis, if achieving higher SNR in a differential signalling link is desirable, then increasing ε_i is the preferred option. Of course, increasing ε_i needs to be done with respect to the span of laser L-I curve linear region to avoid pulse shape distortion.

To validate the work in Section 4.3.4, the BER results from Equ. (4.26) were compared with the simulation data. The parameters adopted for the FSO system investigated are given in Table 4.1. Figure 4.5 shows the predicted and simulated BER versus SNR obtained from the theory as well as the performed simulation based on Equ. (4.26) for the FSO with differential signalling for $\rho_{1,2} = 0$, and 0.8 and $C_n^2 = 1 \times 10^{-15}$ and $2.5 \times 10^{-15} \text{ m}^{-2/3}$. The simulation results are presented by large markers for each case with the error bars to show the tolerance of the simulated values. To obtain each point, 10 iterations were carried out with 1 Mbps of transmit bit stream for each iteration. Note that for $\text{BER} < 10^{-6}$, the simulation results were zero, and therefore are not shown in the graph. It is clear from the figure that the initial assumption that R with a Log-normal

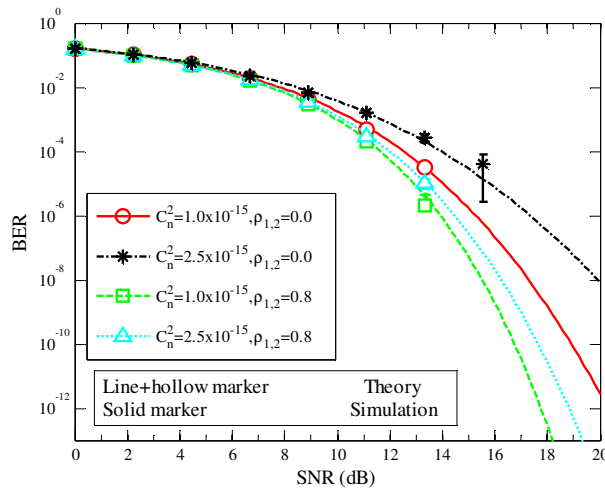


Figure 4.5: BER versus SNR in dB of an FSO system with the differential signalling method. The comparison is carried out for various turbulence strengths (C_n^2) and correlation coefficients ($\rho_{1,2}$). Solid lines marked with small markers are based on the derived equations whilst large markers are obtained from the simulation.

distribution does indeed lead to a good approximation of PDF of the differential signalling method for the weak turbulence regime.

It was discussed in Section 4.2 that when the channels are fully correlated (i.e., $\rho_{1,2} = 1$) the effect of the turbulence has the minimum influence on the received signal. In the next step $C_n^2 = 5 \times 10^{-15} \text{ m}^{-2/3}$ was considered and the correlation according was changed based on Table 4.1. The results in Figure 4.6 show that when the correlation coefficient increases, the performance of differential signalling method improves in term of mitigating the turbulence effect. As shown in Figure 4.6, for $\rho_{1,2} = 1$ the FSO system with the differential signalling scheme offers almost the same performance as in the clear channel. For the uncorrelated case (i.e., $\rho_{1,2} = 0$) in Figure 4.6, the simulation error increases so that the error bars shown are negative, which are not shown in the logarithmic scale

4.3.6 Atmospheric Turbulence Experiment

To prove the concept of differential signalling technique, the experimental work for the proposed system as given in Figure 4.7 will be outlined.

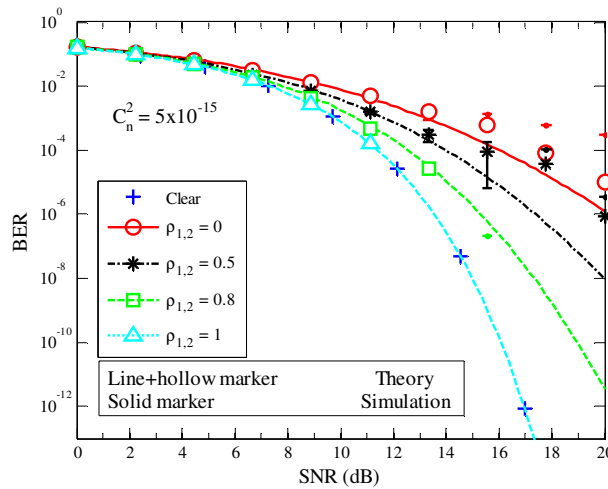


Figure 4.6: BER versus SNR in dB of an FSO system with the differential signalling method for $C_n^2 = 5 \times 10^{-15} \text{ m}^{-2/3}$ and a range of correlation conditions ($\rho_{1,2}$). Solid lines with small markers are based on theory whereas large markers are obtained from simulation. The plus marker denotes the clear channel condition.

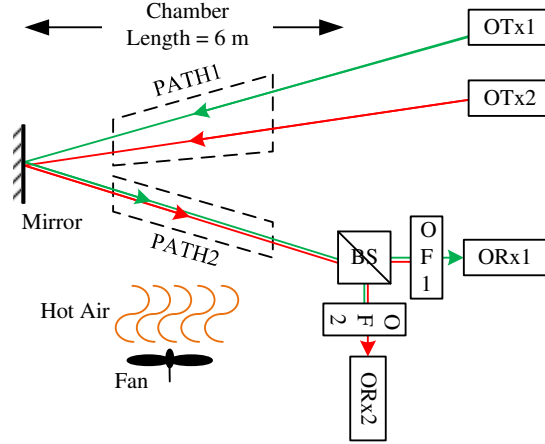


Figure 4.7: Block diagram of the atmospheric turbulence and differential signalling experiment. PATH1 and PATH2 are referring to uncorrelated and correlated paths, respectively. OTx, BS, OF, and ORx are optical transmitter, beam splitter, optical filter, and optical receiver, respectively.

According to proposed scheme shown in Figure 4.1, an experimental setup for the proposed method was developed to evaluate its performance for both uncorrelated (i.e., $\rho_{1,2} = 0$) and correlated (i.e., $\rho_{1,2} \rightarrow 1$) channels conditions as depicted in Figure 4.7. Snapshots of the setup are also shown in Figure 4.8. The laser beams (see Figure 4.8(a)) were launched into a chamber of length 6 m, emulating an outdoor uncorrelated FSO channel (see Figure 4.8(b)). The incident and reflected ray paths are labelled as PATH1 and PATH2, respectively (see Figure 4.7). In PATH1 optical sources were spaced apart by a minimum distance of $d_r > 5$ mm to ensure uncorrelated fading conditions (i.e., $(d_r/\rho_0)^{5/3} > 5$). An adjustable mirror positioned at the other end of the chamber was used to increase the path length by reflecting back the beams. The reflected beams indicated by PATH2 in Figure 4.7 were kept as close as possible to each other to ensure high correlation between the two paths (note that PATH2 in Figure 4.7 corresponds to FSO channel in Figure 4.1).

Heater fans were used to generate turbulence in the chamber, see Figure 4.7. To measure C_n^2 , the method of thermal structure parameter was used (based on temperature gradient measurement) as in [118]. The temperature gradient was measured using 20 temperature sensors positioned along the chamber, see Figure 4.8(b). At the Rx end, the

reflected beams passed through a 50/50 beam splitter and were applied to two identical PIN PDs after optical filters, see Figure 4.7 and Figure 4.8(a). The outputs of PDs were captured using a real-time digital storage oscilloscope for further processing in MATLAB®.

First investigated was the effect of turbulence on the uncorrelated path within the chamber. The reflected beams (i.e., PATH2) were passed through a pipe positioned within the chamber. The pipe ensured that propagating beams inside it did not experience any turbulence, see Figure 4.8(b). Similarly, the effect of turbulence on the correlated path was investigated by isolating the uncorrelated channels (i.e., optical beams in PATH1 propagating through the pipe), see Figure 4.7. The amplitude of S and \bar{S} were then set in order to ensure that both received electrical signals v_1 and v_2 had the same amplitude of ~ 300 mV, which is equivalent to $\Gamma_1 \mathcal{R}_1 G_1 = \Gamma_2 \mathcal{R}_2 G_2$ criterion.

Figure 4.9 illustrates the histogram of the detection threshold level obtained from the experiment. Note that due to the hardware dissimilarities, the average of the detection threshold is non-zero. However, since the offset levels are due to ORx1 and ORx2, then the problem can be resolved by adjusting the offset level of the output signal. Table 4.3

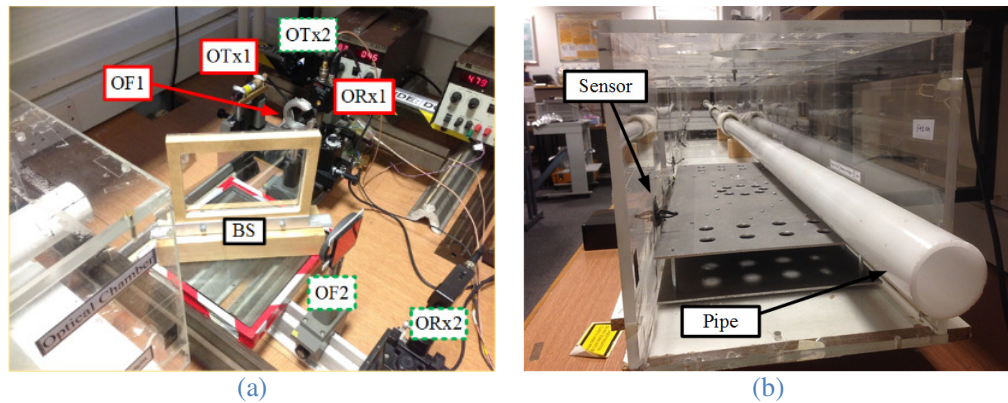


Figure 4.8: Experimental setup of atmospheric turbulence and differential signalling: (a) OTxs and ORxs at one end of the chamber, and (b) atmospheric chamber with temperature sensors to measure temperature gradient, and a pipe to isolate either PATH1 or PATH2 from the turbulent condition of the chamber. OF, OTx, ORx, and BS are optical filter, optical transmitter, optical receiver, and beam splitter, respectively.

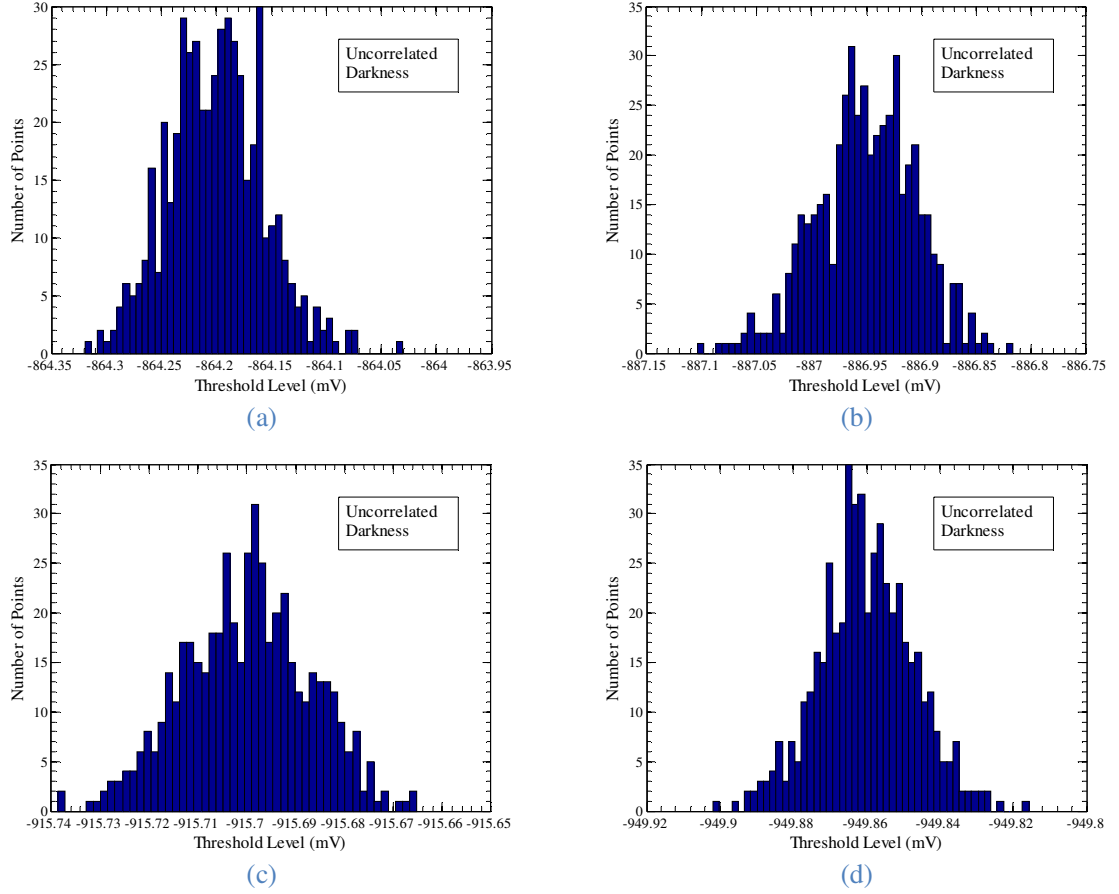


Figure 4.9: Histograms of the detection threshold levels of the differential signal threshold (V_{thresh}) for atmospheric turbulence and differential signalling experiment: (a) uncorrelated channels in dark room, (b) uncorrelated channels in lit room, (c) correlated channels in dark room, and (d) correlated channels in lit room.

shows all the key parameters adopted in the experiment. The recorded data were processed and the detection threshold level was extracted from signals. Figure 4.10 illustrates the sampled signal as well as the obtained detection threshold level of v_1 . The measured mean and standard deviation of V_{thresh} (indicated by Mean and $\sqrt{\text{Var}}$, respectively) as well as C_n^2 values for correlated and uncorrelated channels are summarized in Table 4.4 .

As predicted from Equ. (4.9.a), for both uncorrelated and correlated conditions the measured mean value is zero. Figure 4.11 shows an image taken from the oscilloscope screen illustrating how signals v_1 and v_2 for correlated channels are affected under the same turbulence conditions. Note that turbulence strength and the laser modulation index

Table 4.3: The setup parameters for atmospheric turbulence and differential signalling experimental.

Parameter		Value
Data rate NRZ-OOK		100 kbps
Chamber length L		6 m
Sampling rate		2.5 MSample/sec
Number of recorded points for each iteration		1 M points
Number of total iterations		500
Link 1	Optical transmit power	10 dBm
	Divergence angle	9.5 mDeg
	PD responsivity \mathcal{R}_1	0.3 A/W
	Wavelength λ_1	830 nm
Link 2	Optical transmit power	3 dBm
	Divergence angle	4.8 mDeg
	PD responsivity \mathcal{R}_2	0.4 A/W
	Wavelength λ_2	670 nm
Optical receiver noise rms $\sqrt{\sigma_n^2}$		1.5 mV

in Figure 4.11 were deliberately set to relatively small values in order to better illustrate the correlation between v_1 and v_2 .

It is expected to obtain $\sqrt{\text{Var}} \approx \sqrt{2\sigma_n^2}$ from the measurements. However, given the rms noise of optical Rx in Table 4.3, the measured $\sqrt{\text{Var}}$ in Table 4.4 is different from the predicted value of $\sqrt{2\sigma_n^2} = 2.1$ mV. This difference might be due to imperfect correlation

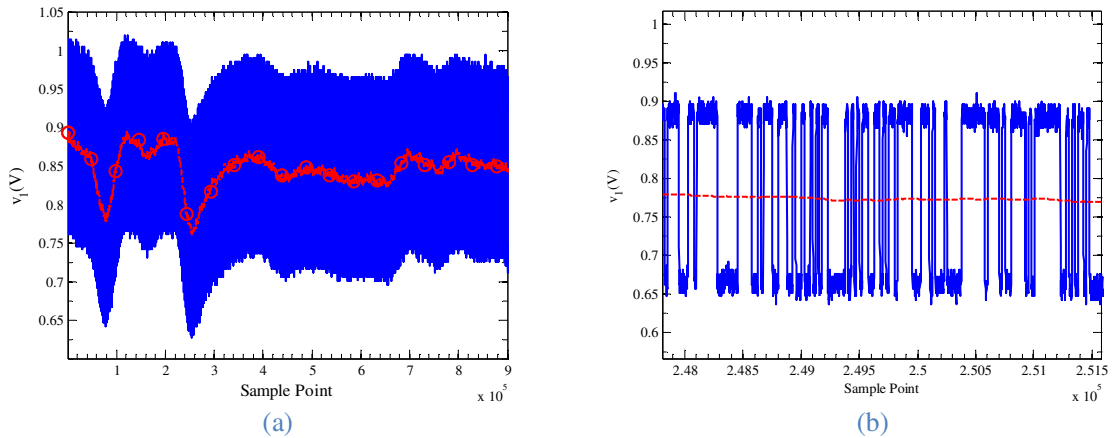


Figure 4.10: The sampled v_1 signal with the estimated detection threshold during atmospheric turbulence experiment. The signal is in blue colour, where the dashed red line with circle markers refers to the estimated detection threshold.

Table 4.4: The summary of the experimental measurement results for turbulence effect on differential signalling. Mean (mv) and $\sqrt{\text{Var}}$ (mv), denote the measured mean of detection threshold, variance of detection threshold of the differential signal. C_n^2 and $\rho_{1,2}$ denote obtained turbulence strength and correlation coefficient.

Channels condition	Mean (mV)	$\sqrt{\text{Var}}$ (mV)	C_n^2 (m ^{-2/3})	$\rho_{1,2}$
Uncorrelated (dark room)	-864.2	43.4	5.11×10^{-11}	0.08
Uncorrelated (lit room)	-886.9	45.5		
Correlated (dark room)	-915.7	12.9	5.21×10^{-11}	0.72
Correlated (lit room)	-949.9	12.9		

between channels in PATH2 and using two (not very close) wavelengths of 670 and 830 nm, which could lead to dissimilar σ_h^2 . In the experiment $\sigma_R^2 \approx 0.17$, which corresponds to the weak turbulence regime [30]. Considering Equ. (4.27.a) and using the rule of thumb, to have $\Delta\sigma_h^2/\sigma_h^2 < 0.1$, it is expected to have $\Delta\lambda/\lambda_0 < 0.09$. Note that in the experiment, the accuracy limit of Equ. (4.9.b) does not apply perfectly (as $\Delta\lambda/\lambda_0 < 0.21$, which corresponds to a maximum wavelength deviation of 160 nm around the central wavelength of 750 nm).

Using measured signals correlation coefficient ($\rho_{1,2}$) was estimated, which are presented in Table 4.4. The estimated $\rho_{1,2}$ (for the correlated case) are relatively high but do not correspond to the ideal case of $\rho_{1,2} = 1$. Other effects that could lead to inaccuracy of the measurement were the noise associated with the oscilloscope and the vibration of the whole setup. However, since it was intended to demonstrate only the difference

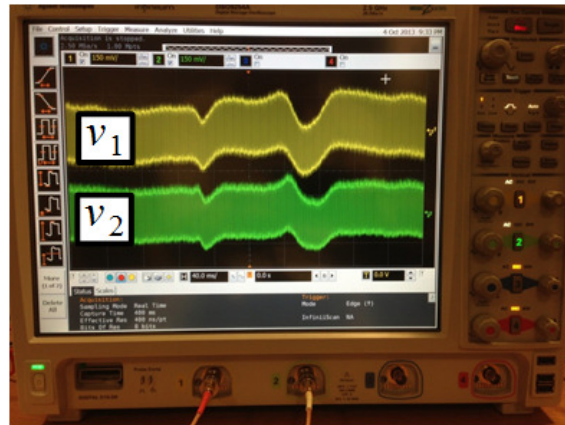


Figure 4.11: Original (v_1 in yellow and top) and inverted (v_2 in green and bottom) signals captured on the oscilloscope during atmospheric turbulence experiment.

between uncorrelated and correlated situations and during the entire measurement the same setup was used, these effects are not critical in the final conclusion. In addition to using two wavelengths and spatially closer beams from Equ. (3.3) it is evident that longer transmission spans will lead to larger values of ρ_0 , which in turn helps to achieve a highly correlated channels condition (i.e., $\rho_{1,2} \rightarrow 1$) [119].

In [35], a similar differential signalling based technique was proposed to reduce the effect of background noise in the received signal. The above experiment was carried out in both dark and fully lit environments (with ambient light power level of -45 dBm and -18 dBm, respectively), see Table 4.4. A negligible difference between the standard deviation of detection threshold results in these two cases is noticed. This testifies that under the experimental conditions, the background noise was not dominant. Thus, the reduction in $\sqrt{\text{Var}}$ values is due to the theory explained in Section 4.2 rather than the background noise level.

Using the derived analytical expression of the variance of the detection threshold, it was shown that the fluctuation in the optimal threshold level highly depended on the correlation between the propagating optical beams. Thus the differential signalling technique is attractive when highly correlated FSO channels can be established. This deduction was validated by means of experimental investigations under uncorrelated and correlated conditions. Also note that to achieve a high correlated channel condition light sources with close wavelengths, spatially closer beams and longer transmission distance are critical to have.

4.4 Differential Signalling and Pointing Errors

4.4.1 Channel Modelling

In the previous sections, the effect of differential signalling system in a turbulence channel was investigated and in this section the performance of the same system with the pointing errors is investigated.

Considering Equ. (4.6), a clear weather condition and negligible atmospheric turbulence is assumed. Also it is assumed that channel coefficient (h_i) includes the geometrical loss and pointing errors effects. The concept outlined in [120] is adopted to describe the pointing errors at Rxs, see Figure 4.12. Rxs are assumed to have the same aperture diameter as well as the same electrical and optical characteristics. The aperture diameter is d_s and the laser beam spot at the Rx transverse plane has a radius of w_{RX} . Besides the instantaneous radial displacement between the beam centroid and the aperture centre is denoted by r . In terrestrial FSO communication systems the fading coefficient due to the geometrical loss and pointing errors h_i is given by [120]:

$$h_i(r; L) \approx A_0 \exp\left(-\frac{2r^2}{w_{eq}^2}\right), \quad (4.29)$$

where A_0 and w_{eq} correspond to the geometrical loss and equivalent beam-width,

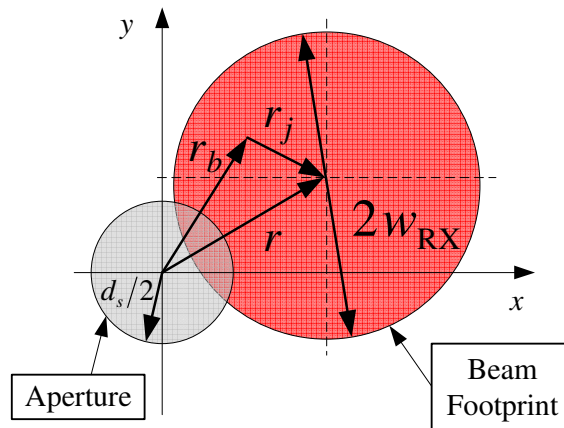


Figure 4.12: Rx aperture and a laser beam footprint at the Rx transverse plane.

respectively. Note that $A_0 = [\text{erf}(v)]^2$ and $w_{\text{eq}}^2 = w_{\text{Rx}}^2 \frac{2\sqrt{\pi}\text{erf}(v)}{2v\exp(-v^2)}$ where $v = \sqrt{\pi/2} \frac{d_s}{2w_{\text{Rx}}}$ and $\text{erf}(x) = \frac{2}{\sqrt{\pi}} \int_0^x e^{-t^2} dt$ [120]. In most practical applications the beam divergence θ is small (i.e., $\theta \ll 1$ Rad), which leads to $w_{\text{Rx}} = \theta L + w_{\text{Tx}}$. Therefore, it is possible to set $w_{\text{Rx},1} = w_{\text{Rx},2}$ by selecting the appropriate values for θ_1 and θ_2 . pointing errors displacement has two components known as the boresight r_b (displacement between beam centre and centre of the detector) and jitter r_j (offset of the beam centre at detector plane) [66].

The boresight displacement (r_b) represents a deviation originating from thermal expansion of the buildings [34] and determines the mean offset of pointing errors [121], whereas r_j is a random variable originating from building sway and vibration [34]. From the statistics point of view the jitter corresponds to the random variation of the beam footprint around the boresight direction with the jitter variance of σ_j^2 [121].

In terrestrial FSO links, the jitter consists of both vertical and horizontal components [34]. Thus, without loss of generality, here the focus will be on the deviation along either vertical or horizontal axis, which can be further extended to the other axis. It is shown in [34] that r has Rician PDF with the average ($\text{Mean}(h_i) = E[h_i]$) and the second moment ($E[h_i^2]$) given by:

$$\text{Mean}(h_i) = E[h_i] = \frac{A_0 \gamma^2}{1 + \gamma^2} \exp\left(-\frac{r_b^2}{2(1 + \gamma^2)\sigma_j^2}\right), \quad (4.30.a)$$

$$E[h_i^2] = \frac{A_0^2 \gamma^2}{2 + \gamma^2} \exp\left(-\frac{2r_b^2}{2(2 + \gamma^2)\sigma_j^2}\right), \quad (4.30.b)$$

where $\gamma = w_{\text{eq}}/2\sigma_j$. Therefore the variance of h_i will be:

$$\text{Var}(h_i) = \frac{A_0^2 \gamma^2}{2 + \gamma^2} \exp\left(-\frac{r_b^2}{(2 + \gamma^2)\sigma_j^2}\right) - \frac{A_0^2 \gamma^4}{(1 + \gamma^2)^2} \exp\left(-\frac{r_b^2}{(1 + \gamma^2)\sigma_j^2}\right). \quad (4.31)$$

Since $E[S^M] = E[\bar{S}^M]$, where M is an integer, thereafter by means of Equ. (4.30), the

average and variance of Equ. (4.6) are derived as:

$$\text{Mean}(V_{\text{thresh}}) = \text{Mean}(h_1) - \text{Mean}(h_2), \quad (4.32.a)$$

$$\begin{aligned} \text{Var}(V_{\text{thresh}}) = \text{Var}(h_1) + \text{Var}(h_2) - 2\rho_{\text{PE}}\sqrt{\text{Var}(h_1)}\sqrt{\text{Var}(h_2)} + \\ 2\sigma_n^2, \end{aligned} \quad (4.32.b)$$

where ρ_{PE} is the correlation coefficient between two channel coefficients of h_1 and h_2 .

Note that to derive Equ. (4.32), it was assumed that $\Gamma_i \mathcal{R}_i G_i = 2/S_{\text{thresh}}$.

The dynamic response of a building with applied live loads depends on the directional stiffness, as well as the height, size and topology. The tip displacements of a tall building can be as large as tens of centimetres due to the normal wind loads. However, irrespective of the height and stiffness of the building, the relative displacement of R_{x1} and R_{x2} is almost zero. The segment of the Rx mast between the two Rxs can be reasonably assumed to be rigid if the mast is properly designed according to the building standards (i.e., earthquake or wind) and if the distance between the two Rxs is very small compared to the overall height of the building ($z_1 \cong z_2 = z$ in Figure 4.13), then $r_{j,1} = r_{j,2} = r_j$. Considering the short distance between the two Rxs the relative displacement due to the thermal expansion, which results in $r_{b,1} = r_{b,2}$, can be neglected. The same is true for the relative displacement between the Tx's. In view of the above, it can be assumed $\sigma_{j,1}^2 = \sigma_{j,2}^2$ and $\rho_{\text{PE}} \cong 1$.

Considering $\sigma_{j,1}^2 = \sigma_{j,2}^2$, Equ. (4.32) will be:

$$\text{Mean}(V_{\text{thresh}}) = 0, \quad (4.33.a)$$

$$\text{Var}(V_{\text{thresh}}) = 2\text{Var}(h_1)(1 - \rho_{\text{PE}}) + 2\sigma_n^2. \quad (4.33.b)$$

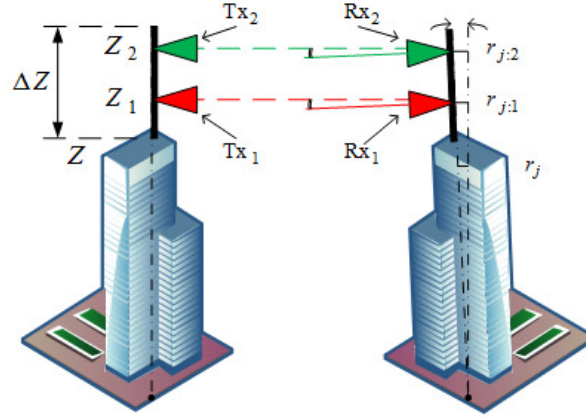


Figure 4.13: Effect of building movement on FSO Rxs with exaggeration. On the left there is the Tx building hypothetically without movement and on the right the Rxs are installed on top of a building, which is influenced by the effect of building movement.

Therefore, regardless of the strength of pointing errors the detection threshold level can be set to zero but will experience fluctuation with the given variance. Considering $\rho_{PE} \cong 1$, Equ. (4.33.b) simplify to $\text{Var}(V_{\text{thresh}}) \approx 2\sigma_n^2$, thus leading to the elimination of pointing errors at the Rx. Therefore for the system shown in Figure 4.1 provided links are identical, and Rxs are mounted on the same fixture structure, the threshold level could be set to zero for a range of pointing errors strength.

To estimate the equivalent parameters of the differential signalling based link, a SISO link with a Rayleigh pointing errors PDF is used as the equivalent link. The pointing errors parameters of the equivalent SISO link is found so that SISO has the same pointing errors variance as differential signalling. For the simplified case where $r_{b,1} = r_{b,2} = 0$, assuming that $\gamma_1 = \gamma_2$ and $A_1 = A_2 = A_{DS}$, and simplifying $\text{Var}(h_{DS}) = \text{Var}(h_1 - h_2)$, the following equation is derived from which γ_{DS} of the equivalent pointing errors PDF can be obtained:

$$\begin{aligned} (2 + \gamma_1^2)(1 + \gamma_1^2)^2 / (2 + \gamma_{DS}^2)(1 + \gamma_{DS}^2)^2 = \\ 2(1 - \rho_{PE})\gamma_1^2 / \gamma_{DS}^2, \end{aligned} \quad (4.34)$$

when $r_{b,1} = r_{b,2} = 0$, Rician distribution becomes Rayleigh and it is assumed that PDF of the equivalent pointing errors to perform comparison is also Rayleigh.

4.4.2 Pointing Errors Experiment

To validate the proposed concept practically the experimental setup shown in Figure 4.14 has been used. Both Tx and Rx modules were located at one end of a 6 m long indoor atmospheric chamber. In order to double the link length a mirror was used at the other end of the chamber to reflect back the beams (note that the mirror is not shown in the figure). Since the optical beams were in parallel with no overlap at the Rx plane, no optical filters were used. The outputs of Rx were recorded using a sampling oscilloscope for further analysis via MATLAB[®]. The amplitude of modulating signal was set such that the Rx output levels were at ~ 10 mV. Table 4.3 summarizes the key system parameters adopted. Note that in this experiment, the number of iterations was only 50 since the vibration had a fixed pattern rather than being random.

To simulate pointing errors condition, both Rx were positioned on a vibration stand vibrating at a frequency of 5 Hz with the deviation of ~ 2 mm in the vertical direction (a sinusoidal waveform was used to stimulate the vibrator). In practical scenarios FSO links will experience vibrations in both axes but here the vibration is generated only on the vertical axis. Note that it has the same effect as for vibrations on the horizontal axis.

Figure 4.15 depicts a captured image from the oscilloscope screen for two signals. Note that the laser modulation index in Figure 4.15 was deliberately set to relatively small

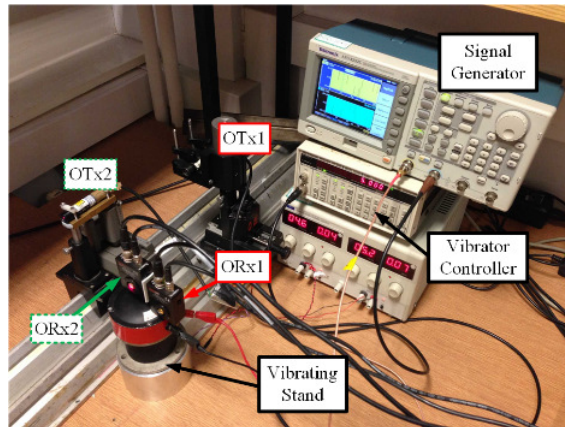


Figure 4.14: The pointing errors and differential signalling experimental setup. OTx and ORx are optical transmitter and optical receiver, respectively.

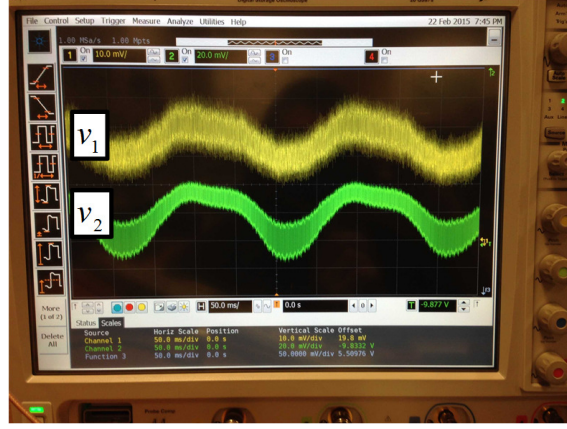


Figure 4.15: An image taken from the oscilloscope screen during the pointing errors and differential signalling experiment. Top yellow signal is v_1 whereas bottom green one is v_2 .

value in order to better illustrate correlation between v_1 and v_2 . As shown the effect of pointing errors on both signals are highly correlated. The recorded data were processed and the detection threshold level was extracted from signals. Figure 4.16 illustrates the sampled signal as well as the detected signal v_2 . The histogram of the recorded threshold levels for the differentiated signal is illustrated in Figure 4.17. As in the previous experiment, the dissimilarity of the offset levels added by ORxs results in a non-zero DC offset in the detection threshold level.

Based on the covariance matrix of the received signals, the correlation coefficient (ρ_{PE}) of 0.92 was obtained from the measurements, which agrees well with the assumption of $\rho_{PE} \rightarrow 1$ made in the analysis. The measured standard deviation of v_1 , v_2 and V_{thresh} are

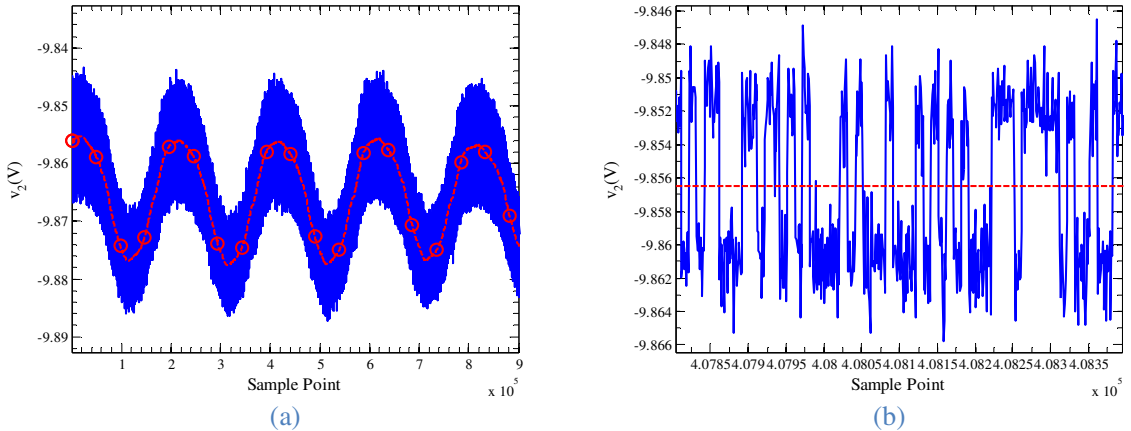


Figure 4.16: The sampled v_2 signal with the estimated detection threshold during pointing errors and differential signalling experiment. The signal is blue colour where the dashed red line with circle markers refers to the estimated detection threshold.

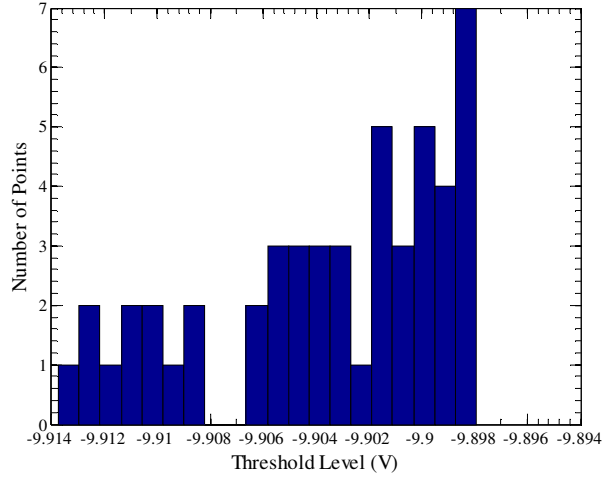


Figure 4.17: Histogram of the detection threshold levels of the differential signal (V_{thresh}) for pointing errors and differential signalling experiment.

presented in Table 4.5.

As discussed before for the same pointing errors jitters (i.e., $r_{j,1} \approx r_{j,2}$), the variance of channel coefficient ($\text{Var}(h_i)$) in Equ. (4.33.b) results in almost the same range for both signals. The close match between the measured values of standard deviation of v_1 and v_2 confirms the deduction.

On the other hand, according to Equ. (4.33.b), if the effects of pointing errors on both signals are highly correlated, then standard deviation will significantly be reduced by $2\sigma_n^2$. However the measured value of 4.58 mv slightly differs from the predicted value of $\sqrt{\text{Var}(V_{\text{thresh}})} \approx \sqrt{2\sigma_n^2} = 2.1$ mV. This can be due to the small difference in the values of $\sqrt{\text{Var}(v_1)}$ and $\sqrt{\text{Var}(v_2)}$. Although the experiment was conducted over a 12 m long FSO link, the investigation can be extended to longer spans. Using the same laser beam, but over a longer link span, the geometrical attenuation and the beam footprint at the Rx will be larger. Higher geometrical loss will reduces A_0 whereas larger optical footprints

Table 4.5: The summery of the measurements results for pointing errors and differential signalling experiment.

Signal	v_1	v_2	V_{thresh}
$\sqrt{\text{Var}}$ mv	24.75	27.00	4.58

will lead to reduced A_0 and increased γ . However, as seen from Equ. (4.33.b), for $\rho_{PE} \rightarrow 1$ these parameters will have no effect on the resultant variance.

Using the predicted γ_{DS} , (from Equ. (4.33)) the variance of equivalent differential signalling pointing errors ($\sigma_{j,DS}$) can be determined for a range of ρ_{PE} . Figure 4.18 depicts the jitter standard deviation against channel correlation (ρ_{PE}) for the SISO link and equivalent link of differential signalling for receiver aperture radius (d_s) of 10 cm, laser beam radius at receiver (w_{Rx}) of 100 cm, and the jitter variances of 10 cm (i.e., $\sigma_{j,1} = \sigma_{j,2} = 10$ cm). It is observed that the pointing errors induced fading effect reduces with increasing value of ρ_{PE} . Also from both Equ. (4.33) and Figure 4.18 it is seen that for $\rho_{PE} \geq 0.5$ one obtains $\gamma_{DS} \leq \gamma_1$.

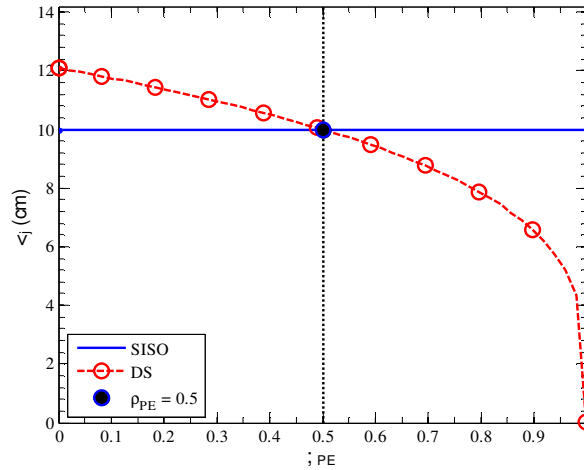


Figure 4.18: Jitter standard deviation of the equivalent differential signalling (DS) pointing errors versus correlation coefficient (ρ_{PE}), for the single-input single-output (SISO) system with differential signalling and for receiver diameter (d_s) of 20 cm, beam radius (w_{Rx}) of 100 cm, and jitter variances of 10 cm (i.e., $\sigma_{j,1}=\sigma_{j,2}=10$ cm).

4.5 Differential Signalling and Manchester Code

4.5.1 System Configuration

To the best of our knowledge, Manchester code has not been used to mitigate the fading

effect of the channel in a FSO link. In fact, Manchester code is used to achieve clock synchronization. It also can be used to remove the DC component of the signal and to avoid a long stream of logic '1' or logic '0' [122]. In this work Manchester code is adopted to remove the need for two parallel highly correlated links in a differential signalling system. Figure 4.19(a) illustrates the proposed concept, where the input bit stream and its inverted version are applied to the encoder, which is fed directly to the optical source. The output of the encoder is the Manchester code (also known as phase encoding) word in which the encoding of each data bit has at least one transition at the centre of each bit period, and has a bandwidth twice that of the input signal [122].

In the proposed differential signalling scheme, the received raw signal is processed prior to quantization. At the Rx the regenerated bit stream is passed through sampler modules and a combiner, which simply subtracts the sampled outputs, to recover the NRZ data stream as shown in Figure 4.19(b). As seen so far in the proposed technique the original and inverted versions of signal are transmitted by means of Manchester code and a single FSO link whereas in Section 4.3 and Section 4.4 this was done using two distinct FSO links. Thus, the proposed method ensures that the channels are highly correlated. Besides, it eliminates the need of optics for combining and separating two FSO links as

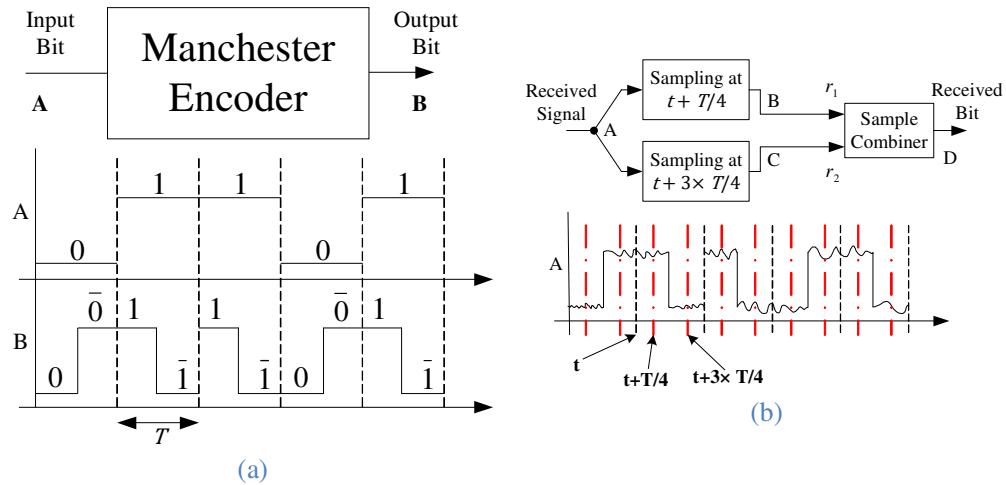


Figure 4.19: The required signal processing to perform differential signalling using one FSO link. The procedure is shown for a sequence of 01101 bits as an example: (a) the required signal shaping at the Tx, and (b) the required signal recovery at the Rx where two samples (i.e., r_1 and r_2) are taken at the presented intervals.

in Section 4.3.3.

4.5.2 Manchester Code Experiment

To prove the validity and benefit of the proposed method an experimental test bed for a SISO FSO link was developed to measure the variation of the threshold level and the Q-factor. The experiment was using the same indoor atmospheric chamber. The method described in Section 4.3.6 was used to estimate C_n^2 (in unit of $\text{m}^{-2/3}$), which is known as refractive index structure coefficient and shows the strength of the turbulence strength. For each scenario 250 data sets were recorded. The summary of the experimental setup for the 830 nm wavelength is summarized in Table 4.3.

The experimental setup also is illustrated in Figure 4.20. Measurements were taken for three different channel conditions, and were also repeated under dark (ambient light power < -45 dBm) and bright (ambient light power ≈ -18 dBm) environments to ensure that the measurement were not influenced by any undesirable

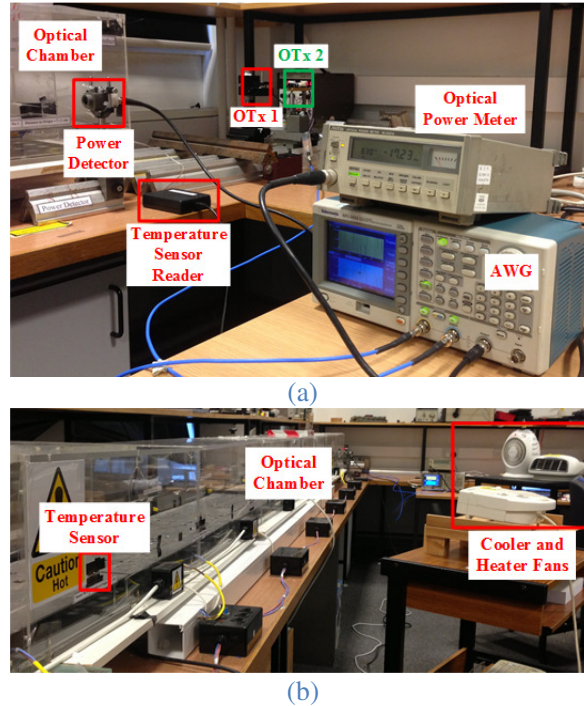


Figure 4.20: The experimental setup: (a) equipment at the Tx side, and (b) artificial atmospheric channel. AWG and OTx denote arbitrary waveform generator and the optical source, respectively.

optical signal. Since the results taken under dark and bright room conditions were almost the same only measured data set for the bright room condition are presented, see Table 4.6. The results clearly show the advantage of the proposed method. For example, for $C_n^2 = 6.06 \times 10^{-11} \text{ m}^{-2/3}$ where SISO link did not provide acceptable signal quality (the Q-factor is less than the required value of 4.75), the proposed method results in a Q-factor which is larger than SISO. Besides, compared to a SISO link, the proposed method effectively reduced the variation of detection threshold. The outcome of the experimental result agrees with the deduction in Section 4.3.3 and Section 4.5.1 in the way that in the proposed scheme the channels are highly correlated, therefore a high performance enhancement was expected.

Table 4.6: The summary of the measurement for single-input single-output (SISO) differential signalling (DS) link. These results are for DS and Manchester code scheme.

$C_n^2 (\text{m}^{-2/3})$	SISO		DS	
	$\sqrt{\text{Var}}$ (mV)	Q-factor ^a	$\sqrt{\text{Var}}$ (mV)	Q-factor ^b
Clear	0.88	[33.0, 5.3]	0.89	[45.3, 1.4]
4.25×10^{-12}	7.35	[7.9, 4.1]	0.91	[40.3, 2.1]
6.06×10^{-11}	40.77	[1.7, 0.6]	1.09	[40.0, 4.1]

^{a, b} The pair shows the simulation outcome in form of expected value and standard deviation pair, respectively.

To conclude this section, the histogram of the recorded signals for a clear channel as well as a turbulent channel for $C_n^2 = 6.06 \times 10^{-11} \text{ m}^{-2/3}$ are included in Figure 4.21. In contrast to the previous cases, the combination of Manchester code and differential signalling method results in a signal with a zero offset.

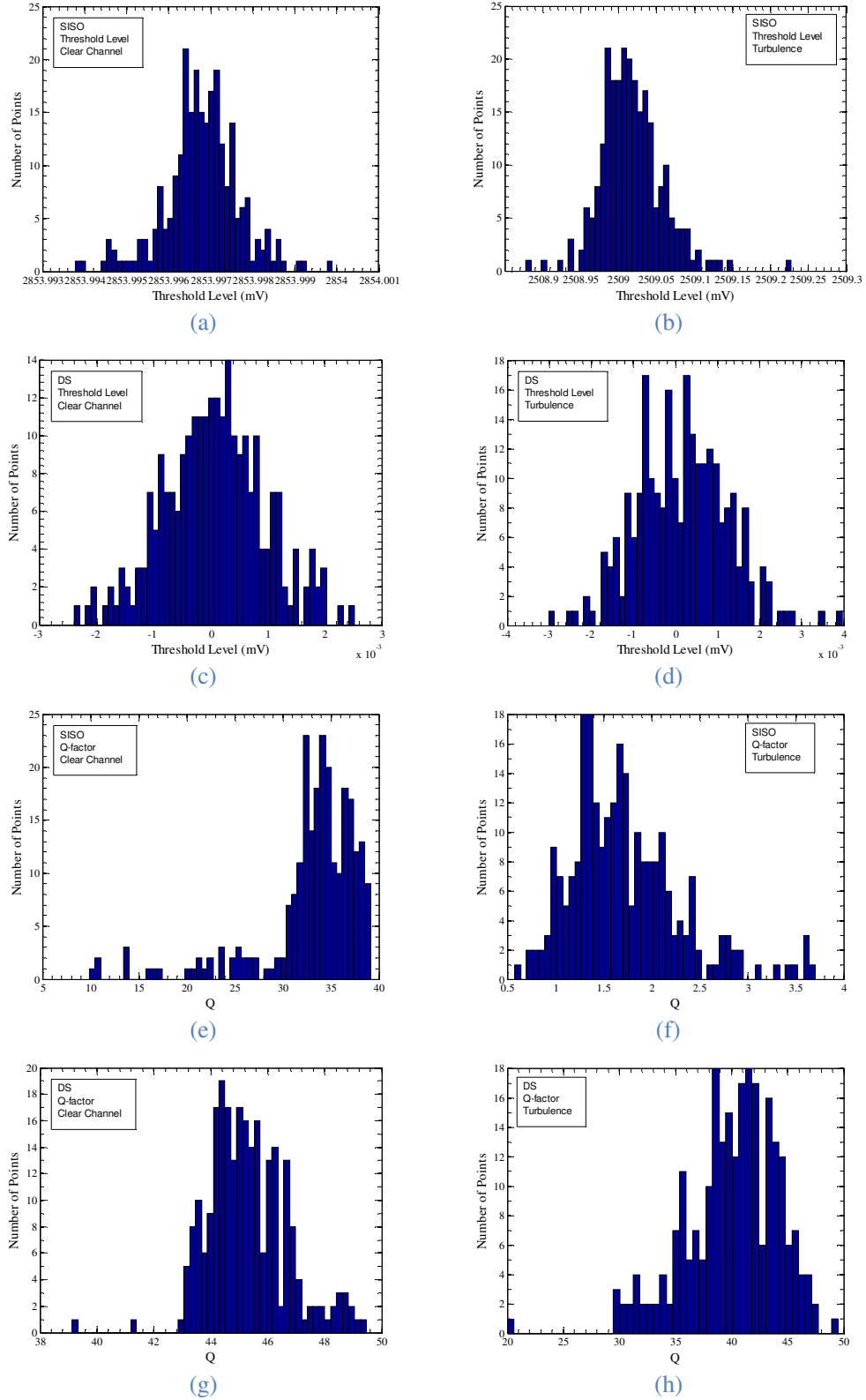


Figure 4.21: (a, b) histograms of the detection threshold levels of the single-input single-output link, (c, d) histograms of the detection threshold levels of the differential signalling (DS) link, (e, f) histograms of the Q-factor of the SISO link, and (g, h) histograms of the Q-factor of the differential signalling link. (a, c, e, f) are for clear conditions whereas (b, d, f, h) are for turbulent channel with $C_n^2=6.06 \times 10^{-11} \text{ m}^{-2/3}$.

4.6 Summary

Using theory, simulation and experiment, the benefits of differential signalling method in turbulence and pointing errors channels were described. Differential signalling has been known as an effective method to mitigate the impact of non-random fading channels (e.g., fog) and cancelling the ambient background noise. In this chapter it was shown that differential signalling also can mitigate the effects of turbulence and pointing errors. In conditions where threshold level of the received signal is varied by turbulence and pointing errors, it was shown that by using the differential signalling method threshold level variation is reduced and the reduction depends on how correlated the channels are. In one experiment the performance of differential signalling under turbulence of $\sigma_R^2 \approx 0.17$ was evaluated. The measurements showed that for differential signalling in uncorrelated channels condition (i.e., $\rho_{1,2} \approx 0$) the threshold level had the standard deviation of 43 mV whereas for the same setup under correlated condition (i.e., $\rho_{1,2} \approx 0.72$) the standard deviation reduced to 13 mV. The appropriate conditions of approaching high correlation were also discussed and it was shown that if the wavelength difference of differential signalling links relative to the central wavelength is less than 0.47, then the channels will have correlation higher than 0.9. In another experiment, the effect of differential signalling under pointing errors fading effect was investigated. The measurement showed that where the standard deviation of threshold level for both links of differential signalling scheme was 25 and 27 mV under the same conditions the threshold level of differential signalling system with correlation coefficient of 0.92 was 5 mV. Finally, an alternative scheme was introduced that in contrary to conventional differential signalling, it only needs one FSO link. The measurements showed that under the same turbulence condition of $C_n^2 = 6.06 \times 10^{-11} \text{ m}^{-2/3}$ using the aforementioned method the Q-factor of the received signal in the new differential signalling scheme was

40 while a SISO link under the same conditions delivers a Q-factor of 1.8.

5 HYBRID FSO/RF ANTENNA

5.1 Introduction

This chapter introduces the idea, describe the characteristics and evaluate the performance of the propose hybrid antenna. The design strategy is based on the geometrical optics and a full wave electromagnetics simulation using CST STUDIO SUITE® [123]. The chapter is composed of the followings. First an introduction on RF antennas is given and based on the required specifications of the hybrid antenna a suitable existing RF design is adopted as the base. Next, an initial hybrid antenna prototype is proposed, where Cassegrain antenna design is combined with the SISO FSO link. The simulation results as well as experimental measurements are compared to the initial design expectations and it is shown that a SISO FSO scheme cannot provide the adequate reliability. Therefore, an alternative SIMO FSO scheme is proposed, where the complete system is simulated, characterized, and tested to confirm the validity of the proposed scheme. Note that the optimisation techniques and detailed electromagnetic analysis of the RF antenna are beyond the scope of this thesis. However, interested readers are referred to appropriate references for further studies.

5.2 Antenna Specifications

As outlined in the previous chapter, as part of the requirement to ensure 100 % link availability at all times and under all weather conditions, it is essential to adopt a hybrid FSO/RF system. Therefore, a backup RF link is required to provide connectivity (through at reduced data rate then FSO) when the FSO link is down due to fog, smoke, etc. The proposed hybrid antenna is intended for “short hop”, typically few kilometres, of wireless link that can be used in a number of applications including last mile, inter-campus connectivity, etc. The final frequency range for the RF link is yet to be determined but is likely to be within the currently available ISM bands around 24 GHz or 61 GHz. In this research work as a proof of concept, the X-band of 8.2-12.4 GHz is adopted in order to demonstrate the proposed concept considering the availability of components, and test and measurement equipment. However, the proposed concept could be implemented at higher frequency range of 30-100 GHz as part the future millimetre/FSO wireless networks.

With reference to Equ. (2.12), the RF link equation is given by:

$$G_{Rx} = CNR + L_{ch} - EIRP + T_R + k_{dB} + 10 \log_{10} BW. \quad (5.1)$$

For $BW = 100$ MHz at the receiver, receiver noise temperature of $T_R = 4100^\circ$ K, and $EIRP = 30$ dBm, path loss 112 dB at 10 GHz over 1 km link distance, and received signal to noise ratio of 10 dB, the required gain for the receiving antenna (G_{Rx}) will be at least ~ 10 dBi. However, in order to compensate for the rain attenuation for the worst scenario (Glasgow rain with attenuation of ~ 18 dB/km), the minimum receiver antenna gain should be 28 dBi. Here, a receiver antenna gain of 30 dBi is adopted which includes a 2 dB link margin for other possible losses in the system, in particular the cable loss. The same gain is considered for the transmitting antenna as well.

5.3 Antenna Base Structure

To design the hybrid antenna, a suitable RF antenna should be selected as the base to provide a 30 dBi gain. Considering a peer-to-peer RF link with high gain and bandwidth, the antenna should have the following specifications:

1. A carrier frequency of 10 GHz
2. A minimum bandwidth of 100 MHz
3. A directive radiation pattern with a maximum half-power beam-width (HPBW) of 5° giving RF radiation footprint of ~ 87 m over a 1 km link span
4. A minimum gain of 30 dBi

As for the antenna gain, the available options are multi-element array antennas and reflector. For a circular open ended-waveguide with a gain of ~ 9 dBi, at least 126 circular open-ended waveguides are required to achieve a 30 dBi gain [70]. Alternatively, an array of patch antennas could be considered to achieve the required gain. However the gain of a single patch antenna is typically ~ 7 dB necessitating a significant increase in the number of elements required [70]. Besides, simple patch antennas cannot provide a high bandwidth. Another issue with array antennas is the maximum element separation, which needs to be no greater than half the operating wavelength to prevent grating lobes. [70]. This limitation results in complex fabrication and making the radiation pattern frequency dependent. Therefore, the array antenna is not considered in this research.

The reflector RF antenna [67, 69, 70], which has been used in many applications including terrestrial link, ground-to-satellite link, and satellite-to-satellite links, is adopted in this work. This type of antenna provides a directive high gain pattern, which is suitable for LOS based link configurations. Operating over a much higher frequency range with a

wide bandwidth also is an advantage, since the physical size of the antenna is smaller (see Figure 2.5). Considering the typical antenna efficiency of 0.55 [67], using Figure 2.5, it is found that the minimum antenna aperture size of ~ 407 mm is required to achieve a 30 dBi gain.

In this work, an aperture with a diameter of 475.2 mm is used (see Table C.3 and Section C.2.4 for more details). Table 5.1 summarises the key required RF antenna specifications. The maximum return loss of the antenna is defined to be -10 dB over the available bandwidth, which is equivalent to a power reflection of 0.1 times the pumped power.

Table 5.1: Required RF antenna specifications.

Parameter	Value
Minimum antenna gain	30 dBi
Maximum half-power beam-width (HPBW)	5 Degrees
Minimum bandwidth	100 MHz
Carrier frequency	10 GHz
Maximum return loss	-10 dB
Antenna type	Reflector

5.4 Reflector Antenna

There are a number of reflector antenna including the parabolic reflector (see Figure 5.1(a)) [69], offset parabolic antenna (see Figure 5.1(b)) [124], spherical reflector antenna (see Figure 5.1(c)) [125], Gregorian reflector antenna (see Figure 5.1(d)) [126], Cassegrain reflector antenna (see Figure 5.1(e)) [127], offset Cassegrain reflector antenna (see Figure 5.1(f)) [124], and reflector fed by dielectric cone (see Figure 5.1(g)) [128] that are widely reported in the literature. In addition to the antenna specification, in order to select the most suitable reflector antenna for this work the following properties are also

considered:

1. Practical reflectors are expected to have a total antenna efficiency within the range of 55 to 85% [67], which is defined as the ratio of total radiated power to total input power of the antenna. Higher efficiency in reflectors means lower power dissipation and improved performance. Factors contributing to the antenna total efficiency will be discussed later on in this chapter.
2. In addition to the main lobe of an antenna, there also exist side-lobes. In outdoor LOS based microwave links, it is essential to keep the side-lobe of the Tx antenna as small as possible to avoid unwanted interference. Here, a side-lobe level (i.e., ratio of the main-lobe peak to the side-lobe peak) of -20 dB is adopted.
3. Frequency scaling of a basic reflector antenna can be accomplished in a straightforward manner.
4. The electromagnetic interference between the RF and optic parts should be kept at a minimum level. The introduction of the required optical components should be done in a manner which causes minimum disturbance to the RF performance. In this design advantage of the RF blocking introduced by the sub-reflector is taken to site the optical components.
5. For a full duplex data link, the antenna should provide an acceptable cross-polarization discrimination. Having a high X-pol discrimination makes it possible to transmit in one polarization and receive in another using the same carrier frequency, while the cross-talk is kept low.

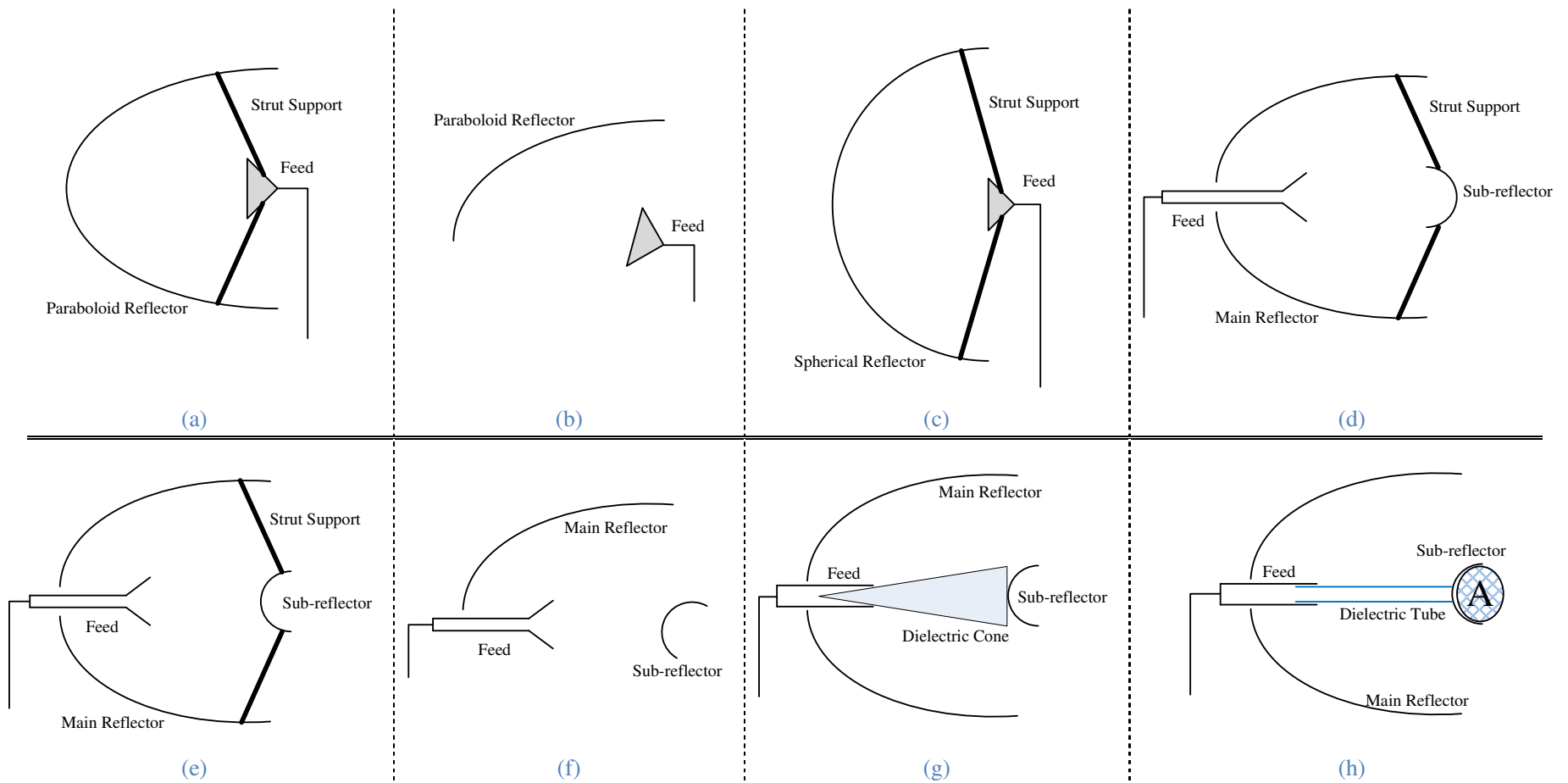


Figure 5.1: (a) to (g) Different reflector antenna configurations, (h) proposed antenna configuration for the project. Hatched area labelled by 'A' is the empty available area in front of the sub-reflector.

Each property of the antennas results in a side-effect, which degrades the performance and, in particular, the aforementioned specifications. Here, these properties and the corresponding effects are outlined [70, 129]:

- **Front-fed design:** This only offers two degrees of freedom including main reflector, and the feed when considering optimisation. In cases that the electrical size of the antenna, which is the physical size relative to the wavelength, is small (i.e., less than 100); having more degrees of freedom is an advantage in optimisation methods.
- **Offset design:** This results in a low X-pol discrimination less than -20 dB [124, 130] and a high fabrication cost due to the reflector geometry. Figure 5.2 depicts the relation between the X-pol discrimination and the reflector offset angle. Note that, the X-pol decreases with reflector offset angle as outlined in [124]. Besides, for wide angle feeds the performance is worse, which restricts the size of the reflector.
- **Spherical reflector:** The whole point of using a paraboloid reflector is to reduce the phase error of the impinging incident power over the reflector surface. In a paraboloid design, all of the radiated electromagnetic waves at the far field have the same phase thus they add up leading to increased total radiation. However, this is not the case for a spherical reflector. Therefore, in general the total efficiency of spherical antennas is less than the paraboloid ones. Also in contrary to the paraboloid reflector, the spherical reflector cannot generate an equiphase front-wave and the incoming waves do not add up in phase at the

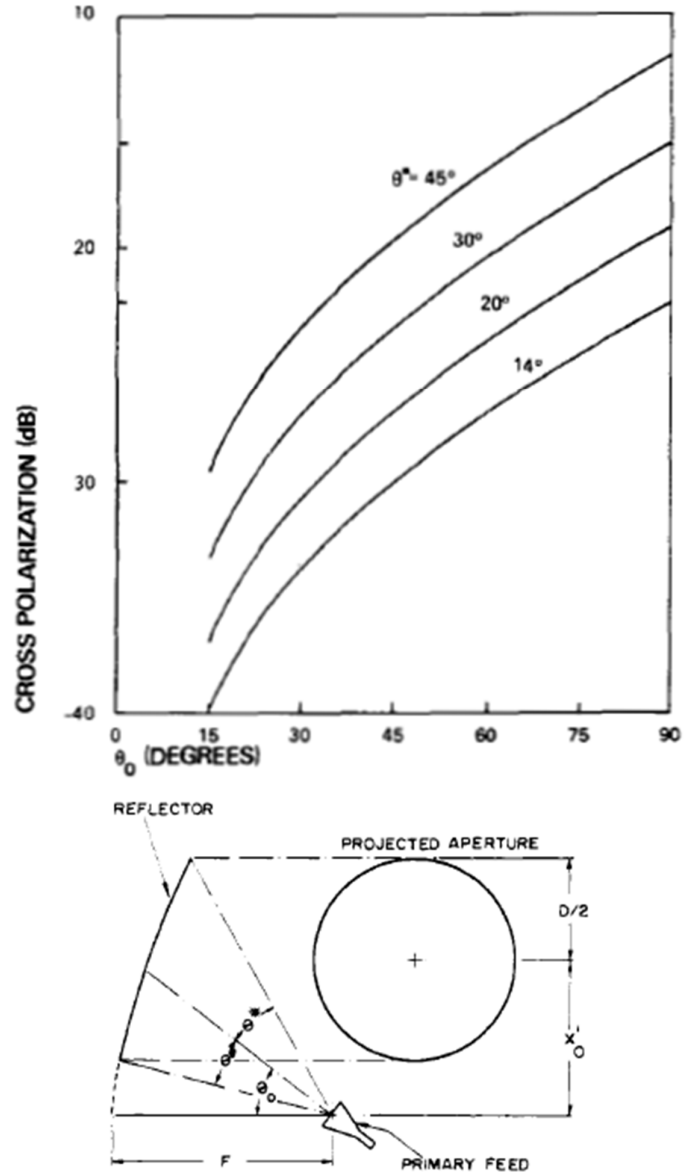


Figure 5.2: X-pol discrimination versus the reflector offset angle. Figure is taken from [124] with permission.

focal point. Therefore, a spherical reflector is not the best option.

- **Strut support:** The existence of struts scatters the fields, which contribute to both the low X-pol discrimination and high side-lobe level. This degradation is higher when larger struts are required to support larger feeds or sub-reflectors. Figure 5.3 illustrates the overall strut efficiency and the blocked area by struts [69].

- **Dielectric cone:** The cost of fabrication of a dielectric cone as well as the protection against environmental damages are the significant issues with this design.
- **Two reflector designs:** The spillover of electromagnetic field creates a surface current on the sub-reflector, which results in sub-reflector radiating an additional field. The total radiated field is the interaction of radiation due to the sub-reflector from the main reflector. The small sub-reflector has a wide angle radiation field, which results in the total field having a lower gain and a higher side-lobe level. In Figure 5.4 the effect of second reflector blockage on both

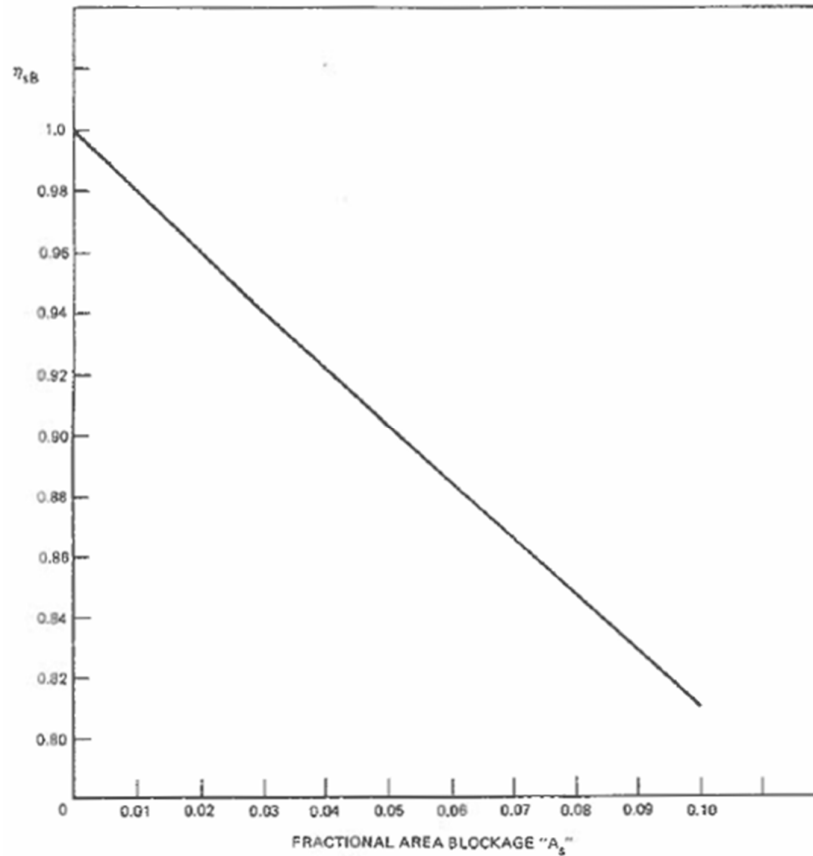
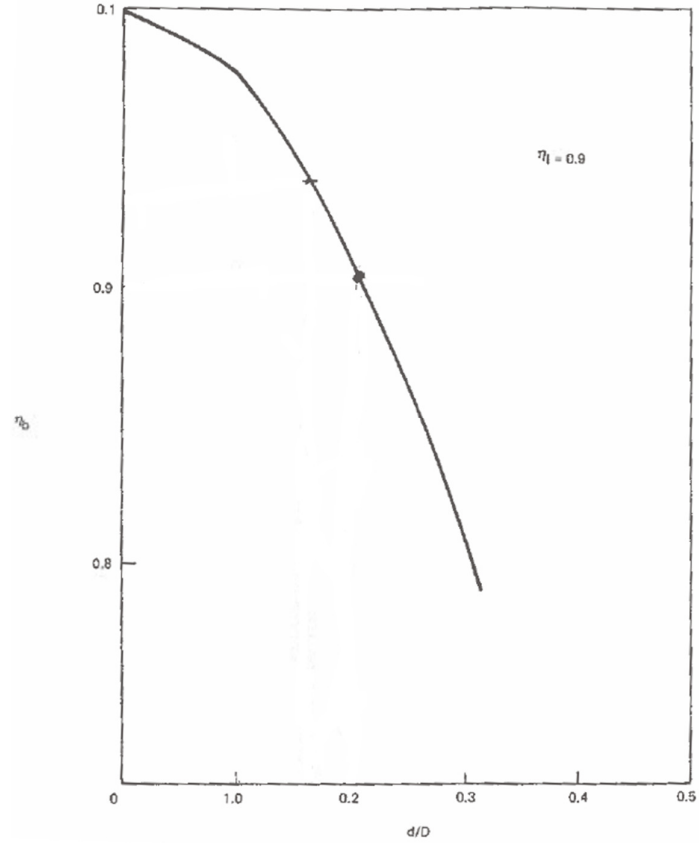
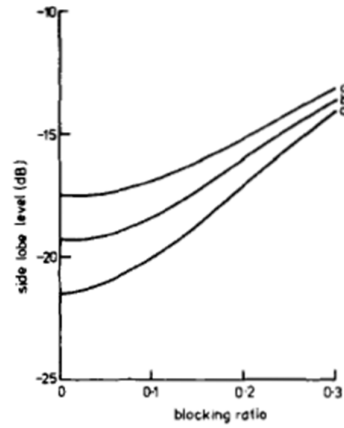


Figure 5.3: Strut blockage overall efficiency versus fractional area blockage. Fractional area blockage is defined as the ratio of the effective blocked area by struts to the total area of aperture. Figure is taken from [69] with permission.



(a)



(b)

Figure 5.4: (a) Blockage efficiency versus the blockage ratio for illumination efficiency of 0.9. Figure is taken from [69] with permission, and (b) side-lobe level versus blockage ratio for various illumination forms. Figure is taken from [129] with permission.

efficiency [69] and side-lobe level [129] is presented.

Based on the discussion so far, it is possible to compare existing options in Figure 5.1 and select the optimum scheme for the antenna. Another important factor, which must be taken into account, is the possibility of adding optical aperture to the antenna structure with a minimum effect on the antenna characteristics. Table 5.2 summarises the

comparison.

Front-fed antenna (parabolic or spherical) is not considered since it makes the combination of RF and FSO difficult. Therefore, other schemes including Cassegrain or Gregorian are considered as possible options. More important, the structure of the antenna selected in this project requires two constraints that a Cassegrain antenna can easily meet:

1. The space available at the front of the sub-reflector is the best possible position for installing the optical transceiver with no blocking or being blocked by the RF antenna.
2. In a single reflector antenna the feed and the supporting struts will block a significant part of the aperture, which will affect the radiation pattern considerably [131]. The scattered power from the obstacles will also increase the overall antenna noise [127, 131].

Cassegrain is preferred to Gregorian since for the same main reflector the distance between the main reflector and the sub-reflector is shorter. Between the off-axis (offset)

Table 5.2: Comparison between antenna schemes in Figure 5.1 according to the required specifications.

Antenna	Schematic	High X-pol discrimination	Low blockage	Low phase error	Easy access to the feed	FSO compatibility	Small size and low cost
Front-fed on-axis parabolic	Figure 5.1(a)	Yes	No	Yes	No	No	Yes
Front-fed Offset parabolic	Figure 5.1(b)	No	Yes	Yes	Yes	No	No
Front-fed offset spherical	Figure 5.1(c)	-	No	No	No	No	Yes
Gregorian on axis	Figure 5.1(d)	No	No	Yes	Yes	Yes	No
Cassegrain on-axis	Figure 5.1(e)	No	No	Yes	Yes	Yes	Yes
Cassegrain offset	Figure 5.1(f)	No	Yes	Yes	Yes	Yes	No
Dielectric cone	Figure 5.1(g)	No	No	Yes	Yes	Yes	No
Proposed Design	Figure 5.1(h)	No	No	Yes	Yes	Yes	Yes

and on-axis reflector antenna (see Figure 5.1(e) and Figure 5.1(f), respectively) fed by a linearly polarized primary feed, the on-axis version of Cassegrain, which offers an improved cross-polarization performance and is also relatively simpler to make [132], is selected in this work.

To improve the performance of the on-axis Cassegrain, it is possible to use the dielectric cone design scheme. However, to avoid the practical disadvantages of solid dielectric cone, the original Cassegrain antenna with a dielectric cone feed is modified and a dielectric tube is used instead for holding the sub-reflector. The new design, which is derived from an on-axis Cassegrain dielectric cone feed antenna, is presented in Figure 5.1(h). Therefore, in addition to the RF properties of the Cassegrain antenna configuration, there is an available shadow region (labelled by ‘A’ in the picture) in front of the sub-reflector, which is the best place for locating the optics. Therefore, among possible reflector antenna configurations, the proposed scheme is selected, which offers a number advantages including [127]:

1. Low noise property since the receiver can be closer to the feed
2. Higher X-pol discrimination compared to the version with struts
3. Three degrees of freedom (i.e., feed, main reflector and sub-reflector) compared to schemes with two
4. Using a hollow tube instead of a solid cone, which makes the design less complex and costly
5. A shadow region in front of the sub-reflector for locating the optical aperture

The summary of the all required specifications for the proposed design is presented in Table 5.3. In the rest of this chapter, we outline how to include the FSO part to the antenna with the specifications outlined in Table 5.3. In situations where the specifications are not met, appropriate solutions are proposed.

Table 5.3: Summary of all required RF antenna specifications.

Parameter	Value
Minimum antenna gain	30 dBi
Maximum half-power beam-width (HPBW)	5 Degrees
Minimum bandwidth	100 MHz
Carrier frequency	10 GHz
Maximum return loss	-10 dB
X-pol discrimination	20 dB
Side-lobe level	-20 dB

5.5 First Hybrid FSO/RF Antenna Design

This section is devoted to the first design of the antenna, which includes a single optical aperture (i.e., collimator) in the shadow region of the sub-reflector. In this section, the aim is to illustrate that implementing a single aperture is not sufficient and later on a detailed design procedure for the proposed scheme is presented in Section 5.6.1.

5.5.1 Design

Cassegrain antenna is composed of a double reflector (parabolic main reflector, and hyperbolic sub-reflector) and a feed, offering a number of interesting features including high total efficiency and easy accessibility to electronic equipment [127]. The aim is to design and build a compact antenna, where the ratio of focal length to the diameter of the available Cassegrain antenna is small 0.26. For such a small antenna, based on geometrical optics design procedure, the distance between the feed and the sub-reflector

will be small, which can degrade the return loss parameter of the antenna [133, 134].

In designing the hybrid antenna, the level of interference between RF and FSO parts must be kept to a minimum level to maintain the quality of the link performance. In the proposed design the available shadow region in front of the RF sub-reflector is used for locating the optical components to ensure a LOS path and a minimum FSO and RF interference (see Figure 5.5). Additionally, to avoid any wiring and blockage because of the OTx and ORx a novel solution is proposed in this work. An optical lens is located within the shadow region of the RF sub-reflector, see Figure 5.5, which is fed with a multimode plastic optical fibre (POF) that runs through the feed waveguide and exits from a small hole placed in the E-plane bend. The POF is used to guide the light from aperture to the optoelectronic circuits. One end of POF is located at the focal length of the lens, while the other end is connected to an OTx or an ORx (see Figure 5.5). For this application POF is the preferred option since more light could be launched and or collected and is less costly compared to the single-mode fibre. The measured total loss including the coupling losses from free space to fibre and fibre to free space and the fibre loss is about 2 dB.

5.5.2 *Simulations Results*

The CST STUDIO SUITE® 2012 software was used to validate the initial design. The initial design was parametrically analysed for improved gain and a radiation pattern using the software. For the parametric analysis, the distance between the feed and the apex of the sub-reflector was changed while other parameters were kept fixed. The dimensions and parameters of the simulated antenna are summarised in Table 5.4. In Section 5.6.1.1, the procedure of obtaining the parameters is described in details.

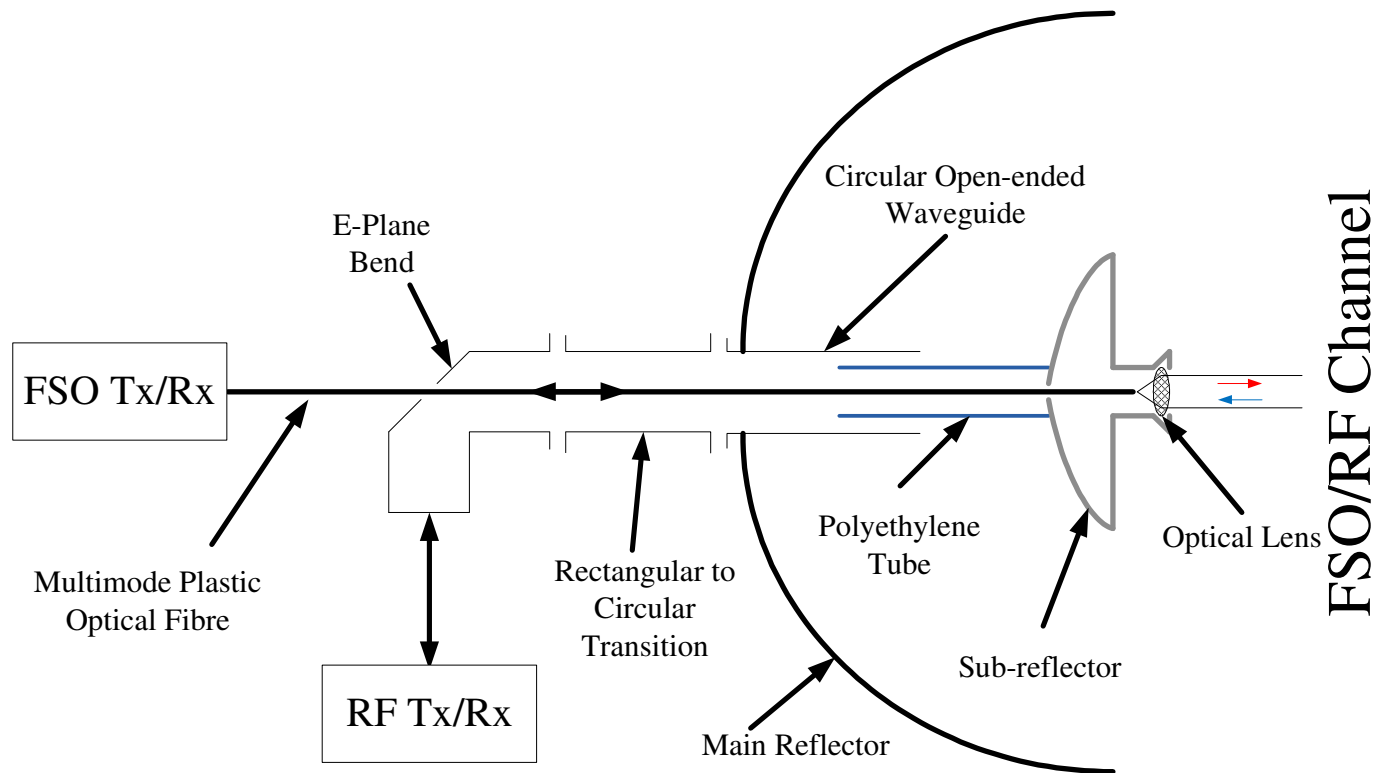


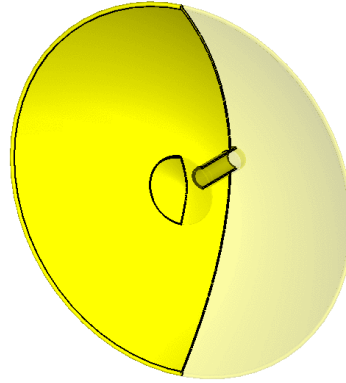
Figure 5.5: The hybrid antenna with single collimator schematic diagram.

Table 5.4: First hybrid antenna with single collimator prototype characteristics.

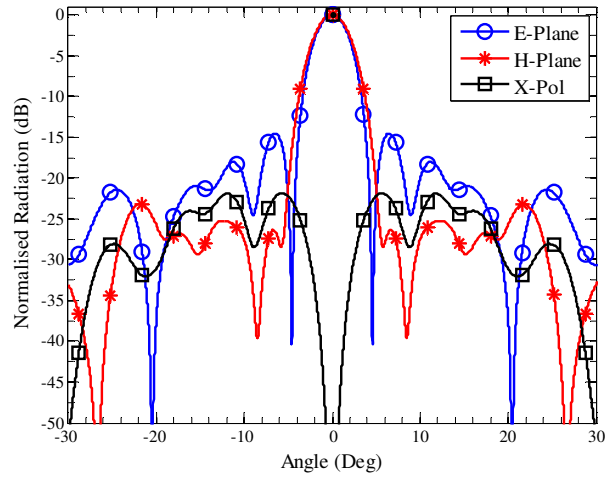
	Parameter	Value
RF Antenna	Central frequency	10 GHz
	Parabola diameter	475 mm
	Parabola focal length to diameter ratio (F/D)	0.26
	Hyperbolic diameter	85 mm
	Hyperbolic focal length	57.65 mm
	Antenna gain	27.52 dBi
	Antenna size (width×height×length)	460×460×470 mm
FSO Antenna	Wavelength	670 nm
	POF length	3.0 m
	POF core diameter	1.0 mm
	POF total diameter	2.2 mm
	Lens diameter	24 mm
	Lens focal length	41.4 mm
	Antenna size (width×height×length)	85×85×100 mm
FSO/RF Antenna	Antenna size (width×height×length)	460×460×680 mm

5.5.2.1 Initial Design with no Tube and Collimator

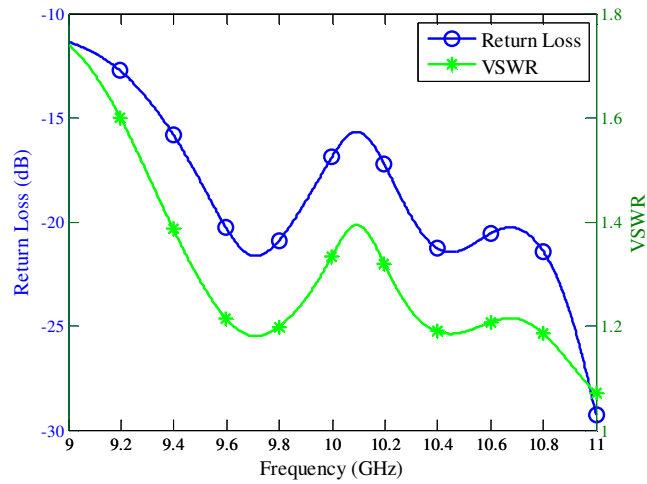
Using the parameters in Table 5.4, the antenna structure is modelled. The profile of the antenna is shown in Figure 5.6(a). For the initial design (i.e., before performing parametric analysis) the distance between the sub-reflector and the feed is determined to be 38.96 mm. The radiation patterns in E- and H-planes, X-pol radiation patterns in E- and H-planes, return loss, bandwidth, side-lobe level, HPBW, and first-null beam-width (FNBW) of the antenna are obtained. The E- plane in this design refers to the vertical direction whereas the H-plane denoted the horizontal one. Figure 5.6(b-d) illustrates the simulated results. Note that the radiation pattern is only presented over the range of -30 to 30 degrees since the main lobe and the first side-lobe are within this range. In addition to the return loss, the voltage standing wave ratio (VSWR) is also included in the results. A VSWR of < 1.92 is equivalent to a return loss of < -10 dB. The summary of the antenna characteristics is also presented in Table 5.5.



(a)



(b)



(c)

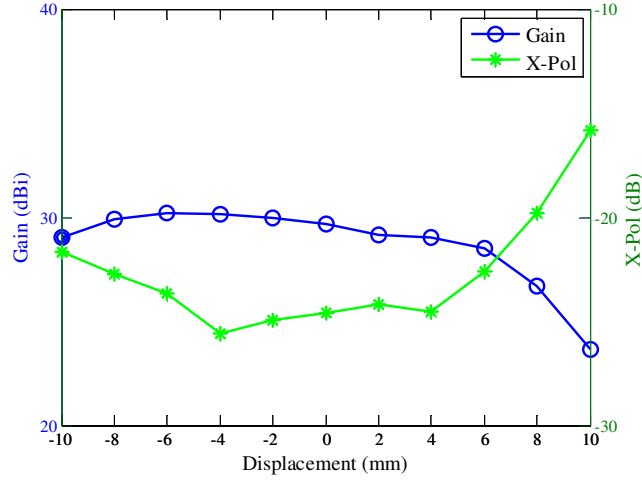
Figure 5.6: Simulation results for initial antenna design scheme with no optical part and tube: (a) antenna profile (the distance between the feed and sub-reflector is 38.96 mm), (b) E-, H-planes, and X-pol radiation normalised to the antenna gain of 28.8 dBi, and (c) return loss and voltage standing wave ration (VSWR) against frequency.

5.5.2.2 Parametric Analysis with no Tube and Collimator

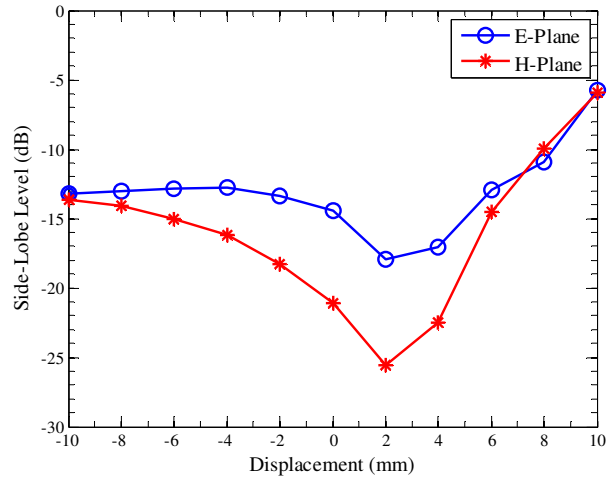
The initial design did not meet the required gain, and E-plane side-lobe level. This was expected and as it was discussed the sub-reflector blockage and small size of the antenna degrades the performance. Therefore, a parametric analysis is performed to study the effect of sub-reflector to feed distance on the performance of antenna while keeping the other parameters fixed. The results are illustrated in Figure 5.7, where the gain, X-pol discrimination, side-lobe level and HPBW are presented against the sub-reflector displacement. The displacement of 2 mm is selected as the optimum value at this stage and the antenna is simulated with the new sub-reflector to feed distance of 40.96 mm. Although the E-plane side-lobe level is still higher than the target level of 20 dB, the other parameters have significantly improved. The characteristics summary of optimised antenna are presented in Table 5.5, while the simulation results are depicted in Figure 5.8. As expected, the improved parameters are due to degradation of HPBW and FNBW. The optimised parameters are used for the remaining simulations and experimental investigation.

5.5.2.3 Optimised Design with Tube and no Collimator

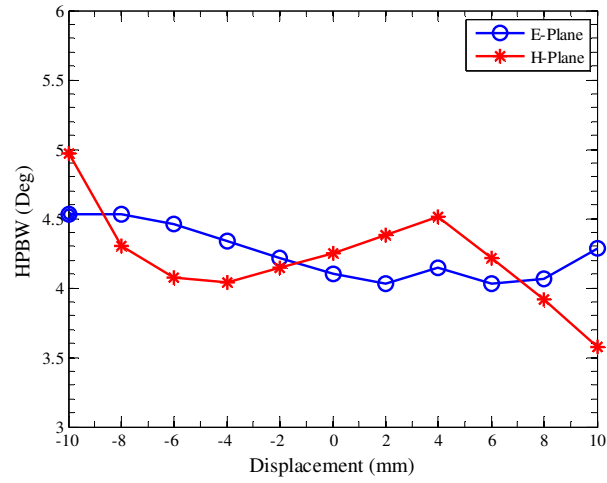
Next, the tube is added to the antenna structure to make it possible to practically implement the antenna with no strut. Details of the tube size and its material are given in Appendix C. The antenna profile and the simulation results are presented in Figure 5.9. Adding the tube has slightly changed the gain. However, side-lobe level in both E- and H-planes are effected and the E-plane side-lobe level is not acceptable. One technique to enhance this feature is investigated in [129], where the profile of the sub-reflector is altered in order to achieve the desired antenna radiation pattern. Investigation and implementing of this technique is out of the scope of this research work and interested readers are referred to the aforementioned reference.



(a)



(b)



(c)

Figure 5.7: Parametric analysis on the initial design with no optical part and tube: (a) gain and X-pol discrimination, (b) side-lobe level in E- and H-planes, and (c) half-power beam-width (HPBW) in E- and H-planes. Negative displacement denotes moving the sub-reflector towards the feed. At displacement of 0 mm, the distance between the feed and sub-reflector is 38.96 mm.

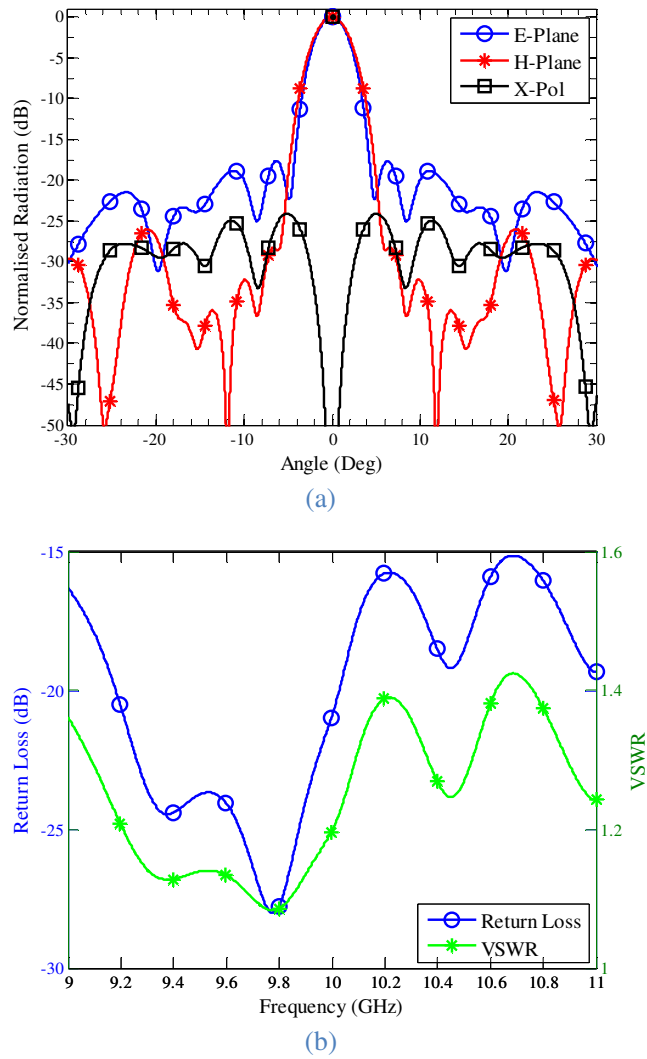


Figure 5.8: Simulation results for the optimised antenna design scheme with no optical part and tube (the distance between the feed and sub-reflector is 40.96 mm): (a) E-, H-planes, and X-pol radiation normalised to the antenna gain of 29.1 dBi, and (b) return loss and voltage standing wave ration (VSWR) against frequency.

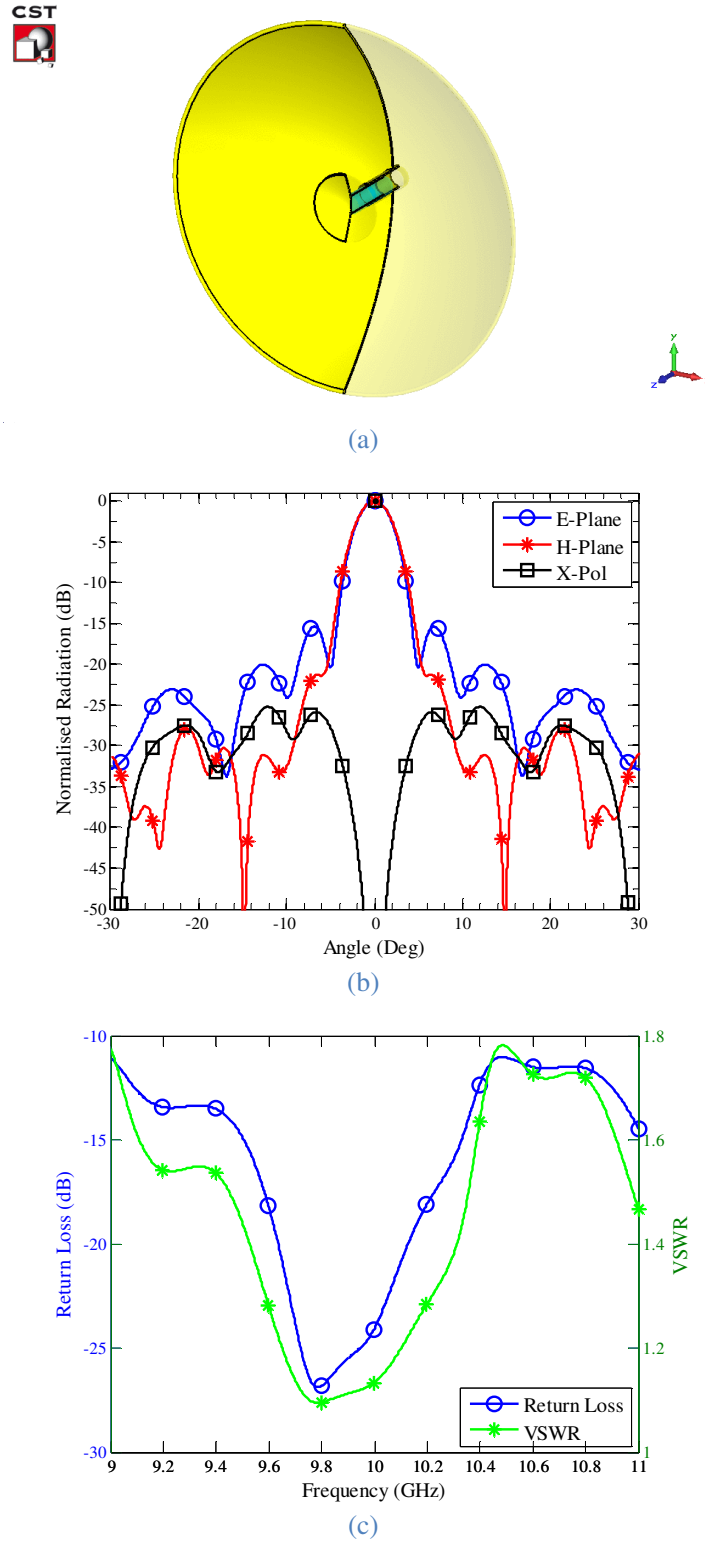


Figure 5.9: Simulation results for initial antenna design scheme with tube and no optical part: (a) antenna profile (the distance between the feed and sub-reflector is 40.96 mm), (b) E-, H-planes, and X-pol radiation normalised to the antenna gain of 30.0 dBi, and (c) return loss and voltage standing wave ration (VSWR) against frequency.

5.5.2.4 Optimised Design with Strut and no Collimator

Before moving to the next step, a comparison between a structure with strut and the proposed scheme is carried out and the results are summarised in Table 5.5. For this simulation a struts with width of 4 mm and a thickness of 1 mm were used. As expected the X-pol performance of the antenna is degraded. Obviously a wider strut will worsen the antenna performance. Therefore, the proposed antenna scheme is preferred to the one with the struts. The antenna profile and simulation results are presented in Figure 5.10.

5.5.2.5 Optimised Design with Tube and Collimator

The final step is to add the single collimator plus the optical fibre to the design. The details on the collimator and fibre are available in Appendix C. The simulation results are presented in Figure 5.11, while the detailed parameters are available in Table 5.5. In contrary to the antenna version with a tube, in the one with a collimator the fibre and tube offer an improved E-plane side-lobe level performance. However, this improvement is due to the decrease in the total bandwidth, FNBW in E-plane, HPBW and also antenna gain. The existence of a collimator in front of the antenna also causes scattering and hence worsening X-pol performance with the X-pol discrimination reduced by ~ 2 dB.

The existence of optical aperture results in electromagnetic power perturbation. Investigating the power distribution makes it possible to better understand the effect of optical aperture. Therefore using CST STUDIO SUITE® software the near field power distribution of the antenna in both E- and H-planes were obtained as in Figure 5.12. One can see from Figure 5.12(a, b) that in the shadow region the power can be as low as ~ 40 dB relative to the maximum power. Although the sub-reflector provides a shadow region, the power distribution in Figure 5.12(a, b) shows the existence of some leaked power in front of the sub-reflector.

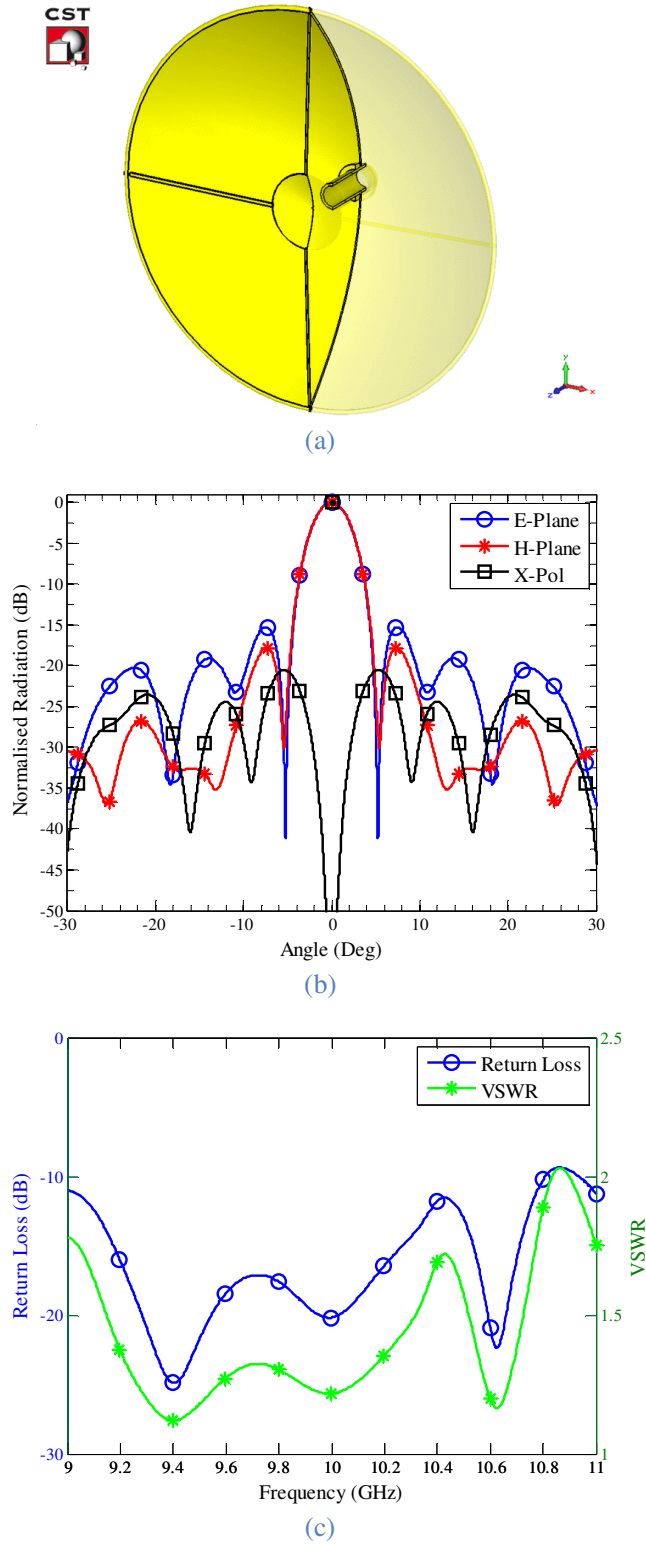


Figure 5.10: Simulation results for initial antenna design scheme with struts and no optical part: (a) antenna profile (the distance between the feed and sub-reflector is 40.96 mm), (b) E-, H-planes, and X-pol radiation normalised to the antenna gain of 29.1 dBi, and (c) return loss and voltage standing wave ration (VSWR) against frequency.

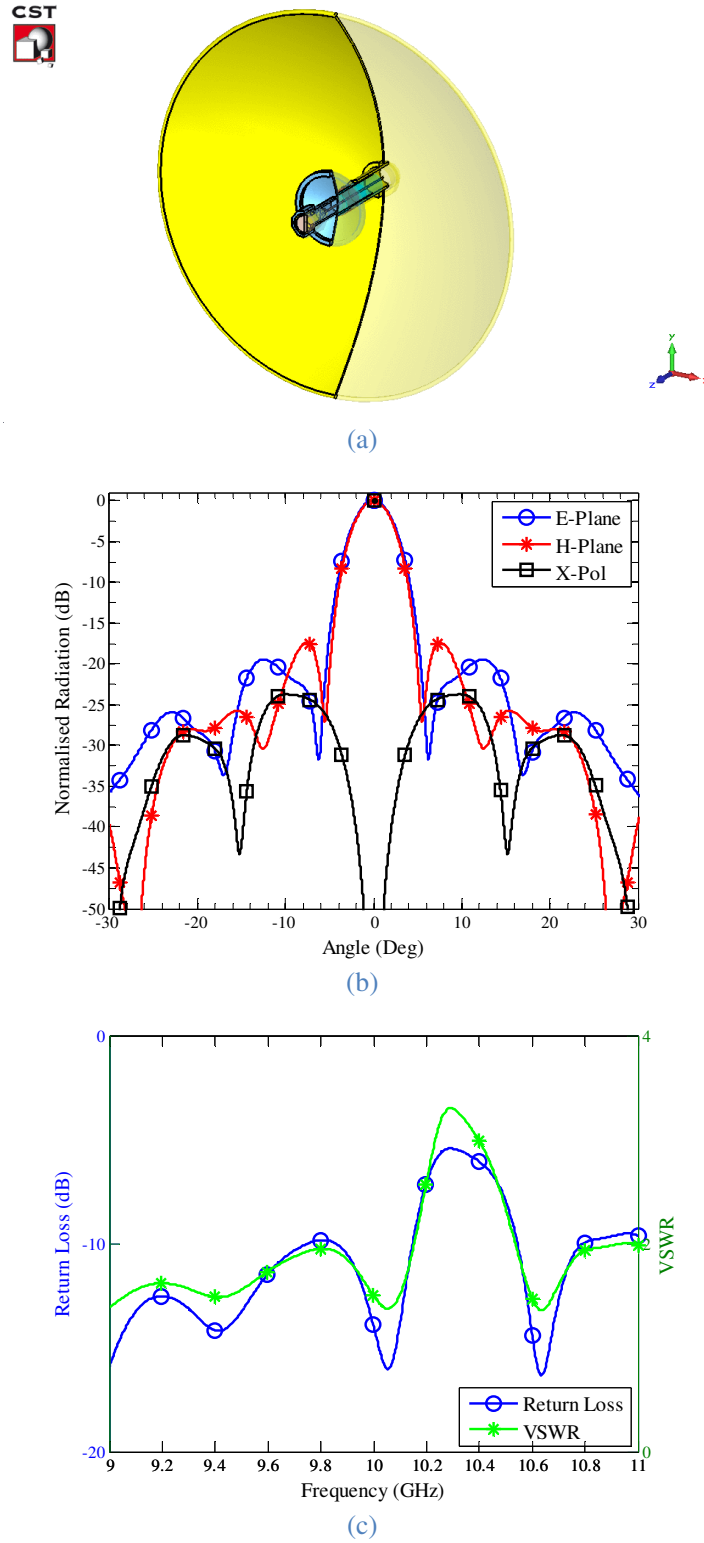
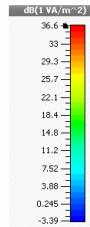
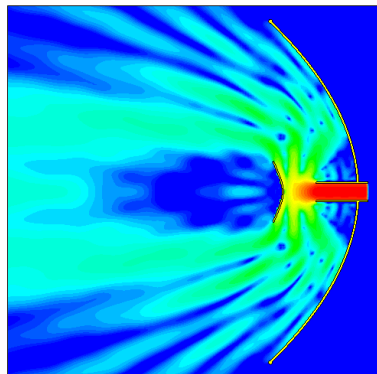


Figure 5.11: Simulation results for initial antenna design with single collimator design scheme including tube: (a) antenna profile (the distance between the feed and sub-reflector is 40.96 mm), (b) E-, H-planes, and X-pol radiation normalised to the antenna gain of 29.7 dBi, and (c) return loss and voltage standing wave ratio (VSWR) against frequency.



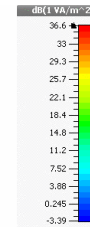
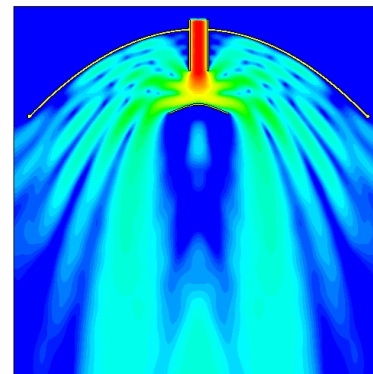
power (f=10) [1] (peak)
Cutplane normal: 1, 0, 0
Cutplane position: 0
Component: Abs
2D Maximum: 4517
2D Minimum: 0
Frequency: 10



(a)



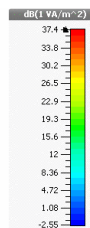
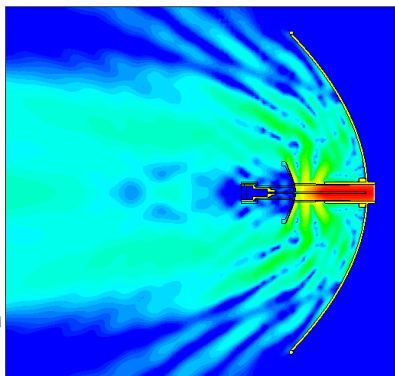
power (f=10) [1] (peak)
Cutplane normal: 0, 1, 0
Cutplane position: 0
Component: Abs
2D Maximum: 4517
2D Minimum: 0
Frequency: 10



(b)



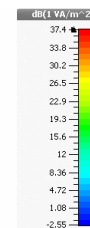
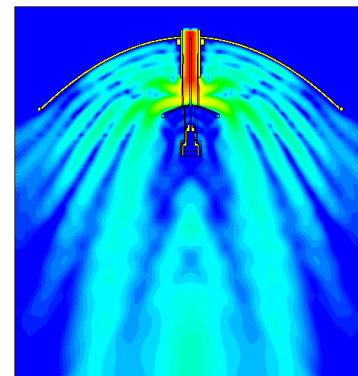
power (f=10) [1] (peak)
Cutplane normal: 1, 0, 0
Cutplane position: 0
Component: Abs
2D Maximum: 5481
2D Minimum: 0
Frequency: 10



(c)



power (f=10) [1] (peak)
Cutplane normal: 0, 1, 0
Cutplane position: -8.612e-11
Component: Abs
2D Maximum: 4607
2D Minimum: 0
Frequency: 10



(d)

Figure 5.12: Near field power distribution of the antenna with and without collimator for single aperture in E- and H-planes: (a) without collimator in E-plane, (b) without collimator in H-plane, (c) with collimator in E-plane, and (d) with collimator in H-plane. The distance between the feed and sub-reflector is 40.96 mm.

The leaked power is due to spillover and diffraction from the sub-reflector edge. Therefore, it is expected that including any conductor in the shadow region would change the local power distribution in the near field, see Figure 5.12(c, d). However, since the far-field region rather than near-field is the significant feature, therefore, the resultant effects in the far-field are important to address.

5.5.3 Hybrid Antenna Fabrication

Based on the available resources and the optimised design, the proposed antenna was fabricated. More details on the fabrication and antenna components are available in Appendix C. Figure 5.13 shows the picture of the assembled prototype.

5.5.4 Hybrid RF Antenna Characteristics

The return loss, radiation pattern, gain, bandwidth, side-lobe level, HPBW and FNBW of the fabricated antennas with a tube and with a tube plus a collimator were measured. The details on the return loss and radiation pattern measurements are presented in the

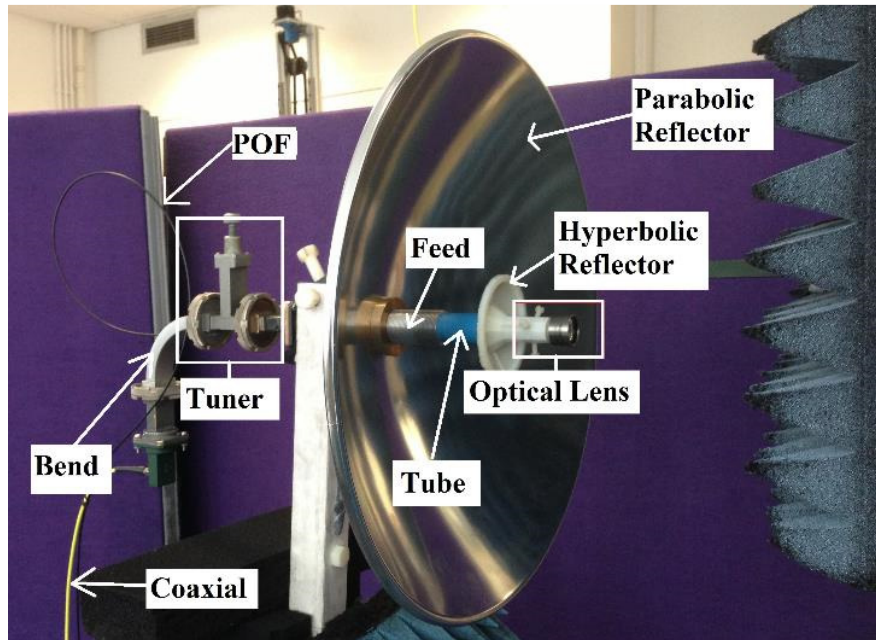


Figure 5.13: The hybrid antenna with single collimator under the pattern measurement test. The distance between the feed and sub-reflector is 40.96 mm.

Appendix D. The comparison of simulation and measurement results of the antenna with a tube are presented in Table 5.5. The difference between the measurements is due to the antenna fabrication inaccuracy and mismatch in the feed line. Although the bandwidth achieved is more than 100 MHz, the measured result is not as good as the simulation, see Figure 5.14.

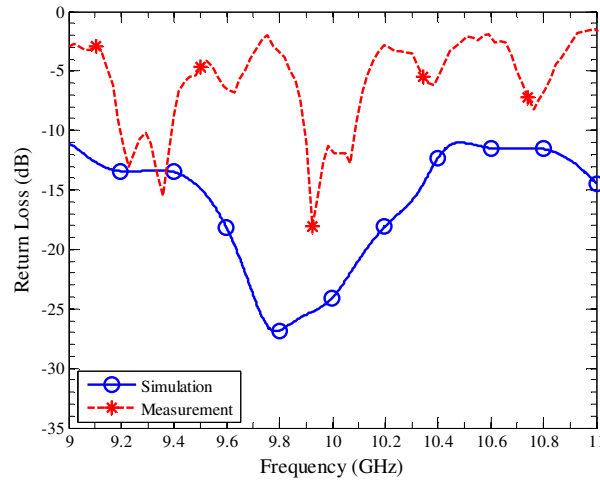
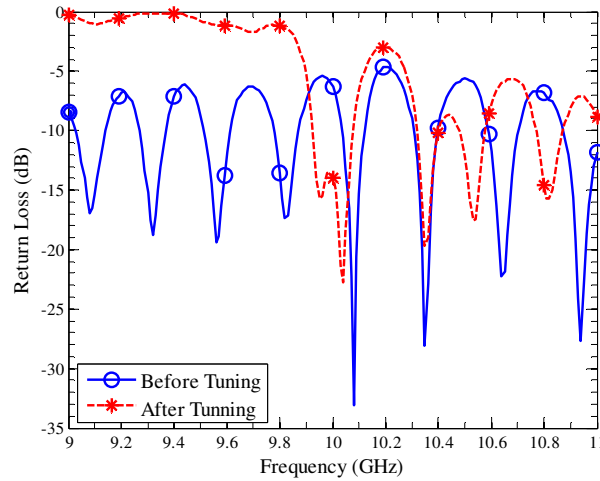


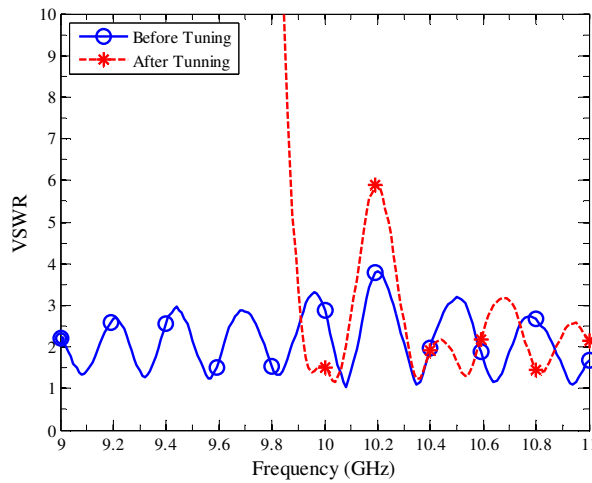
Figure 5.14: The return loss simulation and measurement results of the antenna with tube and no collimator.

The return loss and the equivalent VSWR of the hybrid antenna with a tube and a collimator is depicted in Figure 5.15. The mismatch in the result can be due to the rectangular to circular transition, the E-plane bend and the waveguide to coaxial adaptor that were used in the experimental setup. To overcome the mismatch a waveguide tuner was used to achieve the required bandwidth of 160 MHz. The radiation patterns of the antenna in H- and E-planes were measured using a near field chamber as depicted in Figure 5.16. The details of the measurement are summarised in Table 5.5. The non-symmetrical radiation pattern is due to the design and fabrication inaccuracy and misalignment. The measured gain of the antenna is 27.52 dBi, which is 2.28 dB less than the simulated result. Observing Figure 5.7(a), it is deduced that the gain is dependent on the feed to sub-reflector distance, in particular for more than 2 mm of displacement.

Note that, in the simulations factors such as rectangular to circular transition, E-plane bend and waveguide to coax adaptor were not considered. Therefore, any mismatch due to these factors will result in lower antenna efficiency. The comparison between the simulated and measured data show that with tuning the antenna radiation, in particular the main lobe, is similar to the expected result. The H-plane radiation also shows the same trend for the first side-lobe.

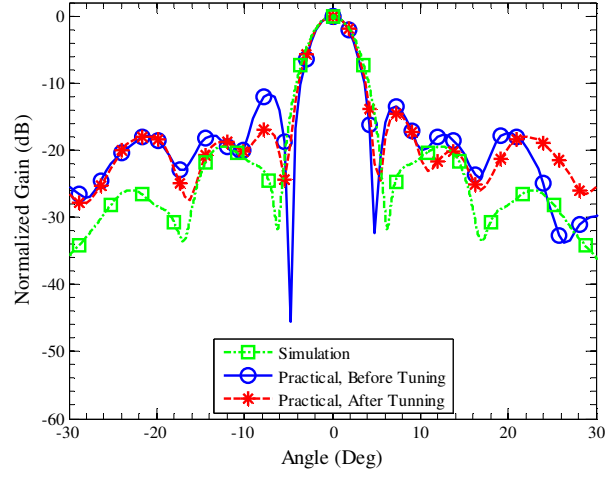


(a)

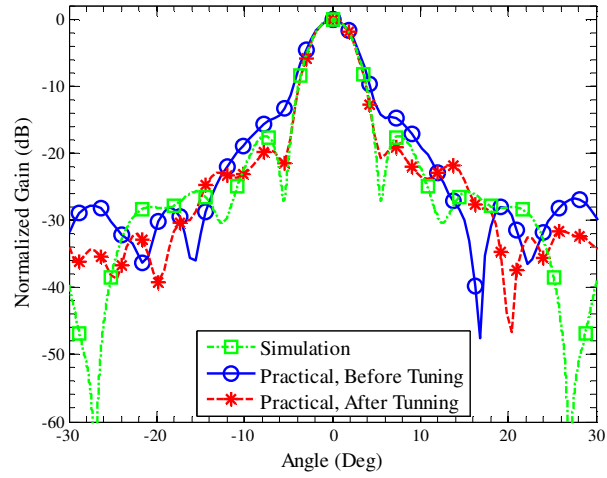


(b)

Figure 5.15: (a) Measured return loss of the antenna with single collimator before and after tuning, and (b) equivalent voltage standing wave ratio (VSWR) from the measurement before and after tuning.



(a)



(b)

Figure 5.16: Radiation pattern of hybrid antenna with single collimator measured in a near field chamber as well as the simulated one for: (a) E-plane, and (b) H-plane.

Table 5.5: The antenna (design with single collimator) characteristics obtained from simulation and measurement. X-pol disc, SLL, HPBW, and FNBW are X-pol discrimination, side-lobe level, half-power beam-width, and first null beam-width, respectively.

Design step ^a	Gain (dBi)	X-pol disc (dB)	E-plane			H-plane			Bandwidth (MHz)
			SLL (dB) ^b	HPBW (Deg)	FNBW (Deg)	SLL (dB) ^b	HPBW (Deg)	FNBW (Deg)	
Target	30	20	< -20	< 5	-	< -20	< 5	-	100
Simulation, initial	28.8	21.9	-14.5	4	9.2	-26.4	4.3	11.5	> 100
Simulation, optimised	29.1	24.1	-17.7	4	9.7	-28.3	4.4	12.1	> 100
Simulation, tube added	30.0	25.2	-15.4	4.2	9.9	-21.3	4.4	11.8	> 100
Simulation, strut	29.1	20.5	-15.3	4.5	10.5	-17.8	4.4	10.8	> 100
Measurement, tube added	27.9	-	[-18.5, -17.5]	4.85	13.7	[-25.3, -24.5]	4.7	12.65	> 100
Simulation, collimator added	29.7	23.8	-19.5	4.7	12.5	-17.4	4.5	11.0	> 100
Measurement, before tuning	26.8	-	[-11.6, -13.5]	4.4	9.6	[-15.2 -14.8]	4.8	10.8	<< 100
Measurement, after tuning	27.5	-	[-17.0, -14.6]	5	10.8	[-19.9, -19.8]	4.6	10.8	160

^a “Target” is based on the desired characteristics in Table 5.3. “Simulation, initial” is simulation of the antenna with no tube and collimator based on the first design. “Simulation, optimised” is the simulation of the optimised antenna with no tube and collimator. “Simulation, tube added” is the simulation of the antenna with tube based on the optimised antenna. “Simulation, strut” is the simulation of the antenna with strut based on the optimised antenna. “Measurement, tube added” is the measurement of the fabricated antenna with tube based on the optimised antenna. “Simulation, collimator added” is the simulation of the antenna with tube and collimator based on the optimised antenna. “Measurement, before tuning” is the measurement of the fabricated antenna with tube and collimator based on the optimised antenna before tuning. “Measurement, after tuning” is the measurement of the fabricated antenna with tube and collimator based on the optimised antenna after tuning.

^b The first number is side-lobe level for negative angles, whereas the second one refers to the positive angles.

5.5.5 Hybrid FSO/RF Simplex Link

The schematic block diagram of the experimental set up is shown in Figure 5.17(a). The RF signal generator is connected to a Tx module, which up-convert the signal from 2.45 GHz to 10.0 GHz and then amplifies the signal. The Tx module output is fed to the antenna. At the Rx, the received signal is fed to an RF Rx module, which down-converts the RF signal from 10.0 GHz to 2.45 GHz. Following amplification and filtering the recovered signal is observed using a spectrum analyser. The optical signal, which is generated using an arbitrary signal generator, is used to intensity-modulate the laser, the output of which is launched into the POF. The output of the POF is passed through a lens prior to transmission over the free space channel. At the Rx the incoming light is coupled into a POF via a lens the output of which is feed to an optical receiver. The optical receiver is composed of a PD and an amplifier with a controllable gain. The far-field distance of the RF antenna is 12.91 m. In order to measure the SNR and the Q-factor for both RF and FSO links, a simplex link with two prototype antennas positioned at 15 m apart was set up as shown in Figure 5.17(b). Details of the experimental setup are shown in Appendix C, while the measurement techniques are explained in Appendix D.

Table 5.6 summarizes the far-field link characteristics. According to [135] a collimated Gaussian laser beam emerging from a Tx aperture with a diameter of 24 mm over a link distance of 2 km will result in a 75 mm foot print diameter. Thus, a Rx with an aperture of 24 mm should be able to capture almost 20% of the received laser power. Obviously using a larger optical lens will improve the Rx total efficiency. In this work a divergent laser beam is implemented to ease the alignment. From Table 5.6 one can see that due to a high field of view (divergence angle) of optical apertures, the ORx with a high gain and a low bandwidth was chosen.

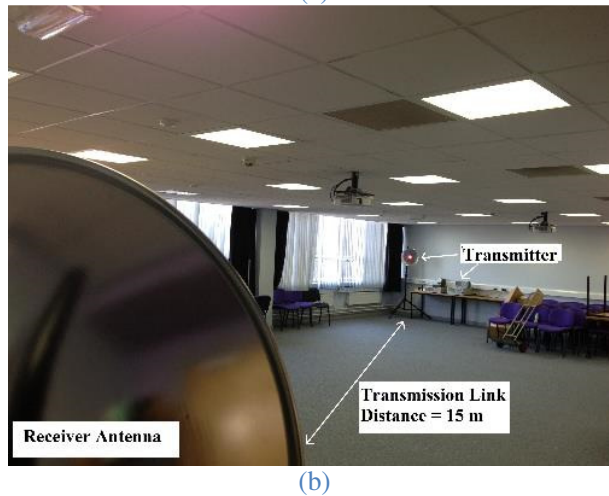
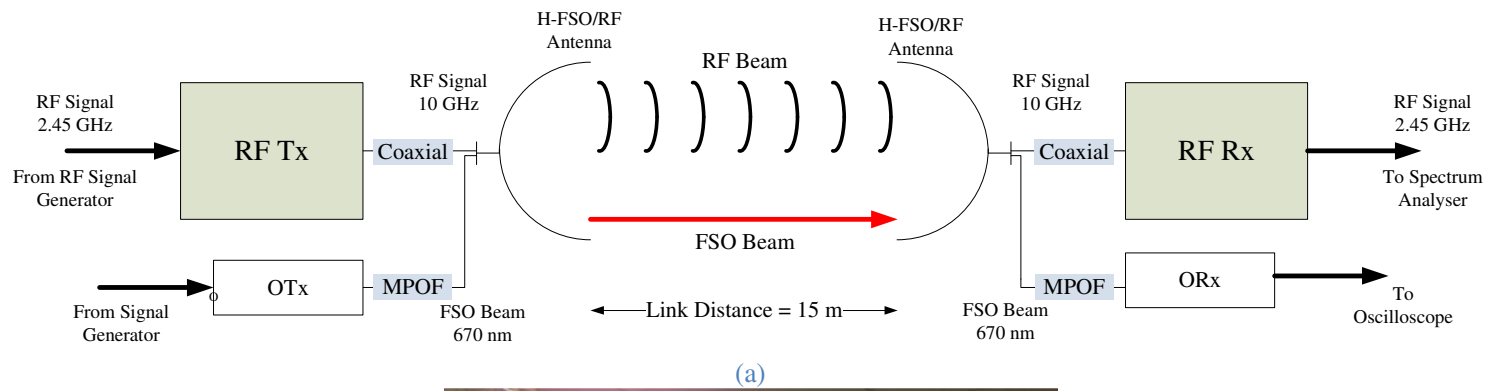


Figure 5.17: (a) hybrid link with single collimator antenna experimental block diagram, and (b) hybrid antenna far-field link setup. OTx, MPOF, and ORx refer to optical transmitter, multimode plastic optical fibre, and optical receiver, respectively.

Table 5.6: The hybrid FSO/RF link characteristics. The antenna with single collimator is implemented in the link.

Link Parameter		Value
RF	Carrier frequency	10 GHz
	Modulation scheme	BPSK
	Data rate	6.7 Mbps
	Antenna input power	-8 dBm
	Channel loss	75.96 dB
	Receiver bandwidth	10 MHz
	Receive noise floor	-86.78 dBm
FSO	Operating wavelength	670 nm
	Modulation scheme	OOK-NRZ
	Bandwidth	50 MHz
	Antenna input power	+3 dBm
	Aperture field of view	45.63 mRad
	Received power at aperture	-27.19 dBm
	Receiver responsivity	0.4 A/W
	Receiver gain	150 kV/A
	Receiver bandwidth	700 kHz
	Receiver noise floor	-59.51 dBm
	POF diameter	1 mm
	POF length	2 m
	POF type	Step-Index
	POF material	PMMA
Measured Parameters	RF SNR	45.68 dB
	FSO Q-factor	15.69

The obtained SNR and the Q-factor are 45.68 dB and 15.69, respectively (see Table 5.6). The method outlined in [118] is adopted to measure the Q-factor whereas the SNR is based on the difference between the average of the RF noise floor and the signal level measured using the spectrum analyser. These parameters show that by using the proposed antenna the hybrid FSO/RF can provide an error free transmission ($\text{BER} < 10^{-6}$, which is much lower than the FEC limit of 10^{-3}) in a clear channel.

5.5.6 Required Modifications

The comparison between the simulation and prototype gain shows an acceptable agreement. However due to the small size of the antenna and a short distance between the feed and sub-reflector, the return loss measurement performance was not applicable. This problem was solved by adding a waveguide tuner before the antenna feed. The radiation patterns of the antenna before and after tuning show that the main lobe characteristics of the prototype were in a good agreement with that of simulation. To evaluate the antenna performance in a communication link, a simplex link with a distance of 15 m was used and it was shown that the antenna is capable of providing an error free ($\text{BER} < 10^{-6}$) transmission.

In addition to these results, by means of experimental investigation the following important design guidelines were also deduced:

1. Using POF for transmission is not practical. Since several modes are propagating within the fibre, then the optical signal coupled into free space will propagate in the form of various modes, with each mode having its own characteristics and beam waist [57]. Note that for the present setup there are almost 2.75 million possible propagation modes inside the fibre. Since the collimators are designed for a single beam waist, therefore only the fundamental mode is collimated properly and the other modes will be divergent. Therefore, it is wise to use a single mode fibre (SMF) at the Tx.
2. Employing only a single small aperture at the Rx does not provide enough gain [93]. Therefore, in the modified design multiple Rx apertures should be used.
3. In addition to using several Rx apertures, the spatial diversity technique should be used to improve the performance of the system, especially under turbulence

condition [7].

4. Since the antenna is intended for the last mile access network outdoor applications, appropriate methods should be used to combat the effect of ambient light [35].
5. Since the optical aperture is mounted on Cassegrain antenna, the movement of Cassegrain antenna on the mast will introduce pointing errors to the FSO system [136], which needs addressing.

Considering the above points, the next section outlines the modified design.

5.6 Final Hybrid FSO/RF Antenna Design

5.6.1 RF Antenna

The schematic diagram of the proposed antenna design is illustrated in Figure 5.18. As mentioned before, the basic concept in this design is to utilize the available shadow region of the sub-reflector for locating the optical elements. This will ensure no blockage because of the OTx and ORx. In order to reduce the interference between FSO and RF signals, the electrical components of the FSO link are not directly placed within the shadow region. Instead, they are located at a distance from the antenna and the light signals are launched and captured using a combination of optical lenses (i.e., transceiver apertures) and optical fibres. In the following subsections, the function and characterization of each part individually will be discussed.

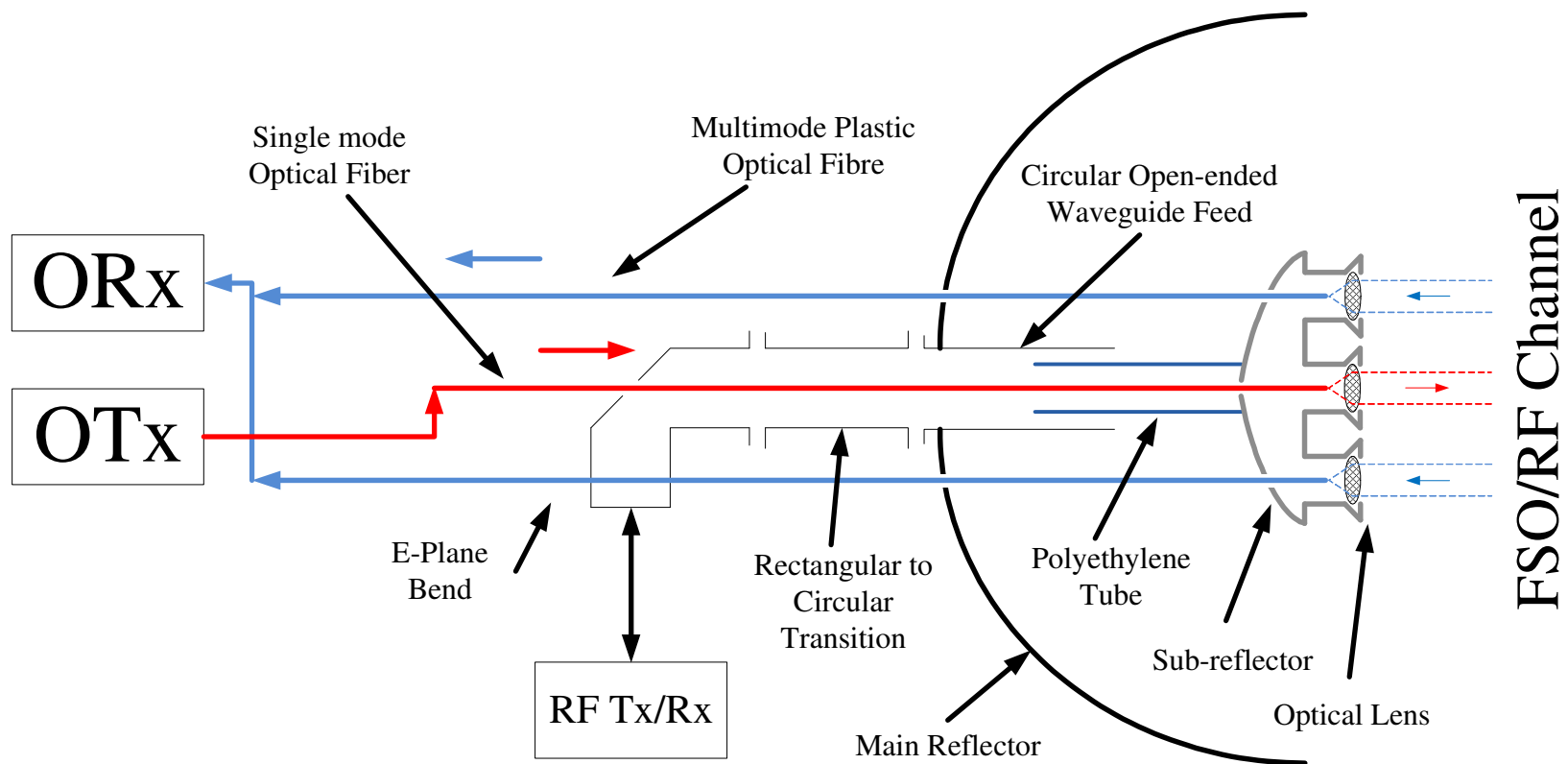


Figure 5.18: Schematic diagram of the proposed hybrid antenna with multiple collimators.

5.6.1.1 Cassegrain Antenna

In [127] a straight-forward design procedure for Cassegrain antennas based on the combination of a parabolic main-reflector and a hyperbolic sub-reflector was given. Considering the schematic diagram depicted in Figure 5.19, the goal is to find out the optimum values for the sub-reflector diameter d_{sr} in order to minimize its blockage effects.

Assuming that the main-reflector diameter D_{mr} and its focal length F_{mr} are known, for minimum blockage, the optimum sub-reflector diameter d_{optm} is given as [127]:

$$d_{\text{optm}} = \sqrt{\frac{2}{k_{\text{B}}} \lambda_{\text{RF}} F_{\text{mr}}}, \quad (5.2)$$

where the feed beam-width constant $k_B = 2$ for an average feed with a 10 dB taper and λ_{RF} is the RF carrier wavelength. If $d_{\text{optm}}/D_{\text{mr}} > 0.2$ then $d_{\text{sr}} = d_{\text{optm}}$, otherwise $d_{\text{sr}} = 0.1D_{\text{mr}}$ [127]. For the available main reflector with given parameters in Table C.3, the sub-reflector diameter is calculated to be ~ 99 mm. However, due to experimental limitations, the sub-reflector diameter of 85 mm will be used in the final prototype.

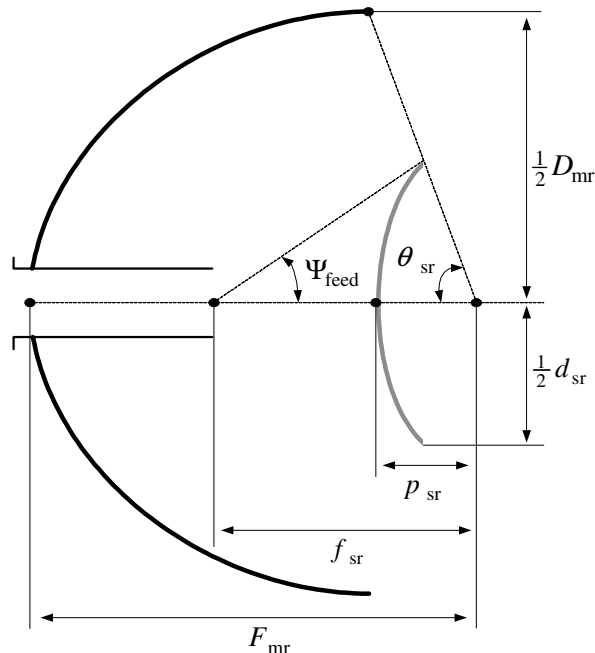


Figure 5.19: Schematic diagram of a Cassegrain antenna.

For a given feed HPBW of $2\Psi_{\text{RF}}$, see Figure 5.19, from the geometry the hyperbolic focal length f_{sr} is given by [127]:

$$f_{\text{sr}} = \frac{F_{\text{mr}} D_{\text{mr}} d_{\text{sr}}}{16} [8F_{\text{mr}} D_{\text{mr}} \cot \Psi_{\text{feed}} + 16F_{\text{mr}}^2 - D_{\text{mr}}^2]. \quad (5.3)$$

And the hyperbolic eccentricity e the distance between the apex and the focal point of the hyperbolic trajectory p_{sr} can be readily determined as [127]:

$$e = \left(D_{\text{mr}} \cot \frac{\Psi_{\text{feed}}}{2} + 4F_{\text{mr}} \right) / \left(D_{\text{mr}} \cot \frac{\Psi_{\text{feed}}}{2} - 4F_{\text{mr}} \right), \quad (5.4.a)$$

$$p_{\text{sr}} = f_{\text{sr}} / \left(D_{\text{mr}} \cot \frac{\Psi_{\text{feed}}}{2} + 4F_{\text{mr}} \right). \quad (5.4.b)$$

These equations are based on geometrical optics and they are applicable if the resultant sub-reflector or the main reflector are electrically large (i.e., $d_{\text{sr}} \geq 10\lambda_{\text{RF}}$ or $D_{\text{mr}} \geq 100\lambda_{\text{RF}}$). Note that for smaller antennas losses due to spillover and blockage will be significant [127]. Diffraction phenomena in small Cassegrain antennas leads to a lower return loss and degradation of the overall radiation pattern [133]. Therefore additional methods like the diffraction methods in [129] are required to modify the design based on Eqs. (5.3) and (5.4). In this thesis, the optimization of the RF antenna is carried out using CST STUDIO SUITE® in order to achieve the maximum gain and the desirable good side-lobe levels.

The gain of Cassegrain antenna is given by [129]:

$$G_{\text{CA}} = \left(\frac{\pi D_{\text{mr}}}{\lambda_{\text{RF}}} \right)^2 \eta_{\text{CA}}, \quad (5.5)$$

where η_{CA} is the total efficiency of Cassegrain antenna for the combination of blockage and spillover losses, illumination, cross-polarization, feed, VSWR, and reflector tolerance (roughness of reflector) efficiencies [69]. These efficiencies are well studied and a number of techniques have been proposed for their improvement [69, 129, 133]. For a typical Cassegrain antennas η_{CA} is in the order of 55% to 85% [129]. Since the Cassegrain

antenna structure are being modified, there will be other efficiency coefficients, which will be the focus of the rest of this chapter.

5.6.1.2 Sub-reflector Shadow Region

Locating the optical aperture in the shadow region of sub-reflector minimizes the deviation in Cassegrain antenna characteristics with an optical aperture from Cassegrain antenna without any optical components. From geometrical optics it is easy to find out a rough estimation for the shadow region. Various scenarios can be used to outline the boundary of the shadow region. The first one is based on pure geometrical optics, which leads to a region that half of it is distinguished by vertical-hatched area in Figure 5.20. In this scenario it is assumed that wave emerging from Cassegrain antenna is traveling along the line-of-sight path and the effect of edges are ignored. This is the least accurate approximation. Due to diffraction phenomena, the propagating wave also exists in front of the sub-reflector. The analysis of diffraction from an edge is given in [137]. In this thesis another approximation is used, which has no complexity of diffraction theory but is still more accurate than the simple geometrical optics approximation. The horizontal-hatched region in Figure 5.20 shows half of this approximation. In the design procedure

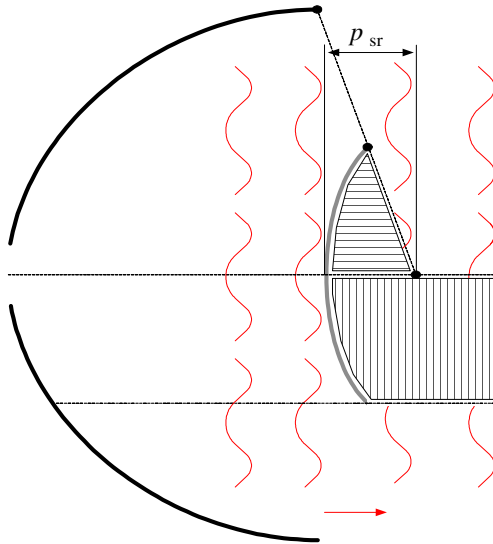


Figure 5.20: Diagram of different shadow region approximations in front of sub-reflector. Two approximations are shown in this figure. The simplest one is outlined with vertical-hatched line, while the more accurate one is shown with horizontal-hatched line. The former is used in this project.

it is aimed to place optical aperture in this region. Note that due to lack of space one can break this rule particularly in case of small Cassegrain antennas. By performing a full wave simulation of Cassegrain antenna with and without an optical aperture one can check the impact of added components.

5.6.1.3 The Sub-Reflector with Optical Fibre

As shown in Figure 5.18, the optical fibre cables are passed through the sub-reflector as well as the main reflector. For simplicity a number of assumption are made; (i) holes (with the diameter of $d_{\text{sr_hole}}$) are located at the apex of the sub-reflector; (ii) the field at the sub-reflector surface is a far-field plane wave; and (iii) the sub-reflector surface is flat and the effect of edge is ignored. As seen from Figure 5.21, a fraction of the incident wave P_1 is leaked through the hole P_3 while the rest is reflected back P_2 . The ideal efficiency of the sub-reflector with a hole is $\eta_{\text{hole}} = P_2/P_1 = 1$, however since $P_3 \neq 0$, that is not the case. For the incident wave with the electrical field amplitude E_0 the total incident power at the sub-reflector P_1 is given by:

$$P_1 = \frac{|E_0|^2}{2Z_0} \pi \left(\frac{D_{\text{mr}}}{2} \right)^2, \quad (5.6)$$

where $Z_0 \approx 376.7 \, \Omega$ is the impedance of free space.

Note that in real scenarios $d_{\text{sr_hole}}$ is a fraction of λ_{RF} , therefore waves cannot propagate through the holes (i.e., if the hole is considered to be as the open end of a circular waveguide, the frequency of the RF signal must be greater than the TE_{11} cut-off frequency of the equivalent circular waveguide). However, the energy can leak through the hole as an evanescence wave. In the case, the thickness of the sub-reflector conductor is slightly greater than skin-depth δ [138] (for an aluminium conductor a thickness of 40 μm was

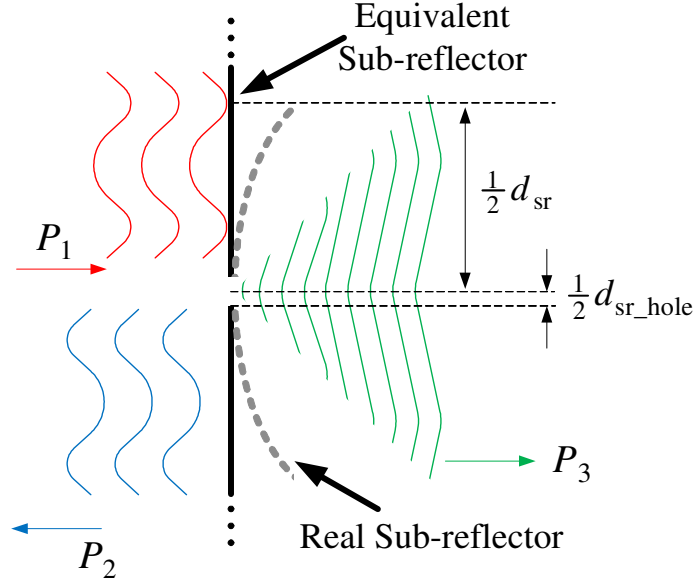


Figure 5.21: Diagram of the power leakage due to the fibre hole in the sub-reflector. P_1 , P_2 , and P_3 are RF power emerging from the feed, RF power reflected back towards the feed, and RF power leaked to the front of the sub-reflector.

used, which is almost 50 times greater than δ). Therefore, based on the evanescence wave propagation, the amplitude of the leaked signal is $E_0 \exp(-40 \times 10^{-6} \times 2\pi / 3 \times 10^{-2}) \approx E_0$. Thus the leaked energy though the hole is given by:

$$P_3 = \frac{|E_0|^2}{2Z_0} \pi \left(\frac{d_{\text{sr_hole}}}{2} \right)^2. \quad (5.7)$$

The imposed loss due to the radiation from the hole, introduces the fibre hole efficiency coefficient $\eta_{\text{hole}} = P_2/P_1 = 1 - P_3/P_1$, which is given by:

$$\eta_{\text{hole}} = 1 - \left(\frac{d_{\text{sr_hole}}}{d_{\text{sr}}} \right)^2. \quad (5.8)$$

5.6.1.4 Polyethylene Tube

Typically, the sub-reflector is fixed by means of the feed support struts. The presence of these struts introduces another blockage that leads to a less efficient Cassegrain antenna [139]. To avoid this issue, a polyethylene tube is used to attach the sub-reflector to the feed. By using this technique not only the blockage is avoided but also the fibre passing though the waveguide can be secured. To study the effect of tube the structure is modelled using the geometrical optics technique, see Figure 5.22.

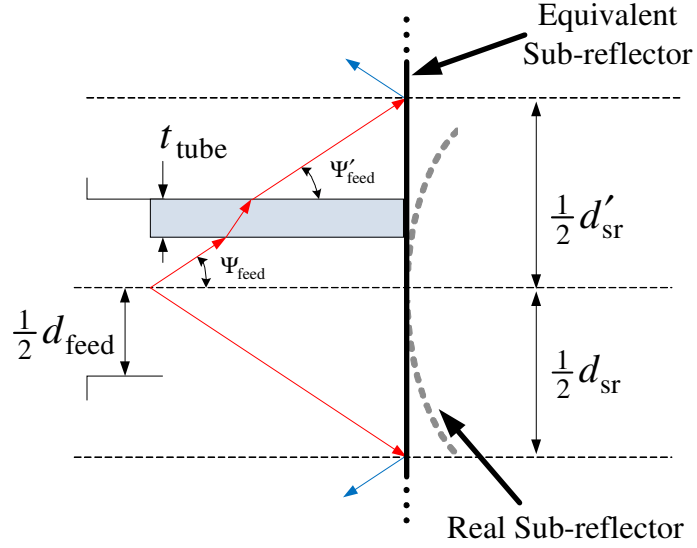


Figure 5.22: Diagram showing the effect of tube on the radiation of the feed.

The feed diameter and the polyethylene tube thickness are d_{feed} and t_{tube} , respectively. Also HPBW after the tube is denoted by Ψ'_{feed} . With no tube, the incident ray is supposed to encounter the equivalent sub-reflector interface at $0.5d_{\text{sr}}$, see Figure 5.22. However, in the presence of the tube due to the refraction phenomena the new incidence point will be $0.5d'_{\text{sr}}$. Given that ϵ_r denotes the relative permittivity of the tube, then from Snell's law [138] and following some mathematical simplifications, one obtains:

$$\Psi'_{\text{feed}} = \Psi_{\text{feed}}, \quad (5.9.a)$$

$$d'_{\text{sr}} = d_{\text{sr}} + 2t_{\text{tube}} \left[1 - \frac{\sin \Psi_{\text{feed}}}{\sqrt{\epsilon_r^2 - \cos^2 \Psi_{\text{feed}}}} \right]. \quad (5.9.b)$$

From Equ. (5.9.a), it can be figured out that the angle of incident at the sub-reflector equivalent surface is the same. However, Equ. (5.9.b) shows that in the presence of tube, the foot print of feed is larger than the sub-reflector area; therefore another loss is added to the Cassegrain antenna total loss. From Equ. (5.6) it is known that the power is proportional to the square of diameter, therefore the tube efficiency $\eta_{\text{tube}} = P_2/P_1$ can be written as:

$$\eta_{\text{tube}} = d_{\text{sr}}^2 / \left(d_{\text{sr}} + 2t_{\text{tube}} \left[1 - \frac{\sin \Psi_{\text{feed}}}{\sqrt{\epsilon_r^2 - \cos^2 \Psi_{\text{feed}}}} \right] \right)^2. \quad (5.10)$$

5.6.1.1 Circular Feed, Rectangular to Circular Transition and Fibre in the Waveguide

The implemented feed in the proposed antenna scheme is an open ended circular waveguide, see Figure 5.19. The fundamental propagating mode inside the circular waveguide is TE_{11} , which gives the following E/H-plane HPBW [70]:

$$\Psi_{\text{feed}}|_{\text{E-Plane}} = 58.4 \frac{\lambda_{\text{RF}}}{d_{\text{feed}}}, \quad (5.11.a)$$

$$\Psi_{\text{feed}}|_{\text{H-Plane}} = 74 \frac{\lambda_{\text{RF}}}{d_{\text{feed}}}. \quad (5.11.b)$$

The average of E- and H-planes HPBW will be considered in the proposed design. A rectangular to circular transition is required to connect the circular-shaped feed to the rectangular-shaped waveguide components [140, 141]. In addition to connecting waveguides with different cross sections, transition guarantee the efficient conversion between the fundamental modes TE_{10} and TE_{11} of the rectangular and circular waveguides, respectively [138, 141].

It is important to ensure that the presence of the optical fibre especially in the feed has a minimum effect on the antenna performance. The existence of a dielectric object within a waveguide changes the propagating guide field distribution. In particular, the enforced boundary conditions change the fundamental mode to a hybrid mode [138]. If the travelling RF wave inside the waveguide is able to generate a propagating mode in the optical fibre as well, then it can be expected that the distribution of the RF electromagnetic field inside the waveguide is also affected by the optical fibre; otherwise the optical fibre only introduces a loss and a local perturbation of the RF electromagnetic field profile inside the fibre. Section 9.5.1 in [70] is devoted to analysis of the propagation mechanism in dielectric waveguides. By solving [138, Eqs. (9-91)], one can investigate the first

HEM₁₁ propagating mode in the fibre.

5.6.1.2 E-Plane Bend and the Fibre Hole

In order to take the optical fibre out of the waveguide, an E-plane bend with a hole on the wall is used as shown in Figure 5.18. The E-plane bend has been studied previously [142, 143] and here only the analysis of the hole on wall of the bend is presented. First it is assumed that the physical structure can be replaced with the hole on the wall of a waveguide. Then as in [144], it is assumed that the hole on the wall with a diameter d_{bend} can be modelled by the infinitesimal electric and magnetic dipoles as [145]:

$$\bar{P}_e = \frac{1}{12} d_{\text{bend}}^3 \vec{E}_n \delta(r - r_0), \quad (5.12.a)$$

$$\bar{P}_m = -\frac{1}{6} \mu_0 d_{\text{bend}}^3 \vec{H}_t \delta(r - r_0), \quad (5.12.b)$$

where μ_0 and r_0 are the vacuum permeability and the hole coordinate, respectively. \vec{E}_n denotes the normal component of the waveguide electrical field whereas \vec{H}_t refers to the tangent component of the waveguide magnetic field at the hole. Sec. 8.2.3 in [138] summarizes a closed-form expressions of the TE₁₀ mode of a rectangular waveguide. Knowing \bar{P}_e and \bar{P}_m , one can calculate the radiated power due to the hole given by [146]:

$$P_4 = \frac{k_{\text{RF}}^4}{6\pi Z_0} (|\bar{P}_e|^2 + c^2 |\bar{P}_m|^2), \quad (5.13)$$

where c is the speed of the light in a vacuum. Considering that the hole is located at the middle of the wall, and following mathematical simplifications, one gets:

$$P_4 = \frac{k_{\text{RF}}^4}{4\pi Z_0} \left(\frac{\pi}{\varepsilon_0 W_{\text{bend}}} \right)^2 \left(\frac{d_{\text{bend}}^2}{6} \right)^3 \left(5 - \left[\frac{\lambda_{\text{RF}}}{W_{\text{bend}}} \right]^2 \right) |E_0|^2, \quad (5.14)$$

where ε_0 is the vacuum permittivity, and W_{bend} denotes the cross section width of the waveguide where, the hole is positioned. On the other hand, the flowing power inside the waveguide is given as [138]:

$$P_5 = \frac{S_{\text{bend}}}{8Z_0} \left(\frac{\pi}{\epsilon_0 W_{\text{bend}}} \right)^2 \sqrt{4 - \left[\frac{\lambda_{\text{RF}}}{W_{\text{bend}}} \right]^2} |E_0|^2, \quad (5.15)$$

where S_{bend} denotes the area of the waveguide cross section. The ratio of $C_{\text{bend}} = P_4/P_5$ will be used to assess the imposed loss.

5.6.2 FSO Antenna

As mentioned earlier, the fundamental concept of the optical transceiver is based on using an optical aperture in the shadow region of the sub-reflector, which connects it to the circuitry by means of optical fibres. Figure 5.23 depicts the schematic diagram of the optical aperture. The optical aperture consists of a Tx lens with a diameter of $2w_{\text{TX}}$ and M -Rx lenses with the diameter d_s and a focal length of f_s . The smallest circumcircle embedding all the lenses has the diameter D_{RX} , see Figure 5.23. A Tx lens is located at the centre whereas the Rx lenses are scattered equally in the circumcircle. The distance of a Rx lens to the centre of the circumcircle is denoted by $d_{\text{r-c}}$. The geometry of the aperture and some mathematical simplifications leads to the following equations:

$$D_{\text{RX}} = d_s + 2d_{\text{r-c}}, \quad (5.16.a)$$

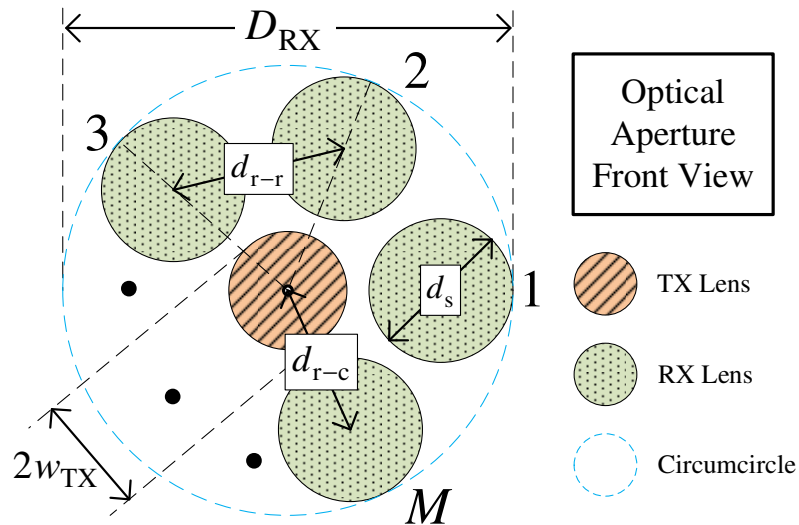


Figure 5.23: Schematic diagram of optical transceiver aperture.

$$\max M = \left\lfloor \pi / \tan^{-1} \left(\frac{4d_{r-c}^2}{d_s^2} - 1 \right)^{-0.5} \right\rfloor, \quad (5.16.b)$$

$$d_{r-r} = 2d_{r-c} \sin \frac{\pi}{M}, \quad (5.16.c)$$

$$\max w_{Tx} = D_{Rx}/2 - d_s. \quad (5.16.d)$$

The effect of turbulence on each individual received optical signal will be independent if the distance between the centres of two adjacent lenses $d_{r-r} > d_0$ or $d_{r-r} > \rho_c \approx d_0^2/\pi\rho_0$ [90]. Since the dependency of the channel degrade the link performance [90], this leads to the following requirement:

$$d_{r-r} \geq \max \left\{ d_0, \frac{d_0^2}{\pi\rho_0} \right\}. \quad (5.17)$$

In addition to the lens configuration, it is also needed to consider optical fibres used for the FSO link. Since in the proposed design OTx and ORx are distinct, they will be dealt with separately. The OTx is basically an SMF positioned in the focal length of the Tx lens, which is connected to a laser source being intensity-modulated with the data signal. As discussed in [147] to achieve efficient conversion of > 0.94 from the optical fibre mode to the fundamental FSO Gaussian mode, the V -number of the optical fibre should be in the range of $1.2 < V < 4.0$. The V -number is defined as $V \triangleq \pi d_{fibre} NA / \lambda_{FSO}$ where d_{fibre} , and NA are the optical fibre's core diameter and numerical aperture, respectively [53]. Having obtained the V -number the optimum FSO beam radius at the output of the step-index SMF can be approximated [147]. By using optical lenses it is possible to collimate the output beam for a given distance and in [114] the required expressions are derived for a single lens collimator system. Although the output beam of the Tx lens is supposed to be collimated, in real systems a small divergence half-angle $\theta_0 \ll 1$ is expected.

The beam radius at the Rx is $w_{Rx} = w_{Tx} + \theta_0 L$ [57]. Letting D_{ap} to be the diameter of a single lens at the Rx of a LOS link, the FSO geometrical attenuation A_{geo} in dB will be given as [62]:

$$A_{geo} = 20 \log \left(\sqrt{2} \frac{w_{Rx}}{D_{ap}} \right). \quad (5.18)$$

Since the Rx proposed here is not made of a single lens, then it is essential to adopt Equ. (5.18). To do this, the plane wave propagation is assumed. Therefore, it can be shown that the ratio of total optical power impinging the circumcircle with the diameter D_{Rx} to the optical power captured by a single lens with diameter is given by:

$$C_{ap} = \frac{I\pi\left(\frac{d_s}{2}\right)^2}{I\pi\left(\frac{D_{Rx}}{2}\right)^2} = \left(\frac{d_s}{D_{Rx}}\right)^2, \quad (5.19)$$

where C_{ap} is the ratio and I is the optical intensity of the plane wave. Therefore, the total attenuation from Tx to a single Rx lens including the geometrical loss is given by:

$$A_{total} = 20 \log \left(\sqrt{2} \frac{w_{Rx}}{d_s} \right). \quad (5.20)$$

At the Rx side the optical beam is captured by each Rx lens and focused onto a multimode fibre (MMF). Note that MMF is used because of its larger NA. The main issue with MMF is the dispersion and since MMF used in the scheme is very short (a few meters long), the dispersion is almost negligible. However, the coupling loss from FSO to the MMF and the fibre loss cannot be ignored. The criterion $d_{fibre} \geq 2\lambda_{FSO}f_s/d_s$ ensures that the spot size of the focused beam after the lens is smaller than the fibre core diameter [148]. In the ORx module, the output beams of MMFs can be used to perform desired combining methods.

5.6.3 Simulation Results

5.6.3.1 Initial Design

The RF part of the antenna was designed based on the steps outlined in Section 5.6.1 with the key parameters summarized in Table 5.7. Note that FSO parameters are also summarized in Table 5.8. Based on the shadow region approximation $D_{\text{Rx}} = d_{\text{sr}}$ (see Figure 5.19 and Figure 5.23) and for the link distance and the FSO wavelength given in Table 5.7, $d_0 \approx 26$ mm. In the practical design $d_s = 25$ mm, and using Equ. (3.10) one obtains $\text{AF} = 0.34$. For the weak turbulence condition (i.e., $\sigma_R^2 = 0.3$), from Equ. (3.6)

Table 5.7: RF antenna with multiple collimators parameters. “Initial Design” is based on the steps given in Section 5.6.1. “Modified Design” refers to design based on the experimental limitations.

	Parameter	Value
Given Parameters	Wavelength λ_{RF} at 10 GHz	29 mm
	Modulation scheme	BPSK
	Tx module total loss	5 dB
	Rx module total gain	10 dB
	Rx noise figure	-91.5 dBm
	Signal Bandwidth	10 MHz
	Parabola diameter D_{mr}	475 mm
	Parabola focal length to diameter ratio $F_{\text{mr}}/D_{\text{mr}}$	0.24
	Required HPBW	5°
	Required gain	> 25 dBi
	HPBW of feed	90°
	Circular feed diameter d_{feed}	23.7 mm
	Tube thickness t_{tube}	2 mm
	Tube relative permittivity ϵ_r	2.3
	Rectangular feed dimensions	22.86×10.16 mm ²
	Fibre hole diameter $d_{\text{sr_hole}}$	2.5 mm
Initial Design	Hyperbolic diameter d_{sr}	99 mm
	Hyperbolic focal length f_{sr}	47 mm
	Hyperbolic position p_{sr}	13 mm
	Feed aperture distance to main reflector apex $f_{\text{sr}} - p_{\text{sr}}$	66 mm
Modified Design	Hyperbolic diameter d_{sr}	85 mm
	Hyperbolic focal length f_{sr}	47 mm
	Hyperbolic position p_{sr}	13 mm
	Feed aperture distance to main reflector apex $f_{\text{sr}} - p_{\text{sr}}$	57 mm

Table 5.8: FSO aperture with multiple collimators parameters. NEP is the receiver noise equivalent power.

	Parameter	Value
Given Parameters	Wavelength λ_{FSO}	670 nm
	Modulation Scheme	NRZ-OOK
	Aperture diameter D_{Rx}	85 mm
	Link length L	1 km
	Rytov variance σ_R^2	0.3
	Fading correlation length d_0	26 mm
	Tx/Rx fibre cable diameter	2.5 mm
	Tx fibre loss	0.2 dB
	Rx fibre loss	2 dB
	Coupling loss from FSO to fibre/fibre to FSO	2 dB
	NEP	35 pW/ $\sqrt{\text{Hz}}$
	Bandwidth	50 MHz
	Full angle beam divergence θ_0	8 mDeg
Initial Design	Rx lens diameter d_s	26 mm
	Rx lens to centre distance $d_{\text{r-c}}$	30 mm
	Maximum M	6
	Tx lens diameter $2w_{\text{Tx}}$	26 mm
Modified Design	Rx lens diameter d_s	25 mm
	Rx lens to centre distance $d_{\text{r-c}}$	26 mm
	Chosen M	3
	Tx lens diameter $2w_{\text{Tx}}$	25 mm
	Rx lens to Rx lens distance $d_{\text{r-c}}$	26 mm

$C_n^2 = 5.7 \times 10^{-15} \text{ m}^{-2/3}$. Thus, using Equ. (3.3) $\rho_0 \approx 19 \text{ mm}$ and hence the criteria $d_{\text{r-r}} \geq \max\{26 \text{ mm}, 11 \text{ mm}\}$. On the other hand, using (5.16.a) $d_{\text{r-c}} = 30 \text{ mm}$, but $d_{\text{r-c}} = d_0 = 26 \text{ mm}$, which makes the aperture smaller and also avoids dependency on the Rx apertures. By using Equ. (5.16.b) and based on the parameters calculated so far, the maximum M of 6 was determined. In the proposed design $M = 3$, thus resulting in $d_{\text{r-r}}$ of 26 mm, which is acceptable based on the criteria of Equ. (5.17). Also the Tx diameter $2w_{\text{Tx}} = d_s$ was selected, which conforms to the criterion $w_{\text{Tx}} \leq D_{\text{Rx}}/2 - d_s$ obtained from Figure 5.23. All the key FSO transceiver aperture parameters are presented in Table 5.8.

The initial sub-reflector was designed based on the given method; and later on the final design was determined by means of CST STUDIO SUITE®. Figure 5.24 illustrates simulated normalized radiation patterns of the initial antenna in E- and H-planes.

5.6.3.2 Parametric Analysis

The side-lobe levels of the antenna based on the steps in Section 5.6.1 for both E- and H-planes are unacceptable. Besides due to the experimental limitation, the feed aperture distance to the main reflector apex must be < 57 mm. Therefore, in the next step, while the sub-reflector diameter is set to 85 mm and the distance from the feed aperture to the main reflector apex is fixed to 57 mm, a parametric analysis is performed to achieve the

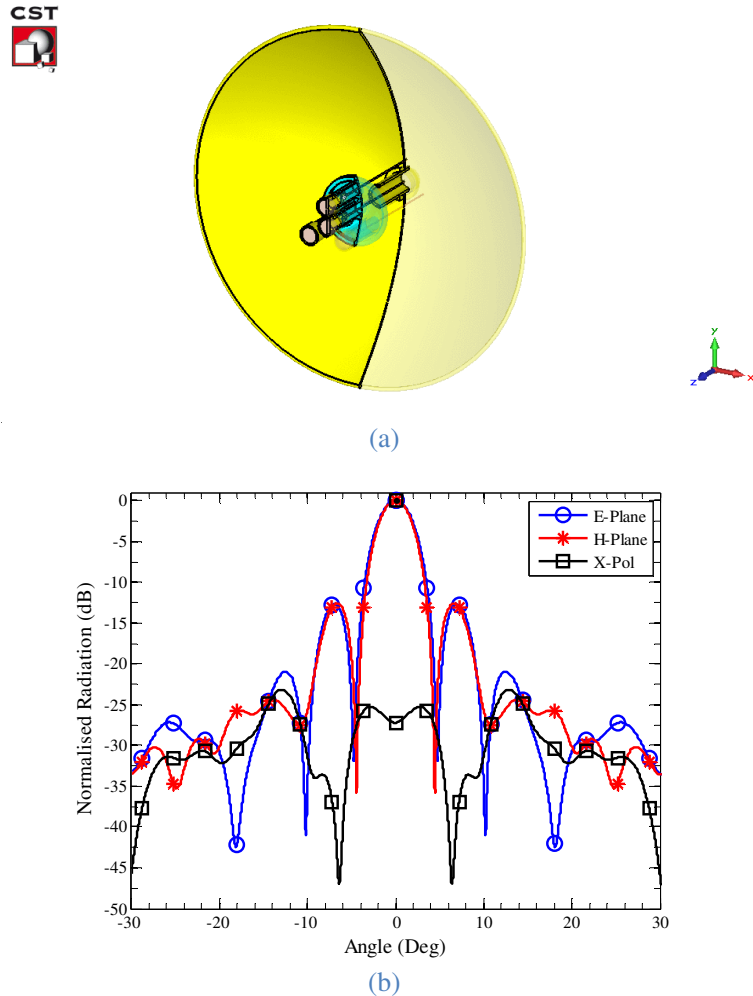


Figure 5.24: Simulation results for initial antenna with multiple collimators design scheme based on steps given in Section 5.6.1: (a) antenna profile (the distance between the feed and sub-reflector is 37.2 mm and the sub-reflector diameter is 99 mm), and (b) E-, H-planes, and X-pol radiation normalised to the antenna gain of 28.2 dBi.

optimum gain, side-lobe level and X-pol performances.

The outcome of the parametric analysis is depicted in Figure 5.25. Based on the analysis, the optimum displacement of 0 mm is chosen. This value was adopted and further simulations on the radiation patterns of the antenna were carried out with results presented in Figure 5.26 and summarised in Table 5.10. To study the effect of adding an optical aperture on the distributions of near fields, the power spatial patterns in E- and H-planes are presented in Figure 5.27. Also shown are power distributions prior to inclusion of an optical aperture. As in Figure 5.12, the power distributions have changed significantly with inclusion of an optical aperture, since the number of apertures is higher than the case in Figure 5.12. However, as it was mentioned before, the performance of

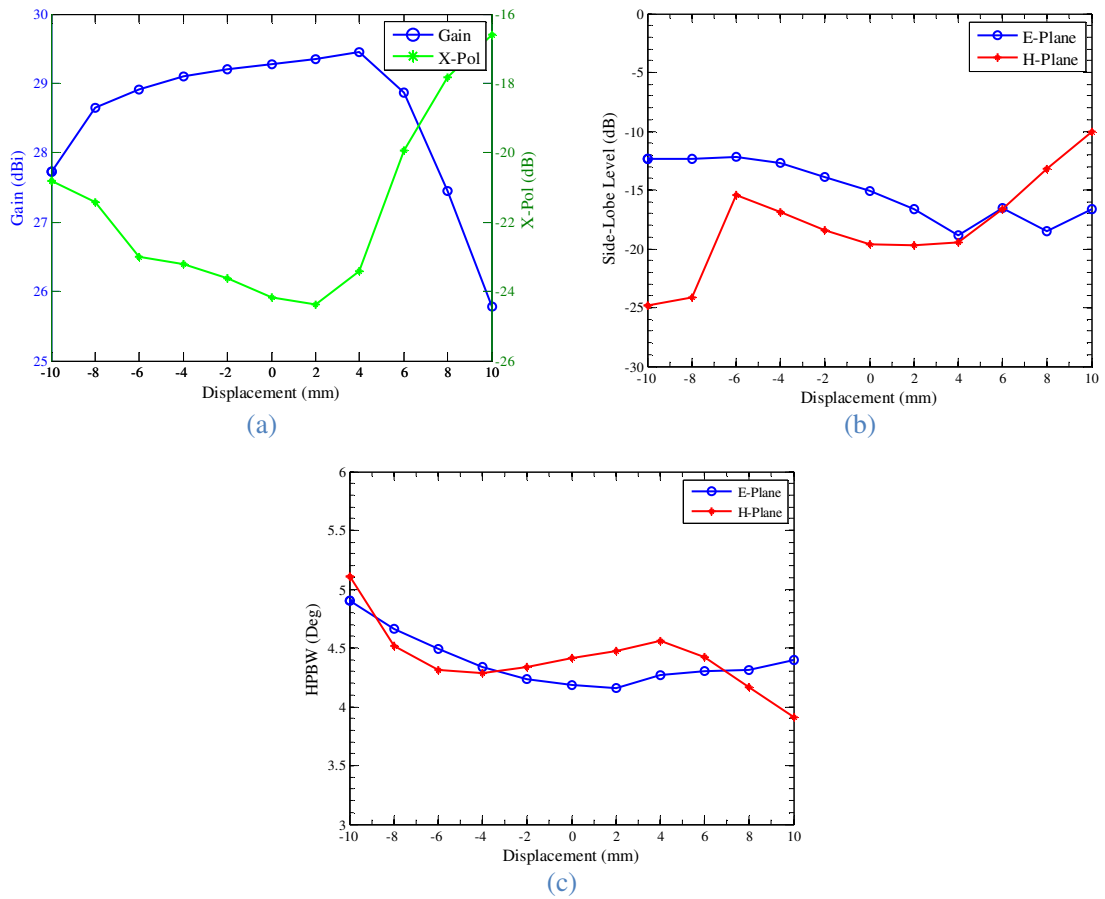


Figure 5.25: Parametric analysis on the initial design with multiple collimator part and tube: (a) gain and X-pol discrimination, (b) side-lobe level in E- and H-planes, and (c) half-power beam-width (HPBW) in E- and H-planes. Negative displacement denotes moving the sub-reflector towards the feed. At displacement of 0 mm, the distance between the feed and sub-reflector is 40.96 mm.

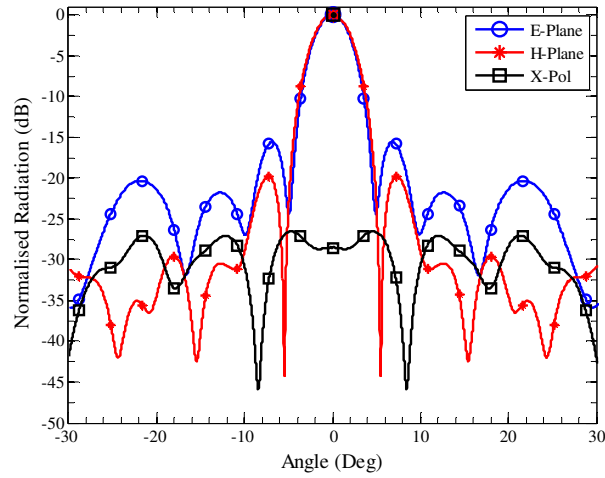


Figure 5.26: Simulated radiation pattern for optimised antenna with multiple collimators design scheme. The distance between the feed and sub-reflector is 40.96 mm and the sub-reflector diameter is 85 mm. E-, H-planes, and X-pol radiation are normalised to the antenna gain of 29.3 dBi.

the antenna in the far-field should be taken into account.

5.6.3.3 Sub-reflector Misalignment Analysis

Furthermore, to see the effect of misalignment of the sub-reflector on the antenna performance, two more analyses are performed. Note that the effect of sub-reflector misplacement is already done in previous section, see Figure 5.25. The goal is to find the effect of sub-reflector rotation along the two vertical (E-plane) and horizontal (H-plane) directions. The result of the analysis is plotted in Figure 5.28, which shows that in contrary to the displacement of sub-reflector, the rotation has no significant effect of the antenna characteristics in the maximum radiation pattern direction.

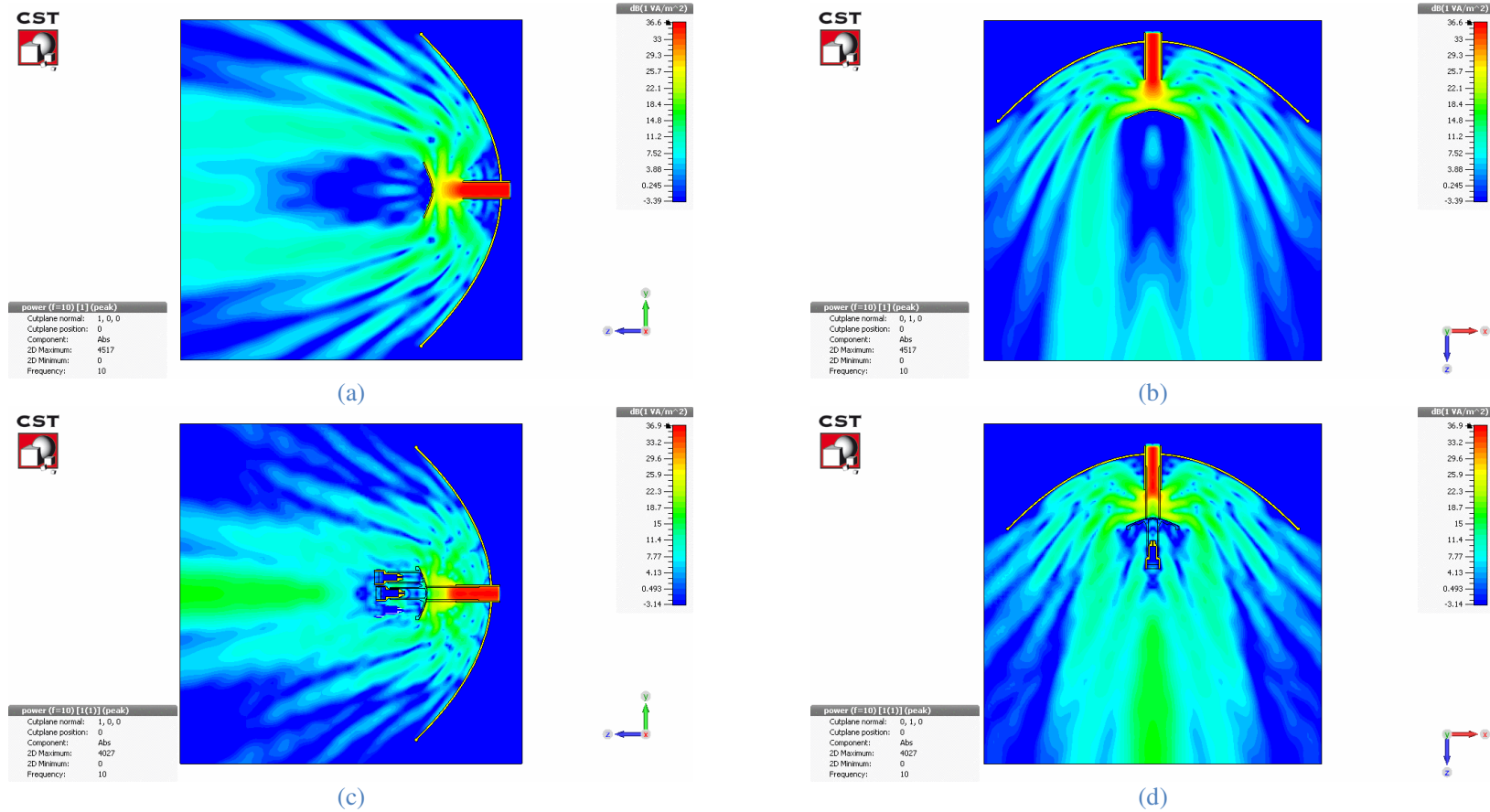


Figure 5.27: Near field power distribution of the antenna with and without optical aperture for multiple collimators scheme in E- and H-planes: (a) without optical aperture in E-plane, (b) without optical aperture in H-plane, (c) with optical aperture in E-plane, and (d) with optical aperture in H-plane. The distance between the feed and sub-reflector, the sub-reflector diameter, and the distance from the feed aperture to the main reflector apex are 40.96 mm, 85 mm and 57 mm, respectively.

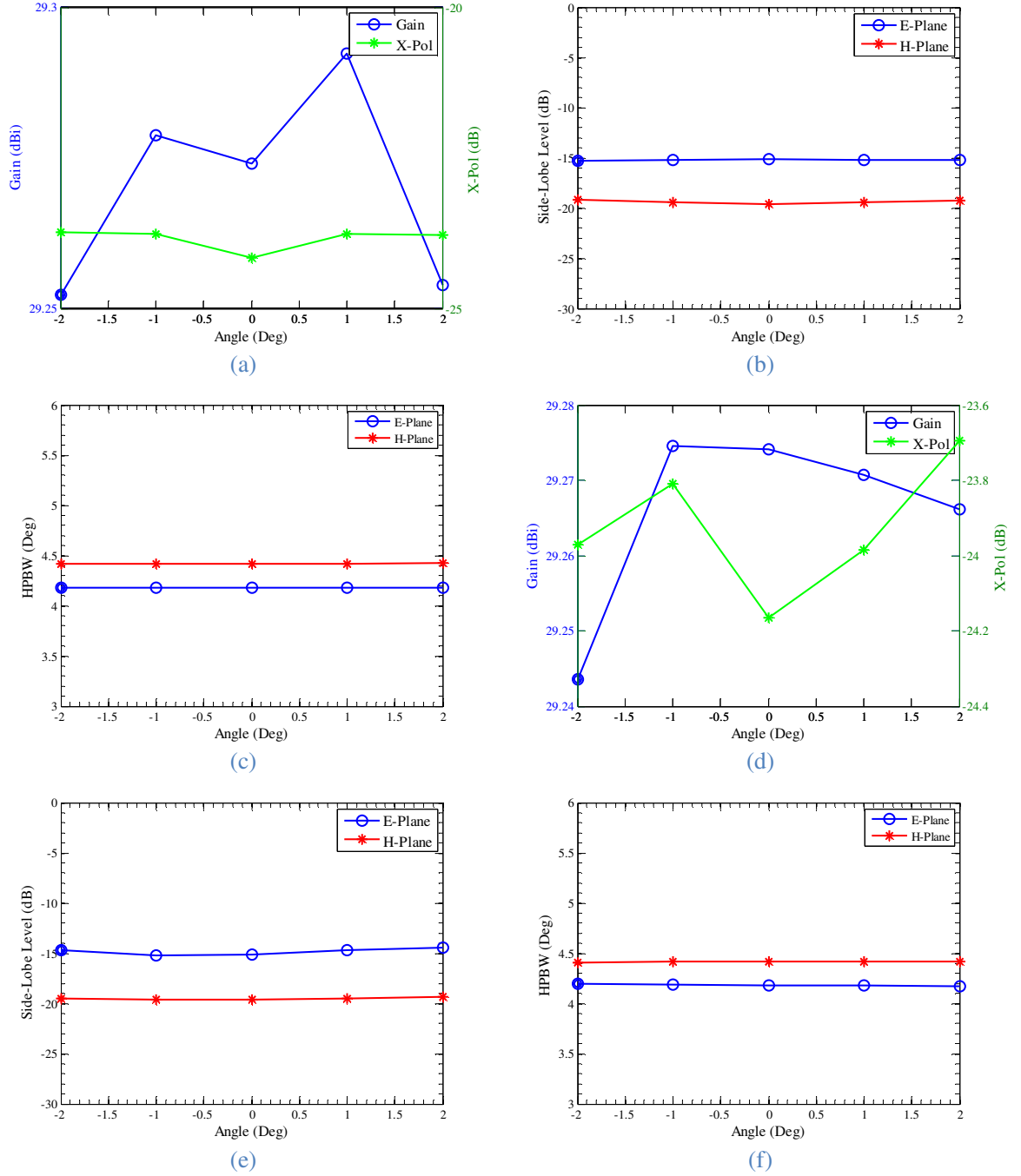


Figure 5.28: Misalignment analysis on the optimised design with no optical part and tube: (a, d) gain and X-pol discrimination, (b, e) side-lobe level in E- and H-planes, and (c, f) half-power beam-width (HPBW) in E- and H-planes. In (a-c) the angle is in vertical (E-plane) direction, whereas (d-f) the angle is in horizontal (H-plane) direction. The distance between the feed and sub-reflector is 40.96 mm.

5.6.4 Design Steps Summary

In this section, the steps taken to design the antenna based on the given parameters (i.e., required RF gain G_{CA} and operating RF wavelength λ_{RF}) as well as the required formulas

from previous sections, are summarised as below:

1. Assuming a typical value for the antenna efficiency (η_{CA}), the required antenna diameter (D_{mr}) is calculated from Equ. (5.5) as:

$$D_{mr} = \frac{\lambda_{RF}}{\pi} \sqrt{\frac{G_{CA}}{\eta_{CA}}}.$$

2. Based on available parabolic diameter and the focal length ratio, focal length of the main reflector (F_{mr}) is determined. (k_B) is also decided based on the available feed. Then using Equ. (5.2), the optimum diameter for the sub-reflector (d_{optm}) is defined as:

$$d_{optm} = \sqrt{\frac{2}{k_B} \lambda_{RF} F_{mr}}.$$

3. If $d_{optm}/D_{mr} > 0.2$ then the sub-reflector diameter (d_{sr}) is set to d_{optm} , otherwise $d_{sr} = 0.1D_{mr}$.
4. If the half of E/H-plane HPBW (i.e., $\Psi_{feed}|^{E\ Plane}$ and $\Psi_{feed}|^{H\ Plane}$) are known, then the step 4 is not necessary. Otherwise for available feed with a known aperture diameter (d_{feed}), the half of E/H-plane HPBW (i.e., $\Psi_{feed}|^{E\ Plane}$ and $\Psi_{feed}|^{H\ Plane}$) are obtained using Equ. (5.11) as given:

$$\Psi_{feed}|^{E\ Plane} = 58.4 \frac{\lambda_{RF}}{d_{feed}},$$

$$\Psi_{feed}|^{H\ Plane} = 74 \frac{\lambda_{RF}}{d_{feed}}.$$

5. Ψ_{feed} can be set to the average of $\Psi_{feed}|^{E\ Plane}$ and $\Psi_{feed}|^{H\ Plane}$. Another option is to set Ψ_{feed} to the maximum value of $\Psi_{feed}|^{E\ Plane}$ and $\Psi_{feed}|^{H\ Plane}$.
6. By using (5.3), the hyperbolic focal length (f_{sr}) is determined as:

$$f_{sr} = \frac{F_{mr}D_{mr}d_{sr}}{16} [8F_{mr}D_{mr}\cot\Psi_{feed} + 16F_{mr}^2 - D_{mr}^2].$$

7. Next step, the geometric parameters of hyperbolic sub-reflector are determined using Equ. (5.4), which are given as:

$$e = \left(D_{mr} \cot \frac{\Psi_{feed}}{2} + 4F_{mr}\right) / \left(D_{mr} \cot \frac{\Psi_{feed}}{2} - 4F_{mr}\right),$$

$$p_{sr} = f_{sr} / \left(D_{mr} \cot \frac{\Psi_{feed}}{2} + 4F_{mr}\right).$$

8. Based on the practical limitation, the sub-reflector diameter (d_{sr}) is set to the available value.
9. Knowing the FSO link wavelength (λ_{FSO}) and required link distance (L), correlation length (d_0) is calculated using Equ. (3.2), which is given by:

$$d_0 \approx \sqrt{\lambda_{FSO}L}.$$

10. With the expected turbulence strength defined in terms of the scintillation index ($\sigma_I^2(0)$), it is possible to calculate the required receiver lens diameter (d_s) using Equ. (3.10), which is given as:

$$d_s = \frac{d_0}{1.2916} \sqrt{\left(\frac{\sigma_I^2(0)}{\sigma_I^2(d_s)}\right)^{6/7} - 1}.$$

11. Based on the practical limitation, the receiver lens diameter (d_s) is set to the available value.
12. Knowing the sub-reflector diameter (d_{sr}), from the step 8 the optical aperture diameter (D_{Rx}) is decided accordingly.
13. Using Equ. (5.16.a), the distance between receiver lenses (d_{r-c}) is determined as:

$$d_{r-c} = \frac{D_{Rx} - d_s}{2}.$$

14. Using Equ. (5.16.b), the maximum number of lenses at the receiver side (M) is obtained, which is given by:

$$\max M = \left\lfloor \pi / \tan^{-1} \left(\frac{4d_{r-c}^2}{d_s^2} - 1 \right)^{-0.5} \right\rfloor.$$

15. The maximum transmitter lens radius (w_{Tx}) is calculated using Equ. (5.16.d) as:

$$\max w_{Tx} = D_{Rx}/2 - d_s.$$

16. In case that the divergence angle of the transmitter (θ_0) is not given and the maximum transmitter lens radius (w_{Tx}) is known, it is possible to ensure the required divergence angle of FSO beam using $\theta_0 = \frac{\lambda_{FSO}}{\pi w_{Tx}}$ [57].

17. The beam radius at the receiver (w_{Rx}) is obtained using $w_{Rx} = w_{Tx} + \theta_0 L$.

18. The geometrical loss for each receiver lens (A_{total}) is calculated using Equ. (5.20), which is given by:

$$A_{total} = 20 \log \left(\sqrt{2} \frac{w_{Rx}}{d_s} \right).$$

19. If the calculated geometrical loss (A_{total}) is more than the acceptable level, by changing the conditions in the step 10 and going through the steps, one should try to approach the required criteria. In case it is not possible to satisfy the entire conditions, a trade-off between the transmitter/receiver lens size and the independency of the receiver apertures might be necessary.

20. In the last step, the structure needs to be simulated to ensure the required characteristics are achieved. Note that by changing the distance between the

sub-reflector and the feed aperture, it is possible to perform a simple optimisation.

The calculation steps for the antenna with multiple collimators is summarised in Table 5.9.

5.6.5 Hybrid Antenna Fabrication

Based on the available resources and the optimised design, the antenna was fabricated. More details on the fabrication and antenna components are available in Appendix C. Figure 5.29 shows the picture of the assembled prototype.

5.6.6 Hybrid Antenna Characteristics

In this section, the main characteristics of the hybrid antenna are presented. The

Table 5.9: Hybrid antenna design calculations based on the steps given in Section 5.6.4.

Step Number	Given Values	Calculated Values
1	$G_{CA} = 30$ dBi, $\eta_{CA} = 0.55$, $\lambda_{RF} = 30$ mm	$D_{mr} = 407$ mm
2	$D_{mr} = 475$ mm, $F_{mr}/D_{mr} = 0.26$, $k_B = 0.7$	$d_{optm} = 99$ mm
3	$d_{optm} = 99$ mm	$d_{sr} = d_{optm}$
4	$d_{feed} = 23.8$ mm	$\Psi_{feed} ^{E \text{ Plane}} = 73.6$ Deg, $\Psi_{feed} ^{H \text{ Plane}} = 93.2$ Deg
5	$\Psi_{feed} ^{E \text{ Plane}} = 73.6$ Deg, $\Psi_{feed} ^{H \text{ Plane}} = 93.2$ Deg	$\Psi_{feed} = 90$ Deg
6	$F_{mr} = 114$ mm, $D_{mr} = 475$ mm, $d_{sr} = 99$ mm, $\Psi_{feed} = 90$ Deg	$f_{sr} = 47.4$ mm
7	$F_{mr} = 114$ mm, $D_{mr} = 475$ mm, $d_{sr} = 99$ mm, $\Psi_{feed} = 90$ Deg, $f_{sr} = 47.4$ mm	$p_{sr} = 13.5$ mm
8	$d_{sr} = 99$ mm	$d_{sr} = 85$ mm
9	$\lambda_{FSO} = 670$ nm, $L = 1$ km	$d_0 = 25.9$ mm
10	$d_0 = 25.9$ mm, $\sigma_f^2(0) = 1$, $\sigma_f^2(d_s) = 0.3$	$d_s = 27$ mm
11	$d_s = 27$ mm	$d_s = 25$ mm
12	$d_{sr} = 85$ mm	$D_{Rx} = 85$ mm
13	$D_{Rx} = 85$ mm, $d_s = 27$ mm	$d_{r-c} = 30$ mm
14	$d_{r-c} = 30$ mm, $d_s = 27$ mm	$\max M = 6$
15	$D_{Rx} = 85$ mm, $d_s = 25$ mm	$\max w_{Tx} = 17.5$ mm
16	$w_{Tx} = 17.5$ mm, $\lambda_{FSO} = 670$ nm	$\theta_0 = 700$ μ Deg
17	$w_{Tx} = 17.5$ mm, $L = 1$ km	$w_{Rx} = 87$ mm
18	$w_{Rx} = 87$ mm, $d_s = 25$ mm	$A_{total} = 14$ dB

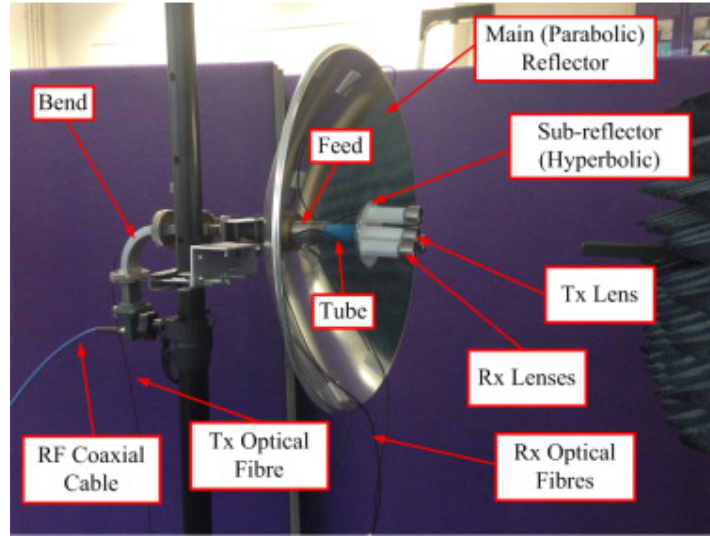
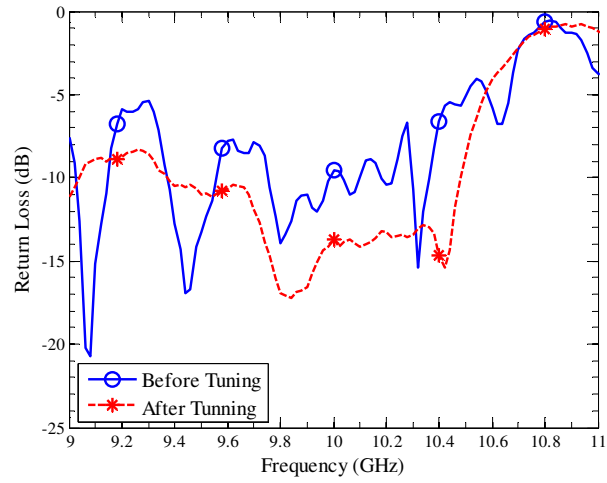


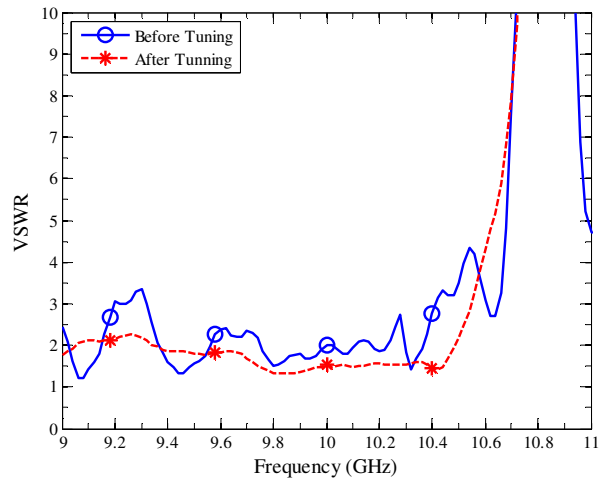
Figure 5.29: Fabricated hybrid antenna with multiple collimators under radiation pattern test. The distance between the feed and sub-reflector is 40.96 mm and the sub-reflector diameter is 85 mm.

parameters are either theoretically calculated or are determined experimentally. The measured return loss and VSWR of the antenna before and after tuning are shown in Figure 5.30. The bandwidth before tuning is in the range of 9.75 GHz-9.98 GHz, where with tuning the correct bandwidth of ~800 MHz is achieved.

Figure 5.31 illustrates the measured and simulated radiation patterns in the E and H-planes. The summary of the radiation pattern measurement including gain, side-lobe level, HPBW, FNBW and bandwidth are presented in Table 5.10. Note the improvement in gain by 2.7 dB, which is due to the increased VSWR efficiency. HPBWs of antenna in both E- and H-planes after tuning are acceptable, however that is not the case for side-lobe level. With the tuner the side-lobe level in the E-plane at both negative and positive angles has improved, but in the H-plane the side-lobe level in the positive angle range shows a significant degradation. Also observed is the asymmetric radiation pattern, which can be enhanced by improving the antenna fabrication process. Next we consider the effect of fibre on the waveguide field distribution, fibre hole efficiency coefficient (η_{hole}), tube efficiency (η_{tube}), and bend hole coupling ratio (C_{bend}).

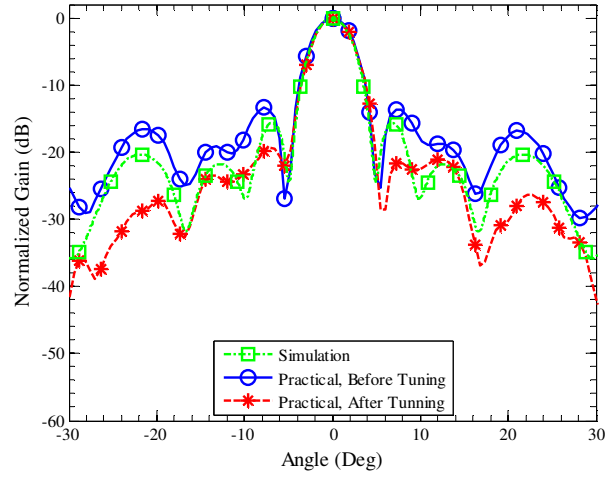


(a)

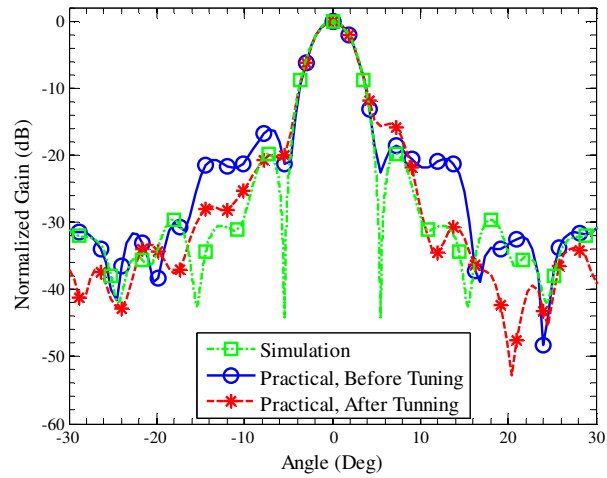


(b)

Figure 5.30: (a) Measured return loss of the antenna with multiple collimators before and after tuning, and (b) equivalent voltage standing wave ratio (VSWR) from the measurement before and after tuning.



(a)



(b)

Figure 5.31: Radiation pattern of hybrid antenna with multiple collimators measured in a near field chamber as well as the simulated one for: (a) E-plane, and (b) H-plane.

Table 5.10: The antenna (design with multiple collimators) characteristics obtained from simulation. X-pol disc, SLL, HPBW, and FNBW are X-pol discrimination, side-lobe level, half-power beam-width, and first null beam-width, respectively.

Design step ^a	Gain (dBi)	X-pol disc (dB)	E-plane			H-plane			Bandwidth (MHz)
			SLL (dB) ^b	HPBW (Deg)	FNBW (Deg)	SLL (dB) ^b	HPBW (Deg)	FNBW (Deg)	
Target	30	20	< -20	< 5	-	< -20	< 5	-	100 MHz
Simulation, initial	28.2	22.9	-12.7	4.2	9.5	-12.6	3.9	9.9	-
Simulation, optimised	29.3	25	-17.7	4.4	10.7	-19.3	4.4	10.8	-
Measurement, before tuning	26.5	-	[-13.4, -13.6]	4.4	10.8	[-16.2, -18.6]	4.3	10.8	< 100
Measurement, after tuning	29.2	-	[-19.2, -21.6]	4.2	10.8	[-20.1, -15.4]	4.3	11.6	> 100

^a “Target” is based on the desired characteristics in Table 5.3. “Simulation, initial” is simulation of the antenna with multiple collimator based on the steps given in Section 5.6.1. “Simulation, optimised” is the simulation of the optimised antenna with multiple collimator based on the experimental limitation and performed parametric analysis. “Measurement, before tuning” is the measurement of the fabricated antenna with tube and multiple collimator based on the optimised antenna before tuning. “Measurement, after tuning” is the measurement of the fabricated antenna with tube and multiple collimator based on the optimised antenna after tuning.

^b The first number is side-lobe level for negative angles, whereas the second one refers to the positive angles.

Given that the fibre's numerical aperture $NA = (n_{\text{core}}^2 - n_{\text{clad}}^2)^{1/2}$ where $n_{\text{core}} = 2.24$ is the refractive index of the dielectric material (jacket is made of hytrel plastic), $n_{\text{clad}} = 1$ is the refractive index of surrounding free space, then the V -number of the dielectric rod is almost zero for the RF wavelength. For $V \approx 0$ the propagation inside the dielectric is literally the same as the propagating mode of the waveguide, see [138, Figure (9-11)]. Knowing that replacing the cladding with other materials will even result in a smaller V -number, it is guaranteed that the presence of the fibre inside the waveguide has no effect on the field distribution within the waveguide.

Next the efficiency coefficients for the fibre holes and the polyethylene tube as defined in Eqs. (5.8) and (5.10), respectively are determined. Assuming identical holes for the Tx and Rx fibres Equ. (5.8) can be re-written as:

$$\eta_{\text{hole}} = 1 - (M + 1) \left(\frac{d_{\text{sr_hole}}}{d_{\text{sr}}} \right)^2. \quad (5.21)$$

For the given parameters given in Table 5.7 and Table 5.8, $\eta_{\text{hole}} = 0.9939$, and $\eta_{\text{tube}} = 0.9392$ meaning that the effect of fibre holes and polyethylene tube are almost negligible. There is an additional effect of the hole on the E-plane bend, due to the inclusion of optical aperture to the RF antenna, defined as $C_{\text{bend}} = P_4/P_5$ where P_4 and P_5 are given by Eqs. (5.14) and (5.15), respectively. Using the parameters Table 5.7, $C_{\text{bend}} = -48.87$ dB, which is quite small and can be ignored. The summary of the calculated parameters is presented in Table 5.11.

Based on the simulation and measurement results so far, the following points are concluded:

- Due to the mismatch of rectangular to circular transition, the E-plane bend and the waveguide to coax adaptor, a tuner waveguide was used to achieve the required bandwidth.

Table 5.11: The hybrid antenna calculated characteristics based on section 5.6.1.

Parameter	Value
V -number of the fibre inside the waveguide	~ 0
Efficiency of the hole on sub-reflector η_{hole} for multiple holes $M = 4$	0.9939
Efficiency of the tube η_{tube}	0.9392
Coupling ratio of the bend C_{bend}	-48.87 dB

- Tuning the antenna improved both the gain and the VSWR efficiency within a certain frequency range.
- The inclusion of optical components had no significant effect on the antenna efficiency, and had the minimum effect on the radiation pattern when the optical aperture is positioned in the shadow region of the sub-reflector.
- Although tuning has improved the radiation pattern including the gain and the side-lobe level, the side-lobe level, which is mainly caused by illumination pattern and radiation from edges, is still not within an acceptable range.

An effective method to address the last comment on the side-lobe level would be to look at the total and illumination efficiencies of the antenna in different steps of the design. Equ. (5.5) can be used to estimate the total efficiency of the antenna $\eta_{\text{CA}} = \eta_{\text{illum}} \times \eta_{\text{misc}}$, where η_{illum} is the total efficiency and η_{misc} represent other efficiencies [69]. Additionally, η_{CA} can be written in terms of the antenna gain and directivity as [70]:

$$\eta_{\text{CA}} = \frac{\text{Antenna Gain}}{\text{Antenna Directivity}}. \quad (5.22)$$

The total efficiencies of the antenna obtained from measurement are summarised in Table 5.12. Considering the side-lobe level, bandwidth, and total efficiencies of the antenna in Table 5.5, Table 5.10, and Table 5.12, it is observed that the fabricated antenna suffers from inefficient illumination and a mismatched impedance. The prototype antenna with a multiple collimator has a total efficiency of ~ 0.6 , which is less than the typical

value of 0.85 for a quality reflector antenna. The ratio of measured gain and measured directivities of the antenna before and after tuning are 0.57 and 0.59, respectively. After tuning the efficiency is still low, therefore considering the geometry of the antenna, the total efficiency is not high due to the low illumination and spillover efficiencies. Thus, an optimisation method is required to address side-lobe level, illumination pattern and mismatched impedance. Optimisation might be employed to improve the profile of reflectors, which is the subject of the future work. For more on this the readers are referred to [129].

Table 5.12: Comparison of gain, directivity and total efficiency (η_{CA}) of the antenna for design steps.

Design step ^a	Gain (dB)	Directivity (dB)	η_{CA}
Target	30.0	31.5	0.55
Measurement, tube added	27.9	31.5	0.44
Measurement, single Collimator, Before tuning	26.8	28.8	0.63
Measurement, single collimator, after tuning	27.5	28.8	0.74
Measurement, multiple collimators, before tuning	26.5	28.9	0.57
Measurement, multiple collimators, after tuning	29.2	31.8	0.59

^a “Target” is based on the desired characteristics in Table 5.3. “Measurement, tube added” is the measurement of the fabricated antenna with tube based on the optimised antenna in Section **Error! Reference source not found.** “Measurement, single collimator, before tuning” is the measurement of the fabricated antenna with tube and single collimator based on the optimised antenna before tuning. “Measurement, single collimator, after tuning” is the measurement of the fabricated antenna with tube and single collimator based on the optimised antenna after tuning. “Measurement, multiple collimators, before tuning” is the measurement of the fabricated antenna with tube and multiple collimators based on the optimised antenna before tuning. “Measurement, multiple collimators, after tuning” is the measurement of the fabricated antenna with tube and multiple collimators based on the optimised antenna after tuning.

5.6.7 Hybrid FSO/RF Simplex Link

5.6.7.1 Link Budget Analysis

The FSO link with the proposed antenna has three aperture receivers. Therefore, there is a need for a combining method. For the FSO link with EGC and SC combining schemes the BER performance has been investigated as a function of the SNR using Eqs. (3.22) and (3.25) for the weak turbulence regime, and Eqs. (3.28), and (3.31) for the strong

turbulence regime as illustrated in Figure 5.32. At a BER of 10^{-6} the target SNR values for the EGC and SC are ~21 dB and ~24 dB, respectively for $\sigma_R^2 = 0.5$. For $\sigma_R^2 = 1$, the SNR values are increased to ~24 dB and ~27 dB for EGC and SC, respectively.

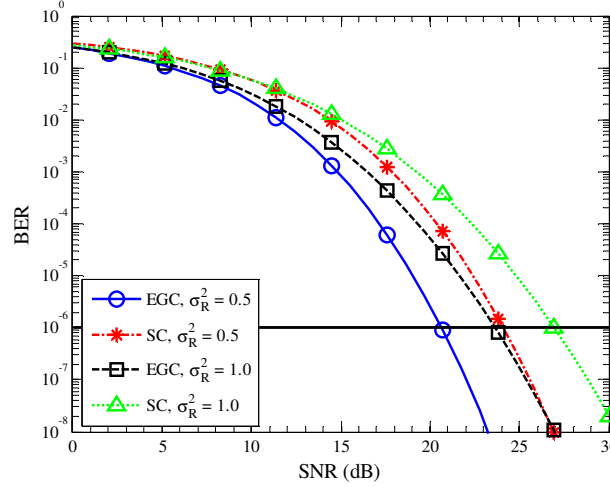


Figure 5.32: BER versus SNR for the FSO link with equal gain combining (EGC) and selection combining (SC) for two turbulence regimes.

The link budget analysis is outlined in Table 5.13 showing the required power values for both turbulence regimes and the combining methods. Note that a high extinction ratio is assumed for the optical source and the receiver is considered with responsivity of 1 A/W. The fibre losses are measured, whereas the total geometrical loss is predicted. The transmit power of the laser is limited due to the health and safety reason. The significance of this table is the achieved link margin for each scenario. EGC offers the best performance even for the moderate turbulence regime.

5.6.7.2 Link Measurements

Finally, for testing the proposed antenna over a hybrid link, the measurement was carried out in an indoor environment over a 13.3 m link span using two antennas with gains of ~28 dBi and ~31 dBi, see Figure 5.33. The FSO and RF transceivers parameters are the base on Table 5.6. The measured received power of the RF signal and measured SNR at the Rx were ~-30 dBm and ~42 dB, respectively. Note that the predicted transmit

Table 5.13: FSO Link budget for different turbulence conditions and combining methods.

Turbulence condition	$\sigma_R^2 = 0.5$		$\sigma_R^2 = 1.0$	
Combining method	EGC	SC	EGC	SC
Required SNR (dB)	20.7	24.1	23.6	26.9
Tx SMF loss (dB)	0.2			
Tx fibre to FSO coupling loss (dB)	2			
Total geometrical loss A_{total} (dB)	14			
Rx FSO to fibre coupling loss (dB)	2			
Rx POF loss (dB)	2			
Total loss (dB)	20.2			
Noise floor (dBm)	-51.06			
Required laser power (dBm) ($\frac{1}{2}\text{SNR} + \frac{1}{2}\text{Noise floor} + \text{Total loss}$)	-10.16	-6.76	-7.26	-3.96
Maximum safe pointer laser power (dBm)	2.2			
Link margin (dB) (Maximum safe pointer laser power – Required laser power)	12.36	8.96	9.46	6.16

power of the RF signal is -26 dBm, which is 4 dB higher than the measured value. This difference is due to antennas misalignment and cable losses. The SNR was measured while a 6.7 Mbps BPSK signal was transmitted over the link. For a BER of 10^{-6} the required SNR for the RF signal is ~8.8 dB [67]. For a longer range transmission link one could include additional amplification stage at the Rx side to achieve the required SNR.

For the FSO path the output power of the Tx aperture was set to be ~0 dBm. The diameter of the optical beam footprint at the Rx was 400 mm, which was much larger than the optical aperture. The measured optical power at the output of fibres were -22.3 dBm, -21.5 dBm, and -22.7 dBm, thus the measured average loss of the free space channel being ~22.2 dB. Considering the RX footprint of 400 m, the predicted value of channel loss is $A_{\text{total}} = 21.1$ dB from Equ. (5.20). For a BER of 10^{-6} in clear channel, the required Q-factor will be 4.8, which is lower than the measured Q-factor of 5.8. The Q-factor of 5.8 is almost equivalent to a SNR of 15 dB [149].

All the measured and predicted values are summarised in Table 5.14. Note that there is a significant difference between the predicted and measured RF SNR, which is due to.

larger noise temperature. The difference between the predicted and measured Q-factor is also due to the ambient noise was not considered in the calculation and the noise floor of the receivers were calculated based on the provided technical specifications.

According to Table 5.13, a minimum SNR value of 21 dB is required to combat the turbulence with $\sigma_R^2 = 0.5$ using the EGC method, which the link with a large optical footprint cannot achieve it. However, by reducing the size of the optical footprint to 85 mm at the Rx, the total loss, including the fibre and coupling, drops down to 11.6 dB. Thus the received optical power level and the SNR will be of -12 dB and ~26 dB, respectively, which are higher than the case with a large optical footprint. With this SNR value it is therefore possible to mitigate even the turbulence (i.e., $\sigma_R^2 = 2$) with employing the EGC method.

Table 5.14: Summary of the measured and predicted link characteristics of the hybrid link of 13.3 m.

Parameter	Predicted	Measured
RF received power	-26 dBm	-30 dBm
RF SNR at the receiver	> 50 dB	42 dB
Received optical power after the fibre 1	-21.1 dBm	-22.3 dBm
Received optical power after the fibre 2	-21.1 dBm	-21.5 dBm
Received optical power after the fibre 3	-21.1 dBm	-22.7 dBm
Optical channel loss	21.1 dB	22.2 dB
Received FSO Q -factor	> 10	5.8

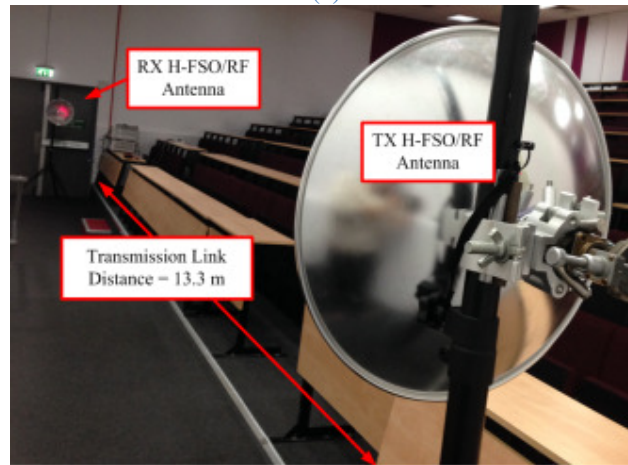
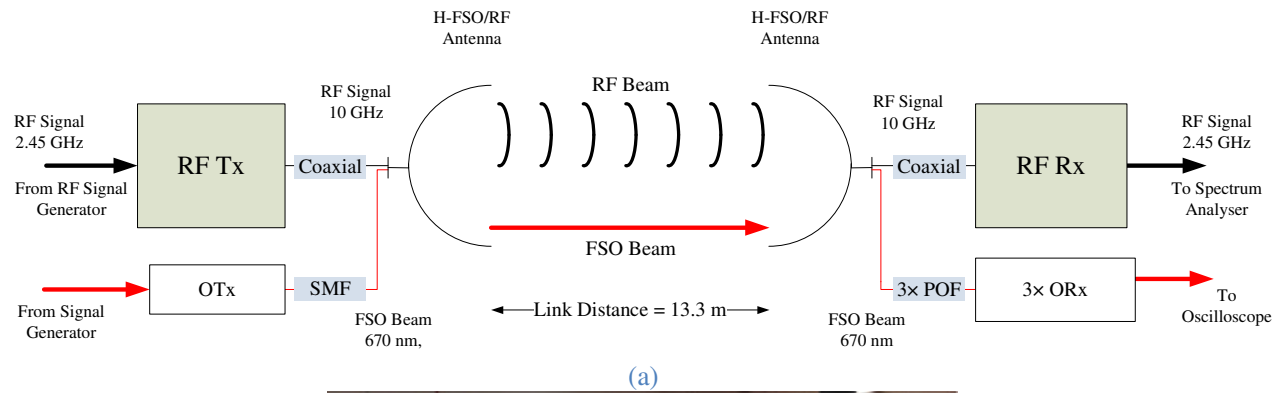


Figure 5.33: (a) Block diagram of the performed hybrid link test, and (b) image taken from the experimental hybrid link setup.

5.7 Detection Method

As mentioned before, a proper method to combat the ambient light effect is also required to improve the performance of the hybrid antenna for outdoor applications. This matter will be discussed in the next chapter.

5.8 Summary

A practical hybrid antenna design was proposed and then characterized. The antenna was based on Cassegrain antenna design with FSO part embedded later on. First in a step by step design guideline, the effect of adding extra parts regarding the FSO antenna was simulated and described. Then closed-form equations were derived to describe the effect of optical part on the RF part. The simulation results were used to support the theory and confirm the design. Then the antenna was fabricated and radiation pattern measurement as well as assessment of the antenna in a hybrid link were carried out. The measurement showed that the initial design of antenna without optical part had a total efficiency of 44% while after optimisation and the inclusion of the FSO part the efficiency reached to 59%. It was shown that the overall low efficiency of antenna was due to insufficient illumination efficiency. A link budget analysis was performed to investigate the performance of the FSO part in weak and moderate turbulence regimes. Since the final design of the antenna implemented FSO spatial diversity, the performance of FSO link using three receiver apertures for EGC and SC combining techniques was also presented. For a test indoor environment, the SNR of received RF signal as well as the Q-factor of received optical signal were measured. To extend the range of hybrid link from the experimental indoor test to an outdoor practical link, the link budget analysis for FSO

part was carried out and the required changes to the system were investigated. Since the ORx had multiple output signals, also the required combining technique to combat the turbulence was discussed, and it was shown that the proposed antenna is operational over a 1 km link under turbulent condition.

6 HYBRID FSO/RF LINK

6.1 Introduction

In this chapter, the performance of hybrid antenna in a real scenario is evaluated, where the condition of the channel is based on the recorded data. First, the chapter outlines a communication system based on the proposed hybrid antenna, and then the process of simulating the performance of the entire system is described. Finally, the requirements of the system to extend the link range, data rate, and system availability are discussed.

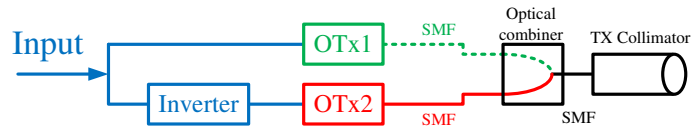
6.2 FSO System Configuration

In Chapter 5, the need for a method to combat the effect of ambient light in FSO system in outdoor applications was mentioned. In [35], the authors used a differential technique to eliminate the background noise in OOK based intensity modulation FSO system. The basic concept outlined is similar to the proposed differential signalling technique in this research, see Chapter 4. Therefore, employing the differential signalling technique at each aperture to mitigate the effects of turbulence and pointing errors will also reject (or reduce) the background noise level. Thus, to mitigate turbulence, pointing errors and background noise, a FSO system implementing the differential signalling technique and spatial diversity method is proposed.

The proposed FSO system is shown in Figure 6.1, where two different wavelengths are adopted for optical transmitters OTx1 and OTx2, which are passed through two individual optical fibres. After combining the optical signals are coupled into free space and transmitted. At the receiver side, three individual collimators are used to capture the received beam. Then two different wavelengths are separated by means of optical splitter and proper optical filters OF1 and OF2 tuned for each wavelength. The received optical powers are converted into electrical signal by using PD ORxs. Three subtractions stages are needed to perform differential signalling and to reduce the background noise and a summation module is used as part of the EGC. Since the same Rx aperture for differential signals are being used, then the channels are assured to be highly correlated in order to significantly reduce effects of weak turbulence and pointing errors, see Chapter 4. Provided the ORxs are not saturated the effect of background illumination is also mitigated as outlined in [35]. However, under severe weather conditions (e.g., fog, smoke, strong turbulence) and severe pointing errors where the FSO link fails to operate the back-up RF link will ensure link availability with maintained performance quality.

6.3 Switching Technique

In hybrid systems, FSO is the default link and in case of any link failure, the data transmission is carried out using the RF link. Switching between FSO and RF link is a vast topic to be studied and the detailed discussion on this is out of the scope of this research.



FSO Channel

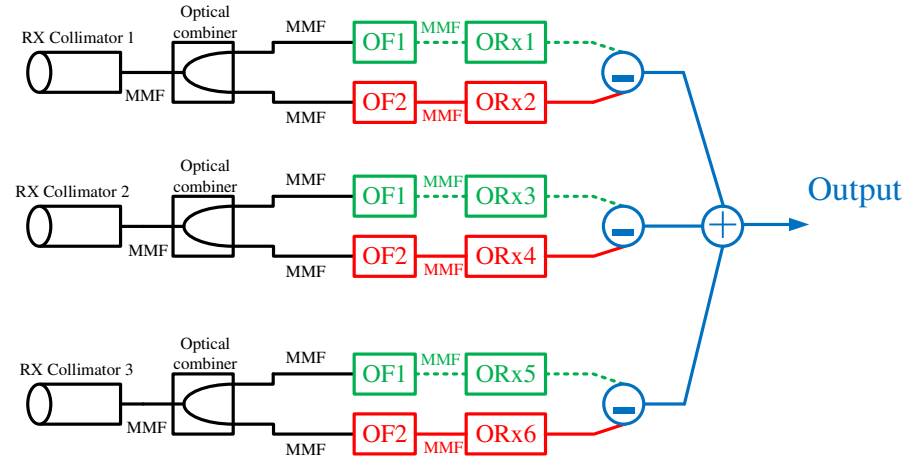


Figure 6.1: The block diagram of the proposed FSO link with hybrid antenna. OTx, SMF, MMF, OF, and ORx are optical transmitter, single mode fibre, multimode fibre, optical filter, and optical receiver, respectively. Green dashed line and solid red line corresponds to two separate wavelengths.

However, in order to evaluate the functionality of the proposed antenna, a simulation will be performed under fog and rain channel situations. The channel conditions are set based on the recorded data from outdoor meteorological instrument over a transmission range of 500 m in the Faculty of Electrical Engineering, Czech Technical University in Prague, Czech Republic. The measurement was performed from 2013 to 2014, which includes the precipitation level in millimetre and the visibility in metre.

6.4 System Specifications

The parameters used for antenna structure are based on Chapter 5, which includes the known gain and coupling losses. Other parameters such as the output power, data rate, etc. are fixed to typical values. All the parameters are given in Table 6.1. For the required BER of 10^{-6} and the NRZ-OOK based FSO system, the required minimum SNR is 13.54 dB. On the other hand, for the RF link with BPSK, the required SNR is at least 8.79 dB. Knowing the required SNRs and the noise floor, the necessary thresholds (i.e., the minimum detectable received power ($\min P_r$)) for both FSO and RF links can be defined as:

$$\min P_r = \text{SNR} + \begin{cases} \text{NEP}\sqrt{\text{BW}}, & \text{FSO Link} \\ k_B(T_e + T_{\text{antenna}})\text{BW}, & \text{RF Link} \end{cases}, \quad (6.1)$$

where NEP ($\text{W}/\sqrt{\text{Hz}}$) denotes the noise equivalent bandwidth of the ORx. BW, k_B , T_e , and T_{antenna} are the bandwidth, Boltzmann's constant, RF Rx noise temperature, and RF antenna noise temperature, respectively. Therefore, the switching threshold levels for FSO and RF links are -21 dBm and -82.71 dBm, respectively.

Table 6.1: hybrid FSO/RF system parameters.

Parameter	Value
$\lambda_{\text{FSO},1}$	780 nm
$\lambda_{\text{FSO},2}$	830 nm
Modulation scheme	NRZ-OOK
FSO data rate	100 Mbps
Noise equivalent power of optical receiver	35 pW/ $\sqrt{\text{Hz}}$
FSO/Fibres coupling losses at receiver	3.5 dB
Optical power after Tx aperture	3 dBm
FSO total geometrical loss	8.57 dB
FSO source extinction ratio	20
FSO PD responsivity	1 A/W
f_{RF}	10 GHz
Modulation scheme	BPSK
RF data rate	6.7 Mbps
RF receiver noise temperature	4.1° kK
Antenna gain	31.4 dBi
RF power before Tx antenna	-10 dBm
Gain from Tx antenna to receiver (direct wired connection)	7.84 dB
Switching method	TH
Time threshold	10 s
Switching delay	1 s
Link Distance	500 m

6.5 Recorded Data

Before describing the simulation procedure, it is a good practice to study the channel conditions. The data collected from meteorological measurement is for the January 2014. The visibility was recorded at the rate of one sample per every 5 seconds whereas the precipitation measurement was carried out at the rate of one measurement per minute.

Figure 6.2(a) illustrates the recorded visibility. The average, standard deviation, minimum and maximum of the recorded visibility in this period are 11.76 km, 6.68 km, 0.14 km, and 20 km, respectively. A maximum range of 20 km was the measurement

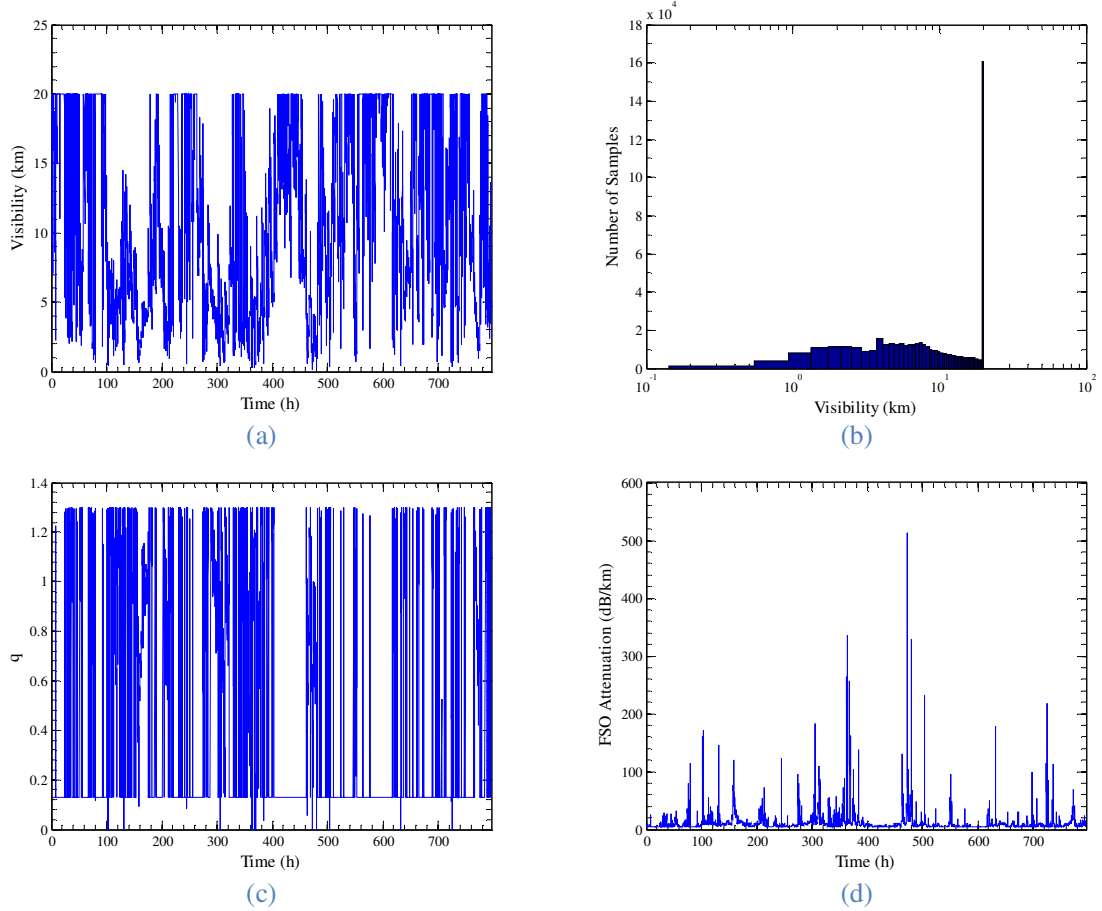


Figure 6.2: (a) Recorded visibility for January 2014; (b) histogram of recorded visibility. The spike is due to the measurement limitation of the gauge and the visibilities more than 20 km are truncated to 20 km; (c) calculated q parameter based on the recorded visibility; and (d) FSO attenuation based on the recorded visibility. The average, standard deviation, minimum and maximum of the recorded visibility in this period are 11.76 km, 6.68 km, 0.14 km, and 20 km, respectively.

device limitation. The histogram of visibility is plotted in Figure 6.2(b). Apart from the spike, which is due to the device limitation, the histogram shows that most of the recorded visibility data are within the visible range of 1 km to 10 km and for only several occasions the visibility is reduced below 1 km. From the visibility plot and Equ. (2.2), the parameter q is determined as depicted in Figure 6.2(c). Having q , it is possible to determine the attenuation of the FSO link in fog condition. As mentioned before, two distinct wavelengths have been used and the shorter wavelength have been considered for the worst case scenario, which results in higher attenuation, see Figure 6.2(d).

Figure 6.3(a) shows the precipitation data with the average, standard deviation, minimum and maximum of 38.05 mm, 12.01 mm, 1.4 mm and 102.3 mm, respectively.

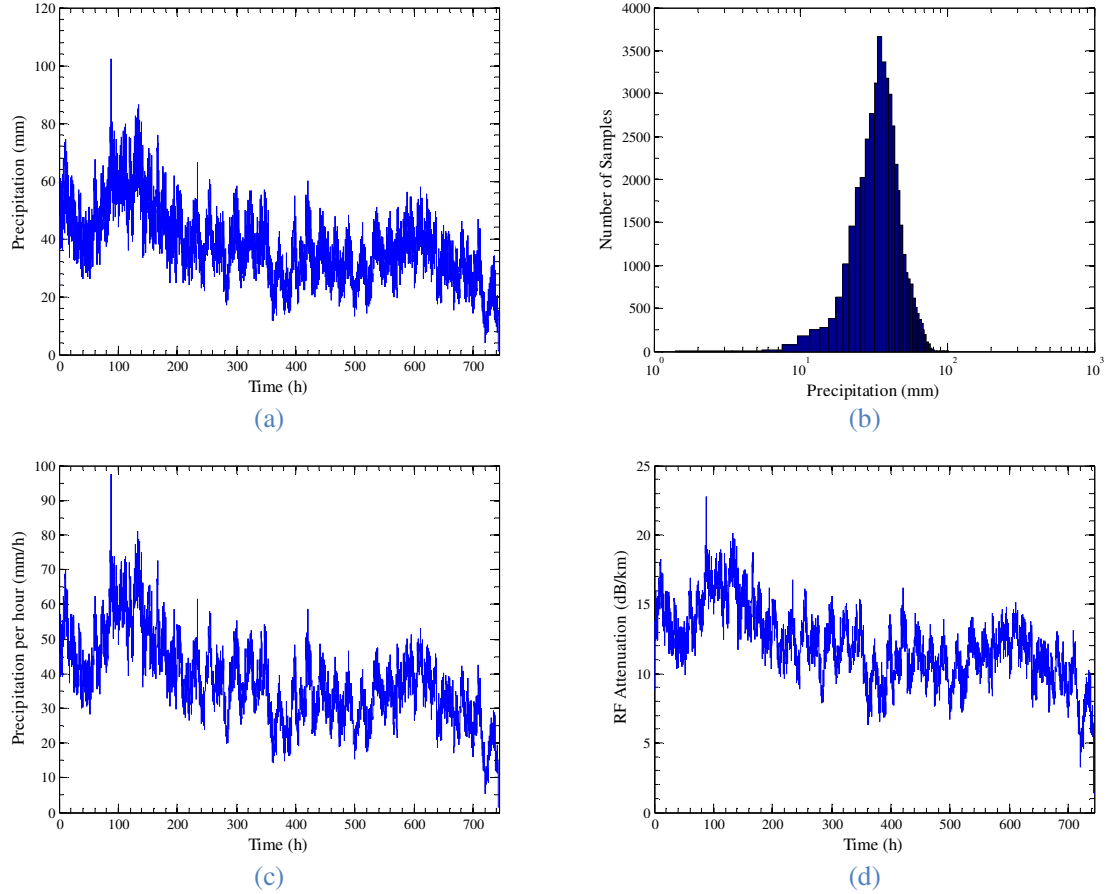


Figure 6.3: (a) Recorded precipitation for January 2014; (b) histogram of recorded precipitation, (c) processed precipitation per hour; and (d) RF attenuation due to the rain. The average, standard deviation, minimum and maximum of the recorded precipitation in this period are 38.05 mm, 12.01 mm, 1.4 mm and 102.3 mm, respectively.

As seen from Figure 6.3(b), the distribution concentrated around a mean value of 38.05 mm shows no significantly heavy rain in that month of the year. To be able to use standard formulas for the rain attenuation, the raw data needs to be changed into precipitation per hour. This was done by performing the moving averaging over 60 span points for the entire month, and the result is illustrated in Figure 6.3(c). The final step was to convert the data in Figure 6.2 into rain induced attenuation. This was easily done by using Equ. (2.14). The rain attenuation based on the recorded data is depicted in Figure 6.3(d).

In the next section the simulation procedure for the given parameters in Table 6.1 is described.

6.6 Simulation Procedure

In the simulation the smallest time step of 5 seconds was chosen. It was assumed that during this period the channel status is the same and information on CSI is already available at both Tx and Rx or provided via a feedback path. Considering these assumptions, the flowchart for the switching mechanism is the same as in Figure 6.4. The simulation was performed based on the algorithm and given parameters.

First, the links status are studied as shown in Figure 6.5(a), which shows two states of ‘Off’ and ‘On’. The ratio of FSO ‘On’ to ‘Off’ state $\mathbb{R}_{\text{FSO}} = 303.64$ (i.e., the FSO link is active and transmitting), which is quite large for the case where the FSO link the dominant transmission path. As for the RF link the histogram is depicted in Figure 6.5(b). The RF ‘On’ and ‘Off’ state ratio \mathbb{R}_{RF} is infinity, which indicates that the RF link is always operational under the given channel condition. The ‘On’ and ‘Off’ ratio is also used as a useful guide to optimize the design. For instance, the transmit power or the amplification at the Rx can be reduced while keeping \mathbb{R}_{RF} as large as possible.

The histogram of the link connectivity is plotted in Figure 6.5(c). “-1” and “+1” are used to indicate ‘On’ and ‘Off’ states of FSO and RF links, respectively. For the case that none of the links are available, “0” is used. The link load for each case is given as:

$$\text{Link Load} = \frac{\text{Number of transmit bits by FSO} \times -1 + \text{Number of transmit bits by RF} \times +1}{\text{Number of total transmit bits}}, \quad (6.2)$$

where $-1 \leq \text{Link Load} \leq +1$. The ideal in a hybrid system is to make Link Load as close as possible to -1. For the given communication system, the Link Load is -0.93. Apart from the aforementioned analysis, one also can use the histogram data to estimate other useful parameters such as the power consumption.

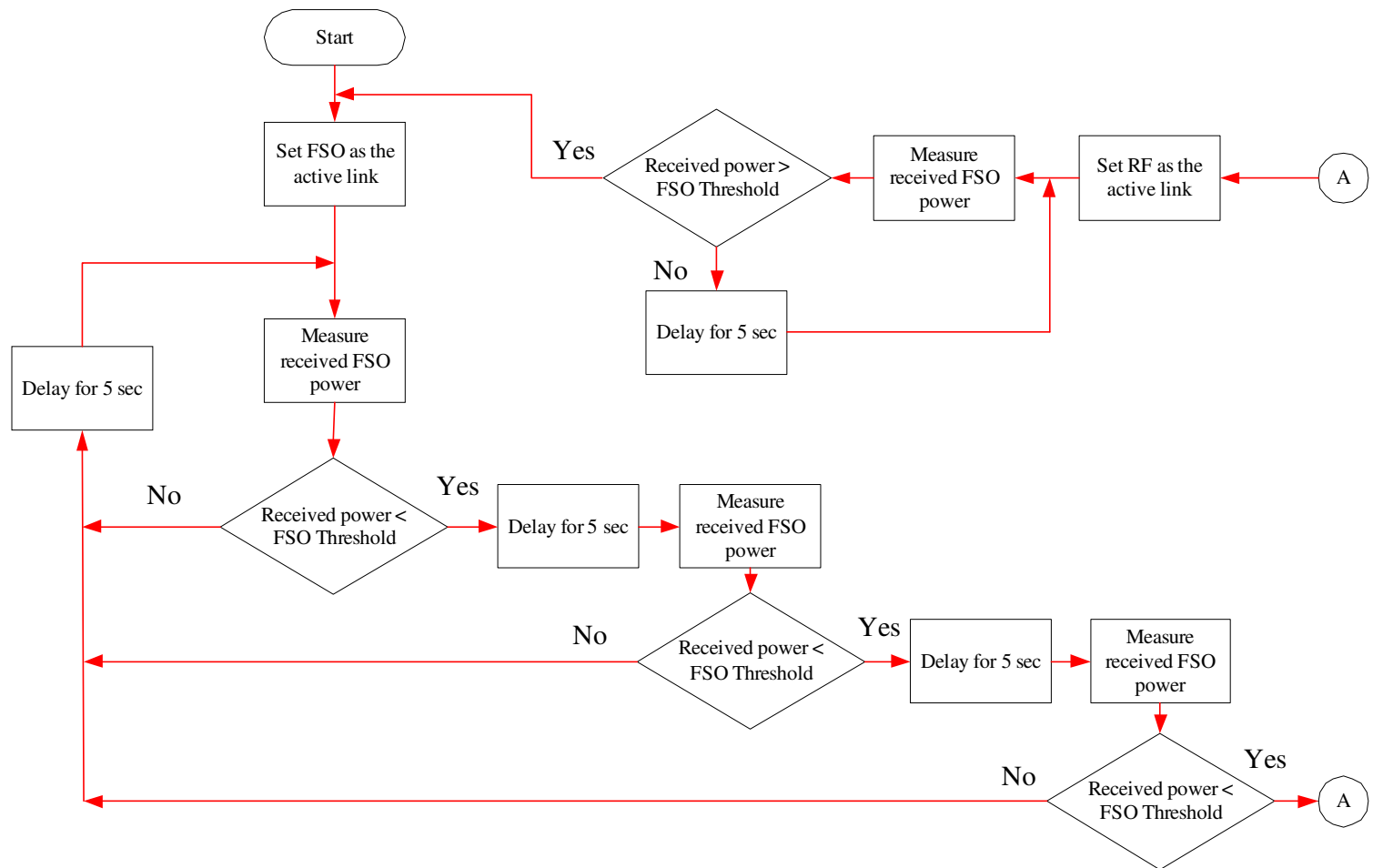


Figure 6.4: The Flowchart of the time hysteresis (TH) switching process in a hybrid communication system. The TH delay is 10 seconds.

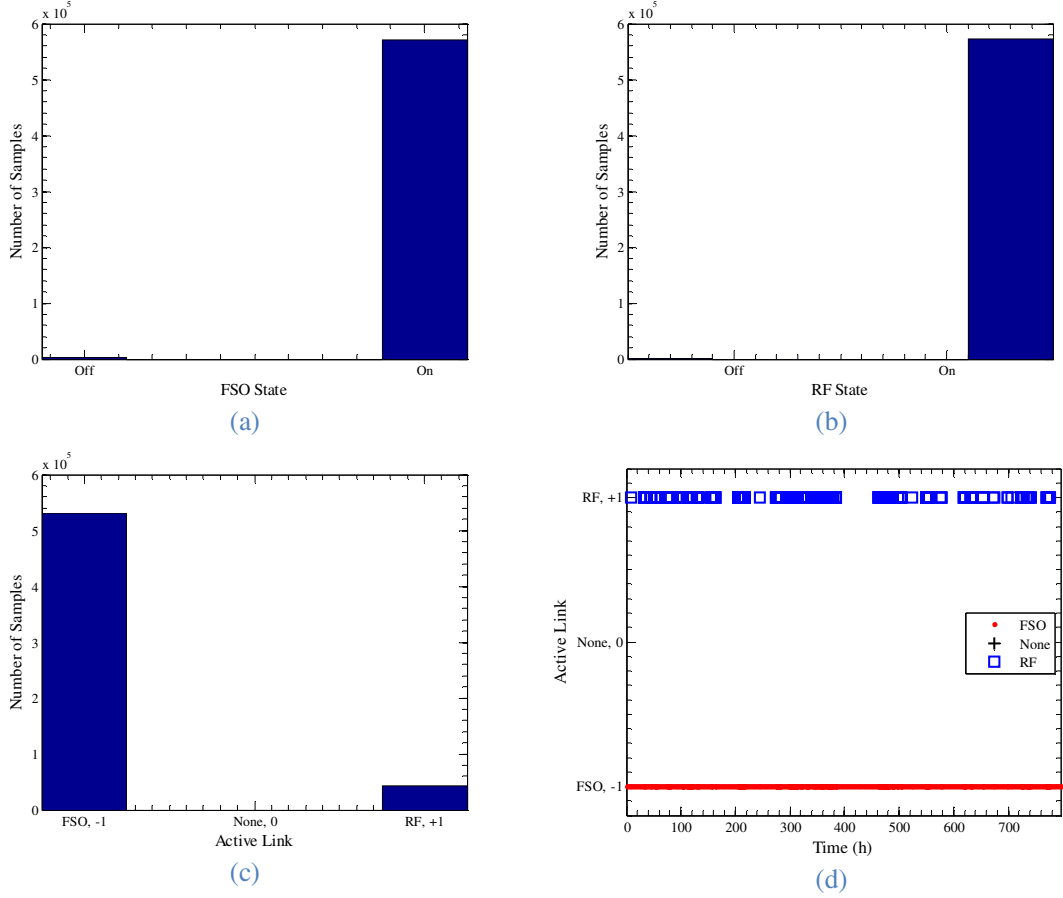


Figure 6.5: (a) Histogram of the FSO link status; (b) histogram of the RF link status; (c) histogram of active link; and (d) trace of active link versus time.

Link load value of -0.93 shows that the FSO link is the dominant link, which is also reflected by observing the link activity trace over the entire time period as shown in Figure 6.5(d). Finally, the link availability and the average data rate were determined by considering the delay time of 1 sec for switching. Based on the simulation, the link availability and the average data rate were 99.9964% and 51.41 Mbps, respectively. Table 6.2 compares the performance of the current system with the results from other investigations including: soft switching [82], raptor code [2], and hard switching [84].

Table 6.2: Comparison between various hybrid system performances in terms of data rate and availability.

Scheme	Reference	Average data rate (Mbps)	Availability (%)
Soft switching, raptor code	[82], [2]	587.9	64%
Hard switching, TH	[84]	66.5	99.28%
Hard switching, PH	[84]	60.6	99.69%
Proposed system	-	51.4	99.99%

Although the proposed system cannot provide the average data rate of 587.9 Mbps (see Table 6.2) as in soft switching method, it provides the same availability range compared to the reported systems in Table 6.2.

6.7 Numerical Analysis

Using the parameter given in Table 6.1 and Equ. (6.1) the calculated minimum required received power of FSO and RF systems for given data rate is shown in Figure 6.6. In the FSO link for a data rate of 1 Mbits/sec the received power of ~ -30 dBm is needed, which increases to ~ -10 dBm for 10 Gbits/sec. Since the maximum RF bandwidth in the existing system is 100 MHz, and using Equ. (2.10) the RF data rate is set to a maximum value of 67 Mbits/sec. However, the data rate of the FSO link is varied from 10 Mbits/sec to 10 Gbits/sec. For a clear channel of 1 km long, the required RF transmit power was obtained to be ~ -32 dBm while for the FSO link transmit power against the data rate of 10 Mbits/sec to 10 Gbits/sec is shown in Figure 6.7. Based on the laser safety regulations, the output power of an infrared laser must be less than 2.5 mW (i.e., ~ 4 dBm) if the laser is a pointer source [150]. However, if a wide collimated laser beam is used, the total

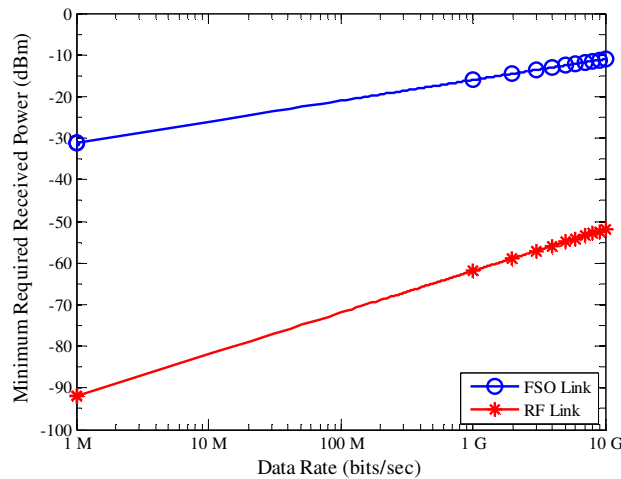


Figure 6.6: Minimum required received power versus data rate for FSO and RF links where the system parameters are based on the values from Table 6.1.

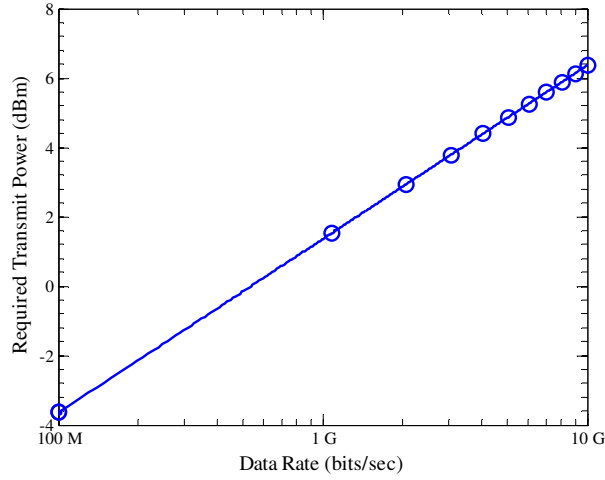


Figure 6.7: Required FSO transmit power versus data rate for 1 km long clear channel where the system parameters are based on the values from Table 6.1.

power could be different. Therefore, first it is essential to calculate maximum permissible exposure (MPE) of the laser given as [151]:

$$\text{MPE} = 10^{2\left(\frac{\lambda_{\text{FSO}}}{1 \mu\text{m}} - 0.7\right)} \times 10^{-3} \left(\frac{\text{W}}{\text{cm}^2}\right). \quad (6.3)$$

For wavelengths of 780 nm and 830 nm the MPEs are $1.5 \text{ mW} \cdot \text{cm}^{-2}$ and $1.8 \text{ mW} \cdot \text{cm}^{-2}$, respectively. The maximum safe output power of the laser with beam radius of w_{Tx} emerging from the collimator is given by:

$$\text{Maximum Safe Power} = \text{MPE} \times \pi w_{\text{Tx}}^2 \text{ (W)}. \quad (6.4)$$

For the collimator used at the Tx aperture, the maximum safe power levels are 11.4 dBm and 12.4 dBm for wavelengths of 780 nm and 830 nm, respectively. Thus, considering the required transmit power for the 10 Gbits/sec data link and the maximum safe powers the link margins are $\sim 5 \text{ dB}$ and $\sim 6 \text{ dB}$, respectively.

6.7.1.1 Fixed Link Distance

In this section, the link distance was fixed to 0.5, 0.75, 1, and 1.5 km and to achieve higher average hybrid link data rate, the FSO data rate was varied from 100 Mbits/sec to 10 Gbits/sec. Following the procedure in Section 6.6 and considering the channel conditions, the link load, average hybrid data rate and availability of the link were

calculated, see Figure 6.8. The link load curve shows that for link spans of 500 m and 750 m, most data transmission is via FSO link, see Figure 6.8(a). However, for a link of 1.5 km long, at higher data rates (i.e., > 8 Gbits/sec for the FSO link) the RF link is the dominant link (note that link load graph drifts towards +1).

The more RF is active, see Figure 6.8(a), the less the average hybrid data rate will be, see Figure 6.8(b). For the link distance of 1.5 km, the FSO link is not available; whereas the RF link is frequently available with an average received power level higher than -72 dBm, see Figure 6.9. For a 1.5 km link span, the average hybrid data rate drops from ~ 150 Mbits/sec to ~ 43 Mbits/sec. Therefore, for this link span, the hybrid system is

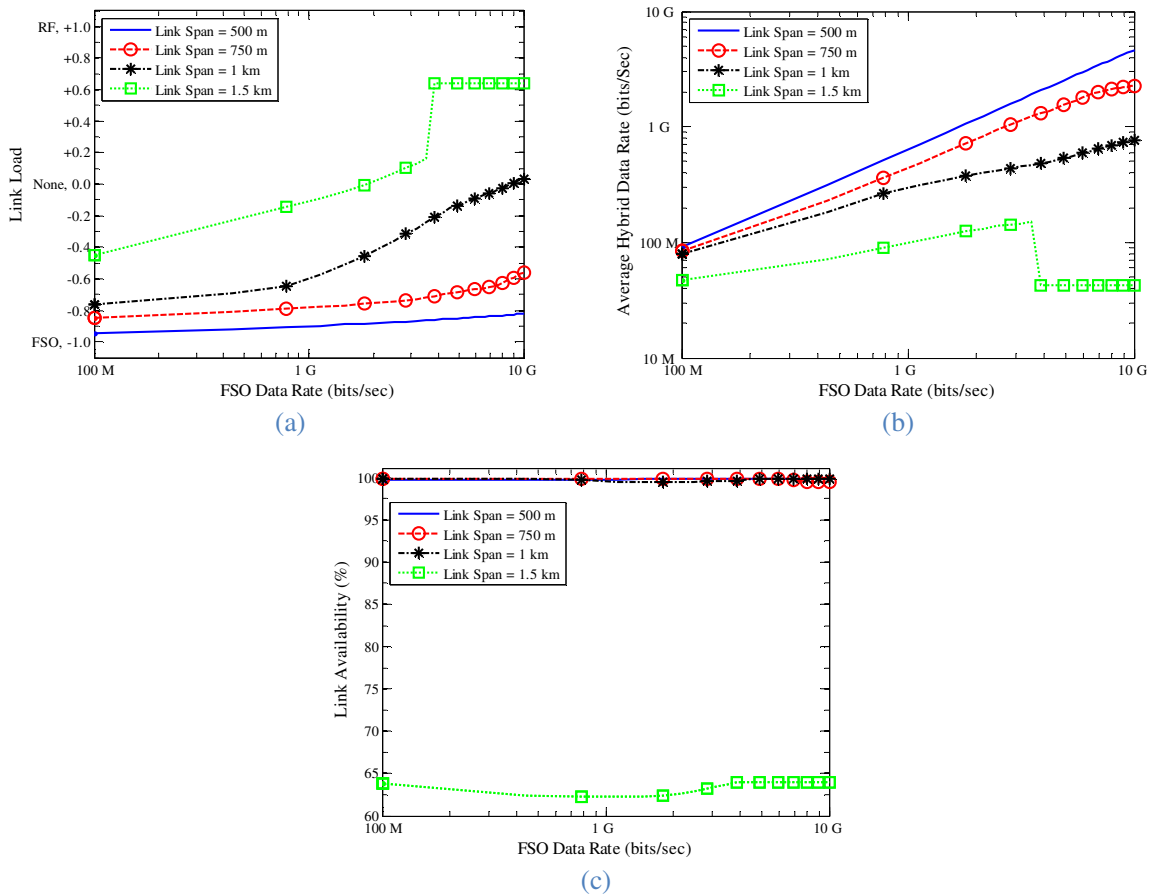


Figure 6.8: Hybrid link simulation for link distances of 500 m, 750 m, 1 km, and 1.5 km for FSO data rate of 100 Mbits/sec to 10 Gbits/sec: (a) link load, (b) average hybrid data rate, and (c) link availability. The RF link has a fixed data rate of 67 Mbits/sec and the other system parameters are according to Table 6.1.

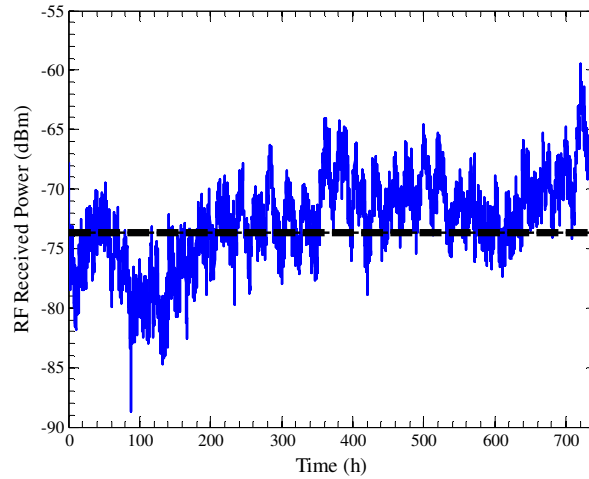


Figure 6.9: Received RF power versus time of channel state. The RF link has a fixed data rate of 67 Mbits/sec, the link span is 1.5 km, and the other system parameters are according to Table 6.1. The black dashed line is the threshold level for acceptable RF performance.

practically not useful and it is better to use a single RF link. Considering the link availability as in Figure 6.8(c) the hybrid link offers lower link availability for a transmission span of 1.5 km. Therefore, it would be wiser to use a single RF link, which offers 64 % link availability and an average data rate of ~ 43 Mbits/sec. The link availability for 500 m, 750 m and 1 km link is > 99.45 % for a given FSO data rate range.

6.7.1.2 Fixed RF and FSO Data Rate

This section includes the assessment, where the data rate of both FSO and RF links are fixed. Here the goal is to change the link span and determine the same parameters as in the previous section, with results depicted in Figure 6.10. For a link distance > 2.5 km both FSO and RF links are not available, see Figure 6.10(a). For short ranges, FSO can deliver the required data rate, but not for longer transmission spans because of increased attenuation. At a distance between 1 km to 2 km, RF attenuation is also high and making it unavailable. Thus, the link load drifts towards 'None' (i.e., none availability of both FSO and RF links), as indicated by the peaks in the link load graphs. Note that, for higher speeds the peak is more noticeable.

The average hybrid data rate illustrated in Figure 6.10(b) shows a rapid drop after a 1

km, reaching 10 kbits/sec for a transmission span of 4 km. Note that, reduction in the average data rate is compatible with the FSO and RF link unavailability as shown in Figure 6.10(a). The hybrid link availability is depicted in Figure 6.10(c), where for a link distance > 2.5 km the hybrid link availability is 0 % as expected. Note that, prior to deterioration of the hybrid link availability both links display a minimum link availability of 99.48 %.

6.7.1.3 Maximum Average Hybrid Data Rate and Guaranteed Link Availability

To increase the hybrid average data rate, one approach would be to increase the FSO data rate. However, for higher data rates a Rx employing a PD with a higher sensitivity and smaller surface area is needed. The latter has implications on the influence of the

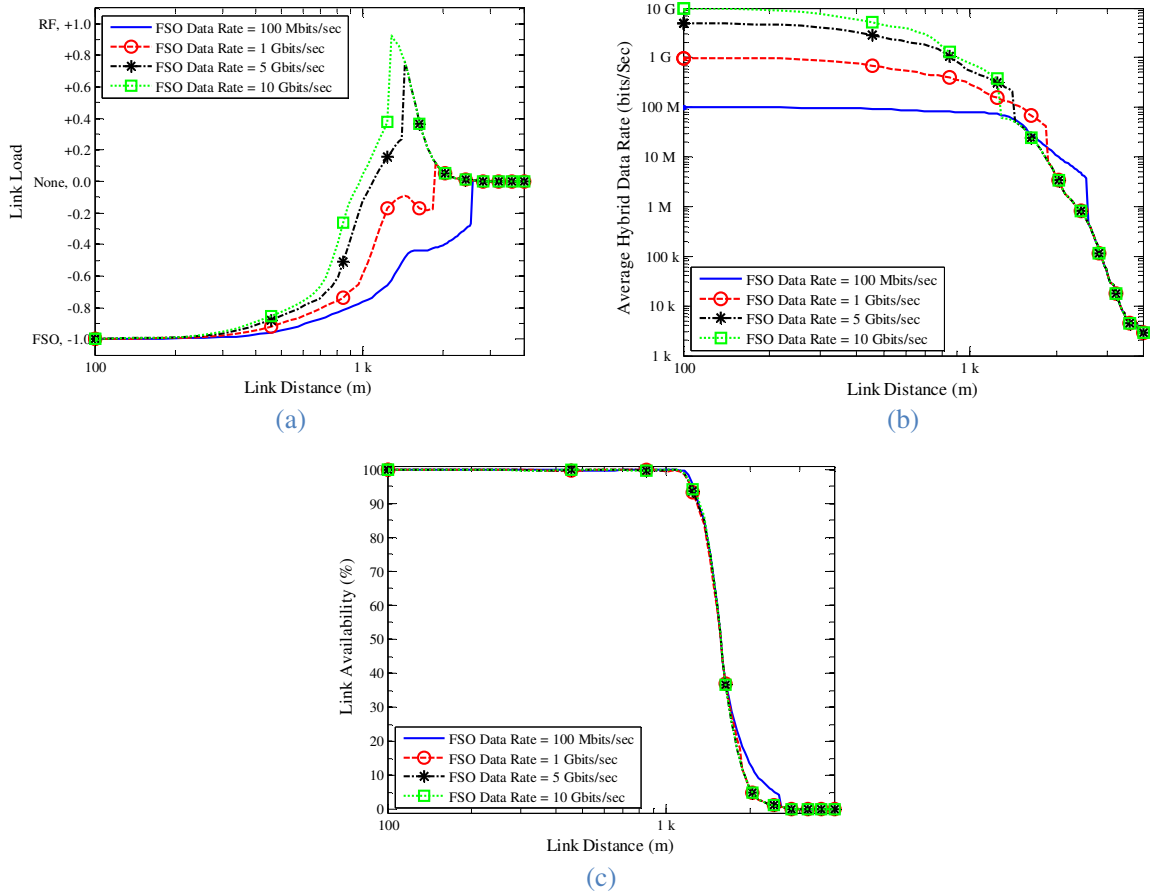


Figure 6.10: Hybrid link simulation for FSO data rate of 100 Mbits/sec, 1 Gbits/sec, 5 Gbits/sec, and 10 Gbits/sec for link distance of 100 m to 4 km: (a) link load, (b) average hybrid data rate, and (c) link availability. The RF link has a fixed data rate of 67 Mbits/sec and the other system parameters are according to Table 6.1.

turbulence as well as the pointing errors (i.e., worsening link performance). Thus for the same Rx system, increasing the FSO bandwidth will not necessarily improve the performance of hybrid link. Therefore, there is a trade-off between the given link distance and availability, Rx size, and the maximum data rate. This is also the case for the RF link. Therefore, this whole design problem turns into an optimisation problem, where the goal is to maximise the average hybrid data rate while the link availability is constrained to be greater than a given value.

Since the states of individual FSO and RF links are dependent on the channel, therefore adopting a closed form expression for the optimisation problem is a challenging task. However, it is possible to solve this problem by means of numerical analysis. Table 6.3 represents a set of results for given specifications determined by means of a trial and error. The RF link is bounded to have a data rate in the range of 1-67 Mbits/sec while the FSO link data rate can be from 10 Mbits/sec to 10 Gbits/sec. The guaranteed link availabilities are 90, 99, 99.5 and 99.8 % and the hybrid link distance are 0.5, 0.75, 1, 1.25, 1.5, 1.75 km. The results in Table 6.3, confirms the previous conclusion that a FSO or a RF link with a higher data rate does not ensure higher link availability or higher hybrid data rate. For example, for a maximum average hybrid data rate of 1990 Mbits/sec and a link distance of 750 m, the FSO link with a data rate of 6.85 Gbits/sec offers improved performance than a FSO data rate of 10 Gbits/sec. Indeed, for the same parameters but for a data rate of 10 Gbits/sec the link availability drops to 99.5 % although the average data rate is 2.2 Gbits/sec.

Solutions to increase the data and achieve higher link availability are: (i) to redesign the optical aperture at the Rx in order to capture more optical power, (ii) more advanced modulation schemes, (iii) increase the transmit optical power, and (iv) employ an ORx

Table 6.3: Maximum average hybrid data rate and guaranteed link availability for various distances. The required FSO and RF data rates are denoted for each case and the other system parameters are according to Table 6.1. The FSO data rate range was from 10 Mbits/sec to 10 Gbits/sec, whereas the RF data rate range was from 1 Mbits/sec to 67 Mbits/sec.

Maximum average hybrid data rate (bits/sec)	Guaranteed link availability (%)	Link distance (m)	FSO data rate (bits/sec)	RF data rate (bits/sec)
346 M	98	1.25 k	10 G	42.68 M
2.28 G	99	750 m	10 G	67 M
340 M	99	1.25 k	10 G	35.74 M
113 M	99	1.5 k	3.16 G	7.95 M
2.12 G	99.5	750 m	7.90 G	67 M
337 M	99.5	1.25 k	10 G	32.26 M
110 M	99.5	1.5 k	3.16 G	4.47 M
39 M	99.5	1.75 k	1.06 G	1 M
4.63 G	99.8	500 m	10 G	67 M
1990 G	99.8	750 m	6.85 G	67 M
770 M	99.8	1 k	10 G	67 M
317 M	99.8	1.25 k	10 G	11.42 M
106 M	99.8	1.5 k	3.16 G	1 M
1 M	99.8	1.75 k	1.59 G	1 M

with much higher sensitivity. For example for the aforementioned case, using an ORx with a NEP of $25 \text{ pW}/\sqrt{\text{Hz}}$ and a data rate of 10 Gbits/sec, an average data rate and a link availability of 1 Gbits/sec and 99.84 %, respectively can be achieved.

6.8 Summary

In this chapter, the detection threshold method, combining method and required switching method were proposed for a communication system employing the hybrid antenna. By using the differential signalling method, the FSO system was protected against the weak turbulence regime, background illumination and pointing errors. It was also discussed that EGC improves the performance of the FSO link under the moderate to strong turbulence regime. Under fog conditions the FSO link was changed to the backup RF link and the link performance was investigated based on the recorded data. Both the link availability and the average data rate were assessed using the recorded

channel condition. Link assessment were performed to investigate the effect of FSO data rate on the link availability, and on the hybrid data rate. It was shown that for higher FSO data rates, the hybrid system offers higher speed but lower link availability. Another assessment where the distance was varied showed that as expected the longer link distances lead to less availability and lower hybrid data rates. Finally, the method to obtain the maximum data rate and a guaranteed availability for a given distance was presented.

7 CONCLUSIONS AND FUTURE WORK

7.1 Conclusions

This thesis has outlined the design, optimisation and evaluation of the hybrid antenna for a hybrid FSO/RF system. The proposed hybrid system benefits from the high speed transmission capability of FSO and the backup link availability of RF in situations where the FSO link is down. The thesis started by introducing the fundamentals of FSO and RF schemes followed by the channel effects such as fog/smoke and rain on the performance and link availability of both FSO and RF links. For the FSO link, three Rx configurations with the spatial diversity scheme as an optimisation and mitigation method to combat the effect of turbulence was introduced. A new combining method of MLC, adopted from RF technology, implemented in the logical domain was further introduced. The closed-form BER expressions for this combining scheme were presented and the link performance in terms of the BER and optical power penalties were assessed and compared. It was shown that the SC scheme offered the lowest implementation complexity, whereas it was shown that the AOT scheme may not be suitable due to its relatively high cost and complexity. The proposed MLC method offered the best performance for $M > 3$ and high SNR values.

The thesis also proposed a detection method based on the differential signalling

technique with no requirement for CSI at the Rx, thus no pilot overhead or any noticeable increase in the Rx computational complexity. Using the derived analytical expression for the variance of the detection threshold, it was shown that the fluctuation in the optimal threshold level highly depended on the correlation between the propagating optical beams. Thus the proposed technique is attractive when highly correlated FSO channels can be established. This deduction was validated by means of experimental investigations under uncorrelated and correlated conditions. Also it was discussed that to achieve a high correlated-channel condition, closer wavelength, spatially closer beams and longer transmission distance are critical.

It was also shown with the IM/DD NRZ-OOK FSO modules mounted on the same fixture structure in a building, employing the differential signalling technique with a zero detection threshold level eliminates the effect of pointing errors. The condition that led to highly correlated received signals was studied and a method to obtain the equivalent jitter standard deviation was given. Experimental investigation was carried out to validate the proposed concept. Measured results confirmed that the effect of pointing errors on the received signal was highly correlated (i.e., $\rho = 0.92$), thus resulting in reduced variance value of the combined signal threshold level.

A practical hybrid antenna design was proposed and then its RF and FSO parts were characterized. The antenna was based on Cassegrain antenna design with the FSO part embedded as part of the design. The closed-form equations to describe the effect of optical components on the RF section were derived and simulations were carried out to confirm the predicted results and validate the proposed design. The antenna was fabricated and its radiation pattern and return loss measurements as well as assessment of the antenna for a hybrid link were determined. The measurement showed that the initial design of antenna without FSO had a total efficiency of 44 %; while following optimisation and inclusion

of FSO, the efficiency was increased to 59 %. It was discussed that the overall low efficiency of antenna is due to insufficient illumination efficiency. For the hybrid antenna, the SNR of received RF signal as well as the Q-factor of received optical signal were measured. It was shown that the predicted results were in a good agreement with the measured values. To extend the range of hybrid link, mainly for outdoor applications, the link budget analysis for FSO part was carried out and the required changes that needed to be made to the system were outlined. The report also showed that the proposed antenna could operate over a 1 km link and it was outlined that the combining technique together with an optical Rx can combat the turbulence effects.

Finally, using the recorded channel data from the measurement carried out in Prague, Czech Republic, the performance of a hybrid FSO/RF system employing the proposed antenna was simulated. The TH switching method was used to control the flow of the data. The evaluation showed that the proposed system is capable of providing a high speed link with high availability. The effects of FSO data rate and the transmission span on the link availability and the hybrid data rate were discussed. It was shown that increasing the FSO data rate did increase the hybrid data rate but at the cost of reduced link availability. As it was expected the longer distances led to lower link availability and data rate. The required modifications to achieve the desirable specifications were discussed, for example it was shown that with the existing system one can achieve 1 Gbits/sec hybrid data link under fog and rain channel conditions by using an optical Rx with NEP of $25 \text{ pW}/\sqrt{\text{Hz}}$ and a data rate of 10 Gbits/sec.

7.2 Future Work

For the future work the following needs investigating:

1. In this thesis only the performance of differential signalling under a weak turbulence regime was considered. As an extension to the current work, one can look at the behaviour of the FSO system using differential signalling under moderate and strong turbulence regimes. The outcome of such investigation can result in the closed-form expression for BER. Also it will be possible to compare the performance of the differential signalling technique with other existing methods;
2. In this work pointing errors without turbulence was investigated. This work can be extended by investigating the FSO link performance with both pointing errors and turbulence.
3. The differential signalling technique was only studied for a two-level signal (i.e., NRZ-OOK), and showed that in addition to the mean value of the received signal the signal levels were also affected. Therefore, the differential signalling technique should also investigated with higher order modulations such as M -order pulse amplitude modulation (M -PAM).
4. Only Cassegrain configuration was considered as in Chapter 6. Alternatives configurations could be investigated considering the critical parameters such as the gain, radiation/illumination efficiency, SLL, beam-width and cross polarization, and then propose a design guidelines and specifications.
5. In this project the antenna with offset structure was not considered due to the degradation of X-pol performance. However, with the offset scheme, it is

possible to integrate the FSO aperture without blocking the RF antenna, one needs to investigate the trade-off between the FSO/RF performance and the X-pol discrimination.

6. To fix the sub-reflector a hollow tube was used. However, another option, as mentioned in the text, would be to use a dielectric cone. Therefore, one can consider the possibility of using a dielectric cone not only to hold the sub-reflector in front of the main reflector but also to alter the illumination pattern of Cassegrain antenna. Note that by optimising the illumination pattern it is possible to improve the illumination efficiency of the antenna.
7. The possibility of integrating an optical system with 1550 nm wavelength needs to be studied. In particular, the possibility of using an optical amplifier to improve the overall system performance is an interesting topic for further investigation.
8. In the Design of the optical aperture, a solid lens was used. As a future work, one can investigate the concept of using Fresnel lens as part of the system design.
9. To evaluate the antenna in a real channel conditions, only one switching method was considered. Future work should consider analyses for other switching methods such as PH and combined method.

APPENDIX A: DERIVATION OF MATHEMATICAL EXPRESSIONS

A.1 Introduction

This appendix is devoted to derivation of mathematical used in the thesis. Note that only the original expressions are included and for the rest the reader is referred to the corresponding reference. Also application formulas used through the thesis are also summarised at the end.

A.2 BER Expression in Weak Turbulence

When dealing with the BER expression in weak turbulence in Euqs. (3.19), (3.22), and (3.25); the mathematical simplification will results in an expression in the following form:

$$P(e|1) = \int_0^{+\infty} \frac{1}{2I} \frac{1}{\sqrt{2\pi\sigma^2}} \exp\left(-\frac{(\ln(I/I_0)-2\mu)^2}{8\sigma^2}\right) Q(\psi I) dI. \quad (\text{A.1})$$

By replacing $I = I_0 \exp(2X)$ where X has a normal random distribution in Equ. (A.1), one will obtain:

$$P(e|1) = \int_0^{+\infty} \frac{1}{2I} \frac{1}{\sqrt{2\pi\sigma^2}} \exp\left(-\frac{(x-\mu)^2}{2\sigma^2}\right) Q(\psi I_0 \exp(2x)) dI. \quad (\text{A.2})$$

By replacing $dI = 2I dx$ and setting the integral range one will have:

$$P(e|1) = \frac{1}{\sqrt{2\pi\sigma^2}} \int_{-\infty}^{+\infty} \exp\left(-\frac{(x-\mu)^2}{2\sigma^2}\right) Q(\psi I_0 \exp(2x)) dx. \quad (\text{A.3})$$

Next step by replacing $u = (x - \mu)/\sqrt{2\sigma^2}$, the expression will become:

$$P(e|1) = \frac{1}{\sqrt{\pi}} \int_{-\infty}^{+\infty} e^{-u^2} Q(\psi I_0 e^{2\mu+u\sqrt{8\sigma^2}}) du. \quad (\text{A.4})$$

And at the end in above expression, one spots the following integral:

$$\int_{-\infty}^{+\infty} e^{-x^2} f(x) dx, \quad (\text{A.5})$$

which can be approximated by Gauss-Hermite quadrature formula as in [105] as:

$$\sum_{i=1}^k \omega_i f(x_i), \quad (\text{A.6})$$

where k is the order of approximation, x_i is the zero of the k th-order Hermite polynomial and ω_i denotes the k th-order weight factor.

A.3 BER Expression in Strong Turbulence

To obtain the BER expression for the SC combining method under a strong turbulence regime, the following expression from Section 3.6.3 is considered:

$$P(e|1) = M \int_0^{+\infty} f_I(I) [F_I(I)]^{M-1} Q\left(\frac{\eta}{\sqrt{2MN_0}} I\right) dI, \quad (\text{A.7})$$

where $f_I(I)$ and $F_I(I)$ are defined as Eqs. (3.12) and (3.30), respectively. one can rewrite Equ. (A.7) as:

$$P(e|1) = M \int_0^{+\infty} e^{-I} g(I) dI, \quad (\text{A.8})$$

where $g(I)$ is defined as:

$$g(I) = e^{+I} f_I(I) [F_I(I)]^{M-1} Q\left(\frac{\eta}{\sqrt{2MN_0}} I\right). \quad (\text{A.9})$$

In Equ. (A.8), one spots the following integral:

$$\int_0^{+\infty} e^{-x} f(x) dx, \quad (\text{A.10})$$

which can be approximated by Gauss-Laguerre quadrature formula as in [105] as:

$$\sum_{i=1}^k \omega_i f(x_i), \quad (\text{A.11})$$

where k is the order of approximation, x_i is the zero of the k th-order Laguerre polynomial and ω_i denotes the k th-order weight factor.

A.4 Tolerance of Parameters in Differential Signalling technique

The criterion in Equ. (4.27) will be described here. To derive Eq. (4.27.a) and (4.27.b), one can start from Eqs. (3.6) and (3.3), respectively. The next step is to use central difference to approximate the definition of derivative as following:

$$f'(u) = \frac{df}{du} \approx \frac{f\left(u+\frac{1}{2}\Delta x\right) - f\left(u-\frac{1}{2}\Delta x\right)}{\Delta x} = \frac{\Delta y}{\Delta x}. \quad (\text{A.12})$$

Therefore, one has:

$$\Delta y \approx f'(u) \Delta x = \frac{df}{du} \Delta x. \quad (\text{A.13})$$

To derive Equ. (4.27.c), one can start from Equ. (4.10) which is as following:

$$\rho_{1,2} = \exp \left[- \left(\frac{d_r}{\rho_0} \right)^{5/3} \right]. \quad (\text{A.14})$$

Taking the derivative with respect to ρ_0 results in:

$$\frac{d\rho_{1,2}}{d\rho_0} = \frac{5}{3} \frac{\rho_{1,2}}{\rho_0} \left(\frac{d_r}{\rho_0} \right)^{5/3}. \quad (\text{A.15})$$

From Equ. (A.14) one has $\left(\frac{d_r}{\rho_0} \right)^{5/3} = -\ln \rho_{1,2}$. Therefore, Equ. (A.15) will be simplified to:

$$\frac{d\rho_{1,2}}{d\rho_0} = -\frac{5}{3} \frac{\rho_{1,2}}{\rho_0} \ln \rho_{1,2}, \quad (\text{A.16})$$

which will be approximated as:

$$\Delta\rho_{1,2} = -\frac{5}{3} \frac{\Delta\rho_0}{\rho_0} \rho_{1,2} \ln \rho_{1,2}. \quad (\text{A.17})$$

Finally $\frac{\Delta\rho_0}{\rho_0}$ can be replaced from Equ. (4.27.b) and one will obtain:

$$\Delta\rho_{1,2} = -2\rho_{1,2} \ln \rho_{1,2} \frac{\Delta\lambda}{\lambda_0}. \quad (\text{A.18})$$

A.5 Applicable Formulas

1- The return loss (RL) to VSWR conversion is defined by:

$$\text{VSWR} = \frac{1+10^{\text{RL}/20}}{1-10^{\text{RL}/20}}. \quad (\text{A.19})$$

2- The S parameter to return loss (RL) conversion is given as:

$$\text{RL} = 20 \log_{10} |S_{11}|. \quad (\text{A.20})$$

3- Far-field distance based on the antenna aperture size (D) and the wavelength (λ) is defined as:

$$\text{Far – field Distance} = \frac{2D^2}{\lambda}. \quad (\text{A.21})$$

4- Number of modes (M) in a fibre with a known V -number is:

$$M \approx \frac{V^2}{2}. \quad (\text{A.22})$$

5- Radius (r) of a circumcircle of a regular polygon with n number of sides and side length of a is given as:

$$r = \frac{a}{2 \sin \frac{\pi}{n}}. \quad (\text{A.23})$$

APPENDIX B: SIMULATION

B.1 Introduction

In this research two types of simulation methods were used for design and confirmation purposes. The commercial package software CST STUDIO SUITE® version 2012 was used for the RF antenna design and optimization whereas for the RF transceiver circuits AWR Design Environment® version 2010 was adopted. In order to carry out simulations related to FSO, Monte-Carlo method code written in MathWorks MATLAB® R2013a script was implemented. In the following sections, each simulation method will be briefly described.

B.2 CST STUDIO SUITE®

CST Microwave Studio is a tool included in CST STUDIO SUITE® package for simulating high frequency electromagnetic structures [123]. CST Microwave Studio has several solvers available to simulate. The time domain finite integration technique (FIT) and frequency domain method of moments (MoM) were used, which are named as ‘time domain solver’ and ‘integral equation solver’, respectively. FIT was used for obtaining the near field distribution on desired planes and return loss of the antenna whilst MoM

simulates the structure to get the far field radiation pattern. The structures used for simulations are illustrated in Figure B.1. The electromagnetic constitutive parameters of materials as well as dimensions were adopted from the physical structure. The same structures were used in both time domain and integral equation solvers. Depending on the complexity of structure and the used solver, the simulator parameters were configured based on the Table B.1.

B.3 AWR Design Environment

AWR Design Environment includes the tool Microwave Office, which is capable of simulating microwave/RF circuits [152]. APLAC linear solver of Microwave Office was used to obtain S parameters of the Tx and Rx. The equivalent components were taken

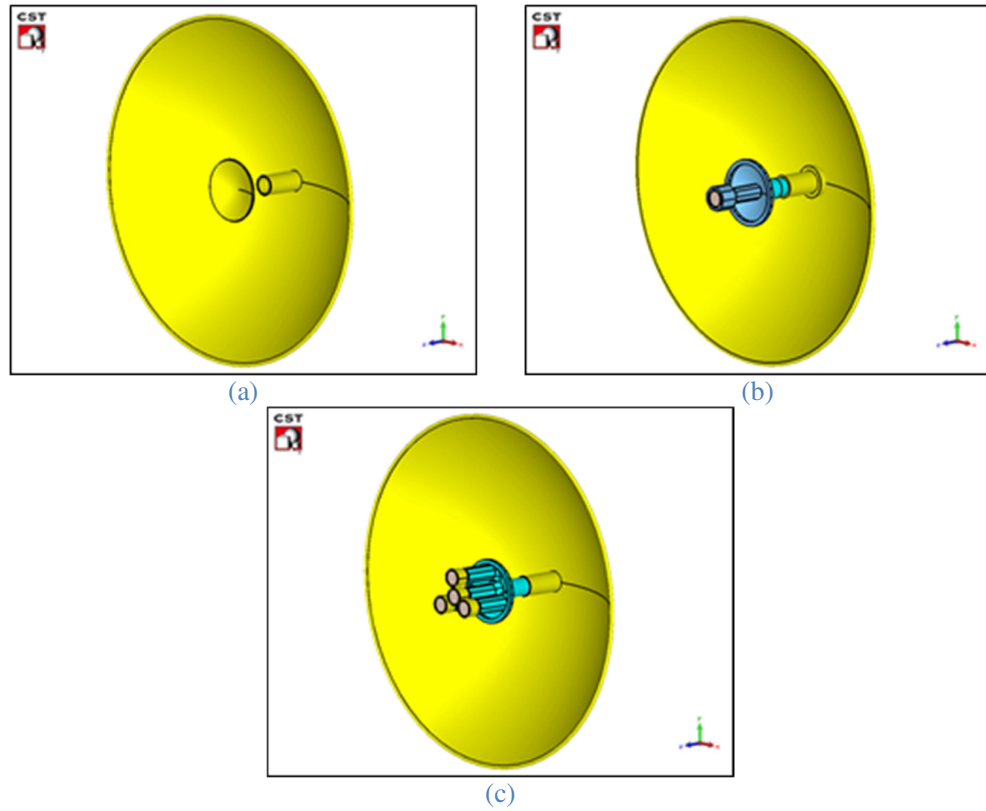
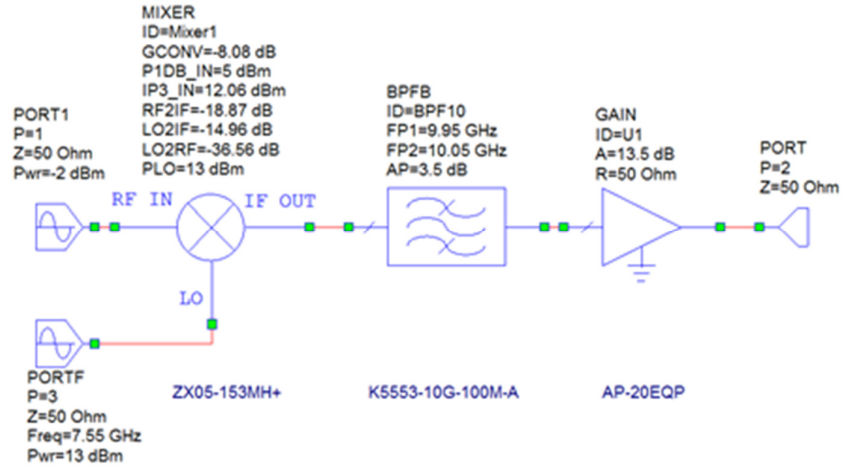


Figure B.1: Antenna physical structure modelled in CST Microwave Studio: (a) RF antenna without FSO aperture, (b) RF antenna with FSO implementing single collimator, and (c) RF antenna with FSO implementing multiple collimators.

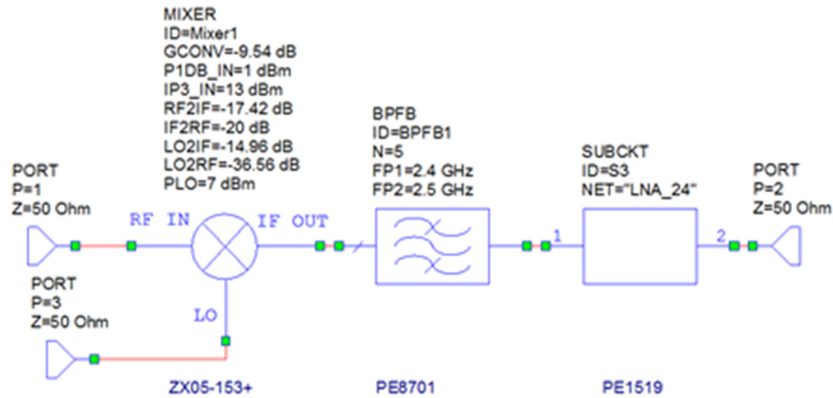
Table B.1: Configuration used in CST Microwave Studio to simulate the antenna structure.

	Time domain	Integral equation
Frequency	9 to 11 GHz	10 GHz
Excitation port	Waveguide port with 1 mode	
Symmetry	Magnet YZ Plane, (Electric XZ Plane)	No symmetry
Cell type	Hexahedral	Surface
Solver accuracy	-50 dB	1e-3
Maximum number of cells	3×10^6	35×10^3

from the available library and connected as seen in Figure B.2. The parameters used for components were adopted from the corresponding datasheets.



(a)



(b)

Figure B.2: Microwave circuit schematic used in Microwave Office: (a) transmitter module and (b) receiver module.

B.4 Monte-Carlo Method

Monte-Carlo method is a popular computational algorithm, which can be used in problems dealing with the random nature. Since turbulence effect in FSO channels are random fading phenomena, which can be describe by well-defined mathematical expressions, Monte-Carlo method was used to simulate an FSO communication link in turbulent conditions. In this section the used procedure will be briefly described and whenever necessary MATLAB functions implemented in the simulation code will be introduced.

The general block diagram of the simulation is illustrated in Figure B.3. A set of random 0, 1 value is created as random data bits. The MATLAB function *randi* is used for this step. Next step is to change the random raw bits into electrical signal. This is done first by resampling each bit into n samples and then scale samples appropriately. The MATLAB function *rectpulse* is used for resampling. Next step will be converting

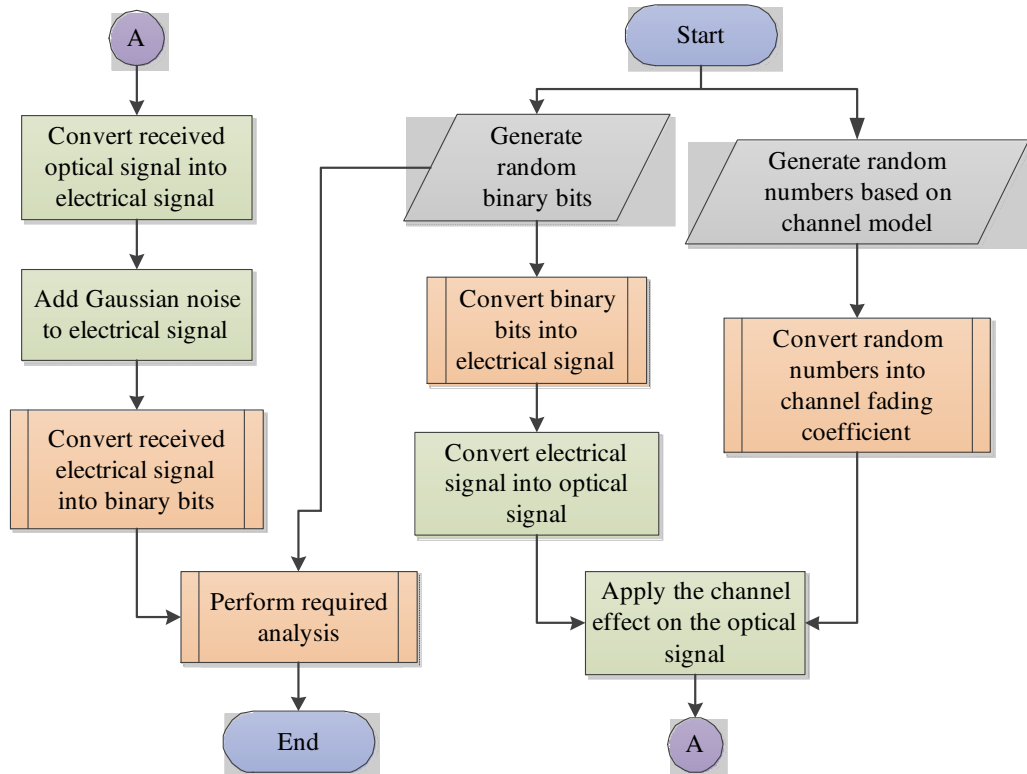


Figure B.3: Block diagram of the performed FSO communication link in turbulence channel based on Monte-Carlo simulation.

electrical signal into optical signal S by changing the scale and applying desirable extinction ratio and also adding required optical DC component.

In parallel, the fading coefficient will be also created to represent the turbulence in the channel. This is done by generating random values based on the desired random distribution. For instance, in weak turbulence regime, the distribution follows Log-normal pattern and the MATLAB function *lognrnd* can be used to generate random values based on given parameters. The only exception is where two correlated channels are required. Therefore, the following steps are taken to produce random numbers:

1. Generating sets of U and V random numbers based on the normal distribution.

The MATLAB function *randn* is used to generate normally distributed random numbers,

2. Creating two auxiliary variables $y_1 = \sigma_1 U + \mu_1$ and $y_2 = \sigma_2(\rho U + \sqrt{1 - \rho^2} V) + \mu_2$ where σ_i^2 , μ_i , and ρ denote variance, mean value and correlation coefficient,

3. Using correlated normal random numbers y_1 and y_2 to create correlated Log-normal numbers L_1 and L_2 where $L_i = \exp(2y_i)$.

Once the random numbers are available, they are resampled with appropriate ratio to obtain the fading channel coefficient h . The required ratio is decided based on the channel coherence time. Considering the FSO turbulence frequency of 400 Hz [117], the channel coherence time of FSO turbulence will be 25 ms.

It is possible to produce the arrived optical signal at the Rx side r by multiplying the optical signal S and the fading channel coefficient h (i.e., $r = S \times h$). Next step will be converting the received optical signal into electrical signal. This is done by applying PD responsivity and TIA gain and adding AWGN regarding the required SNR.

The obtained electrical signal is then resampled at the mid-point of each arrived bit. These samples can be used to calculate Q-factor and SI of the received signal. Also these samples are quantized later and converted into binary bits. By comparing the transmitted and received bits, BER value is also calculated. To calculate BER, the MATLAB function *biterr* is used.

Another important issue is that how many bits are required to achieve a specific BER in either simulation or experiment. To guarantee the required BER with a desired confidence level of CL, one needs to transmit m number of bits with no error as given by [153]:

$$m = \frac{-\ln(1-CL)}{BER}. \quad (B.1)$$

In the thesis, when a BER of 10^{-6} was considered at least 1 million bits with 10 repetitions were transmitted, hence resulting in a confidence level of 99.9955 %. The other case was transmitting 10,000 bits with 500 repetitions, which results in a confidence level of 99.3262 %.

APPENDIX C:

EXPERIMENTAL SETUPS

C.1 Introduction

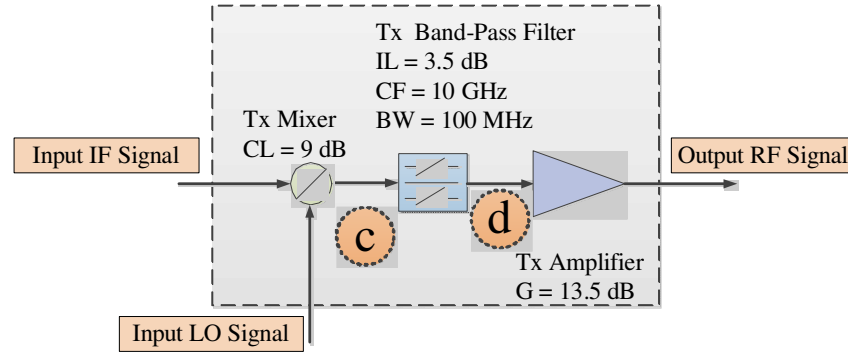
To prove the concept of differential signalling technique and hybrid FSO/RF antenna, various measurements on the provided experimental setups were performed. These setups were carefully designed and prepared for the specific purposes and in this section they are represented. In general, the experiments can be divided into two groups of RF and FSO parts. In this section the manufacturing and setup preparation procedure of tools, components, and devices will be exclusively introduced for each technology (i.e., RF and FSO).

C.2 RF Setups

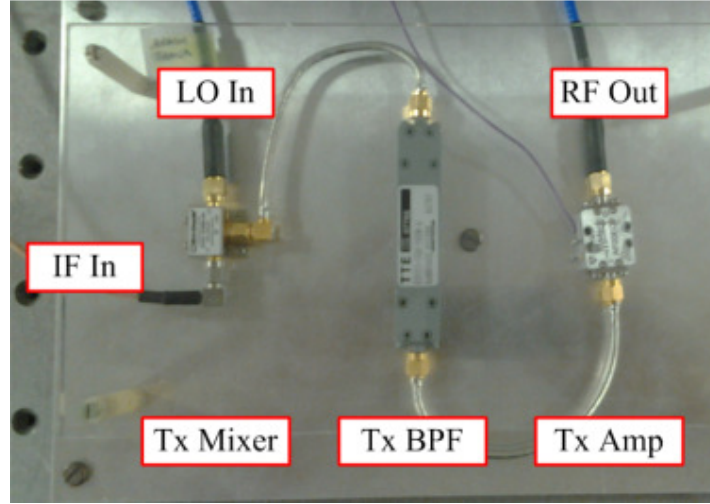
RF setups used in the project are Tx Module, Rx module, Cassegrain antenna.

C.2.1 Tx Module

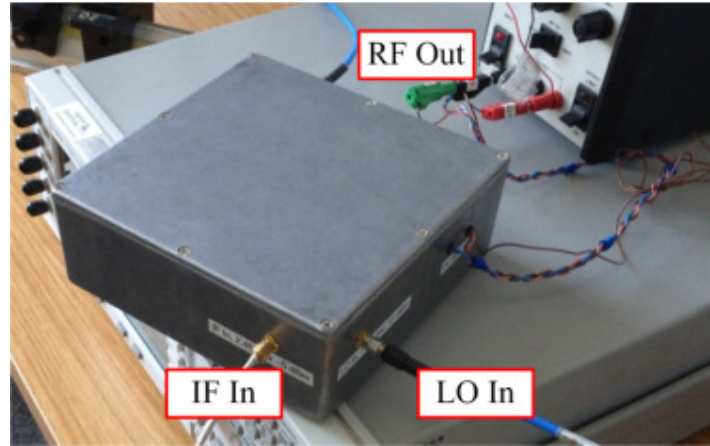
The block diagram of the Tx Module is illustrated in Figure C.1(a). This module consists of a mixer, a band-pass filter (BPF) and an amplifier. The purpose of this module



(a)



(b)



(c)

Figure C.1: RF Tx module: (a) block diagram, (b) practical setup, and (c) packed Tx module. IF, LO BPF, and Amp are intermediate frequency, local oscillator, band-pass filter, and amplifier, respectively.

is to up-convert an intermediate frequency 2.45 GHz signal into RF 10 GHz output while using a local oscillator signal at 7.55 GHz.

The up-conversion operation is done by the mixer component, which gives other products in addition to up-converted version of the signal (see Figure C.1(b)). Thus the

mixer is followed by a BPF tuned at RF desired frequency range (see Figure C.1(b)). Due to mixer conversion loss and BPF insertion loss, an amplifier is also used at the final stage to boost power (see Figure C.1(b)). Table C.1 summarises the measured components characteristics at central operating frequency. Note that the table only includes the parameters required in initial design. The whole Tx module was packed inside a metal box for protection and shielding against electromagnetic interference (see Figure C.1(c)).

To perform simulation in Microwave Office tool S parameters of the BPF and amplifier over the required frequency range were also measured. Figure C.2 depicts the measured values.

C.2.2 Rx Module

The block diagram of the Rx Module is illustrated Figure C.3(a). The same as Tx module, Rx consists of a mixer, a BPF and an amplifier. This module is used to down-convert RF 10 GHz signal into intermediate frequency 2.45 GHz output by using a local oscillator signal at 7.55 GHz. The down-conversion procedure is done by the mixer component which gives other products in addition to intermediate frequency signal (see Figure C.3(b)). Therefore a tuned BPF is required to reject unwanted frequency range (see Figure C.3(b)). To compensate for the channel attenuation and Rx module loss, an

Table C.1: Tx module measured components characteristics at central frequency. CL, LO, IL, and NF are conversion loss, local oscillator, insertion loss, and noise figure, respectively.

	Parameter	Value (dB)
Mini-Circuits Coaxial Package ZX05-153MH+ Mixer	CL	9.0
	LO to RF isolation	40.5
	IF to LO isolation	35.0
	RF to LO isolation	44.4
TTE Elliptical K5553-10G-100M-A BPF	IL	3.5
Marki microwave AP-20 Amplifier	Gain	13.5
	NF	> 3

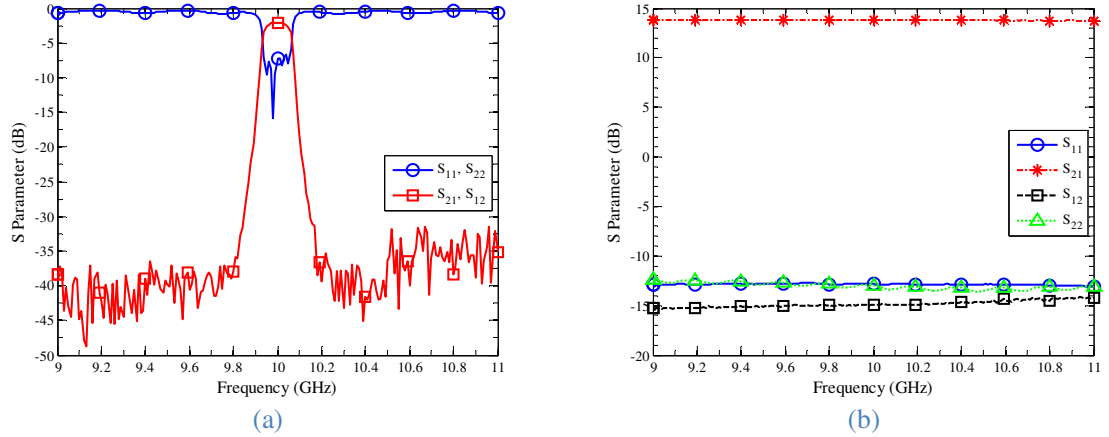


Figure C.2: Measured S parameters of the Tx module: (a) band-pass filter and (b) amplifier.

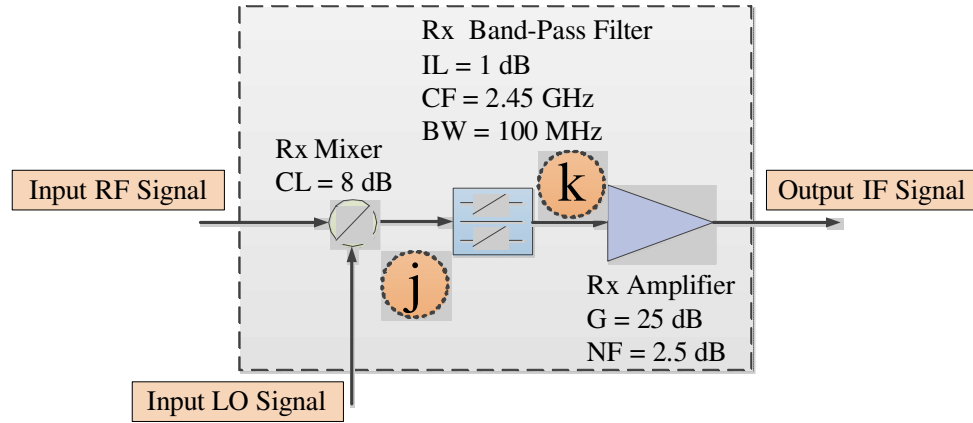
amplifier is used at the final stage (see Figure C.3(b)).

Table C.2 summarises the measured components characteristics at central operating frequency. Note that the table only includes the parameters required in initial design. The same as Tx module, Rx components were packed inside a metal box for protection and shielding against electromagnetic interference (see Figure C.3(c)).

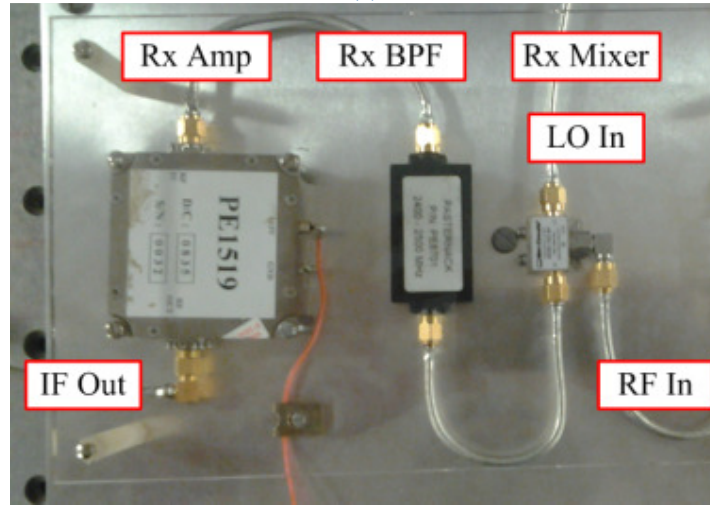
S parameters of the BPF and amplifier used in Rx module were measured over the required frequency range. These values later were used in Microwave Office software for simulation. Figure C.4 depicts these measured values.

C.2.3 RF Transceiver

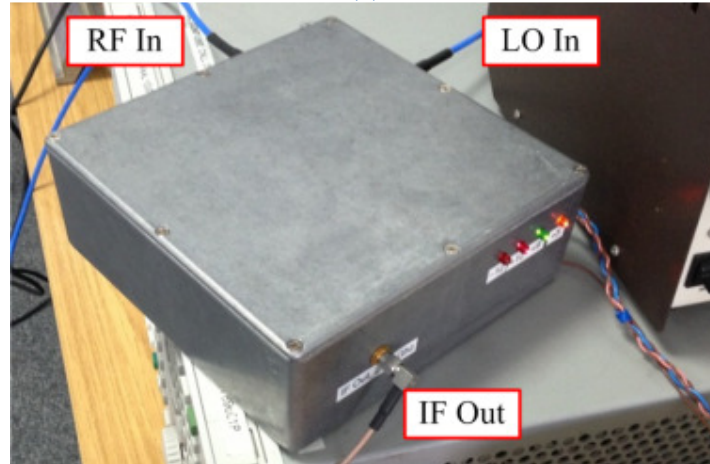
By means of Microwave Office tool the system shown in Figure C.5 was simulated. In the simulation power losses and in particular output power of Rx module were considered. The obtained results can be seen in Figure C.6. The corresponding measuring points are labelled in Figure C.1(a) and Figure C.5. In this section the performance of the whole RF Tx/Rx modules is also presented based on the experiment performed over one metre free space channel and standard horn antennas. This test was done to measure the characteristics of the system in addition to validate the design.



(a)



(b)



(c)

Figure C.3: RF Rx module: (a) block diagram, (b) practical setup, and (c) packed Rx module. LO, Amp, BPF, and IF are local oscillator, amplifier, band-pass filter, and intermediate frequency, respectively.

As seen Figure C.5, a BPSK signal with power of -5 dBm and bit rate of 6.7 Mbps equivalent to bandwidth of 10 MHz at central frequency of 2.45 GHz was used as the test

Table C.2: Rx module measured components characteristics at the central frequency. CL, LO, IF, IL, and NF are conversion loss, local oscillator, intermediate frequency, insertion loss, and noise figure, respectively.

	Parameter	Value (dB)
Mini-Circuits Coaxial Package ZX05-153+ Mixer	CL	8.0
	LO to IF Isolation	15.6
	RF to IF Isolation	23.6
Pasternack Comblane 4 Sections 2400-2500 MHz PE8701 BPF	IL	1.0
Pasternack LNA 1-4 GHz PE1519 Amplifier	Gain	25.0
	NF	2.5

signal. Agilent EGC Vector Signal Generator E4438C [154] was used to produce the IF signal (see Figure C.5).

The local oscillator signal of 16 dBm at 7.55 GHz was generated by Agilent PSG CW Signal Generator E847C [154]. The power and frequency of local oscillator is given in Figure C.5. A 50/50 RF power divider was used to split the same local oscillator signal for both the Tx and Rx modules.

A 3 dB RF attenuator was also implemented to adjust the power level for Rx. Two standard gain horn antennas with gain of ~ 17 dBi were set up over 1 m long free space channel with the channel path loss of 52.44 dB.

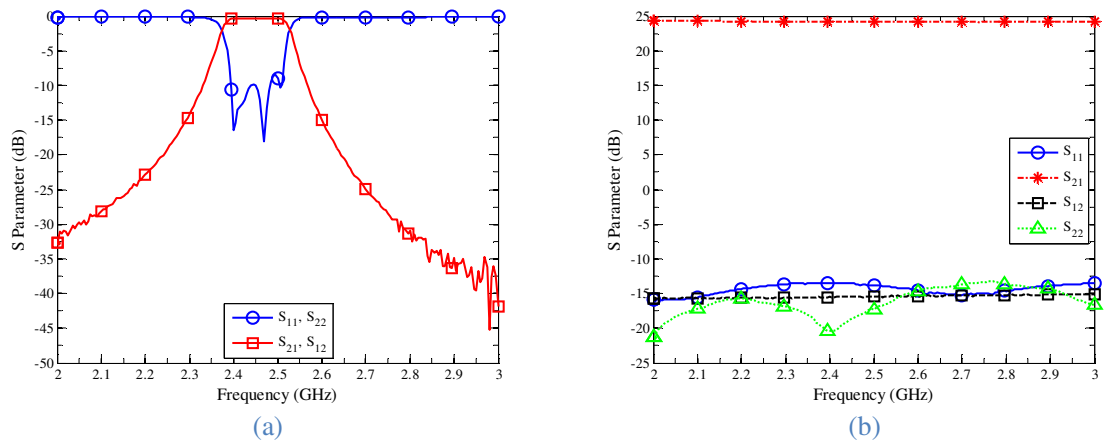


Figure C.4: Measured S parameters of the Rx module: (a) band-pass filter and (b) amplifier.

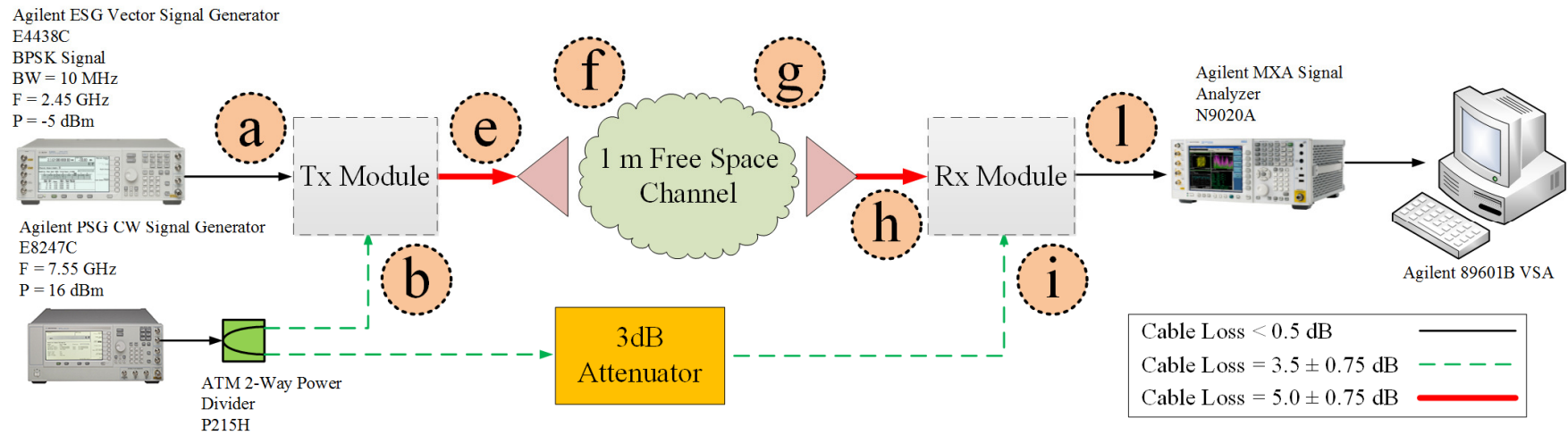


Figure C.5: Block diagram of the RF transceiver test in 1 m free space channel. The cable losses are also included in the diagram.

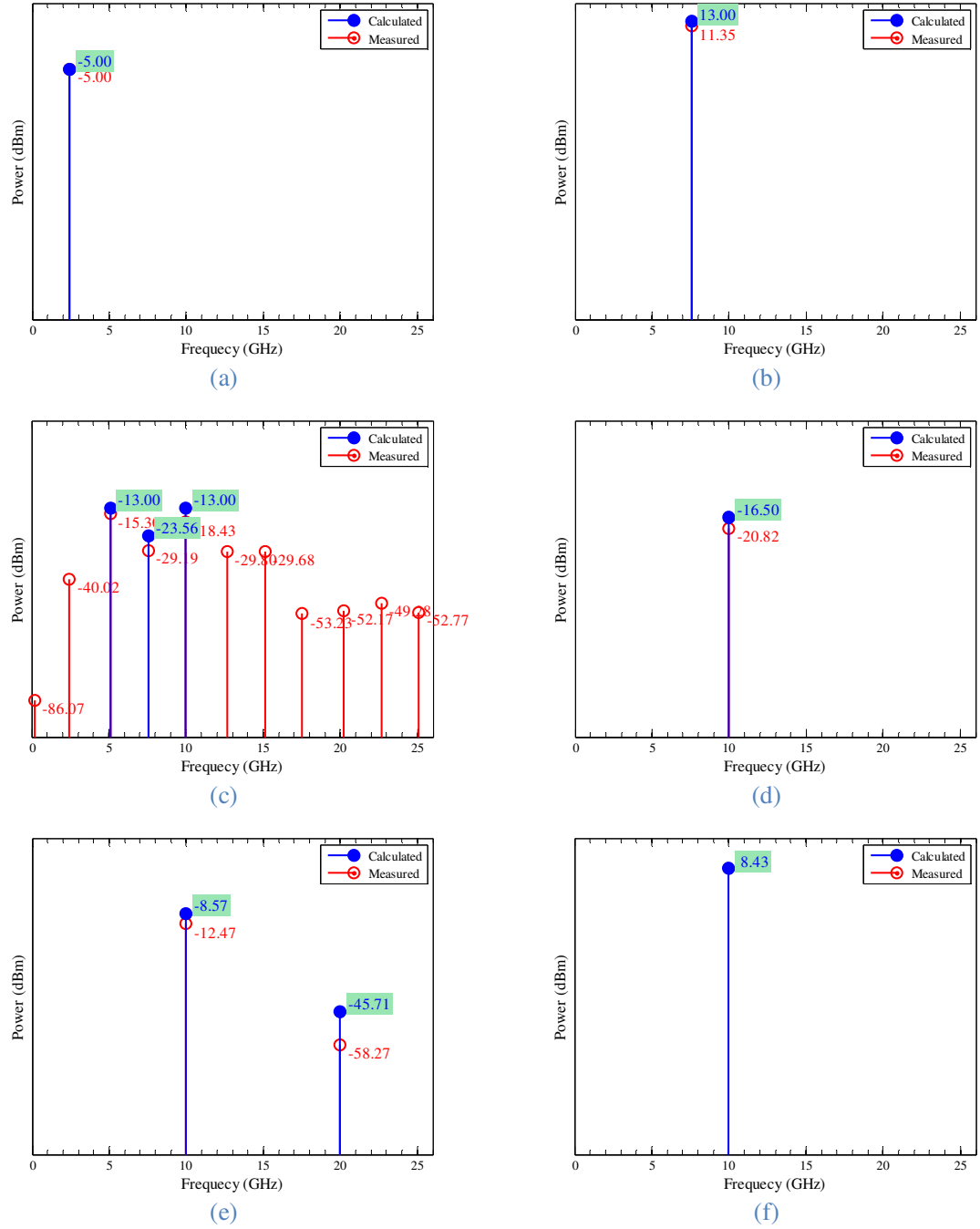


Figure C.6 – Part 1: Simulated and measured powers of the experiment setup in Figure C.5. Each measurement is labelled with corresponding alphabets in Figure C.1(a), Figure C.3(b) and Figure C.5.

At the Rx, the output of Rx module is fed into an Agilent MXA Signal Analyzer N9020A [154] for spectral measurement.

In this experiment, the signal analyser was only used to measure the signal power. However for further measurements, Agilent 89601B VSA software [154] that uses MXA

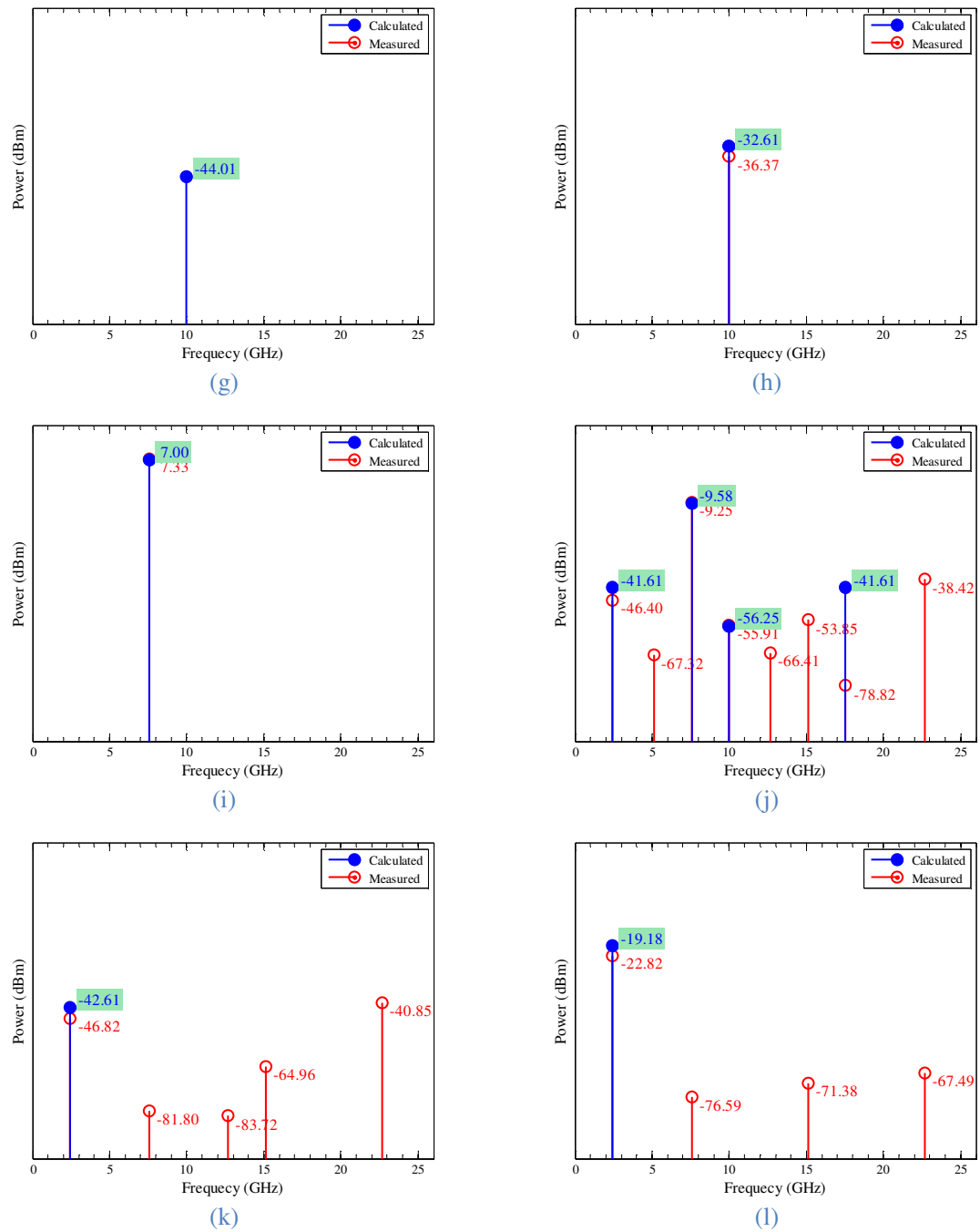


Figure C.6 – Part 2: Simulated and measured powers of the experiment setup in Figure C.5. Each measurement is labelled with corresponding alphabets in Figure C.1(a), Figure C.3(b) and Figure C.5.

Signal Analyzer for signal detection was also used. In several cases VSA software was used to measure SNR of the received signal.

The measured values corresponding to each labelled point is summarized in Figure C.6.

The difference between measured values and simulated values is due to cable losses. As

seen from Figure C.6(c) the mixer produces significant numbers of unwanted harmonics which must be removed due to increasing system performance and channel interference regulations. Another point at the Tx is the nonlinearity of the amplifier, which results in production of second harmonic at 20 GHz. However due to the low power level, this harmonic is not the concern in this thesis and as seen from Figure C.6(h), even after a 1 m of free space channel the second harmonic is reduced considerably. The Rx mixer is also responsible for various harmonic production in Figure C.6(j). The harmonics close to frequency of 2.45 GHz are removed by BPF and the amplifies the final IF signal.

For a 1 m free space channel, the path loss is 52.44 dB and if the link is increased to 1 km the path loss will be 112 dB. This makes the received power level to be -94.29 dBm. To estimate the required amplification to have acceptable signal quality, the BER of 10^{-6} is considered as the required performance and since BPSK is used, it interprets into SNR of 8.8 dB.

Therefore, by knowing the noise power at the output of Rx module it is possible to decide the required power amplification for a 1 km free space RF channel.

If NF_e , T_e , and T_0 denote the noise figure of the Rx module, the noise temperature of the Rx, and room temperature (reference temperature), one has [67]:

$$NF_e = 1 + T_e/T_0. \quad (C.1)$$

On the other hand, for given Rx module, it can be shown that [67]:

$$NF_e = NF_{\text{mixer}} + \frac{NF_{\text{BPF}} - 1}{\text{Gain}_{\text{mixer}}} + \frac{NF_{\text{Amp}} - 1}{\text{Gain}_{\text{BPF}} \text{Gain}_{\text{mixer}}}. \quad (C.2)$$

The loss in components like passive mixer and filters is considered as NF , therefore Eqs. (C.1) and (C.2) will result in [155]:

$$T_e = T_0 \left(CL_{\text{mixer}} + \frac{IL_{\text{BPF}} - 1}{1/CL_{\text{mixer}}} + \frac{NF_{\text{Amp}} - 1}{1/IL_{\text{BPF}} 1/CL_{\text{mixer}}} - 1 \right). \quad (C.3)$$

For given Rx module $NF_e = 11.2$ dB and if $T_0 = 290^\circ$ K one obtains $T_e = 3.8^\circ$ kK. In a 50 Ohms system, the noise power generated at this temperature will be easily calculated by $P_{\text{noise}} = k_B(T_e + T_{\text{antenna}})BW$ where $k_B = 1.38 \times 10^{-23}$ J/K is Boltzmann's constant [67], T_{antenna} is antenna temperature which is typically 290° K for a terrestrial link and BW denote the bandwidth of interest [155], hence $P_{\text{noise}} = -82.47$ dBm. Those losses will increase the required amplification [67]. In this design the first stage of the Rx is a lossy component (i.e., the mixer) which is not practical in real situations. In commercial systems the first stage is an low noise amplifier with high gain and low noise figure, which effectively will reduce the equivalent noise figure of the whole Rx module [155]. However, since this research is only concerned with the hybrid antenna, the designed Rx module will be used just for the proof of concept.

The system depicted in Figure C.5 was used for other measurements, where specific antenna and channel lengths were replaced with the standard gain horn antenna and a 1 m length channel. Of course for other measurements two continuous wave signal generators at 7.55 GHz for local oscillators at Tx and Rx sides were used.

C.2.4 Antenna

The whole antenna structure was assembled at Northumbria University which will be described in this section.

The main part of the antenna is a parabolic reflector illustrated in Figure C.7 with the characteristics summarised in Table C.3. The sub-reflector of the antenna was the only part fully fabricated in the university. The procedure of manufacturing included importing the model from CST Microwave Studio into 3DS CAD SOLIDWORKS® software [156]. This tool was used to convert the model to STL format [157] which is used with most commercial 3D printers [158] (see Figure C.8). Desktop OBJET24 3D printer [159] was



Figure C.7: RF Main reflector with given specification in Table C.3.

used to print the sub-reflector out of VeroWhitePlus FullCure 835 material. The electrical characteristics of FullCure are given in Table C.4.

These electrical parameters are measured at low frequency range and the real values at microwave bands are different, in particular that in the design and simulation the material was considered to be lossless.

Table C.3: Main reflector characteristics summary.

Parameter	Value
Effective focal length (mm)	114
Diameter (mm)	475
Height (mm)	142.24
Thickness (mm)	1
Material	Aluminium

The same procedure was used for different sub-reflectors made for the project. Once the structure was ready, an aluminium foil with thickness of almost 40 μm was used to cover it. Figure C.9 shows the printed sub-reflector as well as final conductive sub-reflector.

The sub-reflector is positioned and held in front of the antenna by means of a

Table C.4: Sub-reflector dielectric material characteristics summary.

Parameter	Value
Relative permittivity ϵ_r	~ 4
Relative permeability μ_r	~ 1

polyethylene tube. The tube was cut in required length and then one end of it was glued to the sub-reflector. The other end was put inside the feed. Table C.5 summarises the required parameters of the tube whilst Figure C.10 shows an instance of the used tube.

Table C.5: Polyethylene tube material characteristics summary.

Parameter	Value
Relative permittivity ϵ_r	~ 2.3
Thickness (mm)	2

A standard open-ended circular waveguide with an inner diameter of 23.8 mm was used as the feed. This waveguide (see Figure C.11) can support mid-range of X-band microwave frequency (i.e., 8.5 to 11.6 GHz). To characterize the feed, in particular the radiation pattern and HPBW, a simulation was performed. The simulated results are presented in Figure C.12, which shows the feed HPBW of 65.1 and 64.6 degrees in E- and H-planes, respectively.

The feed is directly connected to a transition component which adopts a waveguide

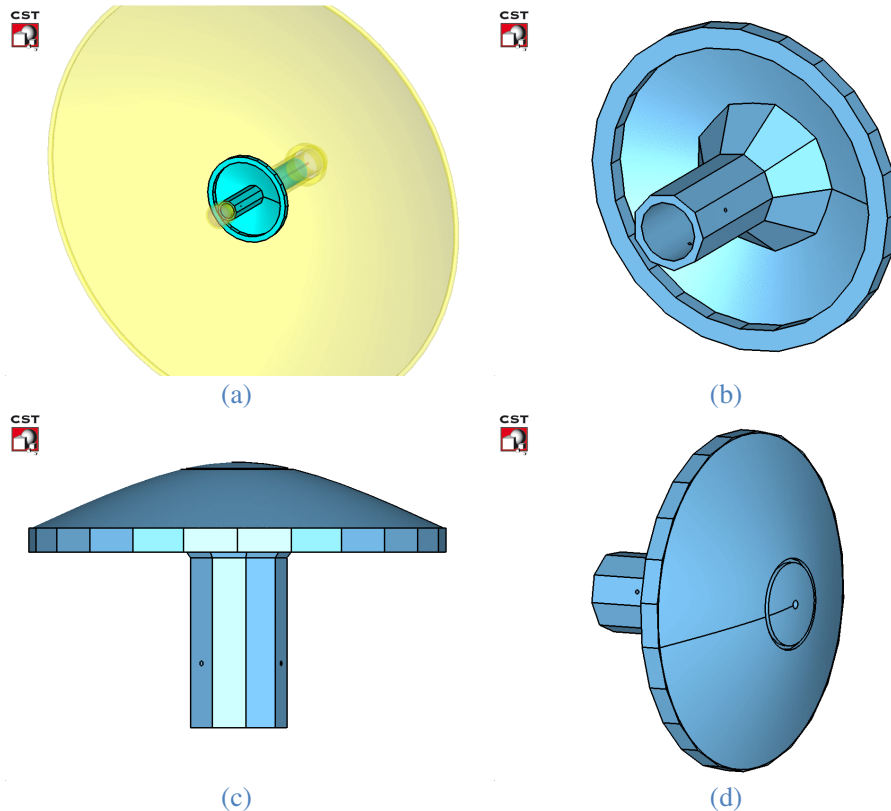


Figure C.8: Modelled sub-reflector in different views used for manufacturing procedure.



Figure C.9: A prototype of the printed sub-reflector: (a) without conductive cover and (b) with conductive cover.

with circular cross-section to another with rectangular cross-section. In Figure C.11, also the transition is shown. The transitions must smoothly and efficiently convert the fundamental mode in circular waveguide to the one in rectangular waveguide.

The transition converts the aforementioned circular waveguide cross-section to WR-90 X-band 22.7 mm×10.2 mm rectangular waveguide.

In the experiments it was observed that the antenna was not matched to 50 Ohms line, thus a tuner waveguide to match the antenna was needed.

It is better to position the tuner close to the unmatched component to reduce the loss due to impedance incompatibilities, thus the waveguide tuner in Figure C.13 was used immediately after the transition. This tuner has two arms to change the field distributions

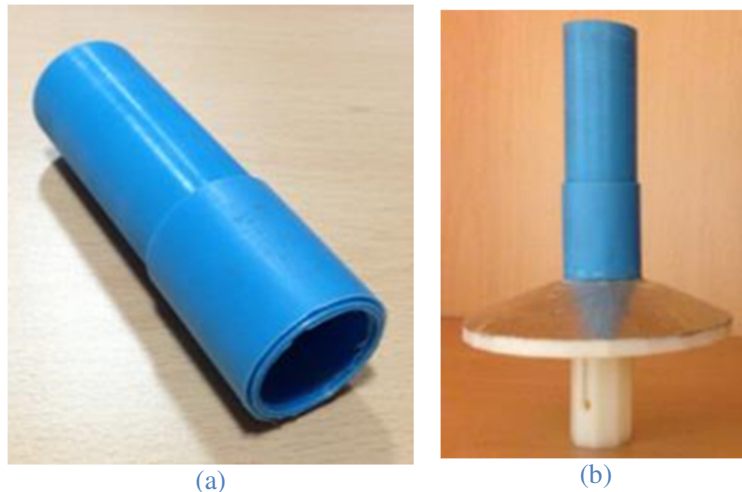


Figure C.10: The Polyethylene tube used to hold sub-reflector.

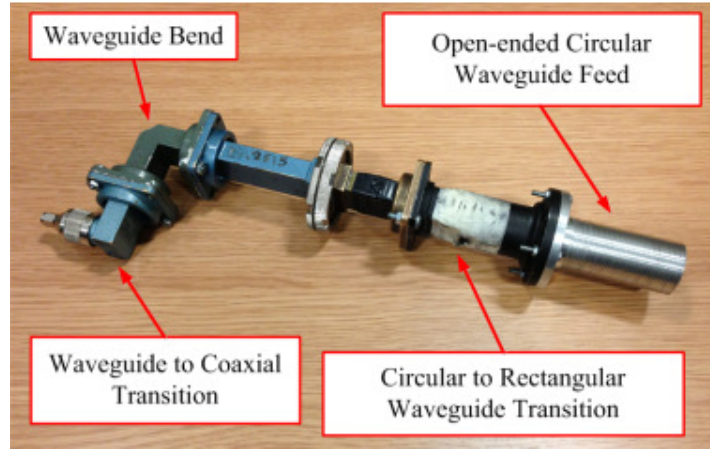


Figure C.11: Assembled feed, circular to rectangular transition, bend, and waveguide to coaxial transition.

in E- and H-planes independently.

As mentioned before, a waveguide bend was used to make it possible to take the optical fibre out of the waveguide. Depending on the plane the bending occurs there will be two types of E- and H-plane bends. In the project an E-plane bend (see Figure C.11) in which the bending happens long E-plane wall (narrow wall) of the waveguide was used. Another aspect of bends is the way bending is made.

The bending can be in a shape of a curvature which is called precisions bent with given bending angle or in a right-angled bend which is called mitred casting. In this work both were used.

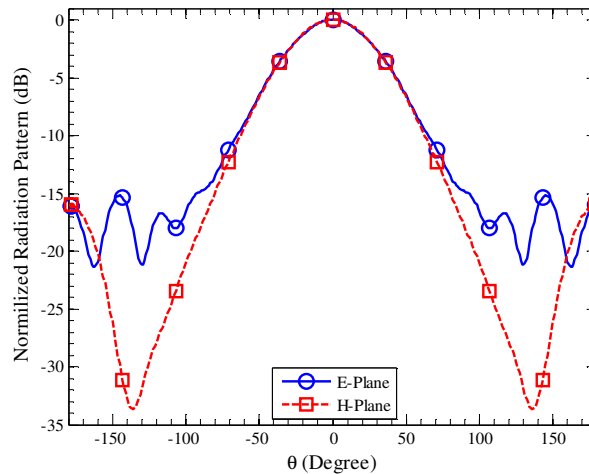


Figure C.12: Simulated normalised radiation pattern of the open-ended circular waveguide with an inner diameter of 23.8 mm.



Figure C.13: Rectangular waveguide tuner with two tuning arms in E- and H- planes.

The same as transition, a bend should smoothly and efficiently convert the input field to output desired field. Smooth and efficient conversion, refers to a low return loss and less production of extra modes other than fundamental one at the output.

The last part of the RF antenna is the rectangular waveguide to coaxial transition (adaptor) which transfer the electromagnetic energy from the waveguide into a 50 Ohms coaxial cable and vice versa. The waveguide to coaxial transition is highlighted in Figure C.11.

C.3 FSO Setups

The optical setup consists of optical transceiver aperture, SMF, MMF, OTx and ORx.

C.3.1 Optical Transceiver Aperture

The aperture which is fixed in the shadow region of the sub-reflector was basically fabricated by means of commercial collimators for appropriate wavelength and appropriate fixture. In this case THORLABS F810FC-780 collimators with the characteristics summarised in Table C.6 were used. The fixture of optical transceiver

aperture was designed as a part of sub-reflector which made it possible to fix collimators in proper positions. Figure C.14 depicts a prototype of single Tx/Rx collimator.

Table C.6: THORLABS F810FC-780 collimator characteristics summary.

Parameter	Value
Aperture diameter (mm)	24
Full angle beam divergence (mDeg)	8
Central wavelength (nm)	780

To specify the output pattern of the collimator, the radiation pattern of the collimator for two types of available fibres, SMF and MMF with 670 nm visible red laser were measured. Figure C.15 illustrates the measured radiation pattern of the collimator with SMF at various distances from the collimator aperture. It is seen that the radiation almost decays at the rate of 4.5 dB/cm for three measured distances. The profile seems to be Gaussian and the output beam radius at e^{-2} is almost 3.45 cm. Since the profile seems to be the same for various distances, it can be deduced that the output beam of SMF at 670 nm is collimated with a good approximation. Note that the order of collimation will be larger if the laser wavelength drifts towards 780 nm. Therefore, the aforementioned configuration is a good candidate for the Tx aperture.

As another alternative, MMF can be used with a collimator. However, since various modes are propagating inside MMF, the output of fibre and consequently the collimator will not be single fundamental mode of Gaussian. In that case, the output beam of the



Figure C.14: A prototype of the optical transceiver with single Tx/Rx collimator.

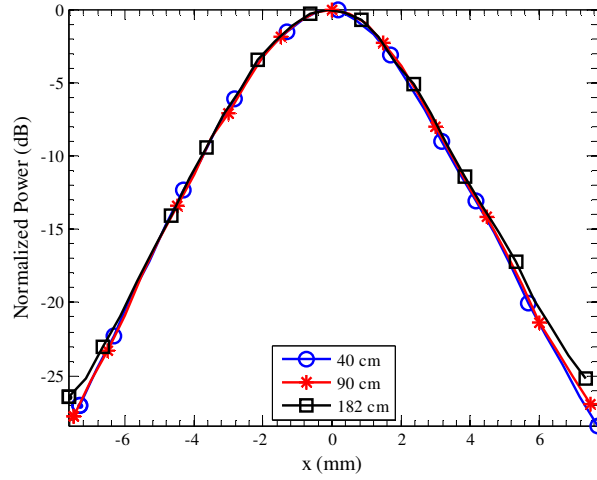


Figure C.15: Measured output radiation pattern of the collimator with SMF at 670 nm at different distances.

collimator is a combination of several modes, each propagating with different characteristics.

Since each mode has its own beam waist, thus for each mode an individual lens is required to perform collimation. However, the collimator has a fixed lens optimized for the fundamental mode meaning that a collimator cannot be expected to give acceptable result for a MMF case. The output radiation pattern of the collimator with MMF at 670 nm at 182 cm was measured, which is depicted in Figure C.16.

The output pattern of collimator+MMF seems to have a top-hat shape and from the

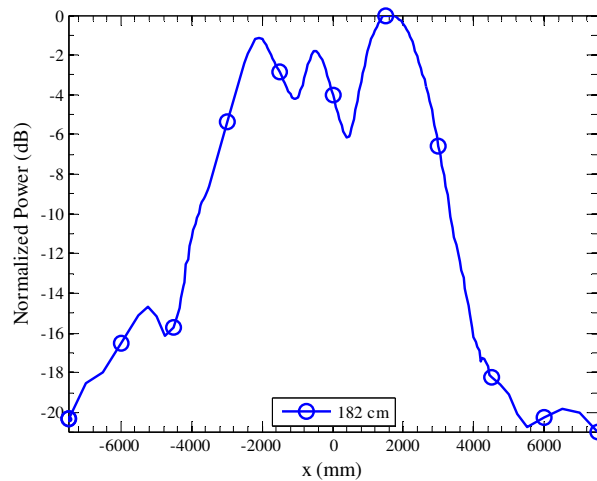


Figure C.16: Measured output radiation pattern of the collimator with MMF at 670 nm at 182 cm distance.

measurement it is found out that the output beam diverges with the angle of 45.63 mRad. Such large divergence angle makes it impossible to use collimator+MMF as Tx. However, since usually MMF has a large NA value, in this case 0.5, it is a suitable candidate for Rx aperture. The coupling loss of fibre to FSO was measured to be almost 2 dB for both MMF and SMF cases.

Another component used in optical transceiver was fibre. As mentioned in previous paragraphs, two types of SMF and MMF are considered for Tx and Rx parts. SMF cable used in the experiment was a standard silica fibre for the operating range of 633 to 780 nm with NA of 0.1 to 0.14. The attenuation of the such fibre in this range is less than 15 dB/km [160]. The MMF fibre however was a standard step-index polymethyl metacrylate (PMMA) with core diameter of 1 mm with NA of 0.5. The attenuation of the MMF is almost 200 dB/km [161].

The optical Tx used in the project was basically a Beta-Tx FSO red laser operating at 670 nm with the bandwidth of 50 MHz. The output power of the laser was ~3 dBm. To launch the laser into SMF, THORLABS 50-850-FC GRIN lens was used whereas for the MMF experiments, the laser was directly focused into the fibre. Depending on the coupling and alignment a minimum coupling loss of ~2 dB was expected. Figure C.17 shows the fixture used to couple the red laser into MMF.

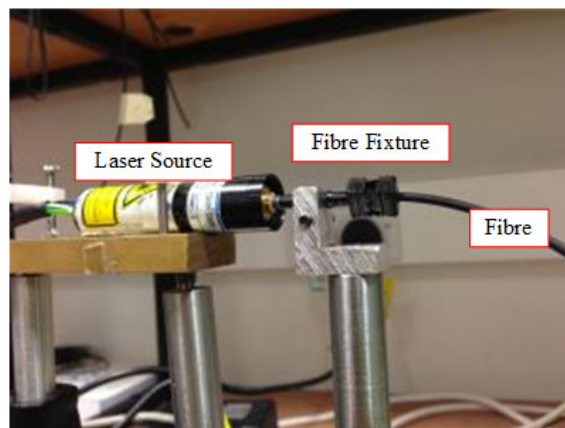


Figure C.17: The red laser to MMF fibre coupling structure.

For ORxs THORLABS PDA10A-EC fixed gain detectors with 180 MHz bandwidth were used. The ORx is basically for FSO application. However, a holder as shown in Figure C.18 was used to adopt it with fibre applications.

Depending on the performed experiment, OTx and ORx were directly used in FSO channel or fibres as well as collimators at Tx and Rx sides were implemented between FSO channel and OTx/ORx (see Figure C.19(a)). The block diagram of the typical FSO setup used in the PhD is also depicted in Figure C.19(b). A Tektronix arbitrary waveform generator (AWG) was used to generate modulating signal for the laser. The required signal was previously arranged in MATLAB software and then downloaded into AWG. Depending on the experiment, one or two channels of AWG and lasers were used. In the experiments where only the link performance in clear chamber matters, the oscilloscope was used directly to analyse the received signal. However, in experiments where random fading channel is present, the output of PD was sampled by an Agilent oscilloscope connected to a computer and the captured voltage was controlled and recorded by LabVIEW software. In next appendix the details of analysing the captured data is briefly described.

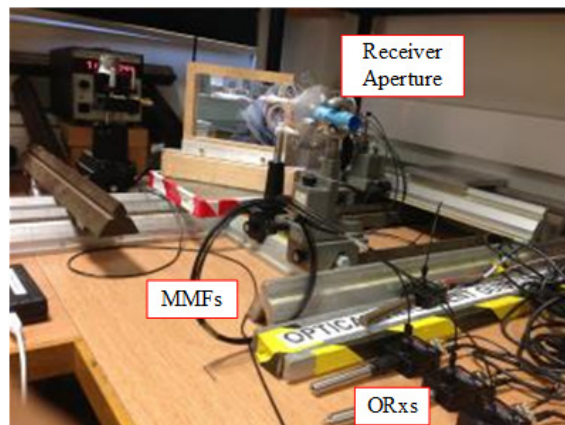


Figure C.18: Coupling multimode fibres (MMFs) to optical receivers (ORxs).

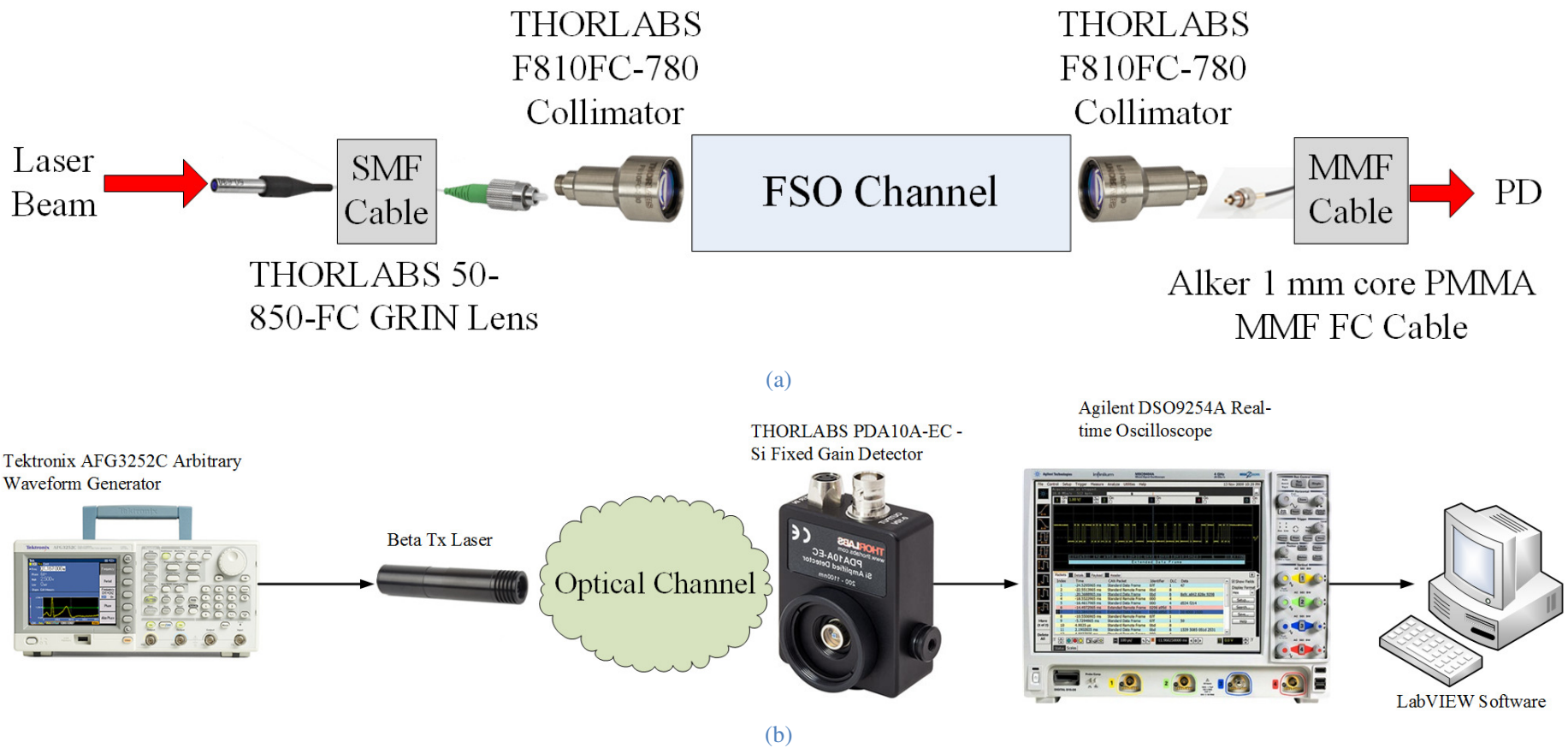


Figure C.19: (a) Laser to PD connection block diagram, and (b) FSO experiment block diagram. SMF and MMF are multimode fibre and single-mode fibre, respectively.

C.4 Antenna Components Dimensions

A graphical representation of the antenna size and dimensions, in particular the sub-reflector dielectric is illustrated in Figure C.20. Note that the sizes of other parts are already presented in the previous sections.

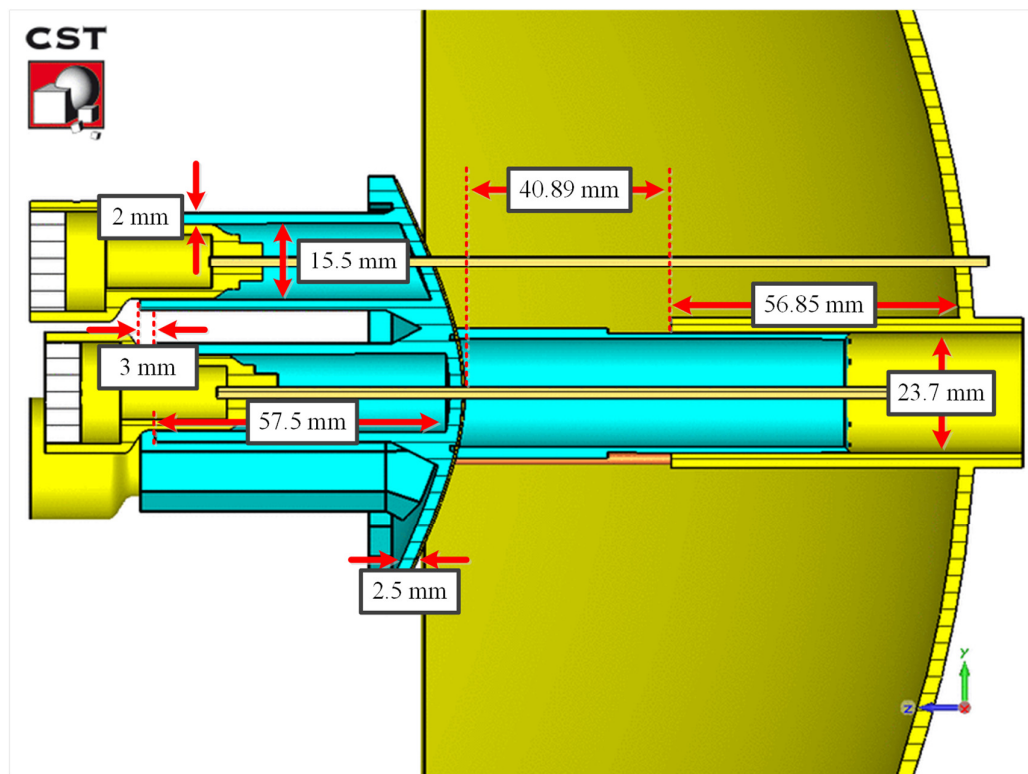


Figure C.20: Sub-reflector, tube, and feed size and dimension diagram.

APPENDIX D: EXPERIMENTAL MEASUREMENTS

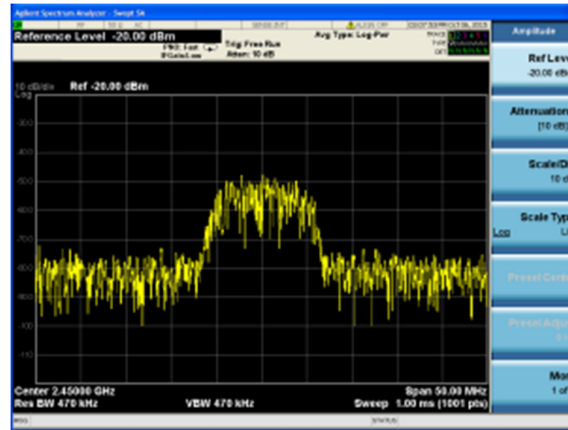
D.1 Introduction

In this appendix it is tried to briefly explain the practical measurements performed during the PhD. Basically two types of measurements were performed, RF and FSO setup measurements. RF measurement includes measuring return loss, SNR of the received signal and radiation pattern of the antenna. For FSO, measuring statistical features such as scintillation index, Q-factor, C_n^2 , and detection threshold level are discussed.

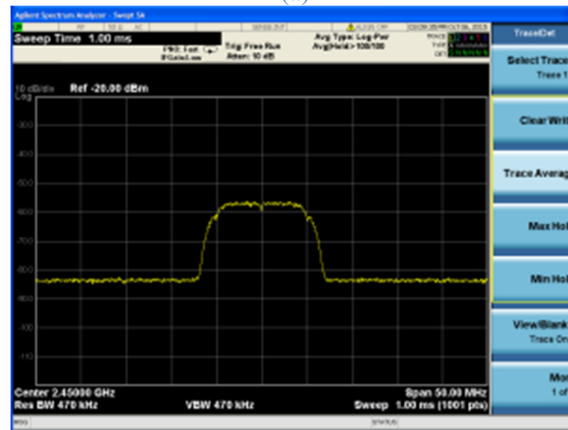
D.2 RF Measurement

Return losses of the RF modules were all measured by means of Agilent E8364B PNA Series Network Analyzer. The details of return loss measurement method can be found in [162]. The other important RF parameter to measure was SNR of the received RF signal. The term ‘the received signal’ is refereeing to the output of Rx Module in Figure C.5 where the down-converted signal is ready to be analysed by MXA device. It is possible to measure SNR automatically by means of VSA software; however an easier

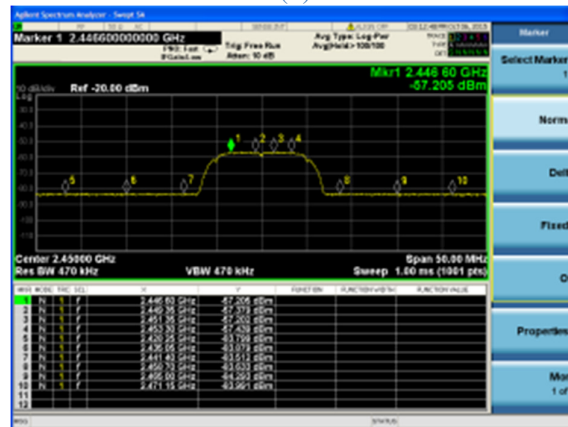
way is to estimate it based on power spectrum of the signal. Assume that the spectrum in Figure D.1(a) is the received signal. This spectrum belongs to a 10 Mbps BPSK signal at 2.45 GHz. The first step is to average the received signal to get rid of noise variations. Depending on how fast the equipment can do averaging, one can set the appropriate averaging order. For the experiment the default 100 averaging order was used. After



(a)



(b)



(c)

Figure D.1: RF received signal captured using the spectrum analyser: (a) received signal, (b) received signal after averaging, and (c) received signal with markers.

averaging the signal looks like Figure D.1(b).

It is assumed that the noise level within the signal is almost the same as adjacent frequencies and since the power unit spectrum is in dBm, then by measuring the difference between signal and noise floor, SNR value is obtained approximately. However, to increase the accuracy, in particular when the spectrum is not uniform, it is better to consider various points within the bandwidth of the signal and around it. Figure D.1(c) depicts the same signal which is marked by several markers. Having the measured power levels, it is possible to estimate SNR using the following expression:

$$\text{SNR} = \frac{1}{N_s} \sum_{i=1}^{N_s} P_{s,i} - \frac{1}{N_n} \sum_{i=1}^{N_n} P_{n,i}, \quad (\text{D.1})$$

where N_s , $P_{s,i}$, N_n , and $P_{n,i}$ denote the number of measured powers within the signal, i -th measured power within the signal, the number of measured noise powers, and i -th measured noise power, respectively. Thus for the signal in Figure D.1, SNR is 26.54 dB.

To measure the radiation pattern of an antenna the near-field measurement system, available at the university was used. The near-field system is patented technique by Nearfield Systems Inc. (NSI) to visualize the far-field of any radiator based on the near-field sampled fields [163]. The basic idea of near-field system is to measure the near-field radiation of antenna under test (AUT) and convert the measurement near-field data set to far-field radiation pattern. This approach is done by means of fast Fourier transform (FFT). The simplified block diagram of the available NSI-200V-5×5 near-field system is plotted in Figure D.2. In the available system, the AUT was fixed while the probe was travelling. Both AUT and probe were connected to a network analyser (Agilent N5230A PNA-L Network Analyzer). The probe was a standard open-ended rectangular waveguide with part number of NSI-RF-WR90. The probe mobility was possible through a mechanical structure which could move the probe in a two dimensional plane. The movement of the probe as well as the network analyser synchronization was controlled

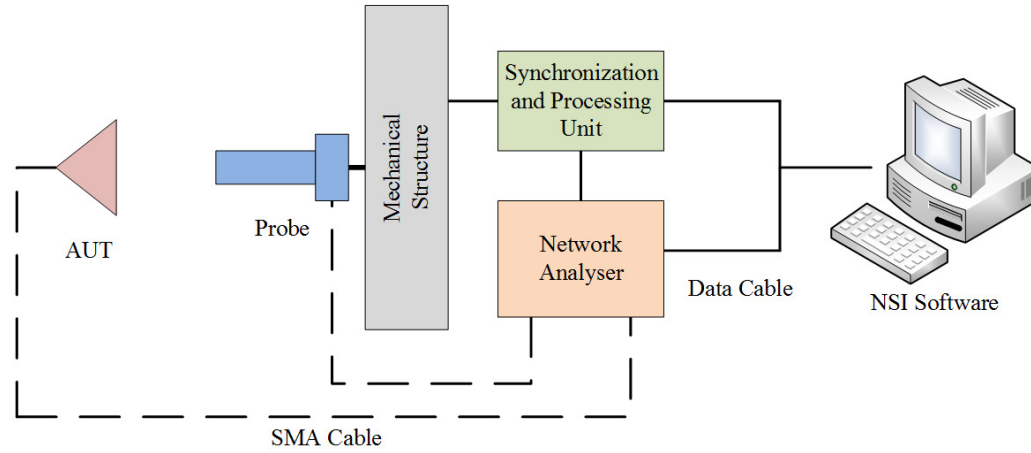


Figure D.2: The block diagram of the near-field system. AUT denotes antenna under test.

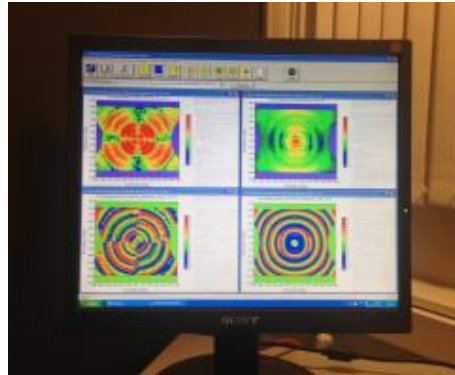
by a separate unit, which is labelled as Synchronization and Processing Unit in Figure D.2.

Finally, the whole process was conducted by a software called Antenna Measurement Software NSI2000 Standard Edition 4.11.202. The software also was in charge of collecting measured near-field data, performing FFT, and delivering the results [164]. Depending on the operating frequency, distance between AUT and the probe, and required far-field radiation pattern angle; the system calculated proper scanning span. Once the near-field measurement is complete, it is possible to convert the measured data set to far-field radiation.

However, in this way a normalized radiation pattern is obtained. If the gain is also required, a calibration has to be done before the main measurement. This calibration can be performed by connecting the SMA cables attached to Network Analyser, or by means of antenna with a known gain at the same position of AUT. The former method was used to do the calibration. Figure D.3(a) shows the near-field system whereas the typical produced results by the software are depicted in Figure D.3(b). The calculated results



(a)



(b)

Figure D.3: (a) Near-field system used for radiation pattern measurement, and (b) produced results by NSI software.

were transferred to MATLAB for further work.

In the experimental results for the return loss an odd periodic behaviour was observed, which could be due to impedance mismatch between cables and connectors, in particular cables connected to the network analyser, see Figure 5.15. To confirm the origin of the periodic mismatch, two individual return loss measurements with two different cables and the same antenna tuned for 10 GHz were performed. The measured data are plotted in Figure D.4. Apart from the ripples, the peaks and troughs of the return loss response are almost at the same frequencies. Therefore, the measured periodic pattern is not due to cables.

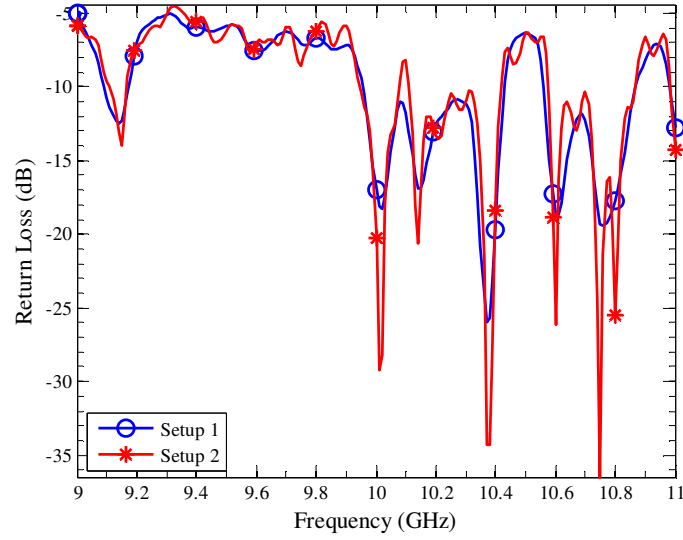


Figure D.4: Performed return loss measurement for the same tuned antenna set and two different cable connections.

D.3 FSO Measurement

In contrary to RF, FSO measurements deal with statistical data. It means that the same measurement needs to be repeated several times and appropriate statistical analysis are required to extract the final desired data set. Several experiments in the FSO artificial turbulence channel at NCRLab, Northumbria University, Newcastle upon Tyne, UK were performed. The interesting parameters were SI, Q-factor, C_n^2 , and detection threshold level that deal with channel situation and the effect of channel on the signal, respectively. The block diagram of the experimental setup is depicted in Figure D.5 and Figure D.6 shows the image of the setup used for most of the turbulence channel experiments.

The Tx side (see Figure D.6(a)) consists of any number of LD (for this example two LDs) driven by appropriate modulating signal. An AWG is used to produce transmit signal based on random bits and the used data rate to perform the measurement and in this project NRZ-OOK signal was used. To check the ambient light at the desired wavelengths, a pair of optical power meter and optical detector was used.

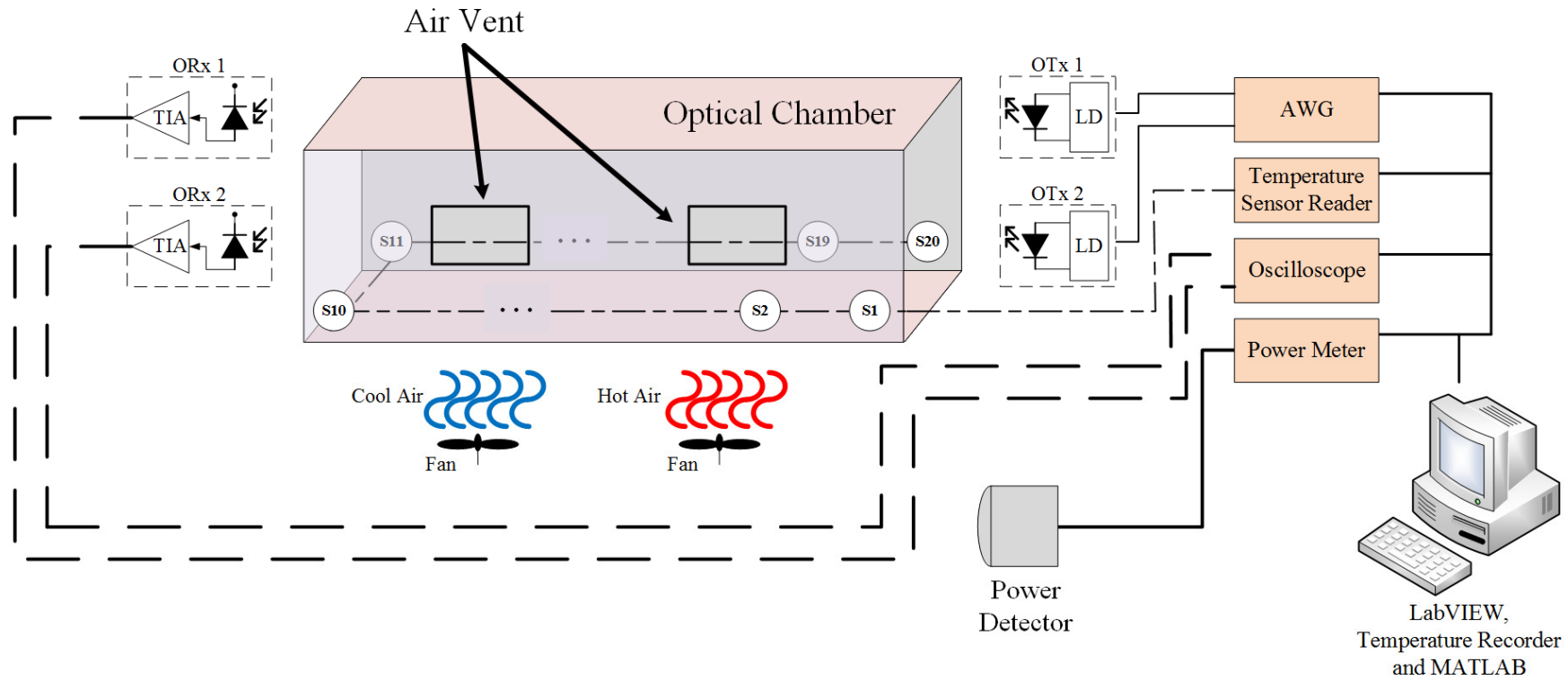


Figure D.5: The block diagram of the experimental FSO setup. This setup was used for turbulence assessment purposes. ORx, TIA, S_i , OTx, LD, and AWG are optical receiver, transimpedance amplifier, i -th temperature sensor, optical transmitter, laser diode, and arbitrary waveform generator, respectively.

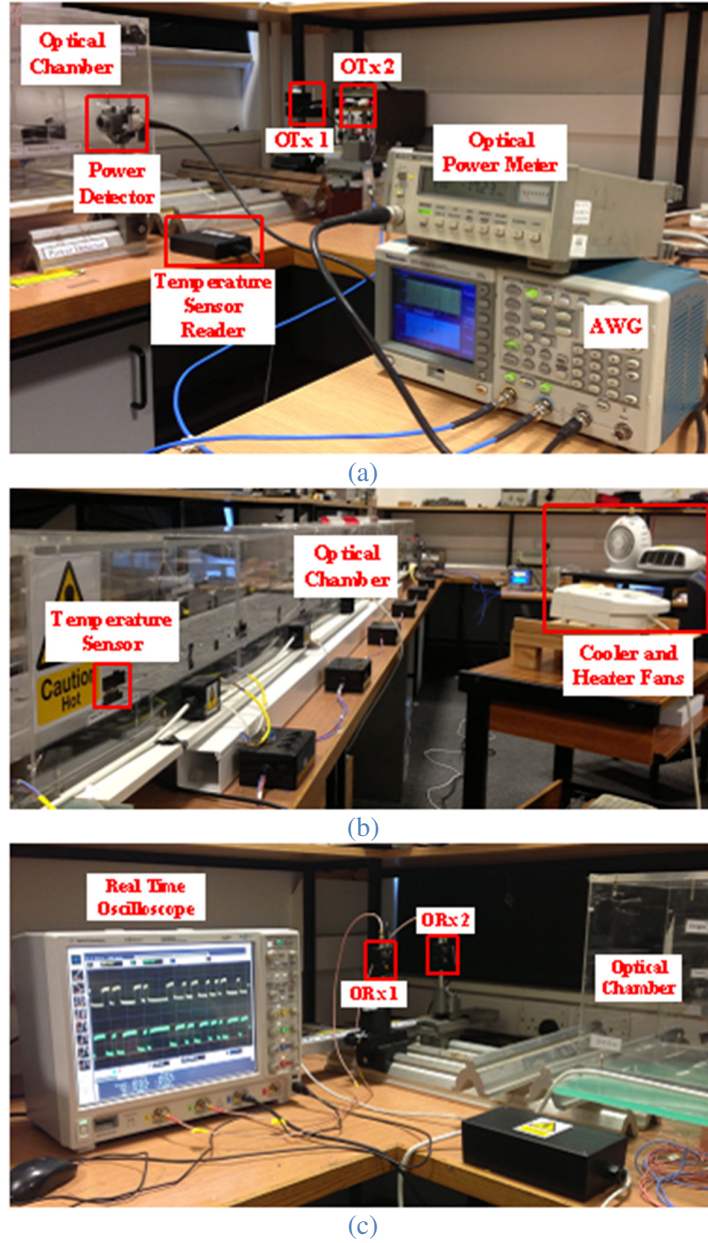


Figure D.6: Typical FSO experimental setup: (a) transmitter side, (b) channel, and (c) receiver side. OTx, AWG, ORx are optical transmitter, arbitrary waveform generator, and optical receiver, respectively.

Logically, the power detector should be used at the same location of Rx. However, in this case the ambient light was almost the same in the laboratory area, thus the power detector was used at the Tx side.

Depending on the experiment, the channel (see Figure D.6(b)) could be equipped with sophisticated accessories. For instance in the case of turbulence twenty thermal sensors (S1 to S20 in Figure D.5) were planted inside the chamber (ten on each side wall) at equal

distances. To generate turbulence, cooler and heater fans were used to blow hot and cool air into the optical chamber. According to [118] and [165] in a fixed pressure condition the turbulence is generated due to the temperature gradients along the optical channel. Thus by controlling the intensity of blowing air into the chamber one can change the gradient of temperature along the chamber and as a consequence can control the turbulence intensity.

The optical chamber was 5.5 m long with a cross section in shape of a 280 mm × 280 mm rectangle. The cooler and heater fans are set to blow air in this sub-chamber through the air vents of 60 mm × 85 mm size on the side wall.

An exhaust of the same size on the top wall was considered as the outlet. Using this structure, it is guaranteed that the artificial turbulence affects the beams where both pass through the same channel. The temperature sensors read the temperature every 4 seconds and were monitored during the experiment and after all the temperatures reached a stable status the measurements were carried out.

At the Rx side, the arrived optical power is converted to electrical signal by means of ORxs and a real time oscilloscope (in the experiments either Agilent DSO9254A infiniiium Mixed Signal Oscilloscope, or Agilent DSO80604B infiniiium High Performance Oscilloscope were used) was used to record the voltages. A virtual instrument script in National Instrument (NI) LabVIEW 2012 [166] was developed to control devices and record required data sets, see Figure D.5 and Figure D.7. The captured signals were processed in MATLAB. To evaluate the quality of each signal two parameters were extracted from the captured signals. The first parameters is normalized variance of the intensity fluctuation (σ_I^2) or scintillation index which is defined as [30]:

$$\sigma_I^2 = \frac{\langle I^2 \rangle}{\langle I \rangle^2} - 1, \quad (\text{D.2})$$

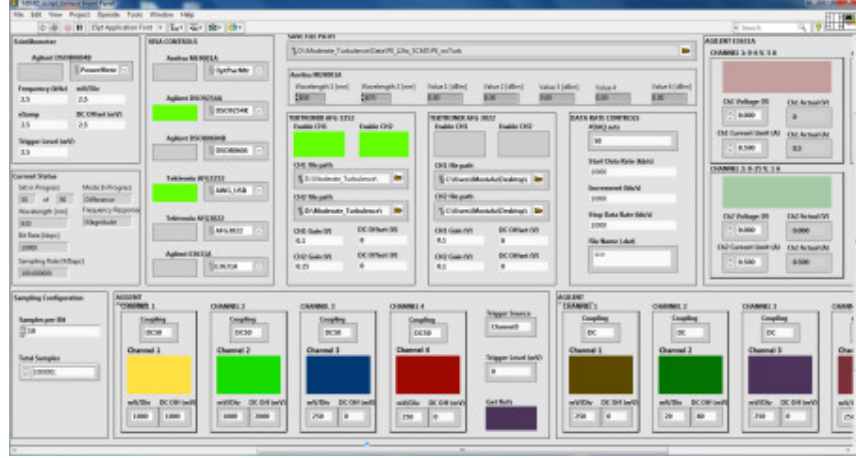


Figure D.7: The screenshot of the virtual instrument script created in NI LabVIEW.

where I is the received optical signal intensity and $\langle \cdot \rangle$ denotes ensemble average. Assuming that the received power over PD area A_{PD} is constant and by introducing the amplifier gain G_{TIA} and PD responsivity \mathcal{R} , one can write the received optical intensity as:

$$I = \frac{v}{G_{TIA} A_{PD} \mathcal{R}}, \quad (D.3)$$

where v is the ORx output voltage. Thus (12) can be rewritten as:

$$\sigma_I^2 = \frac{\langle v^2 \rangle}{\langle v \rangle^2} - 1. \quad (D.4)$$

σ_I^2 can be used to evaluate the effect of turbulence inside the chamber on the optical signal so that $\sigma_I^2 \ll 1$ and $\sigma_I^2 \gg 1$ denote weak and strong turbulences [91]. Another parameter which quantifies the optical link performance is Q-factor calculated as following [116]:

$$Q = \frac{v_H - v_L}{\sigma_H + \sigma_L}, \quad (D.5)$$

where v_H and v_L denote average of received high and low voltages. σ_H and σ_L also refer to standard deviations for high and low voltages, respectively. In MATLAB each captured signal is filtered using a second order Butterworth digital low pass filter with a cut-off frequency twice as signal bandwidth. Since in most practical optical Rx's the received

signal is AC coupled, the DC component of the captured signal is removed from the signal thus Eqs. (D.4) and (D.5) consider only AC part of received signal. The signal is then sampled at the middle of each bit and entire calculations of Eqs. (D.4) and (D.5) are carried out using these sampled values.

To calculate C_n^2 , first the recorded temperatures are averaged to obtain twenty mean temperature values. Knowing the thermal distribution along the FSO path, it is possible to determine the temperature structure constant C_T^2 , which depends on the temperature difference between two selected adjacent thermal sensors $T_1 - T_2$ distant by $L_{p,i}$ as [30]:

$$C_T^2|_i = (T_i - T_{i+1})^2 / L_{p,i}^{2/3}. \quad (D.6)$$

The refractive index structure parameter $C_n^2|_i$ is given as [30]:

$$C_n^2|_i = (79 \times 10^{-6} \frac{P}{T_{avg}^2})^2 C_T^2|_i, \quad (D.7)$$

where P is the atmospheric pressure in millibar and $T_{avg} = (T_i + T_{i+1})/2$ is the average temperature in Kelvin. Thus the variance of log-intensity signal fluctuation defined by Rytov variance σ_R^2 is given by [91]:

$$\sigma_R^2 = 1.23 k^{\frac{7}{6}} \sum_{i=\{1,3,\dots,19\}} C_n^2|_i \times L_{p,i}, \quad (D.8)$$

where $k = 2\pi/\lambda$ is the wavenumber, and λ is the transmission wavelength.

To obtain the detection threshold level of a stream of bits, first both high and low levels of signal corresponding to bits ‘1’ and ‘0’ were extracted. Then by performing the averaging over the adjacent high and low bits, the appropriate detection threshold level was determined. In this thesis averaging was performed for the sequential bit stream of ‘0’ and ‘1’.

APPENDIX E: STUDENT'S T-TEST

E.1 Introduction

The experimental investigation generated a large sets of raw data which were statistically processed in MATLAB. In particular, the data related to the differential signalling were taken for uncorrelated and correlated channels; and it was shown that there is a significant enhancement in term of detection threshold standard variation when channels are correlated. In this Appendix, the t-test method is adopted to show that the observed enhancement is statistically significant.

E.2 Student's t-test

A t-test is a statistical exercise based on the t-distribution, which is used to show if two sets of data are significantly different [167]. Consider two sets of data X and Y , where both have normal distributions. Based on the t-test, a null hypothesis means that mean values of $X - Y$ is zero (i.e., X and Y have the same mean value).

By setting $d = X - Y$, one can define t_s as:

$$t_s = \frac{\bar{d}}{\sigma_d/\sqrt{n}}, \quad (\text{E.1})$$

where \bar{d} , σ_d , and n are mean value, standard deviation, and number of samples of d , respectively. With t_s and defining the degree of freedom as $n - 2$, a null hypothesis is assumed and by using the t-distribution the p -value for the observed data is determined.

In MATLAB, the *ttest* function can be used to perform the test. Outputs of the function are H and p , which are interpreted as:

1. If $H = 0$ then t-test does not reject the null hypothesis at 5% significance level.
2. If $H = 1$ then t-test rejects null hypothesis at 5% significance level.
3. A small p means that null hypothesis is not valid.

E.3 Results

Table E.1 summarises the t-test results for the measured differential signalling data. The obtained detection threshold levels for uncorrelated and correlated data sets are used as the input data.

Table E.1: Student's t-test calculated results for performed differential signalling experiments in the thesis. For each case, uncorrelated and correlated data sets are used as input data.

Experiment	Section	t_s	Calculated H	Calculated p -value
Turbulence, dark room	4.3.6	2.5×10^4	1	0
Turbulence lit room	4.3.6	2.9×10^4	1	0

References

- [1] <https://support.apple.com/en-gb/HT201587>, access date: 10/07/2016.
- [2] F. Nadeem, B. Geiger, E. Leitgeb, S. S. Muhammad, M. Loeschig, and G. Kandus, "Comparison of link selection algorithms for free space optics/radio frequency hybrid network," *IET Commun.*, vol. 5, pp. 2751-2759, 2011.
- [3] A. Eslami, S. Vangala, and H. Pishro-Nik, "Hybrid channel codes for efficient FSO/RF communication systems," *IEEE Trans. Commun.*, vol. 58, pp. 2926-2938, 2010.
- [4] F. Nadeem, E. Leitgeb, M. S. Awan, and G. Kandus, "FSO/RF hybrid network availability analysis under different weather condition," in *Next Generation Mobile Applications, Services and Technologies, 2009. NGMAST '09. Third International Conference on*, 2009, pp. 239-244.
- [5] S. Vangala and H. Pishro-Nik, "Optimal hybrid RF-wireless optical communication for maximum efficiency and reliability," in *Information Sciences and Systems, 2007. CISS '07. 41st Annual Conference on*, 2007, pp. 684-689.
- [6] F. Nadeem, E. Leitgeb, M. S. Awan, and G. Kandus, "Forward prediction of FSO received signal for FSO/RF hybrid network," in *Satellite and Space Communications, 2009. IWSSC 2009. International Workshop on*, 2009, pp. 196-200.
- [7] M. A. Khalighi and M. Uysal, "Survey on free space optical communication: a communication theory perspective," *IEEE Commun. Surveys Tuts.*, vol. 16, pp. 2231-2258, 2014.
- [8] F. Nadeem, M. Gebhart, E. Leitgeb, W. Kogler, M. S. Awan, M. S. Khan, and G. Kandus, "Simulations and analysis of bandwidth efficient switch-over between FSO and mmW links," in *Software, Telecommunications and Computer Networks, 2008. SoftCOM 2008. 16th International Conference on*, 2008, pp. 356-361.
- [9] W. Popoola, "Subcarrier intensity modulated free-space optical communication systems," Doctoral, School of Computing, Engineering and Information Sciences, Northumbria University, 2009.

- [10] X. Tang, E. University of Northumbria at Newcastle. School of Computing, and I. Sciences., *Polarisation shift keying modulated free-space optical communication systems*, 2012.
- [11] <http://www.freespaceoptics.org/>, access date: 22/10/2015.
- [12] <http://www.fsona.com/index.php>, access date: 22/10/2015.
- [13] D. Rodewald, "MRV introduces industry's first 10G ethernet wireless point-to-point system," MRV Communications, Inc, Chatsworth, CA, USA2008.
- [14] G. T. Djordjevic, M. I. Petkovic, A. M. Cvetkovic, and G. K. Karagiannidis, "Mixed RF/FSO relaying with outdated channel state information," *IEEE J. Sel. Areas Commun.*, vol. 33, pp. 1935-1948, 2015.
- [15] L. Jeong-Ho and H. Seung-Hoon, "Selection diversity-aided subcarrier intensity modulation/spatial modulation for free-space optical communication," *IET Optoelectr.*, vol. 9, pp. 116-124, 2015.
- [16] Z. Jiayi, D. Linglong, Z. Yu, and W. Zhaocheng, "Unified performance analysis of mixed radio frequency/free-space optical dual-Hop transmission systems," *J. Lightw. Technol.*, vol. 33, pp. 2286-2293, 2015.
- [17] Z. Ghassemlooy, S. Rajbhandari, and W. Popoola, *Optical wireless communications: system and channel modelling with MATLAB*. Boca Raton, FL: Taylor & Francis, 2013.
- [18] H. Willebrand and B.S.Ghuman, "Free space optics: enabling optical connectivity in today's networks," *Sams Publishing, London*, 2002.
- [19] A. Sikora and V. F. Groza, "Coexistence of IEEE802. 15.4 with other Systems in the 2.4 GHz-ISM-Band," in *Instrumentation and Measurement Technology Conference, 2005. IMTC 2005. Proceedings of the IEEE*, 2005, pp. 1786-1791.
- [20] L. Rakotondrainibe, Y. Kokar, G. Zaharia, and G. El-Zein, "60 GHz high data rate wireless communication system," in *Vehicular Technology Conference, 2009. VTC Spring 2009. IEEE 69th*, 2009, pp. 1-5.
- [21] D. Sinefeld, D. Shayovitz, O. Golani, and D. M. Marom, "Adaptive rate and bandwidth WDM optical sampling pulse streams with LCoS-based photonic spectral processor," in *Optical Fiber Communication Conference*, 2013.
- [22] J. I. Saari, M. M. Krause, B. R. Walsh, and P. Kambhampati, "Terahertz bandwidth all-optical modulation and logic using multiexcitons in semiconductor nanocrystals," *Nano letters*, 2013.

- [23] G. e.-S. Initiative, "SMART 2020: Enabling the low carbon economy in the information age," *press release, Brussels, Belgium, June*, vol. 20, 2008.
- [24] A. Chaaban, J. Morvan, and M. Alouini, "Free-space optical communications: capacity bounds, approximations, and a new sphere-packing perspective," *IEEE Trans. Commun.*, vol. PP, pp. 1-1, 2016.
- [25] M. Bhatnagar and Z. Ghassemlooy, "Performance analysis of Gamma-Gamma Fading FSO MIMO links with pointing errors," *J. Lightw. Technol.*, vol. PP, pp. 1-1, 2016.
- [26] X. Li, N. Bamiedakis, X. Guo, J. McKendry, E. Xie, R. Ferreira, E. Gu, M. Dawson, R. V. Pentty, and I. H. White, "Wireless visible light communications employing feed-forward pre-equalization and PAM-4 modulation," *J. Lightw. Technol.*, vol. PP, pp. 1-1, 2016.
- [27] A. S. Hamza, J. S. Deogun, and D. R. Alexander, "Wireless communication in data centers: a survey," *IEEE Commun. Surveys Tuts.*, vol. PP, pp. 1-1, 2016.
- [28] P. Jaedon, L. Eunju, C. Chan-Byoung, and Y. Giwan, "Outage probability analysis of a coherent FSO amplify-and-forward relaying system," *IEEE Photon. Technol. Lett.*, vol. 27, pp. 1204-1207, 2015.
- [29] K. Kikuchi, "Fundamentals of coherent optical fiber communications," *J. Lightw. Technol.*, vol. 34, pp. 157-179, 2016.
- [30] L. C. Andrews and R. L. Phillips, *Laser beam propagation through random media*, Second Edition (SPIE Press Monograph Vol. PM152) ed.: SPIE Publications, 2005.
- [31] J. Libich and S. Zvanovec, "Measurement statistics of three joint wireless optical links," in *Optical Wireless Communications (IWOW), 2012 International Workshop on*, 2012, pp. 1-3.
- [32] M. Ijaz, Z. Ghassemlooy, J. Pesek, O. Fiser, H. Le Minh, and E. Bentley, "Modeling of fog and smoke attenuation in free space optical communications link under controlled laboratory conditions," *J. Lightw. Technol.*, vol. 31, pp. 1720-1726, 2013.
- [33] M. Ijaz, "Experimental characterisation and modelling of atmospheric fog and turbulence in FSO," Doctoral, Faculty of Engineering and Environment, Northumbria University, 2013.
- [34] Y. Fan, C. Julian, and T. A. Tsiftsis, "Free-space optical communication with nonzero boresight pointing errors," *IEEE Trans. Commun.*, vol. 62, pp. 713-725, 2014.
- [35] M. A. Khalighi, F. Xu, Y. Jaafar, and S. Bourennane, "Double-laser differential signaling for reducing the effect of background radiation in free-space optical systems," *J. Opt. Commun. Netw.*, vol. 3, pp. 145-154, 2011.

- [36] M. Gregory and P. A. Hoeher, "Adaptive channel coding for maritime FSO channels with RF feedback link," in *Space Optical Systems and Applications (ICSOS), 2011 International Conference on*, 2011, pp. 351-357.
- [37] E. Leitgeb, M. Gebhart, U. Birnbacher, W. Kogler, and P. Schrotter, "High availability of hybrid wireless networks," *SPIE Proceedings*, vol. 5465, pp. 238-249, 2004.
- [38] N. Letzepis, K. D. Nguyen, Guille, x, F. n i, x, A. bregas, and W. G. Cowley, "Hybrid free-space optical and radio-frequency communications: Outage analysis," in *Information Theory Proceedings (ISIT), 2010 IEEE International Symposium on*, 2010, pp. 2048-2052.
- [39] M. Gregory and S. Badri-Hoeher, "Characterization of maritime RF/FSO channel," in *Space Optical Systems and Applications (ICSOS), 2011 International Conference on*, 2011, pp. 21-27.
- [40] H. Moradi, M. Falahpour, H. H. Reafi, P. G. LoPresti, and M. Atiquzzaman, "Availability modeling of FSO/RF mesh networks through turbulence-induced fading channels," in *INFOCOM IEEE Conference on Computer Communications Workshops , 2010*, 2010, pp. 1-5.
- [41] F. Nadeem, E. Leitgeb, and G. Kandus, "Comparing the cloud effects on hybrid network using optical wireless and GHz links," in *Communication Systems Networks and Digital Signal Processing (CSNDSP), 2010 7th International Symposium on*, 2010, pp. 553-557.
- [42] F. Nadeem, V. Kvicera, M. S. Awan, E. Leitgeb, S. Muhammad, and G. Kandus, "Weather effects on hybrid FSO/RF communication link," *IEEE J. Sel. Areas Commun.*, vol. 27, pp. 1687-1697, 2009.
- [43] K. Kumar and D. K. Borah, "Hybrid symbols for parallel optical/rf channels using BICM-ID," *IET Electr. Lett.*, vol. 47, pp. 1189-1190, 2011.
- [44] H. Tapse, D. K. Borah, and J. Perez-Ramirez, "Hybrid optical/RF channel performance analysis for turbo codes," *IEEE Trans. Commun.*, vol. 59, pp. 1389-1399, 2011.
- [45] N. Trung Thanh and L. Lampe, "Channel coding diversity with mismatched decoding metrics," *IEEE Commun. Lett*, vol. 15, pp. 916-918, 2011.
- [46] Y. Tang, M. Brandt-Pearce, and S. G. Wilson, "Adaptive coding and modulation for hybrid FSO/RF systems," in *Signals, Systems and Computers, 2009 Conference Record of the Forty-Third Asilomar Conference on*, 2009, pp. 1644-1649.
- [47] Y. Tang, M. Brandt-Pearce, and S. G. Wilson, "Link adaptation for parallel channels with encoder rate and modem symbol rate

- constraints," in *GLOBECOM Workshops (GC Wkshps), 2010 IEEE*, 2010, pp. 1000-1004.
- [48] I. B. Djordjevic, "Coding for free space optical communications," in *IEEE Lasers and Electro-Optics Society, 2008. LEOS 2008. 21st Annual Meeting of the*, 2008, pp. 884-885.
 - [49] J. Liao, J. Zeng, S. Deng, V. Joyner, A. Boryssenko, K. Connor, and Z. R. Huang, "Packaging of optoelectronic and RF components with shared elements for dual-mode wireless communications," *IET Electr. Lett.*, vol. 45, pp. 411-412, 2009.
 - [50] L. Jun, Z. Juan, D. Shengling, A. O. Boryssenko, V. M. Joyner, and Z. R. Huang, "Packaging of dual-mode wireless communication module using RF/optoelectronic devices with shared functional components," *IEEE Trans. Adv. Packag.*, vol. 33, pp. 323-332, 2010.
 - [51] J. R. Bruzzi and B. G. Boone, "Dual band radio frequency (RF) and optical communications antenna and terminal design methodology and implementation," US8094081 B1, 2012.
 - [52] S. Wilcken and J. S. Clair, "Hybrid RF/optical communication system with deployable optics and atmosphere compensation system and method," US20060008274 A1, 2006.
 - [53] G. Keiser, *Optical fiber communications*, 4th ed. ed. New York: McGraw-Hill Companies, 2011.
 - [54] http://www.digikey.com.au/Web%20Export/Supplier%20Content/RFM_583/PDF/rfm-an-ook-ask-fsk-comparison.pdf, access date: 12/07/2016.
 - [55] G. P. Agrawal, *Fiber-optic communication systems*, 4th ed. ed. New York: Wiley, 2010.
 - [56] K. Tsukamoto, A. Hashimoto, Y. Aburakawa, and M. Matsumoto, "The case for free space," *IEEE Microw. Mag.*, vol. 10, pp. 84-92, 2009.
 - [57] B. E. A. Saleh and M. C. Teich, *Fundamentals of photonics*. New York, Chichester: Wiley, 1991.
 - [58] <https://webstore.iec.ch/publication/3587>, access date: 03/02/2016.
 - [59] <https://www.lia.org/store/ANSI+Z136+Standards>, access date: 03/02/2016.
 - [60] <http://standards.globalspec.com/std/9861660/cenelec-en-60825-1>, access date: 03/02/2016.
 - [61] https://www.lia.org/PDF/Z136_1_s.pdf, access date: 21/08/2016.
 - [62] P. Ales, "Atmospheric effects on availability of free space optics systems," *Optical Eng.*, vol. 48, p. 066001, 2009.
 - [63] M. Ijaz, Z. Ghassemloooy, J. Perez, V. Brazda, and O. Fiser, "Enhancing the atmospheric visibility and fog attenuation using a

- controlled FSO channel," *IEEE Photon. Technol. Lett.*, vol. 25, pp. 1262-1265, 2013.
- [64] J. M. Kahn and J. R. Barry, "Wireless infrared communications," *Proc. IEEE*, vol. 85, pp. 265-298, 1997.
 - [65] H. E. Nistazakis, A. N. Stassinakis, Sinanovic, x, S., W. O. Popoola, and G. S. Tombras, "Performance of quadrature amplitude modulation orthogonal frequency division multiplexing-based free space optical links with non-linear clipping effect over Gamma-Gamma modelled turbulence channels," *IET Optoelectr.*, vol. 9, pp. 269-274, 2015.
 - [66] D. K. Borah and D. G. Voelz, "Pointing error effects on free-space optical communication links in the presence of atmospheric turbulence," *J. Lightw. Technol.*, vol. 27, pp. 3965-3973, 2009.
 - [67] G. r. Maral, M. Bousquet, and Z. P. Sun, *Satellite communications systems: systems, techniques and technology*, 5th ed. ed. Chichester, West Sussex, U.K: John Wiley, 2009.
 - [68] D. J. Cohen, "Necessary bandwidth of digital modulation," in *Electromagnetic Compatibility, 1988. Symposium Record., IEEE 1988 International Symposium on*, 1988, pp. 247-251.
 - [69] A. W. Rudge, *The Handbook of antenna design; Volumes 1 and 2*. Stevenage: Peregrinus on behalf of the Institution of Electrical Engineers, 1986.
 - [70] C. A. Balanis, *Antenna theory: analysis and design*, 3rd ed. ed. Hoboken, N.J [Great Britain]: Wiley-Interscience, 2005.
 - [71] http://www.ofcom.org.uk/static/archive/ra/publication/ra_info/ra365.htm, access date: 20/11/2015.
 - [72] J. R. Norbury, C. J. Gibbins, and D. N. Matheson, "A study into the theoretical appraisal of the highest usable frequencies," Radio Communications Research Unit 2003.
 - [73] "Specific attenuation model for rain for use in prediction methods," Rec. ITU-R P.838-3, 2005.
 - [74] J. P. Camacho, *Federal radar spectrum requirements [microform] / report author: Joseph P. Camacho*. [Washington, D.C.] :: U.S. Dept. of Commerce, National Telecommunications and Information Administration, 2000.
 - [75] <http://www.phys.hawaii.edu/~anita/new/papers/militaryHandbook/antennas.pdf>, access date: 12/07/2016.
 - [76] L. D. P. D. R. Office of Engineering and Technology, *Guidance determining ERP and EIRP*. Washington, D.C. :: U.S. G.P.O., Supt. of Docs, 2010.
 - [77] R. P. Standard, "Maximum exposure levels to radiofrequency fields—3 KHz to 300 GHz," *Radiation Protection Series*, 2002.

- [78] "Attenuation due to clouds and fog," Rec. ITU-R P.840-3, 1999.
- [79] Z. Wenzhe, H. Steve, and S. Ce, "Soft-switching hybrid FSO/RF links using short-length Raptor codes," *IEEE J. Sel. A. Commun.*, vol. 27, pp. 1698-1708, 2009.
- [80] S. Bloom and W. S. Hartley, "The last-mile solution: hybrid FSO radio," *white paper available at <http://www.airfiber.com/index.shtml>*, 2002.
- [81] M. Tatarko, L. Ovsenik, and J. Turan, "Management of switching in hybrid FSO/RF link," in *Carpathian Control Conference (ICCC), 2015 16th International*, 2015, pp. 532-536.
- [82] Z. Wenzhe, S. Hranilovic, and S. Ce, "Soft-switching hybrid FSO/RF links using short-length raptor codes: design and implementation," *IEEE J. Sel. Areas Commun.*, vol. 27, pp. 1698-1708, 2009.
- [83] F. Nadeem, B. Geiger, E. Leitgeb, S. S. Muhammad, M. Loeschnig, and G. Kandus, "Comparison of link selection algorithms for free space optics/radio frequency hybrid network," *IET Commun.*, vol. 5, pp. 2751-2759.
- [84] F. Nadeem, B. Geiger, E. Leitgeb, M. S. Awan, and G. Kandus, "Evaluation of switch-over algorithms for hybrid FSO-WLAN systems," in *Wireless Communication, Vehicular Technology, Information Theory and Aerospace & Electronic Systems Technology, 2009. Wireless VITAE 2009. 1st International Conference on*, 2009, pp. 565-570.
- [85] S. M. Navidpour, M. Uysal, and M. Kavehrad, "BER performance of free-space optical transmission with spatial diversity," *IEEE Trans. Wireless Commun.*, vol. 6, pp. 2813-2819, 2007.
- [86] W. Zixiong, Z. Wen-De, F. Songnian, and L. Chinlon, "Performance comparison of different modulation formats over free-space optical (FSO) turbulence links with space diversity reception technique," *IEEE Photon. J.*, vol. 1, pp. 277-285, 2009.
- [87] K. P. Peppas and P. T. Mathiopoulos, "Free-space optical communication with spatial modulation and coherent detection over H-K atmospheric turbulence channels," *J. Lightw. Technol.*, vol. 33, pp. 4221-4232, 2015.
- [88] X. Zhu and J. M. Kahn, "Free-space optical communication through atmospheric turbulence channels," *IEEE Trans. Commun.*, vol. 50, pp. 1293-1300, 2002.
- [89] G. R. Osche, *Optical detection theory for laser applications*. New York: Wiley, 2002.
- [90] C. Zhixiao, Y. Song, W. Tianyi, W. Guohua, W. Shaoling, and G. Wanyi, "Channel correlation in aperture receiver diversity systems for

- free-space optical communication," *J. Optics*, vol. 14, p. 125710, 2012.
- [91] R. L. Fante, "Electromagnetic beam propagation in turbulent media," *Proc. IEEE*, vol. 63, pp. 1669-1692, 1975.
 - [92] Z. Hajjarian, J. Fadlullah, and M. Kavehrad, "MIMO free space optical communications in turbid and turbulent atmosphere (Invited Paper)," *Journal of Communications*, vol. 4, pp. 524-532, 2009.
 - [93] M. A. Khalighi, N. Schwartz, N. Aitamer, and S. Bourennane, "Fading reduction by aperture averaging and spatial diversity in optical wireless systems," *J. Opt. Commun. Netw.*, vol. 1, pp. 580-593, 2009.
 - [94] C. Abou-Rjeily and S. Haddad, "Inter-relay cooperation: a new paradigm for enhanced relay-assisted FSO communications," *IEEE Trans. Commun.*, vol. 62, pp. 1970-1982, 2014.
 - [95] N. D. Chatzidiamantis and G. K. Karagiannidis, "On the distribution of the sum of Gamma-Gamma variates and applications in RF and optical wireless communications," *IEEE Trans. Commun.*, vol. 59, pp. 1298-1308, 2011.
 - [96] R. Paudel, Z. Ghassemlooy, H. Le Minh, S. Rajbhandari, and E. Leitgeb, "Lambertian source modelling of free space optical ground-to-train communications," presented at the CSNDSP 2012: 8th International Symposium on Communication Systems, Networks and Digital Signal Processing, Poznan, Poland, 2012.
 - [97] M. A. Kashani, M. Uysal, and M. Kavehrad, "A novel statistical channel model for turbulence-induced fading in free-space optical systems," *J. Lightw. Technol.*, vol. 33, pp. 2303-2312, 2015.
 - [98] R. S. Kennedy, "Communication through optical scattering channels: An introduction," *Proc. IEEE*, vol. 58, pp. 1651-1665, 1970.
 - [99] R. Kennedy and E. Hoversten, "On the atmosphere as an optical communication channel," *IEEE Transactions on Information Theory*, vol. 14, pp. 716-725, 1968.
 - [100] M. Razavi and J. H. Shapiro, "Wireless optical communications via diversity reception and optical preamplification," *IEEE Trans. Wireless Commun.*, vol. 4, pp. 975-983, 2005.
 - [101] A. A. Abu-Dayya and N. C. Beaulieu, "Comparison of methods of computing correlated lognormal sum distributions and outages for digital wireless applications," in *Vehicular Technology Conference, 1994 IEEE 44th*, 1994, pp. 175-179 vol.1.
 - [102] I. A. Stegun and M. Abramowitz, *Handbook of mathematical functions: with formulas, graphs and mathematical tables*. [S.l.]: National Bureau of Standards, 1970.

- [103] T. A. Tsiftsis, H. G. Sandalidis, G. K. Karagiannidis, and M. Uysal, "Optical wireless links with spatial diversity over strong atmospheric turbulence channels," *IEEE Trans. Wireless Commun.*, vol. 8, pp. 951-957, 2009.
- [104] T. Eng, "On majority-logic diversity combining in Rayleigh fading," in *Military Communications Conference, 1996. MILCOM '96, Conference Proceedings, IEEE*, 1996, pp. 1055-1058 vol.3.
- [105] I. S. Gradshtein, A. Jeffrey, and I. M. Ryzhik, *Table of integrals, series, and products*, 5th ed. ed. Boston, London: Academic Press, 1994.
- [106] S. Tianyu and K. Pooi-Yuen, "A robust GLRT receiver with Implicit channel estimation and automatic threshold adjustment for the free space optical channel with IM/DD," *J. Lightw. Technol.*, vol. 32, pp. 369-383, 2014.
- [107] S. Hitam, M. Abdullah, M. Mahdi, H. Harun, A. Sali, and M. Fauzi, "Impact of increasing threshold level on higher bit rate in free space optical communications," *J. Opt. Fiber Commun. Res.*, vol. 6, pp. 22-34, 2009/12/01 2009.
- [108] M. R. Bhatnagar and Z. Ghassemlooy, "Performance evaluation of FSO MIMO links in Gamma-Gamma fading with pointing errors," in *Communications (ICC), 2015 IEEE International Conference on*, 2015, pp. 5084-5090.
- [109] X. Zhu and J. M. Kahn, "Markov chain model in maximum-likelihood sequence detection for free-space optical communication through atmospheric turbulence channels," *IEEE Trans. Commun.*, vol. 51, pp. 509-516, 2003.
- [110] X. Zhu and J. M. Kahn, "Pilot-symbol assisted modulation for correlated turbulent free-space optical channels," in *Proc. SPIE 4489, Free-Space Laser Communication and Laser Imaging*, 2002, pp. 138-145.
- [111] M. L. B. Riediger, R. Schober, and L. Lampe, "Fast multiple-symbol detection for free-space optical communications," *IEEE Trans. Commun.*, vol. 57, pp. 1119-1128, 2009.
- [112] I. S. Ansari, M. S. Alouini, and J. Cheng, "Ergodic capacity analysis of free-space optical links with nonzero boresight pointing errors," *IEEE Trans. Wireless Commun.*, vol. 14, pp. 4248-4264, 2015.
- [113] H. Moradi, H. H. Refai, and P. G. LoPresti, "Spatial diversity for fiber-bundled FSO nodes with limited mobility," *J. Lightw. Technol.*, vol. 30, pp. 175-183, 2012.
- [114] K. Yoshida, K. Tanaka, T. Tsujimura, and Y. Azuma, "Assisted focus adjustment for free space optics system coupling single-mode optical fibers," *IEEE Trans. Ind. Electron.*, vol. 60, pp. 5306-5314, 2013.

- [115] A. Leon-Garcia, *Probability and random processes for electrical engineering*. Reading, Mass: Addison-Wesley, 1989.
- [116] "G.976 : Test methods applicable to optical fibre submarine cable systems," in *ITU-T Recommendation G.976*, ed: ITU, 06/2004.
- [117] D. P. Greenwood, "Bandwidth specification for adaptive optics systems," *J. Opt. Soc. Am.*, vol. 67, pp. 390-393, 1977/03/01 1977.
- [118] Z. Ghassemlooy, H. Le Minh, S. Rajbhandari, J. Perez, and M. Ijaz, "Performance analysis of ethernet/fast-ethernet free space optical communications in a controlled weak turbulence condition," *J. Lightw. Technol.*, vol. 30, pp. 2188-2194, 2012.
- [119] G. Yang, M. A. Khalighi, S. Bourennane, and Z. Ghassemlooy, "Fading correlation and analytical performance evaluation of the space-diversity free-space optical communications system," *J. Optics*, vol. 16, p. 035403, 2014.
- [120] A. A. Farid and S. Hranilovic, "Outage capacity optimization for free-space optical links with pointing errors," *J. Lightw. Technol.*, vol. 25, pp. 1702-1710, 2007.
- [121] D. K. Borah, D. Voelz, and S. Basu, "Maximum-likelihood estimation of a laser system pointing parameters by use of return photon counts," *Applied Optics*, vol. 45, pp. 2504-2509, 2006/04/10 2006.
- [122] R. Forster, "Manchester encoding: opposing definitions resolved," *Eng. Scien. Educ. J.*, vol. 9, pp. 278-280, 2000.
- [123] <https://www.cst.com/Products/CSTMWS>, access date: 24/08/2015.
- [124] A. W. Rudge and N. A. Adatia, "Offset-parabolic-reflector antennas: a review," *Proc. IEEE*, vol. 66, pp. 1592-1618, 1978.
- [125] L. Tingye, "A study of spherical reflectors as wide-angle scanning antennas," *IEEE Trans. Antennas Propag*, vol. 7, pp. 223-226, 1959.
- [126] C. J. E. Phillips and P. J. B. Clarricoats, "Optimum design of a Gregorian-corrected spherical-reflector antenna," *Proc. Instit. Electr. Eng.*, vol. 117, pp. 718-734, 1970.
- [127] P. Hannan, "Microwave antennas derived from the cassegrain telescope," *IEEE Trans. Antennas Propag*, vol. 9, pp. 140-153, 1961.
- [128] P. J. B. Clarricoats and C. E. R. C. Salema, "Antennas employing conical-dielectric horns. Part 2: The Cassegrain antenna," *Proc. Instit. Electr. Eng.*, vol. 120, pp. 750-756, 1973.
- [129] P. J. B. Clarricoats and G. T. Poulton, "High-efficiency microwave reflector antennas-a review," *Proc. IEEE*, vol. 65, pp. 1470-1504, 1977.
- [130] T. Milligan, *Modern Antenna Design*, 1 ed.: Wiley-IEEE Press, 2005.
- [131] J. R. Fisher, "Prime focus efficiency, blockage, spillover, and scattering calculations on the HP 9825A calculator," National Radio

Astronomy Observatory, Green Bank, West Virginia November 1976
1976.

- [132] A. W. Rudge and N. A. Adatia, "New class of primary-feed antennas for use with offset parabolic-reflector antennas," *IET Electr. Lett.*, vol. 11, pp. 597-599, 1975.
- [133] G. T. Poulton, "The design of cassegrain antennas for high efficiency and low V.S.W.R.," in *Microwave Conference, 1975. 5th European*, 1975, pp. 61-65.
- [134] R. E. Collin, "Aperture efficiency for paraboloidal reflectors," *IEEE Trans. Antennas Propag.*, vol. 32, pp. 997-1000, 1984.
- [135] Norman Hodgson and H. Weber, *Laser resonators and beam propagation*: Springer-Verlag, 2005.
- [136] W. Gawronski, J. A. Mellstrom, and B. Bienkiewicz, "Antenna mean wind torques: a comparison of field and wind-tunnel data," *IEEE Antennas Propag. Mag.*, vol. 47, pp. 55-59, 2005.
- [137] G. D. Durgin, "The practical behavior of various edge-diffraction formulas," *IEEE Antennas Propag. Mag.*, vol. 51, pp. 24-35, 2009.
- [138] C. A. Balanis, *Advanced engineering electromagnetics*. New York, Chichester: Wiley, 1989.
- [139] S. Srikanth, "Aperture efficiency for prime focus paraboloidal reflectors and Cassegrain antennas," National Radio Astronomy Observatory, Green Bank, West Virginia 277, 1988.
- [140] S. B. Cohn, "Optimum design of stepped transmission-line transformers," *IEEE Trans. Microw. Theory Tech.*, vol. 3, pp. 16-20, 1955.
- [141] V.s.bagad, *Microwave engineering*: Technical Publications Pune, 2009.
- [142] B. Gimeno and M. Guglielmi, "Multimode equivalent network representation for H- and E-plane uniform bends in rectangular waveguide," *IEEE Trans. Microw. Theory Tech.*, vol. 44, pp. 1679-1687, 1996.
- [143] I. o. E. Engineers., R. H. Dicke, E. M. Purcell, and C. G. Montgomery, *Principles of microwave circuits*: Peregrinus on behalf of the Institution of Electrical Engineers, 1987.
- [144] D. M. Pozar, *Microwave engineering*, 2nd ed. ed. New York ,Chichester: Wiley, 1998.
- [145] A. J. Sangster, "Circularly polarized linear waveguide array," *IEEE Trans. Antennas Propag.*, vol. 21, pp. 704-705, 1973.
- [146] J. van Bladel, "Small holes in a waveguide wall," *Proc. Instit. Electr. Eng.*, vol. 118, pp. 43-50, 1971.

- [147] D. Marcuse, "Loss analysis of single-mode fiber splices," *Bell System Technical Journal*, vol. 56, pp. 703-718, 1977.
- [148] A. E. Siegman, *Lasers*. Mill Valley, Calif Oxford: University Science Books, 1986.
- [149] G.-I. Kweon, "Optical-amplifier noise-figure measurement by Q-factor analysis," *J. Korean Phys.Soc.*, vol. 43, pp. 714-721, 2003.
- [150] J. Alwan, "Eye safety and wireless optical networks (WONs)," *white paper available at <http://www.airfiber.com/index.shtml>*, 2001.
- [151] <http://www.research.northwestern.edu/ors/forms/laser-safety-handbook.pdf>, access date: 21/08/2016.
- [152] <http://www.awrcorp.com/products/microwave-office>, access date: 24/08/2015.
- [153] <http://www.lightwaveonline.com/articles/print/volume-17/issue-5/features/calculating-statistical-confidence-levels-for-error-probability-estimates-53462167.html>, access date: 21/08/2016.
- [154] <http://www.keysight.com/>, access date: 28/08/2015.
- [155] B. Razavi, *RF microelectronics*: Prentice Hall PTR, 1998
- [156] <http://www.3ds.com/products-services/solidworks/>, access date: 28/08/2015.
- [157] [https://en.wikipedia.org/wiki/STL_\(file_format\)](https://en.wikipedia.org/wiki/STL_(file_format)), access date: 28/08/2015.
- [158] https://en.wikipedia.org/wiki/3D_printing, access date: 28/08/2015.
- [159] <http://www.stratasys.com/3d-printers/design-series/objet24>, access date: 28/08/2015.
- [160] J. Goward, *Optical communication systems*, 2nd ed. ed. New York, London: Prentice Hall International, 1993.
- [161] O. Ziemann, J. Krauser, P. E. Zamzow, and W. Daum, *POF handbook optical short range transmission systems*, 2 ed.: Springer-Verlag Berlin Heidelberg, 2008.
- [162] <http://cp.literature.agilent.com/litweb/pdf/5965-7917E.pdf>, access date: 14/10/2015.
- [163] <http://www.nearfield.com/>, access date: 28/08/2015.
- [164] http://ww2.nearfield.com/amta/amta89_1.htm, access date: 28/08/2015.
- [165] H. Kaushal, V. Kumar, A. Dutta, H. Aennam, V. K. Jain, S. Kar, and J. Joseph, "Experimental study on beam wander under varying atmospheric turbulence conditions," *IEEE Photon. Technol. Lett.*, vol. 23, pp. 1691-1693, 2011.
- [166] <http://uk.ni.com/>, access date: 14/10/2015.

[167] https://www.encyclopediaofmath.org/index.php/Student_test, access date: 13/09/2016.